# Digital Low Level RF Control Techniques and Procedures Towards the International Linear Collider

# 国際リニアコライダーのための デジタル低電力高周波源の制御技術

M.Sc. Mathieu Omet

DOCTOR OF PHILOSOPHY

Department of Accelerator Science

School of High Energy Accelerator Science

The Graduate University for Advanced Studies

2014

| | |
|---|---|
| Supervisor: | Shinichiro Michizono |
| Head Examiner: | Eiji Kako |
| Examiner: | Hiroyuki Ao |
| | Toshihiro Matsumoto |
| | Kensei Umemori |
| | Seiya Yamaguchi |
| Day of final evaluation: | 31st of July 2014 |
| Day of submission: | 19th of September 2014 |

Für alle, die mich unterstützt haben.
For all who supported me.

# Abstract

In this work digital Low Level Radio Frequency (LLRF) control techniques and procedures developed and successfully tested in the scope of the International Linear Collider (ILC) are described.

One central requirement for the operation of ILC is the high gradient near (5% below) quench limit operation during the whole flattop of multiple cavities driven by a single klystron. In order to achieve such an operation, for every cavity the driving power ($P_k$) and the loaded quality factor ($Q_L$) have to be controlled individually. Thus this operation mode is called $P_kQ_L$ operation. At the superconducting RF test facility (STF) at KEK in the scope of the Quantum Beam (QB) project two superconducting 9–cell cavities were driven by a single klystron. At this setup an automated procedure was developed and tested, resulting in the world's first actual and fully successful $P_kQ_L$ operation. A stable one hour long–time run with a beam of in average 6.4 mA current was achieved. The cavity gradients were 16 and 24 MV/m and with this 5% below the virtual quench limits of 16.8 and 25.2 MV/m. The achieved vector sum gradient and phase stabilities were $\Delta A/A = 0.009\%$ and $\Delta\phi = 0.009°$, respectively. Furthermore in a simulation a successful automated $P_kQ_L$ setting procedure and $P_kQ_L$ operation for 39 cavities fulfilling all ILC requirements were demonstrated.

Due to the $P_kQ_L$ operation a further requirement in scope of ILC is to operate the cavities at high loaded quality factors. In order to demonstrate the feasibility of such an operation, the loaded quality factors of both superconducting 9–cell cavities at KEK STF in the scope of the QB project were set to $Q_{L,cav1} = Q_{L,cav2} = 2 \cdot 10^7$. Under this condition a stable one hour long–time operation with a beam of in average 6.1 mA current was conducted. Both cavity gradients were 20 MV/m. The achieved vector sum gradient and phase stabilities were $\Delta A/A = 0.011\%$ and $\Delta\phi = 0.015°$, respectively.

At ILC it is planned to operate the klystrons 7% in power below their full saturation. Due to the saturation behavior in amplitude the control gain converts to 0 at this region, which inhibits effective control. In order to keep the control gain constant up to the point of saturation and with this allowing effective control up to this point, predistortion–type FPGA–based klystron linearization algorithms were decided to be used. Four different kinds of algorithms have been developed, successfully tested, and compared. The best algorithm is based on lookup tables combined with a linear interpolation. In a simulation it was demonstrated that an extension of this algorithm with an adaptive grid spacing further improves the linearization performance.

For offline tests of the klystron linearization algorithms an FPGA–based klystron and cavity simulator was developed, implemented, and tested.

# Zusammenfassung

In der vorliegenden Arbeit wird die Entwicklung und der erfolgreiche Test von digitalen Low Level Radio Frequency (LLRF) Prozeduren beschrieben, die nötig für den Betrieb des zukünftigen International Linear Collider (ILC) sind.

Eine zentrale Anforderung für den Betrieb des ILC ist der Betrieb vieler Kavitäten, die durch einen einzelnen Klystron betrieben werden, mit hohen Gradienten nahe (5% unterhalb) ihrer individuellen Quenchlimits über das gesamt Flattop hinweg. Um dies zu erreichen, müssen für jede Kavität einzeln die zugefürten Leistungen ($P_k$) und die belasteten Güten ($Q_L$) geregelt werden. Daher wird diese Art des Betriebs $P_kQ_L$–Betrieb genannt. Im Rahmen des Quantum Beam (QB) Projects wurden an der KEK Superconducting RF Test Facility (STF) zwei supraleitende Neunzellkavitäten mit einem Klystron betrieben. Für diese wurde eine automatisierte Prozedur entwickelt und getest, deren Ergebnis der weltweit erste vollständig erfolgreiche $P_kQ_L$–Betrieb war. Ein stabiler einstündiger Langzeitbetrieb mit einem Strahstrom von 6.4 mA im Mittel wurde durchgeführt. Dabei lagen die Kavitätengradienten mit 16 und 24 MV/m 5% unter den virtuellen Quenchlimits von 16.8 und 25.2 MV/m. Die erreichten Stabilitäten für die Vektorsummen Gradienten und Phasen waren $\Delta A/A = 0.009\%$ und $\Delta\phi = 0.009°$. Darüber hinaus wurde in einer Simulation erfolgreich eine Prozedur mit anschließendem $P_kQ_L$–Betrieb von 39 Kavitäten, der alle Anforderungen des ILC erfüllt, demonstriert.

Aufgrund des $P_kQ_L$–Betriebs ist eine weitere Anforderung des ILCs der Betrieb der Kavitäten mit hohen belasteten Güten. Im Rahmen einer Machbarkeitsstudie wurden die belasteten Güten der beiden supraleitenden Kavitäten am KEK STF während des QB Projektes auf $Q_{L,cav1} = Q_{L,cav2} = 2 \cdot 10^7$ angehoben. Ein stabiler einstündiger Langzeitbetrieb mit einem Strahstrom von 6.1 mA im Mittel wurde durchgeführt. Die erreichten Stabilitäten für die Vektorsummengradienten und –phasen waren $\Delta A/A = 0.011\%$ und $\Delta\phi = 0.015°$.

Im Rahmen von ILC ist geplant die Klystrons bezüglich der Leistung 7% unter der vollständigen Sättigung zu betreiben. Aufgrund des Sättigungsverhaltens der Ausgangsamplitude strebt das Gain der Reglung in diesem Bereich gegen 0, was eine effektive Reglung verhindert. Um das Gain bis hin zum Punkt der Sättigung konstant zu halten, kann eine FPGA–basierte Klystronlinearisierung mittels einer Vorverzerrung benutzt werden. Vier verschiedene solcher Algorithmen wurden entwickelt, erfolgreich getestet und miteinander verglichen. Die beste Lösung ist die basierend auf einem Lookup table mit anschließender linearer Interpolation. In einer Simulation wurde gezeigt, dass mit einer Erweiterung des Algorithmus mit einem adaptiven Generieren der Stützpunkgitterabstände das Ergebnis der Linearisierung weiter verbessert werden kann.

Um Tests von Klystronlinearisierungsalgorithmen ohne den Betrieb eines Klystrons oder einer Kavität durchführen zu können, wurde ein auf einem FPGA basierender Klystron– und Kavitätensimulator entwickelt und getestet.

# Contents

# Chapter 1

# Introduction

## 1.1 General Introduction

Nowadays particle accelerators are used for a huge variety of purposes covering e.g. medical treatment, research in biology, material science, and other sciences. One central and prominent purpose is the probing of theoretical concepts in physics, such as the Standard Model in particle physics. The Standard Model describes the fundamental constituents of matter and its interactions. The interactions are the strong, the weak, and the electromagnetic interaction. With the experimental confirmations of e.g. the top quark or the tau neutrino, it is a very successful model. Recently at Large Hadron Collider (LHC) at CERN the Higgs boson, which also was predicted by the Standard Model, was discovered.

The LHC is a double ring collider with a circumstance of about 27 km. In the LHC protons or lead ions are accelerated to energies of up to 7 TeV per nucleon, which results in collision energies of up to 14 TeV. Since at LHC baryonic particles are used, the energy during the collision is distributed among quarks, antiquarks, and gluons. The analysis of the highly complex collision progress is very challenging and does not allow a very precise characterization of the Higgs boson.

One of the main purposes of future International Linear Collider (ILC) [1] will be the high precision investigation of the Higgs boson. ILC will be a linear collider with a length of about 31 km. At ILC electrons and positrons will accelerated within two linacs to beam energies of up to 250 GeV. This yields a center–of–mass energy at the collision point of 500 GeV. Since both electrons and positrons are leptons, they have no substructure. This makes

the analysis of the collision process much easier in comparison to the collisions at LHC, which will allow a much more precise characterization of the properties of the Higgs boson.

A further purpose of ILC will be the investigation of dark matter [3]. There are several possibilities about the properties of dark matter. In the case dark matter has low mass (<10 GeV), ILC can be utilized for its study. Furthermore, in the case dark matter only couples to leptons or via a spin dependent interactions, ILC would offer a unique possibility to discover dark matter.

Beside this extra dimensions via the seesaw mechanism can be probed at ILC [4]. In this scenario the decay process of an electron–positron collision is analyzed. It is theorized that from this the masses and cross sections of Kaluza–Klein neutrinos can be measured. Furthermore neutrino oscillation parameters can be extracted, which gives information about the origin of low–energy neutrino masses.

In order to conduct those experiments and let ILC fulfill its purpose, adequate qualities of the electrons and positron beams have to be achieved and maintained. In order to accelerate the beams, high gradient accelerating field are generated within superconducting 9–cell TESLA–like cavities using high power RF amplifiers, namely klystrons. The goal of digital LLRF systems is to control and maintain the stabilities of the cavity accelerating fields by means of feedback loops. Due to this digital LLRF control is a crucial element in the realization and operation of ILC.

## 1.2 Goal of this Study

The goal of the presented study was to develop and test digital LLRF control techniques and operation procedures towards ILC. To this end previously performed work had to be taken into account.

The main issues dealt with were stable operation of multiple cavities driven by a single klystron at high gradients close to their respective quench limits over the whole flattop, stable long–time operation of cavities with a high loaded quality factors, and the improvement of existing as well as the development of new predistortion–type klystron linearization algorithms. For all of this three issues first the theoretical background had to be analyzed. Based on this, new operation procedures and concepts had to be developed.

In the case of close quench limit cavity operation and the implementation of new klystron linearization algorithms, computer simulations had to be used in order to demonstrate the feasibility of realization. If the requirements were met, the algorithms had to be implemented and tested at actual hardware and accelerators. The development and implementation had to be rated successfully in the case all defined requirements were met. These requirements follow the requirements for the operation of the cavities of the ILC main linacs [2].

In the case of the near–quench–limit operation with flat gradients of multiple cavities driven by a single klystron the amplitude and phase stabilities for the accelerating fields during a long–time operation with beam had to be better than 0.07% and 0.35°, respectively. Furthermore the cavities should be operated 5% below their respective quench limits. In order to achieve such an operation, both the individual cavity driving powers ($P_k$) and the individual cavity loaded quality ($Q_L$) factors had to be controlled. Such a kind of operation was never actually realized before. Goal was to successfully demonstrate such an operation.

In the case of the long–time operation with beam of cavities with a high loaded quality factors ($Q_L = 2 \cdot 10^7$) the same amplitude and phase stabilities for the accelerating fields of better than 0.07% and 0.35°, respectively, had to be met. A stable long–time operation with a high–current beam of cavities at such high loaded quality factors has not been realized before. Target was the successful demonstration of such an operation.

In the case of the implementation of the klystron linearization algorithms a linearization over the whole output power range had be realized. This requirement originates from the planned overhead of 7% in power during the operation of the klystrons at the ILC main linacs. The goal was to develop linearization algorithms with higher efficiency and linearization performance compared to the ones implemented in the past.

The ultimate goal of the development of control techniques and procedures presented in this study is to provide key technologies required for the realization of ILC. The purpose of the successful demonstrations of those is to prove the feasibility of the realization of ILC.

## 1.3 Structure of the Thesis

The dissertation is organized in eight chapters. A short overview of the content of every chapter is given in the following.

- In chapter 2 introductions to ILC and to the ILC–like accelerators around the world are given.
- In chapter 3 an introduction to the principle of digital LLRF control is given. Furthermore the LLRF systems at KEK STF, FNAL ASTA, and FLASH are outlined.
- In chapter 4 a short introduction to cavity modeling, on which the following chapters are based, is given.
- In chapter 5 already performed efforts towards ILC, such as S1–Global and the 9mA tests at FLASH are summarized.

The chapters until this point give an overview of the past studies performed in the scientific community as an important background for the studies performed in the scope of this dissertation as described in the following chapters.

- In chapter 6 the development and the world's first time successful test of an automated actual $P_k Q_L$ controlled operation is described. This covers also the development and usage of preparatory procedures such as the identification of RF phases for on–crest beam acceleration, beam–based gradient calibration, and automated beam compensation.
- In chapter 7 the successful test of a stable long–time operation of cavities with high loaded quality factors is described. Also the characterization of the possible range of the loaded quality factors at KEK STF in the scope of the QB project and the impact on the cavity phases is covered.
- In chapter 8 the development and test of three different predistortion–type FPGA–based klystron linearization algorithms at FNAL NML is described. Furthermore the reimplementation of a klystron linearization at DESY in the scope of the uTCA.4 standard is covered. Beside this the development of an FPGA–based klystron and cavity simulator at KEK is described.

# Chapter 2

# Overview of ILC and ILC–like Electron Accelerators

In this chapter an overview over the features of the International Linear Collider (ILC) is given. Furthermore ILC–like accelerators around the world are introduced. At most of those research and development in scope of ILC was or is conducted. Beside this control systems used at KEK, FNAL, and DESY are outlined. In case of KEK and FNAL these were utilized in the scope of the studies presented in this dissertation.

## 2.1 ILC

The International Linear Collider is a future high–luminosity linear collider for electrons and positrons with a length of about 31 km [1]. Its purpose is the high–precision investigation on the Higgs–boson, the investigation on dark matter, and the probing on extra dimensions. A schematic of ILC is shown in Figure 2.1.

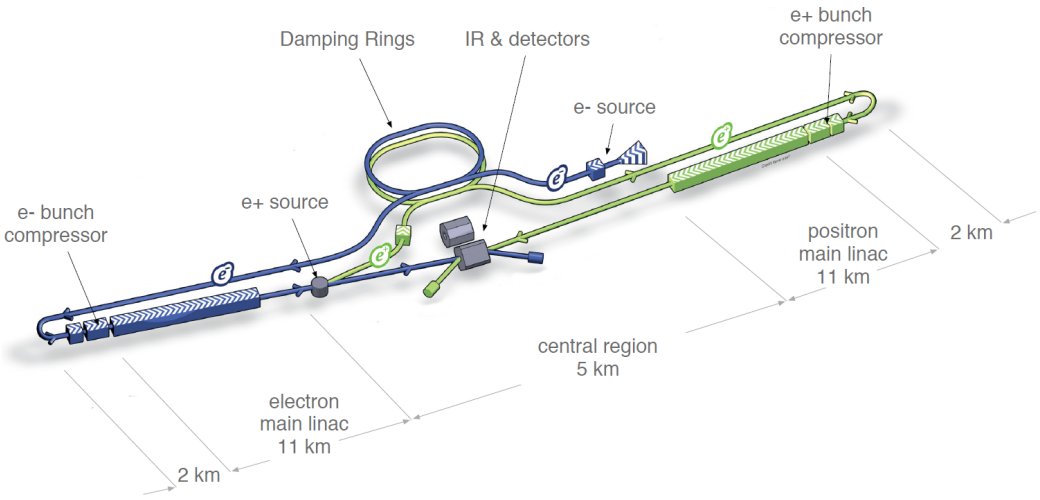


Figure 2.1: *Schematic layout of ILC covering all major subsystems [1] such as the electron source, the damping rings, the electron bunch compressor, the electron main linac, the positron source, the positron bunch compressor, the positron linac and the interaction region with two detectors.*

A photocathode DC gun serves as a source for polarized electrons. The source for polarized positrons are electron–positron pairs, which are created by the conversion of high–energy photons produced by high–energy electrons passing an undulator after the electron main linac. The electron and positron beams are stored in the respective damping rings for 200 ms in order to reduce the beam emittances by six orders and remove jitter from the sources. After extraction, the electron and positron beams pass respective two–staged bunch–compressor systems. Table 2.1 lists the RF stability requirements at the bunch–compressor systems limited by the timing stability at the interaction point.

Table 2.1: RF stability requirements at the bunch–compressor systems [2].

| Parameter | Value | Unit |
|---|---|---|
| All klystron correlated amplitude change | 0.5% | |
| All klystron correlated phase change | 0.32 | ° |
| Klystron to klystron uncorrelated amplitude change | 1.6% | |
| Klystron to klystron uncorrelated phase change | 0.60 | ° |

In the respective main linacs, with a length of 11 km each, the beams are accelerated to a center–of–mass energy of up to 500 GeV. The detailed beam parameters are listed in Table 2.2.

Table 2.2: Beam parameter for the ILC main linacs. [2].

| Parameter | Value | Unit |
|---|---|---|
| Beam current | 5.8 | mA |
| Beam phase | 5 | $^\circ$ |
| Beam (peak) power per cavity | 190 | kW |
| Beam pulse length | 727 | $\mu$s |
| Repetition rate | 5 | Hz |
| Number of bunches | 1312 | |
| Bunch charge | 1.9 | nC |
| Bunch population | $2 \cdot 10^{10}$ | |
| Bunch repetition rate | 1.8 | MHz |
| Bunch separation | 555 | ns |
| EMS bunch length | 0.3 | mm |
| $e^-$ RMS energy spread | 0.124% | |
| $e^+$ RMS energy spread | 0.07% | |
| $e^-$ polarization | 80% | |
| $e^+$ polarization | 30% | |
| Horizontal emittance | 10 | $\mu$m |
| Vertical emittance | 35 | $\mu$m |
| IP horizontal beta function | 11 | mm |
| IP vertical beta function | 0.48 | mm |
| IP RMS horizontal beam size | 474 | nm |
| IP RMS vertical beam size | 5.9 | nm |
| Luminosity | $1.8 \cdot 10^{34}$ | $cm^{-2}s^{-1}$ |
| Average energy loss | 4.5% | |
| Number of pairs/bunch crossing | $139 \cdot 10^3$ | |
| Total pair energy/bunch crossing | 344.1 | TeV |

For the acceleration in the main linacs a total of about 15814 superconducting TESLA–like [5] 9–cell cavities with an elliptical shape made of niobium will be used. Figure 2.2 shows a picture of such a cavity. These will be driven by 10 MW multi–beam klystrons in groups of 39 cavities per klystron.

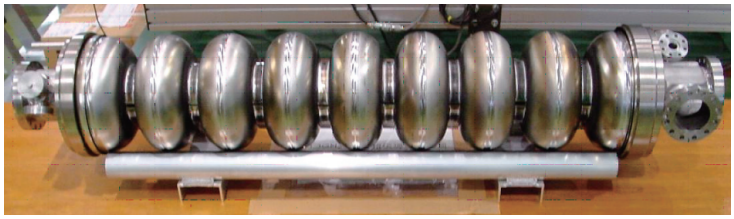

Figure 2.2: Picture of a 9–cell TESLA–like cavity [7].

In order to achieve superconductivity the cavities are cooled down in the cryomodules to about 2 K. Table 2.3 gives and overview of the cavity and RF parameters in case of the main linacs.

Table 2.3: ILC main linac cavity and RF parameters [2].

| Parameter | Value | Unit |
|---|---|---|
| Resonance frequency | 1.3 | GHz |
| Average accelerating gradient | 31.5 | MV/m |
| Q factor $Q_0$ | $1 \cdot 10^{10}$ | |
| Matched loaded Q ($Q_L$) | $5.5 \cdot 10^6$ | |
| Matched driving power ($P_k$) | 190 | kW |
| Effective length | 1.038 | m |
| r/Q | 1036 | $\Omega$ |
| Accepted operational gradient spread | $\pm$20% | |
| Cavity fill time | 923 | $\mu$s |
| Cavity flattop time | 727 | $\mu$s |
| Total RF pulse length | 1650 | $\mu$s |
| RF–to–beam power efficiency | 44% | |
| Total number of cavities | 15814 | |

From the limitation in the beam energy stability of $\leq 0.1\%$ follow the allowed changes in amplitude and phase of the accelerating fields within the main linac cavities. These are listed in Table 2.4.

Table 2.4: RF stability requirements for the accelerating field in the ILC main linac cavities [2].

| Parameter | Value | Unit |
|---|---|---|
| All klystron correlated amplitude change | 0.07% | |
| All klystron correlated phase change | 0.35 | $^\circ$ |
| Klystron to klystron uncorrelated amplitude change | 1.05% | |
| Klystron to klystron uncorrelated phase change | 5.6 | $^\circ$ |

Since the cavity gradient tilts and RF fluctuations induce transverse beam orbit changes [6], a stable beam acceleration requires flat cavity gradients during the beam transient. As listed the average acceleration gradient is 31.5 MV/m with a random cavity–to–cavity gradient spread of ±20%. This spread originates from manufacturing tolerances. It is planned to operate every cavity 5% below the individual quench limit over the whole flattop. For a better understanding Figure 2.3 shows a schematic of an example of two cavities (cavity 1 and cavity 2) and their vector sum gradients versus time beside the individual cavity quench limits and the RF drive pulse shape for three different situations. It is assumed that both cavities are driven by a single klystron and that the diving power ratio to both cavities is adjustable. In the first situation as shown in Figure 2.3 a) both cavity gradients are flat 5% below their respective quench limits over the whole flattop. The different cavity gradients are achieved by adjusting the driving powers $P_k$s individually. In the case shown the $Q_L$ values of both cavities are the same and no beam is present.

In the second situation as shown in Figure 2.3 b) the beam is turned on and the driving powers are increased in order to compensate the beam. The ratio between the individual cavity driving power is unchanged. Furthermore the $Q_L$ values are unchanged. It can be observed that the change in the cavity gradients due to the beam loading (pink dashed lines) are the same for all cavities and does not depend on the cavity gradients or $Q_L$ values. Since the $Q_L$ values are not adjusted the change in cavity gradient slopes due to the beam and due to the driving powers are not in balance. In the case of the cavity 1 flattop a negative slope is induced, which makes the gradient during the flattop not flat anymore. In the case of cavity 2 a positive slope is induced, which leads the cavity 2 gradient to exceed the quench limit during the flattop. This situation is not suitable for operation.

In Figure 2.3 c) the $Q_L$ values were adjusted individually for every cavity. With this the changes in cavity gradient slopes induced by the beam and the driving powers are in balance. By this operation with flat gradients during the flattop region for both cavities could be achieved even under beam operation with cavities with different gradients. Since both the cavity driving powers $P_k$ and the $Q_L$ values are adjusted individually, this operation mode is called $P_kQ_L$ operation. It can be adopted also in the case of 39 cavities driven by a single klystron. It is one of the central requirements for the operation of the cavities in the ILC main linac. For a more detailed description refer to section 4.4. At ILC the range in $Q_L$ values will be from $3 \cdot 10^6$ to $10 \cdot 10^6$.

The parameters of the 10 MW multi–beam klystrons, which will be used

at ILC, are listed in Table 2.5.

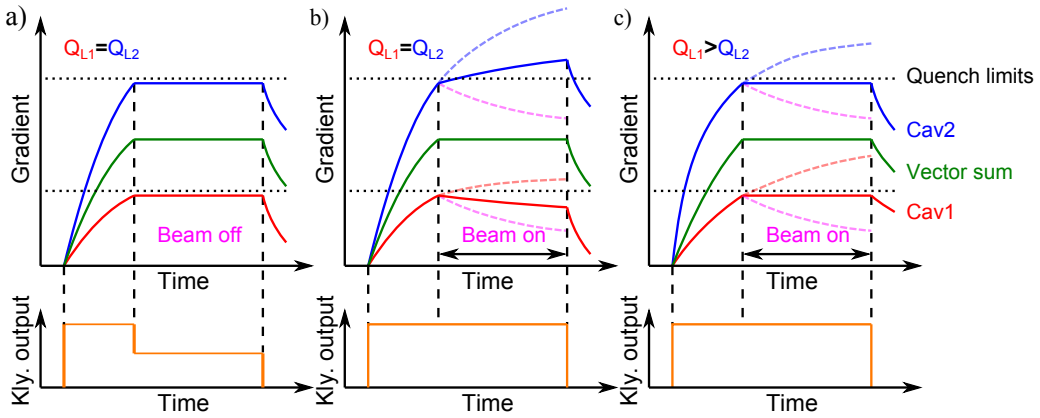


Figure 2.3: Schematic of cavity 1 (red), cavity 2 (blue), and vector sum (green) gradients versus time beside the individual cavity quench limits (dotted lines) on top and the RF output pulse shape on the bottom: a) no beam, same $Q_L$ values, low RF power during flattop, b) beam on (pink), same $Q_L$ values, high RF power during flattop, and c) beam on (pink), adjusted $Q_L$ values, high RF power during flattop.

Table 2.5: ILC main linac multi–beam klystron parameter [2].

| Parameter | Value | Unit |
|---|---|---|
| Frequency | 1.3 | GHz |
| Peak power output | 10 | MW |
| RF pulse width | 1650 | $\mu$s |
| Repetition rate | 5 | Hz |
| Average power output | 82.5 | kW |
| Efficiency | 65% | |
| Saturated gain | $> 47$ | dB |
| LLRF overhead power | 7% | |
| Cavities per klystron | 39 | |
| RF power for 39 cavities | 7.4 | MW |
| Total number of klystrons | 378 | |

Klystrons in general are nonlinear devices. Their input to output power characteristics features a point of saturation. Figure 2.4 shows such a characteristics for a Toshiba 10 MW multi–beam klystron (red). Commonly klystrons are operated about 40% in power below their point of saturation.

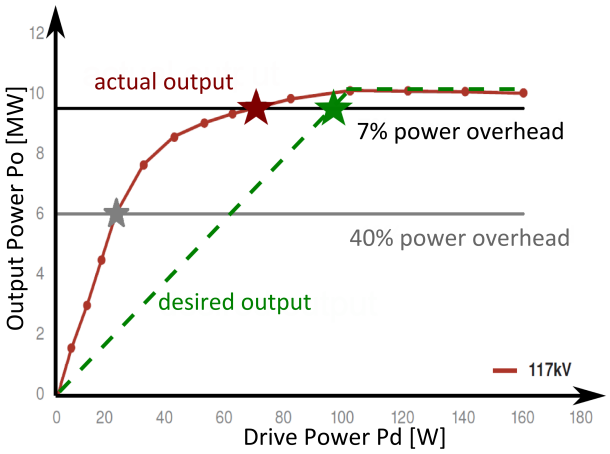


Figure 2.4: Output power [MW] versus drive power [W] of a Toshiba 10 MW multi–beam klystron with an high voltage of 117 kV [2] not linearized (red) and linearized (green). The gray star indicates the working point with an power overhead of 40%, the red star of 7% (not linearized), and the green star of 7% (linearized).

In Figure 2.4 this operation point is indicated by a gray star. This is done in order to operate the klystron in its linear region. The control gain in feedback operation follows the slope of the input to output power characteristics. The advantage is that the control gain stays constant in the linear region of the klystron. At ILC it is intended to operate the klystron 7% in power below the point of operation. This working point is indicated in Figure 2.4 by a red star. The advantage of such an operation is that the klystron can be operated with a power efficiency. The disadvantage is that the control gain decreases (less than $\frac{1}{10}$ compared to the linear region) and makes feedback operation impossible. In order to overcome this disadvantage the klystron output characteristics has to be linearized as represented by the green dashed line (for more details refer to Chapter 8). In the case the output characteristic is linear until the point of saturation, also the control gain stays constant until this point allowing feedback operation even close to saturation. Due to this the development and usage of klystron linearization algorithms are a requirements for the operation of ILC.

As shown in Table 2.5 and mentioned above, at ILC it is planned to drive the superconducting cavities of the main linacs in groups of 39 cavities per klystron. Figure 2.5 shows a detailed schematic of the waveguide distribution and its elements of such a group. Each group is divided into three sections covering 13 cavities in a 4–4–5 configuration.

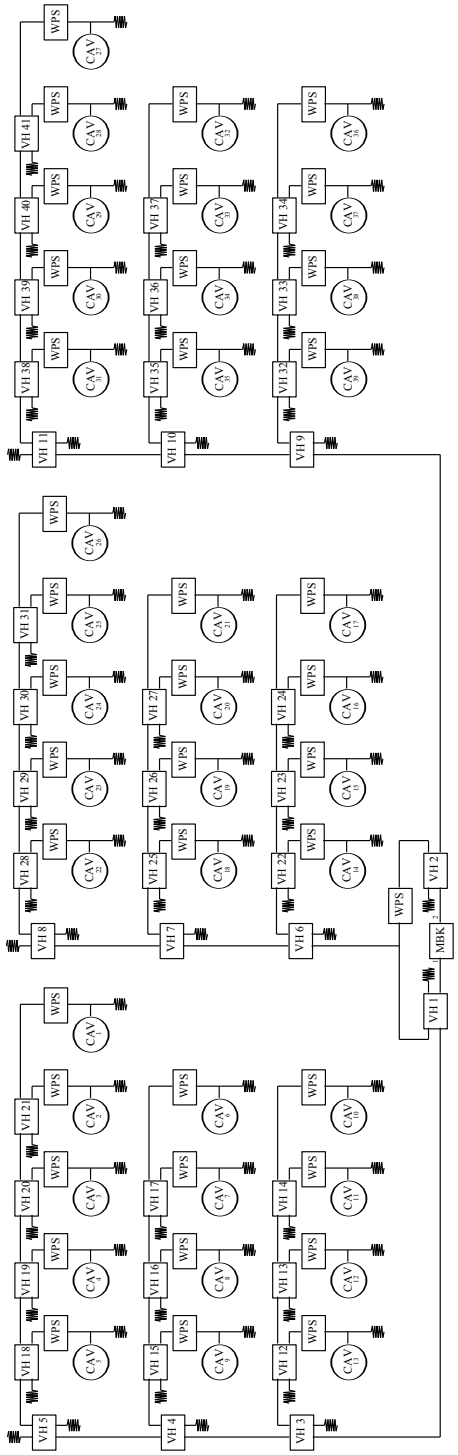


Figure 2.5: Schematic of the ILC waveguide system covering the multi–beam klystron (MBK), variable hybrids (VH), waveguide phase shifters (WPS), cavities (CAV), and loads.

Figure 2.6 shows a computer graphic of the planned setup of one of such a group. Furthermore Figure 2.7 shows a cross section of an Kamaboko–shaped ILC main linac tunnel with the cryomodules housing the superconducting cavities on the left side, the shielding in the middle, and the RF systems on the right side.

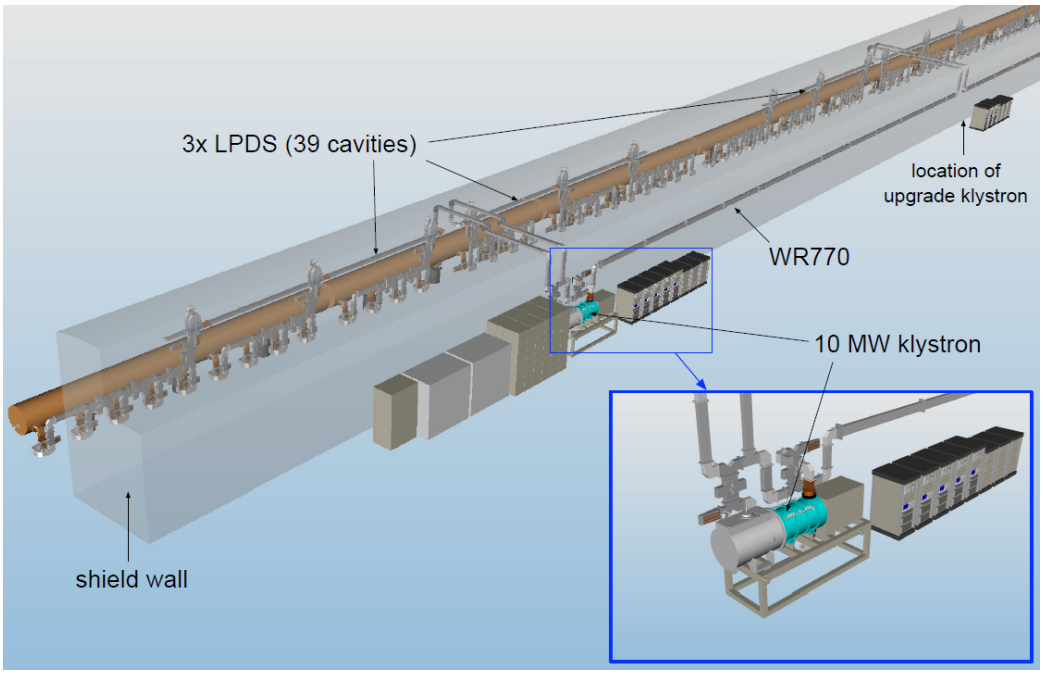


Figure 2.6: Computer graphics of an ILC main linac klystron–cavity groups: one multi–beam klystron, cryomodules housing 39 superconducting cavities, and the waveguide distribution system connecting the klystron with the cavities [2]. The klystrons and the cryomodules are separated by the shielding.

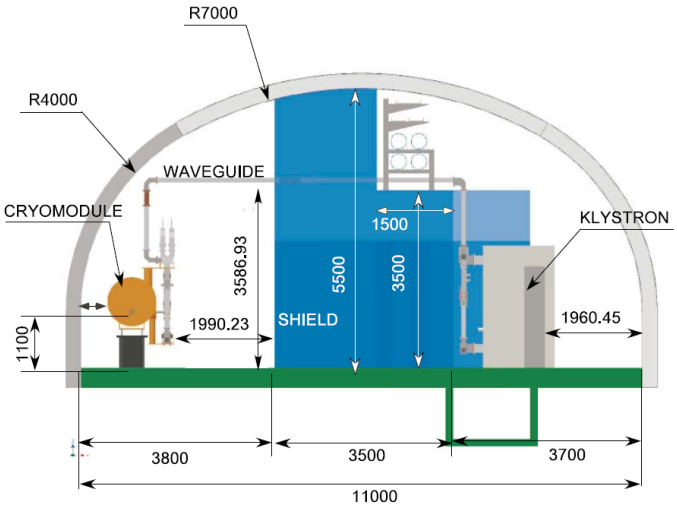


Figure 2.7: Cross section of the ILC main linac (Kamaboko–shaped) tunnel: the cryomodules housing the superconducting cavities on the left side, the shielding in the middle, and the RF systems on the right side [2].

At ILC it is intended to implement digital LLRF control systems for the groups of 39 cavities per klystron. To this end a configuration of master and slave boards distributed over several racks is planned. Figure 2.8 shows a schematic of the proposed LLRF loop for the ILC main linacs. LLRF front–end controllers (slave boards) compute partial vector sums and send those to the central LLRF controller (master board). The central LLRF controller controls the klystron, which drives all 39 cavities.

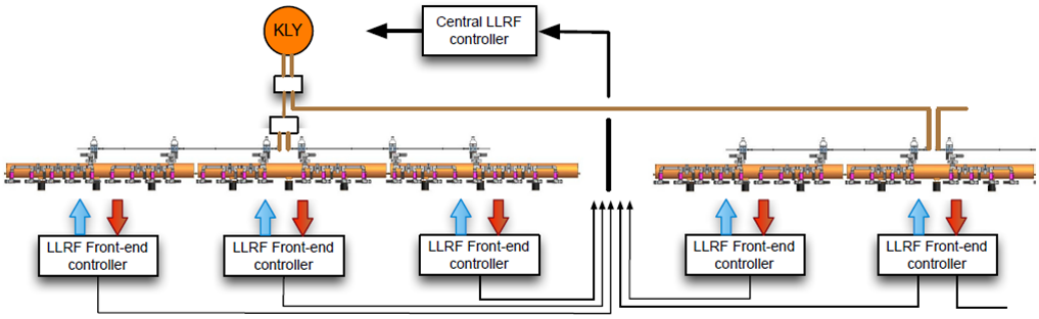


Figure 2.8: Schematic of the proposed LLRF loop for the ILC main linacs: LLRF front–end controllers compute partial vector sums, send those to the central LLRF controller, which controls the klystron driving the cavities [2].

After the acceleration of the electron and positron beams in the main linacs, each beam passes the respective beam–delivery system. These have a length of 2.2 km each and are bringing the beams into collision at a crossing angle of 14 mrad. The interaction point is occupied by one of two detectors in a push–pull configuration.

## 2.2 KEK STF

At the High Energy Accelerator Research Organization (KEK) in Japan the Superconducting RF Test Facility (STF) is operated. The purpose of STF is the development and demonstration of high–gradient superconducting accelerator technology aiming to ILC. Beside this, also high–pressure rinsing of TESLA–like cavities, cavity tuning, and cryomodule assembly is performed at the STF complex.

### 2.2.1 The Quantum Beam Project

From April 2012 to March 2013 the Quantum Beam (QB) project [8] was conducted at KEK STF. The purpose was the demonstration of high–brightness x–ray creation by inverse laser Compton–scattering. To this end an linear electron accelerator was set up. A schematic covering the main components is shown in Figure 2.9.

In a photo–cathode radio frequency (RF) gun [10] an electron beam is created by photo–effect and accelerated in a 1.5–cell cavity to about 3 MeV. Then the beam is accelerated to about 40 MeV by two superconducting 9–cell TESLA–like L–band cavities, which are mounted in one cryomodule. Both superconducting cavities were driven by a 800 kW klystron mounted beside the capture cryomodule inside the accelerator tunnel. The cavities were controlled by digital LLRF control techniques. For the implementation of the LLRF system $\mu$TCA conform hardware was used. For more details refer to section 3.2. Before dumped, the electron beam in sent through a bend as well as through an optical cavity. In the optical cavity the beam is collided with a laser beam. By inverse laser Compton–scattering an X–ray beam is created, which is detected in a X–ray detector [11]. Beside the studies in scope of the QB technology also R&D work in the scope of ILC was performed as descried in Chapters 6 and 7.

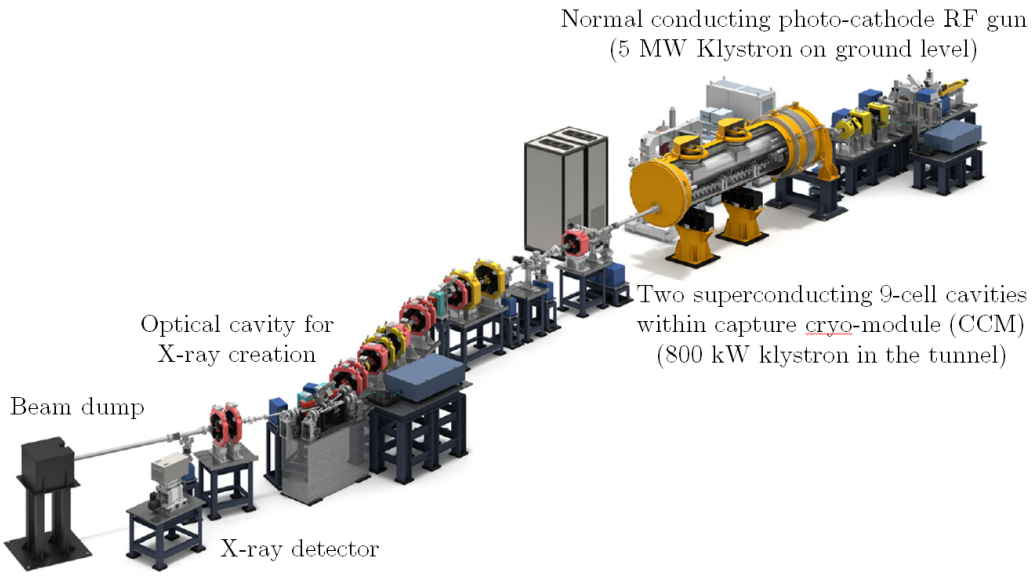


Figure 2.9: *Schematic of the linear electron accelerator set up in the scope of the QB project [9] consisting mainly of a normal conducting photo–cathode RF gun driven by a 5 MV klystron on ground level, two superconducting 9–cell cavities within the capture cryomodule driven by a 800 kW klystron located in the accelerator tunnel, an optical cavity for X–ray creation with a corresponding X–ray detector, and a beam dump.*

### 2.2.2 STF–2

STF–2 is a future electron accelerator at KEK STF devoted to R&D in the scope of ILC [2]. Figure 2.10 shows its schematic. The 9 mA RF gun and the two superconducting cavities within the capture cryomodule from the QB project will be reused. The beam energy up to this point will be 40 MeV. The main linac will be installed in two phases. In the first phase 12 superconducting cavities (SCCs) within two cryomodules (CM–1 with 8 SCCs and CM–2a with 4 SCCs) will be installed until the end of 2014. The final beam energy in this configuration will be 418 MeV. In the second phase the main linac will be upgraded by another 12 superconducting cavities within two cryomodules (CM–2b with 4 SCCs and CM–3 with 8 SCCs). With the additional cavities a final beam energy of 796 MeV will be achieved. The upgrade is planned to be finished by the year 2017.


Figure 2.10: *STF–2 accelerator plan for the final stage covering a normal conducting photo–cathode RF gun, two superconducting 9–cell cavities in the capture cyro–module, eight superconducting 9–cell cavities in the cryomodule CM–1, four superconducting 9–cell cavities in the cryomodules CM–2a, CM–2b, CM–3a, and CM–3b each, and a beam dump.*

The digital LLRF control system of the superconducting cavities of the main linac of STF–2 will be realized using MTCA.4 conform hardware in a master–slave configuration. Figure 2.11 shows a schematic of the control loop. In the first phase of STF–2, the 12 superconducting cavities within CM–1 and CM–2a are controlled using only the master card. The vector sum is calculated and used for the feedback. In the second phase the pickup signals of the 12 superconducting cavities from CM–2b and CM–3 are sent to the slave card. A partial vector sum is calculated, which is sent via a fast optical communication to the master card. On the master card both vector sums are combined and used for the feedback. In both phases all superconducting cavities of the main linac will be driven by a singe 10 MW multi–beam klystron.

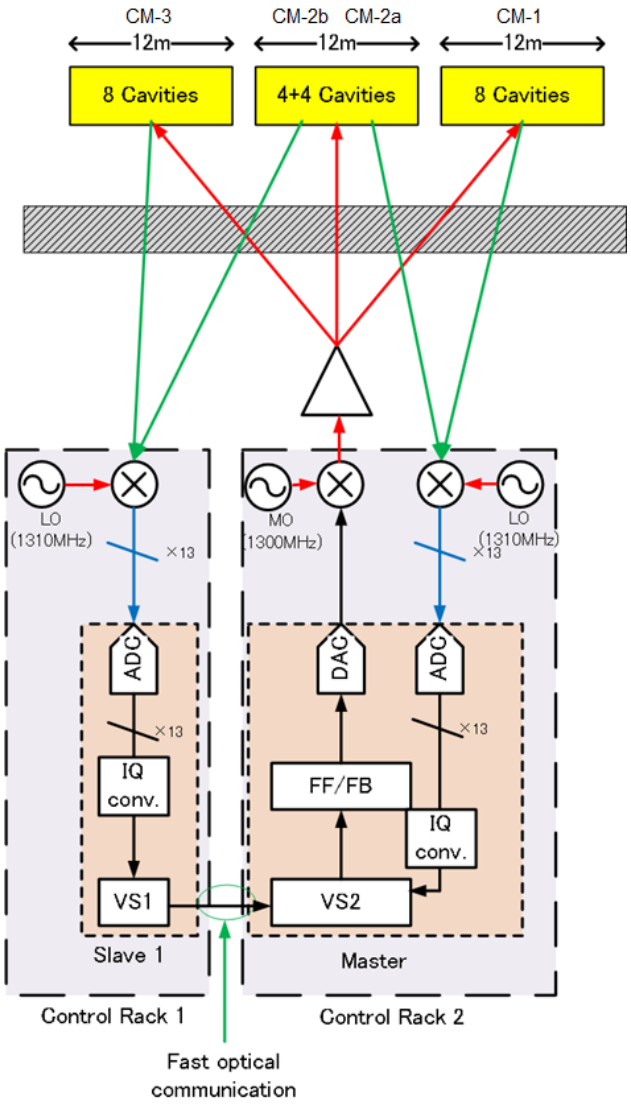


Figure 2.11: *Schematic of the MTCA.4–based LLRF control system for STF–2 consisting of a master and a slave hardware in control rack 1 and 2. The cavity pickup signals of CM–1 and CM–2a are digitized on the master hardware. The cavity pickup signals of CM–2b and CM–3 are digitized on the slave hardware. The partial vector sum is sent from the slave card to the master card via a fast optical link. The total vector sum is calculated on the master board, which controls the klystron driving all 24 cavities.*

### 2.2.3 Control System at KEK STF

The control system at KEK STF is the Experimental Physics and Industrial Control System (EPICS) [12, 13]. EPICS is a system consisting of a variety of open source tools and applications in order to build an infrastructure for distributed control systems for large scientific facilities, as for example a particle accelerator. It is mainly based on a channel access (CA) servers and clients structure, in which all components are connected by a network (see Figure 2.12).

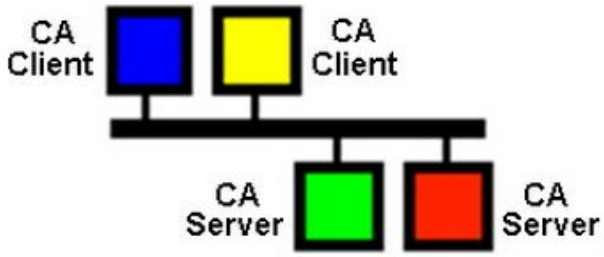


Figure 2.12: *Most basic structure of an EPICS system [13] in which several channel access (CA) clients and channel access (CA) servers are connected to a common network.*

As an CA client interface, in order to establish the connection between Matlab and EPICS, LabCA is used at KEK STF. This allows monitoring the status as well the control of devices, which are part of the accelerator. In this environment it is easy and straight forward to implement and apply control algorithms, operation procedures, monitoring, and data acquisition using Matlab scripts. These possibilities were widely used in order realize the procedures described in the chapters 6 and 7.

## 2.3 FNAL ASTA

At the Fermi National Accelerator Laboratory (FNAL) in the United States of America the New Muon Lab (NML) is operated. Currently it is housing the Advanced Superconducting Test Accelerator (ASTA) [14].

### 2.3.1 Advanced Superconducting Test Accelerator

ASTA is designed as both, an ILC R&D facility as well as a user machine. It is currently under construction. Figure 2.13 shows an overview of all stages planned until the year 2018 [15].

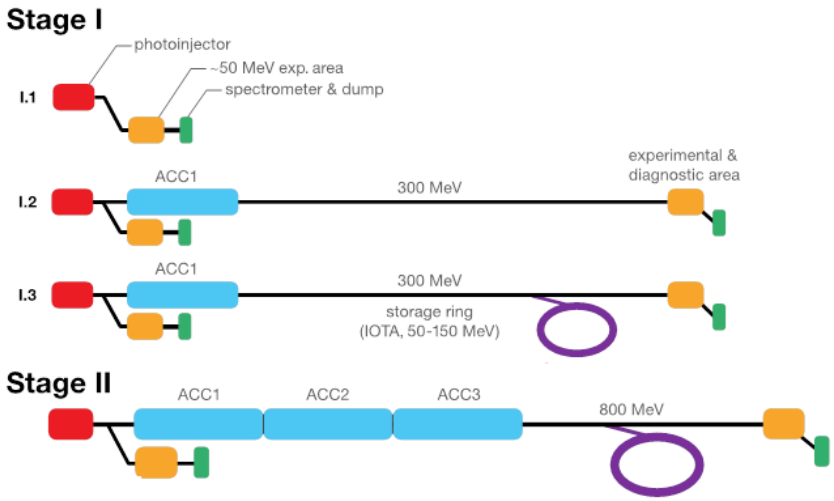


Figure 2.13: *Stages of the Advanced Superconducting Test Accelerator [15]. Stage I.1 covers the photo injector, a 50 MeV experimental area, a spectrometer, and a damp. In stage I.2 the accelerator is extended by a second beam line with an eight 9–cell cavities in ACC1 with a experimental and diagnostics area, and a second beam dump. In stage I.3 a storage ring is added. In stage II the two cyro–modules ACC2 and ACC3 are added.*

In the stage I.1 the beam from the photo injector with an energy of about 50 MeV is sent to an experimental area and to a beam dump. In stage I.2 the beam can be sent in a second beam line though an ILC RF unit, which is a cryomodule with 8 superconducting 9–cell cavities. Beam energies of about 300 MeV will be achieved. The beam will be sent to experimental and diagnostic areas and to a beam dump. In stage I.2 a storage ring called Integrable Optics Test Accelerator (IOTA) is added, which covers an energy range of 50 to 150 MeV.

In stage II two additional ILC RF units will be added, yielding beam energies of up to 800 MeV. Figure 2.14 shows a more detailed schematic of the configuration of ASTA in stage II.

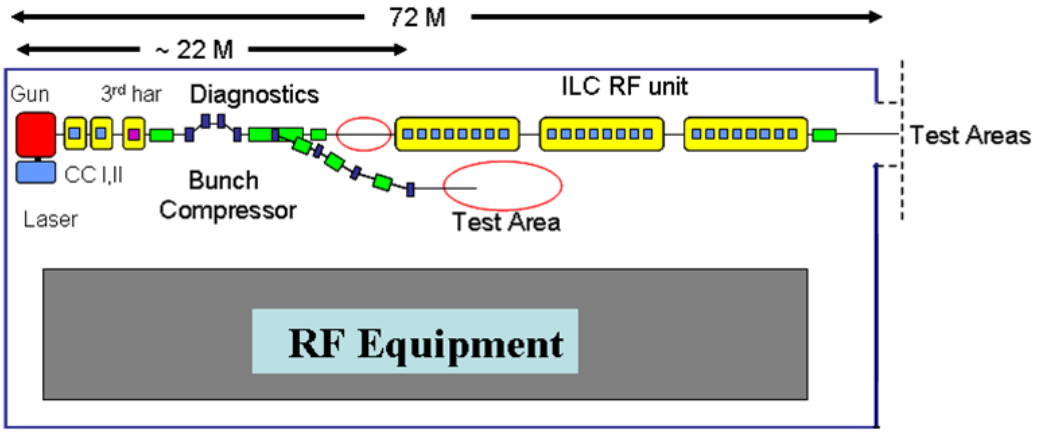


Figure 2.14: *Schematic of the Advanced Superconducting Test Accelerator cave during stage II: Inside the case the accelerator is located. It mainly consists of the RF gun, two 3rd harmonic superconducting cavities, a bunch compressor, one beam line towards a low beam energy test area, and one beam line with three cryomodules with eight superconducting cavities each towards a high beam energy test area. Outside the cave the RF equipment is located.*

### 2.3.2 Control System at FNAL

The control system used at FNAL is the Accelerator Network (ACNET). It is a development by FNAL originally in 1983 for the operation of the Tevatron [43]. Due to its universality it is used to control all accelerators and technical equipment throughout the entire institute. ACNET consists of three layers, namely the application layer, the central layer, and the front–end layer. Figure 2.15 shows the corresponding schematic.

All device names in ACNET consist of 8 characters. Every device can have certain properties, such as a reading, a setting, a digital status and control, and alarms. The properties for reading and setting can be single values or arrays. In the application layer in a central database all device names are stored.

For communication general networks (Ethernet) as well as fast real–time networks are used. The protocol is the layered, task–directed, and custom–made ACNET protocol.

Throughout the whole complex the Tevatron clock (TCLK) is distributed and used for triggering events. To this end corresponding to every kind of operation of one or more accelerators, a time line with the required pattern of trigger events is created. The time line can be sent a single time or can be repeated periodically. The length of the time line is user–defined.

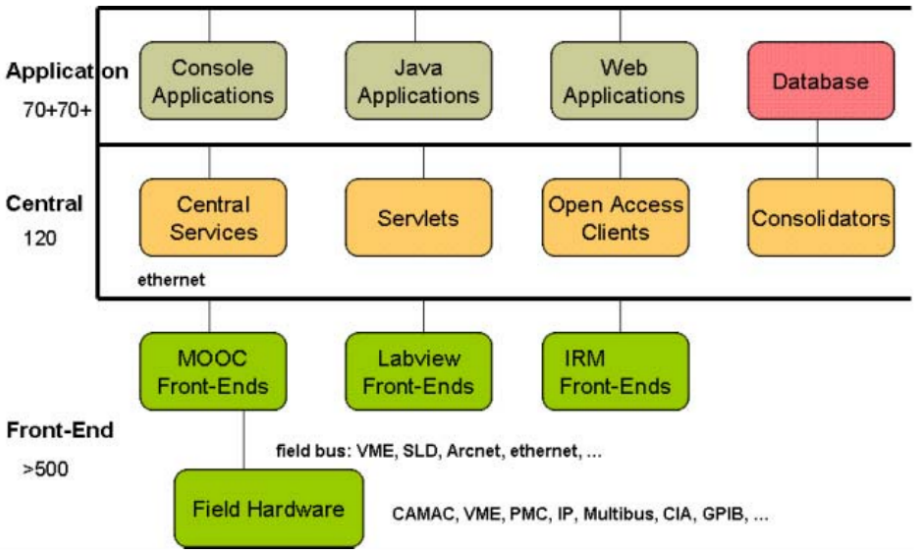


Figure 2.15: *Schematic of organization structure of ACNET [43]. It is organized in the application layer, the central layer, and the front–end layer. All kinds of applications belong to the application layer. Central services, servlets, open access clients, and consolidators belong to the central layer. All kinds of front–end such as MOOC, Labview, or IRM belong to the front–end layer. To those front–ends all kind of field hardware is connected.*

At the application layer two major frameworks are available, namely the original VAX–based console framework and a later developed Java–based framework. Beside this several utility applications have been developed, which run in web browsers.

At the central layer a central database, a number of persistent processes, and Java servlets for supporting web–based applications are provided. All device and node information as well as application data, save/restore data, and Tevatron shot data are stored.

## 2.4 DESY

At Deutsches Elektronen–Synchrotron (DESY) the Free Electron Laser in Hamburg (FLASH) is operated since 2005. Beside this the European X–ray Free Electron Laser (European X–FEL) is currently under construction.

### 2.4.1 FLASH

FLASH is a free electron laser (FEL) based on self–amplified stimulated emission (SASE) [17] in the XUV and soft X–ray regime [18] corresponding to wavelength between 45 and 4 nm.

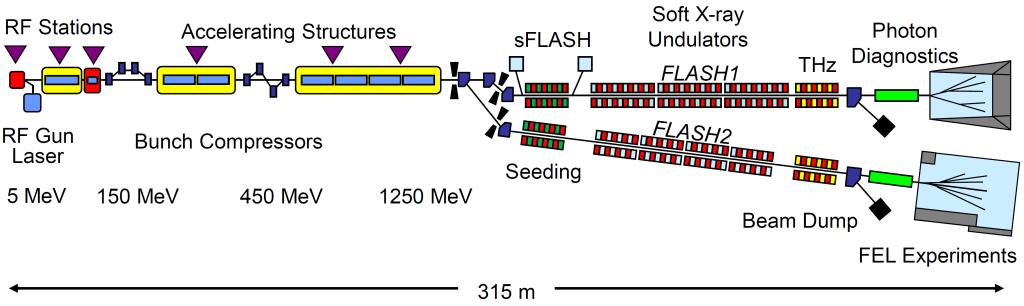


Figure 2.16: *Schematic of the Free Electron Laser in Hamburg at DESY [16]. It mainly consists of the RF gun, seven cryomodules with eight superconducting cavities each, bunch compressors, and two beam lines with soft X–ray undulators, beam dumps, photon diagnostics, and FEL experiments.*

FLASH consists of a superconducting L–band (1.3 GHz) linac, of a soft X–ray undulator, and a photon transportation line with 5 experimental beam lines for users. Currently an upgrade to FLASH II including a second undulator and additional experimental beam lines is under construction.

The electron bunches are generated with charges between 0.08 nC and 1.0 nC in a warm photo cathode RF gun. The bunch repetition frequency is 1 MHz. Bunch trains of up to 800 bunches per train are possible, which corresponds to an RF pulse flattop length of 800 $\mu$s. The repetition rate is 10 Hz.

With this the FEL is driven by a superconducting linac with an RF photo cathode and a two stage bunch compression system. Electron energies from 0.37 to 1.25 GeV can be achieved.

### 2.4.2 European X-FEL

The European X–FEL [19] is a 17.5 GeV coherent light source, which provides 27,000 flashes per second. The wavelength of the light is as low as 0.05 nm with a peak brilliance of $5 \cdot 10^{33}$ photon/s/mm$^2$/mrad$^2$/0.1% bandwidth. The European X–FEL is currently under construction at DESY. It consists of 808 superconducting 9–cell TESLA–type cavities with a resonance frequency of

1.3 GHz. The cavities are mounted in 101 8–cavity cryomodules, which are organized in 25 RF stations for the main linacs. The 32 cavities in every RF station are driven by a 10 MW klystron each. Every three RF stations are grouped to a cryo–string. A schematic of the X–FEL accelerator is shown in Figure 2.17.

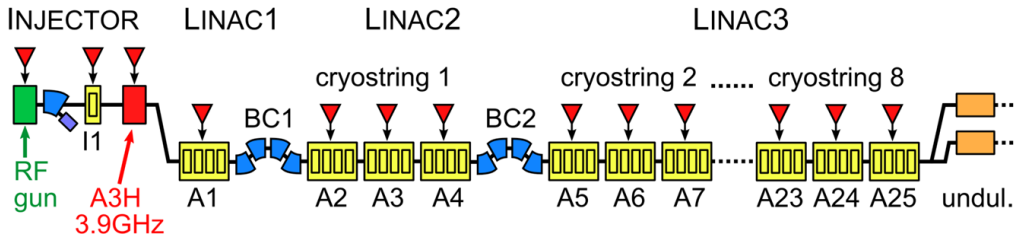


Figure 2.17: *Schematic of the European X–FEL at DESY [20]. The injector mainly consists of a RF gun, a injector cryomodule, and a 3rd harmonic cryomodule. The main linac is divided in sections of cryomodules with superconducting cavities and bunch compressors. Downstream the linac the beam can be delivered to two beam lines, both with undulators and experimental areas.*

### 2.4.3 Control System at DESY

The control system at DESY is the Distributed Object Oriented Control System (DOOCS) [47]. Originally it was designed in the scope of the TESLA Test Facility (TTF) linac, which is now FLASH. It also covers the European X–FEL and the corresponding test facilities, such as Accelerator Module Test Facility (AMTF). DOOCS is entirely written in C++. It is structured in three layers as shown in Figure 2.18, namely the front–end, the middle layer, and the client layer.

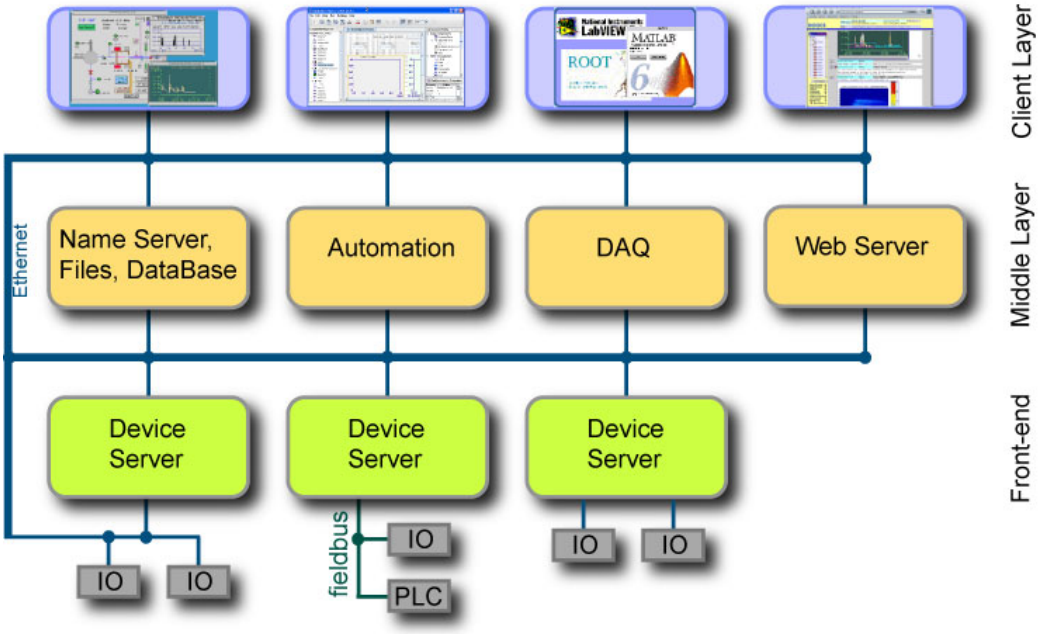


Figure 2.18: *Architecture of DOOCS [47]. It is organized in three layers. In the client data can be monitored, viewed, or processed using software based on Java, Matlab, etc.. In the middle layer name organization, data organization, data storage, data acquisition, automation, and web servers are realized. In the front–end layer device servers are connected to actual devices in the facility.*

The latest graphical user interface of the control system panels at the client layer is written in Java and is called Java DOOCS Data Display (JDDD) [48].

## 2.5 Comparison of STF, ASTA, and FLASH

Table 2.6 shows a comparison of design parameter and system properties of KEK STF in the scope of the QB project, of FNAL NML in scope of ASTA, and DESY FLASH.

Table 2.6: Comparison of design parameters and system properties of KEK STF (QB Project), FNAL NML (ASTA), and DESY FLASH.

| System | Parameter | Unit | KEK STF (QBP) | FNAL NML (ASTA) | DESY FLASH |
|---|---|---|---|---|---|
| RF Gun | RF Gun | | Photo effect (laser) | Photo effect (laser) | Photo effect (laser) |
| | RF gun cavity | | normal conducting | normal conducting | normal conducting |
| | Pickup in RF gun cavity | | no | yes | no |
| | RF gun klystron power | MW | 5 | 5 | 5 |
| SCC | Number of cryo modules | | 1 | 2 (as of 13th of June 2013) | 7 |
| | Number of SCC per module | | 2 | 1, 8 (as of 13th of June 2013) | 8 |
| | Cavities per klystron | | 2 | 1, 8 (as of 13th of June 2013) | 8, 16 |
| | Number of klystrons for SCC | | 1 | 2 | 4 |
| | Max klystron output power | MW | 0.8 | 5, 10 | 5, 10 |
| | DAC limiter | | rectangular in I, Q | rectangular in I, Q | circular in I, Q |
| | Klystron linearization | | no | no | yes |
| | Design cavity gradients | MV/m | 16, 24 | 31.5 | 16 - 35 |
| | Average gradient | MV/m | 20 | 31.5 | |
| | Typical filling time | us | 540 | 580 | 500 (800 flattop) |
| | $Q_L$ setting via | | waveguide reflector | coupler | coupler |
| | $Q_L$ range | | 2e6 - 5e7 | 1e6 - 1e7 | 1e6 - 1e7 |
| | Range of WPS | ° | 120 | 60 | 90 |
| LLRF | RF frequency | GHz | 1.3 | 1.3 | 1.3 |
| | LO frequency | GHz | 1.31 | 1.313 | 1.354 |
| | IF frequency | MHz | 10.16 | 13 | 54.17 |
| | Loop delay | us | between 1 and 2 | 2.5 (estimation by U. Mavric) | between 1 and 2 |
| | Card standard | | uTCA | 19 inch, directly rack mounted | uTCA.4 |
| | FPGA | | Xilinx | Altera | Xilinx |
| | ADC sampling rate | MHz | 81.25 | 65 | 81.25 |
| | Beam compensation (Beam FF) | | automatically customized | flat | scaled per bunch |
| | Control interface | | EPICS | ACNET | DOOCS |
| Beam | Repetition rate | Hz | 5 | 5 | 5 or 10 |
| | Beam pulse length | ms | 1 | 1 | 1 |
| | Bunch spacing | MHz | 162.5 | | 1 to 3 |
| | Bunches | | 162500 | | 2400 |
| | Beam current | mA | 10 | | 9 |
| | Energy | MeV | 40 | 600 | 1250 |
| | Charge | pC/bunch | 62 | | 20 - 3000 |

# Chapter 3

# State of the Art LLRF Techniques

In this chapter the principles of digital LLRF control are introduced. Furthermore the three different sampling methods, namely undersampling, IQ sampling, and oversampling are discussed. The LLRF control systems at KEK STF, at FNAL ASTA, and the MTCA.4–based LLRF control system at DESY are introduced. These topics are an essential background for the studies presented in this dissertation.

## 3.1 Principle of Digital LLRF Control

### 3.1.1 Down Conversion in Frequency

The superconducting 9–cell TESLA–like cavities of all facilities mentioned in chapter 2 are driven with a sinusoidal 1.3 GHz RF. This means also the picked up signal has a frequency of 1.3 GHz, which can be described as

$$S_{RF}(t) = A_{RF} \cdot \sin(2\pi \cdot f_{RF} \cdot t + \phi_{RF}) \ , \tag{3.1}$$

where $A_{RF}$ is the amplitude of the RF signal, $f_{RF} = 1.3$ GHz the RF frequency, and $\phi_{RF}$ the RF phase. In the following we assume that $A_{RF} = 1$ and $\phi_{RF} = 0$. Since it is intended to control the cavity fields in feedback operation using digital controller techniques, the pickup signal has to be digitized. Although nowadays the technology of analog–to–digital converters (ADCs) is highly advanced, the GHz frequency regime is too high. ADCs are commonly suitable for a MHz regime. In order to overcome this situation, the picked up signal is down converted in frequency. This is done by mixing the

signal with a similar signal with a slightly different frequency, corresponding to

$$S_{LO}(t) = A_{LO} \cdot \sin(2\pi \cdot f_{LO} \cdot t + \phi_{LO}) \ , \tag{3.2}$$

where $A_{LO}$ is the LO amplitude, of the $f_{LO}$ LO frequency (in the case of KEK STF 1.31 GHz), and $\phi_{LO}$ the LO phase. Also in this case we assume in the following that $A_{LO} = 1$ and $\phi_{LO} = 0$. LO stands for local oscillator, since this frequency is created locally e.g. by frequency dividers, which are driven by the main oscillator. The mixing of the LO and the RF signals yields

$$\begin{aligned} S_{LO\cdot RF}(t) &= \sin(2\pi \cdot f_{LO} \cdot t) \cdot \sin(2\pi \cdot f_{RF} \cdot t) \\ &= \frac{1}{2} \left( \cos(2\pi \cdot (f_{LO} - f_{RF}) \cdot t) - \cos(2\pi \cdot (f_{LO} + f_{RF}) \cdot t) \right) \ , \end{aligned} \tag{3.3}$$

in which a low frequency (lower sideband, $(f_{LO} - f_{RF})$) and a high frequency (upper sideband, $(f_{LO} + f_{RF})$) component can be recognized. In case of STF using a low pass filter with a cutoff frequency higher than 10 MHz and lower than 2.61 GHz only the low frequency or intermediate frequency (IF) component

$$S_{IF}(t) = \frac{1}{2} \cos(2\pi \cdot f_{IF} \cdot t) \tag{3.4}$$

can be extracted. In case of STF, using this technique, the 1.3 GHz signal is down converted to a 10 MHz signal, while the amplitude and phase information are proportional to the original ones and with this are being preserved. It should be noted that a change in phase or phase jitter at the RF signal is exactly translated to the IF signal. Since the frequency is converted to a lower level, the control techniques making use of this method are called low level radio frequency (LLRF) control techniques.

The signal, down converted to the MHz regime, can be digitized by an ADC. The process of digitizing the IF signal corresponds to a conversion from a function continuous in time to a series of points discrete in time. The Nynquist–Shannon theorem demands that the sampling frequency is more than two times higher than the frequency of the signal to be digitized in order to be able to reconstruct it. There are three possibilities for sampling the IF signal by an ADC: IQ sampling, undersampling, and oversampling. These are described in the following sections.

The data signal processing of the digitized signal on the field programmable gate array (FPGA) is not done in a polar representation (in terms of amplitude and phase) but in Cartesian coordinates (in terms of the in–phase (I)

or real part and the quadrature (Q) or imaginary part). Figure 3.1 shows the representation of a vector in the complex plane using polar as well as Cartesian coordinates.

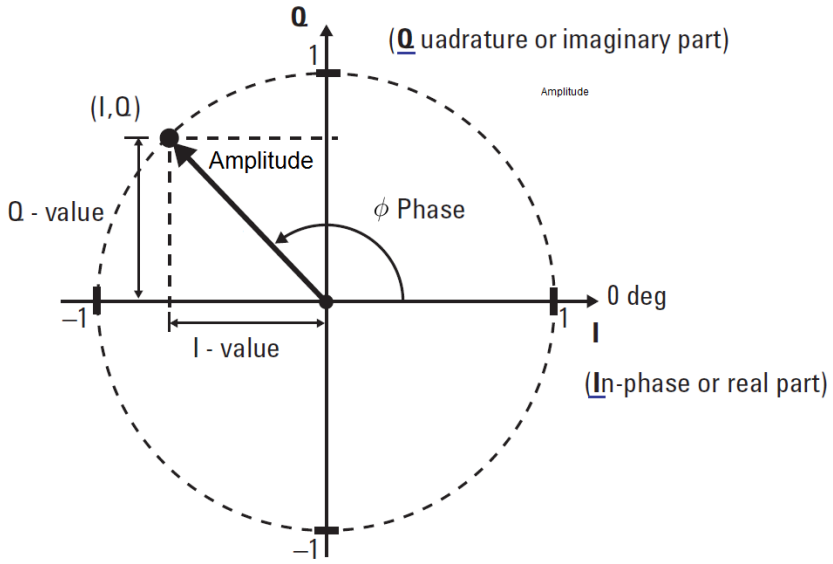


Figure 3.1: Representation of a vector in the complex plane using amplitude ($A$) and phase ($\phi$) as well as I (in–phase or real part) and Q (quadrature or imaginary part) values.

The conversion between both systems can be written as

$$\begin{aligned} I &= A\cos(\phi) \\ Q &= A\sin(\phi) \\ A &= \sqrt{I^2 + Q^2} \\ \phi &= \operatorname{atan}\left(\frac{Q}{I}\right) \quad . \end{aligned} \tag{3.5}$$

Signal processing on the FPGA is performed in Cartesian coordinates, because it is faster to retrieve those values from the IF signal compared to polar coordinates. The polar coordinates would have to be calculated corresponding to equations (3.5), which could be done e.g. by using a CORDIC algorithm. The CORDIC algorithm would have to be used a second time for a reverse conversion to I and Q values, which are sent to the DACs. These two conversions would be very time consuming. The goal when designing an

FPGA–based controller is to keep the loop delay as low as possible due to stability reasons.

### 3.1.2 IQ Sampling

The condition for IQ sampling is that the sampling frequency $f_s$ is

$$f_s = 4 \cdot f_{IF} \ . \tag{3.6}$$

This means the phase advance between the sampled points is 90° (or $\frac{\pi}{2}$). For four consecutive sampling points it can be defined that

$$\begin{aligned} f_{IF}(0) &= Q \\ f_{IF}(\frac{\pi}{2}) &= I \\ f_{IF}(\pi) &= -Q \\ f_{IF}(\frac{3\pi}{2}) &= -I \ . \end{aligned} \tag{3.7}$$

In Figure 3.2 a schematic of this sampling method is shown.

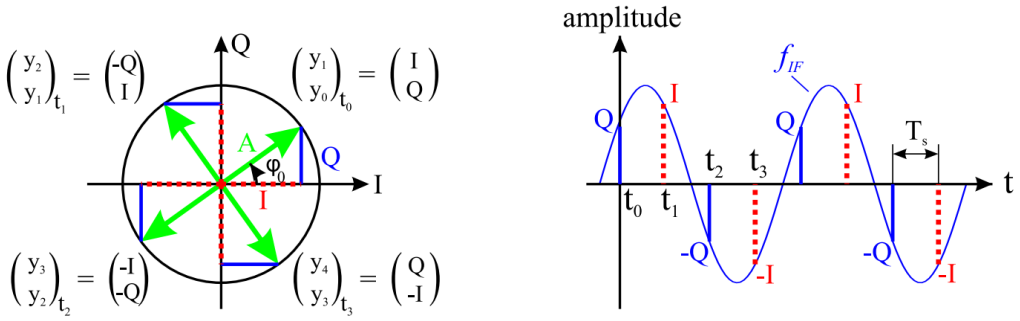


Figure 3.2: Schematic of IQ sampling [21]. On the left hand side the acquired vectors (green arrows) are represented in the complex plane. The corresponding $y_n$ vector components are obtained during two consecutive sampling clocks $n$ and $n+1$. On the right hand side the intermediate frequency signal is shown in a plot amplitude versus time. At every point in time $t_n$, which are equidistant by the sampling time $T_s$, the amplitude is sampled resulting in Q, I, -Q, -I values.

The I and Q values can be calculated by

$$\begin{pmatrix} I \\ Q \end{pmatrix}_n = \begin{pmatrix} \cos(\Delta\phi_n) & -\sin(\Delta\phi_n) \\ \sin(\Delta\phi_n) & \cos(\Delta\phi_n) \end{pmatrix} \cdot \begin{pmatrix} f_{IF,n+1} \\ f_{IF,n} \end{pmatrix} \tag{3.8}$$

in the time of two consecutive sampling points, where the vector is rotated by $\Delta\phi = 0$, $-\frac{\pi}{2}$, $-\pi$, or $-\frac{3\pi}{2}$. The rotation algorithm is performed at the sample rate $f_s$.

For a more detailed description of the calculation of the I and Q values in the case of IQ sampling refer to Appendix A.

### 3.1.3 Undersampling and Oversampling

It is also possible in a more general case to choose the sampling frequency as an multiple of the IF frequency:

$$\frac{f_s}{f_{IF}} = \frac{M}{L} = m \ , \tag{3.9}$$

where $M$ and $L$ are integers. The case of $m = 4$ corresponds to the IQ sampling. The case of $m < 2$ corresponds to undersampling and $m > 2$ to oversampling. In the general case the phase advance between two consecutive samples is

$$\Delta\phi = \frac{2\pi}{m} \ . \tag{3.10}$$

In the case amplitude and phase of the IF signal do not change significantly, the IF signal is sampled at the same locations for every period. For two consecutive samples the following set of linear equations is obtained

$$\begin{pmatrix} I_n \\ Q_n \end{pmatrix}_n = \begin{pmatrix} \cos(\Delta\phi) & \sin(\Delta\phi) \\ -\sin(\Delta\phi) & \cos(\Delta\phi) \end{pmatrix} \cdot \begin{pmatrix} I_{n+1} \\ Q_{n+1} \end{pmatrix} \ . \tag{3.11}$$

This can be rewritten as

$$\begin{pmatrix} I_n \\ Q_n \end{pmatrix}_n = \frac{1}{\sin(\Delta\phi)} \begin{pmatrix} 1 & -\cos(\Delta\phi) \\ 0 & \sin(\Delta\phi) \end{pmatrix} \cdot \begin{pmatrix} y_{IF,n+1} \\ y_{IF,n} \end{pmatrix} \ , \tag{3.12}$$

where $y_{IF,n}$ is the amplitude of the IF signal at the time step $n$. Also in this case the vector has to be rotated back for comparison with the initial vector by the angle $-n\Delta\phi$. This yields for the initial I and Q values $I_0$ and $Q_0$:

$$\begin{pmatrix} I_0 \\ Q_0 \end{pmatrix}_n = \frac{1}{\sin(\Delta\phi)} \begin{pmatrix} \cos(n\Delta\phi) & -\cos((n+1)\Delta\phi) \\ -\sin(n\Delta\phi) & \sin((n+1)\Delta\phi) \end{pmatrix} \cdot \begin{pmatrix} y_{IF,n+1} \\ y_{IF,n} \end{pmatrix} \ . \tag{3.13}$$

Furthermore for a more general case an user defined rotation by $-\phi$ can be included. Is this considered the I and Q values compute as

$$\begin{pmatrix} I \\ Q \end{pmatrix}_n = \frac{1}{\sin(\Delta\phi + \phi)} \begin{pmatrix} \cos(n\Delta\phi + \phi) & -\cos((n+1)\Delta\phi + \phi) \\ -\sin(n\Delta\phi + \phi) & \sin((n+1)\Delta\phi + \phi) \end{pmatrix} \cdot \begin{pmatrix} y_{IF,n+1} \\ y_{IF,n} \end{pmatrix} . \tag{3.14}$$

Figure 3.3 shows a schematic of the algorithm.

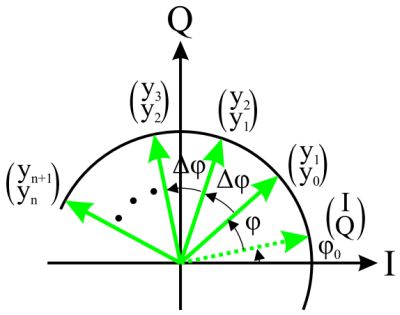


Figure 3.3: Schematic of sampling in the case of $\Delta\phi = 2\pi/m$ [21] represented in the complex plane. At every sample time the sampled vectors (green arrows) consisting of $y_n$ and $y_{n+1}$ values.

The absolute I and Q values can in the case of non–IQ sampling can be calculated as follows.

$$\begin{aligned} I &= \frac{2}{m} \sum_{n=0}^{m-1} y_n \cos\left(\frac{2\pi n}{m}\right) \\ Q &= \frac{2}{m} \sum_{n=0}^{m-1} y_n \sin\left(\frac{2\pi n}{m}\right) \end{aligned} \tag{3.15}$$

The advantage of undersampling is that the due to the lower sampling rate the requirements for the ADC, such as e.g. power consumptions, are more relaxed. The lower data rate, which needs to be processed, further relaxes timing requirements on the FPGA. This affects the choice of the FPGA and with this the cost of the design. Beside this in the case of undersampling it is possible to detect IF signals with higher frequencies than the ADC sampling rate.

The advantage of oversampling is that more data points per period are collected. Due to this an averaging in the calculation of the I and Q values,

which can be seen in equations (3.15), reduces their noise. Furthermore in the case of oversampling the choice of the IF location in the first Nyquist is more flexible, corresponding e.g. to the available analog anti–aliasing low pass filters or to the ADC circuit optimization.

## 3.2 LLRF Feedback Loop at STF

The simplified schematic of the LLRF control loop for the superconducting cavities at STF is shown in Figure 3.4.

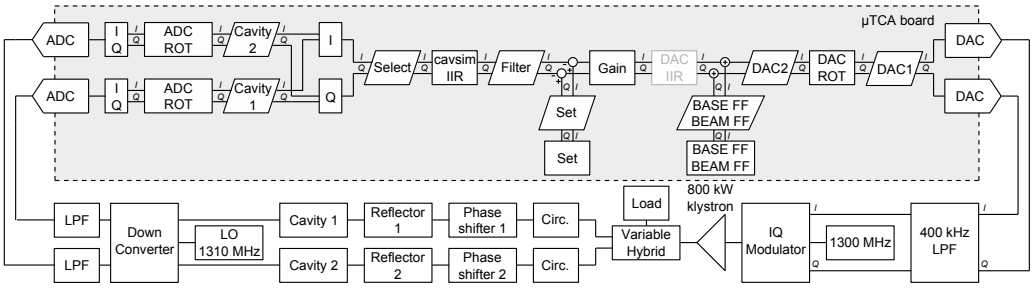


Figure 3.4: Schematic of the digital LLRF feedback loop controlling two superconducting cavities at STF. Hardware and software components are represented by rectangles and data channels accessible on the $\mu$TCA board via EPICS by rhombi.

The cavity pickup signals are down converted to an IF frequency of 10 MHz (1.3 GHz/128) using mixers. In a next step the signals are low pass filtered. The filtered signals are digitized by 16–bit ADCs (LTC2208) on the $\mu$TCA board [22]. Thereby the sampling frequency is 80 MHz (1.3 GHz/16), which corresponds to the oversampling technique for digitalization. Referring to equation (3.9) $M = 8$, $L = 1$, and $m = 8$. The cavity signals are converted to baseband and I and Q values. In a next step individual rotations for those cavity pickup I and Q values are possible. From those signals the vector sum in term of I and Q values is calculated. The vector sum is filtered and subtracted from the set point table resulting in I and Q error signals. To those a proportional gain is applied and the base feedforward (FF) as well as the beam FF tables are added. In a next step a rotation can be applied. The I and Q signals are converted from digital to analog by 16–bit DACs (AD9783, 2 channel per chip). The analog I and Q signals are filtered by an analog 400 kHz low pass filter in order to suppress the excitation of $8/9\pi$–modes [23] in the cavities. The filtered signals are up converted in frequency

to 1.3 GHz by an IQ modulator. This RF signal is preamplified and sent to the 800 kW klystron, which drives both superconducting cavities. To this end the klystron output power is divided by a variable hybrid [24], which has a range from 0 dB to -6 dB for the through port. The cavity phases are optimized individually by remotely controlled waveguide phase shifters [24]. Those have a range of about 120°. Since a remote control for the coupler positions is not available, remotely controlled waveguide reflectors are used in order to adjust the loaded quality factor of the cavities ($Q_L$) by changing the coupling. The possible range in $Q_L$ is from $2.5 \cdot 10^6$ to $5 \cdot 10^7$. Lorentz force detuning in the cavities is compensated dynamically by piezo tuners, which are operated using a sine wave form voltage [25].

## 3.3 Digital LLRF Control System at ASTA

A simplified schematic of the digital LLRF feedback loop for controlling the eight superconducting cavities within the ILC RF unit at ASTA is shown in Figure 3.5. The pickup signals of all eight cavities are sent to the 8 channel receiver board, on which they are down converted in frequency. The LO is 1.313 GHz yielding an IF of 13 MHz. The eight down converted cavity pickup signals then are transferred to the multi–channel field controller (MFC) board [26], on which they are digitized. To this end 12–bit ADCs (AD9222) with a sampling rate of 65 MHz are used [26]. This corresponds to 5 sampling points per period and with this to oversampling ($M = 5$, $L = 1$, and $m = 5$). From the digitized pickup signals the vector sum is calculated and the controller is applied. A more detailed description of the implemented signal processing on the MFC board including the controller follow in the following paragraph. The output of the MFC board is converted to analog using 14–bit DACs (ISL5927). The signal is up converted and sent as the RF drive signal to the 5 MW klystron, which drives all eight cavities.

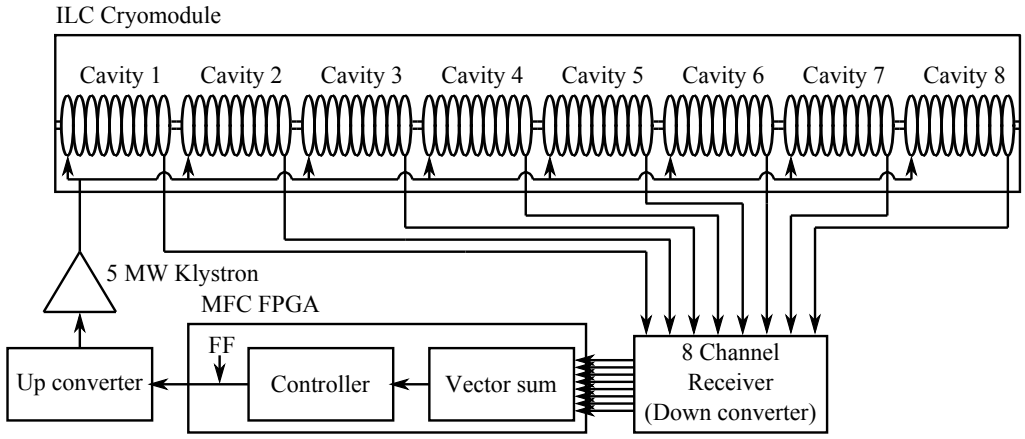


Figure 3.5: *Simplified schematic of the LLRF system setup at ASTA for the ILC RF unit. The cavity pickup signals are down converted on the 8 channel receiver board. These signals then are digitized and processed on the MFC board. Its FPGA includes beside others the calculation of the vector sum, the controller, and the addition of feedforward tables. The output of the MFC is up converted and sent to the klystron, which drives all eight cavities.*

Figure 3.6 shows the schematic of the implemented signal processing on the MFC board. The main part of the described signal processing is performed on an Altera Cyclone II FPGA. The cavity pickup signals, down converted to IF, are digitized by 12 bit ADC (1.29 Vpp) with a sampling rate of 65 MHz. To the generated I and Q values a band pass filter is applied. The signals can be arbitrarily scaled (by a factor between 0 and 1.99) and rotated in phase. Furthermore the signals are down converted to base band. From all eight cavity pickup signals the vector sum is computed. A CIC filter, a multiplication by 4, and a low pass FIR filter are applied. From this signal the set point is subtracted. The resulting I and Q signals are clamped. The next element in the signal processing is a switch, by which the signal generated can be transmitted or interrupted. By this the on–off switch for the feedback is realized. The signal is split up into two paths. In the first path the proportional gain is applied. In the second path the integral part of the controller is realized. To this end the integral gain is multiplied to the signal. The product is summed with a time delayed and with the integrator pole multiplied version of itself. The output of the proportional and the integral controllers are summed. To the controller output a feedforward table is added, which can be switched on or off. The resulting signal can be scaled (by a factor between 0 and 1.99) and rotated in phase. After a up conversion

and clamping the I and Q signals are digital to analog converted by 14 bit ADCs (0.5 Vpp).

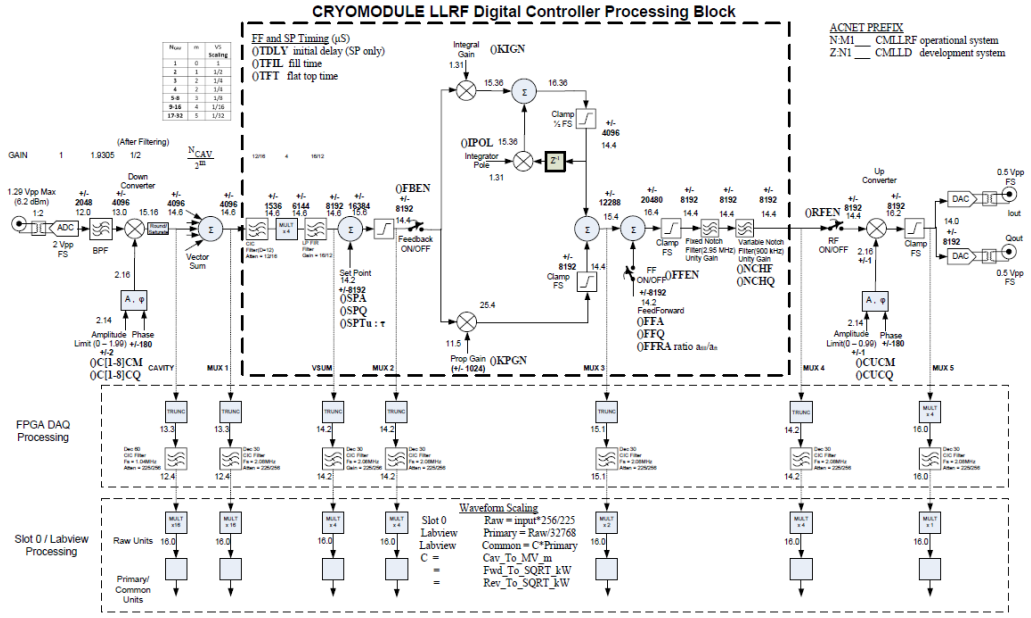


Figure 3.6: *Detailed schematic of the implemented signal processing on the MFC board. The eight down converted cavity pickup signals are digitized and the vector sum is computed. The filtered I and Q signals are subtracted from the set point and in parallel a proportional and an integral gain is applied. The output is again filtered and, if the RF switch is on, sent to the DACs.*

## 3.4 Digital MTCA.4–based LLRF System at DESY

At FLASH, X–FEL, AMTF, and CMTB digital LLRF control systems based on the MTCA.4 standard are implemented [44, 45]. Main features of such a rack are 12 slots at the front and at the back, which are hot swappable. At the front Advanced Mezzanine Cards (AMC) are used. At the back Rear Transition Modules (RTM).

Figure 3.7 shows a typical configuration for one cryomodule with 8 superconducting 9–cell cavities. It consists of three down converter cards (uDWC), which are RTMs. The inputs are a clock signals, the LO signal of 1.354 GHz, and depending on each card 8 channels probe signals, 8 channels forward signals, or 8 channel reflected signals. The to IF (54.17 MHz) down converted

signals are sent to three digitizer boards (uDAQ). Each board digitizes 8 channels of the IF of the probe signals, forward signals, or reflected signals. The sampling rate is 81.25 MHz, which means that the digitalization is done using undersampling. Referring to equation (3.9) this corresponds to $M = 2$, $L = 3$, and $m = 1.5$. The digitized signals are converted to I and Q values, filtered, rotated, and the partial vector sum of the 8 signals is calculated. Via the backplane the three partial vector sums are sent to the LLRF controller card (uTC). On this card the vector sum of all partial vector sums is computed. In the shown schematic shown in Figure 3.7 there is only one partial vector sum, but in the schematic shown in Figure 3.8 there are two partial vector sums. To the vector sum the set point is applied, the feedback is applied, and FF tables are added. The resulting I and Q signals are sent to the vector modulator board (uVM), which also receives the LO and the clock signal. On the uVM by up conversion the RF drive signal is generated, which is sent to the preamplifier of the klystron.

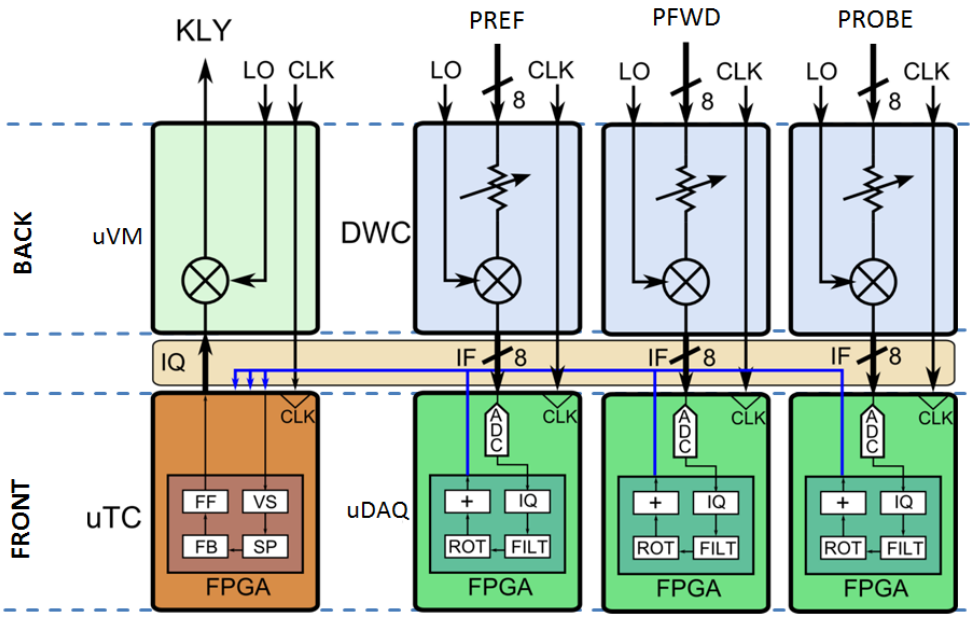


Figure 3.7: *Schematic of the MTCA.4 LLRF System [46]. Eight cavity probe, forward, and reflected signals are down converted on three DWC boards. All down converted signals are sent to three uDAQ boards, on which they are digitized and beside others filtered. The digital probe signals are sent to the uTC board. On its FPGA beside others the vector sum is computed and the controller is applied. The output then is transmitted to the uVM board, on which the signal is up converted and sent to the klystron.*

Figure 3.8 shows a schematic of a second configuration case covering more details about the architecture of the LLRF controller firmware. In this case 4 cryomodules with 8 superconducting 9–cell cavities each are controlled. All cavities are driven by a single klystron. The LLRF control is realized in a master–slave configuration of two racks. In the master rack a combination of 6 uDWCs and 6 uDAQs is used in order to down convert and digitize the probe, forward and reflected signals of the 16 cavities of the first two cryomodules. In the slave rack a similar combination of 6 uDWCs and 6 uDAQs is used for the down conversion and digitalization of the probe, forward and reflected signals of the 16 cavities of the last two cryomodules. In the slave rack the partial vector sum (PVS) is calculated on the uTC and sent to the uTC in the master rack. There the partial vector sums are combined, to which the set point is applied. The set point is changed by the beam based feedback (BBFB). The controller type used is a multiple input multiple output (MIMO) controller. Around this a learning feedforward (LFF) loop is wrapped. Beside this also user defined FF tables can be added. After this the beam loading compensation (BLC) is added and a rotation correction is applied. As a last processing step on the uTC a linearization algorithm is applied. The I and Q signals then are sent to the uVM, which generates the RF drive signals, which is sent to the klystron preamplifier and the klystron.

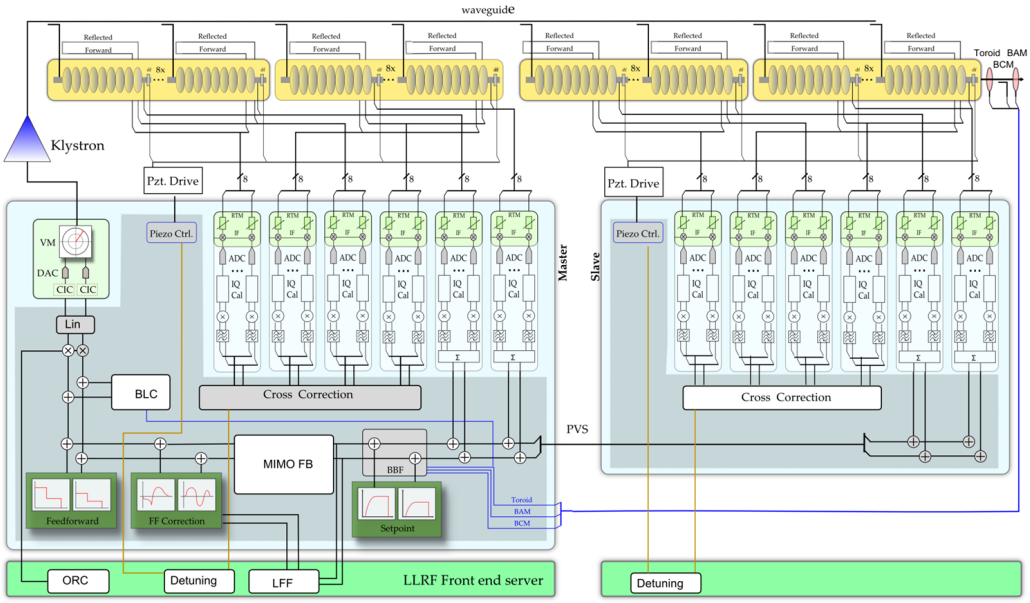


Figure 3.8: *Detailed Schematic of the MTCA.4 LLRF System [46]. On the slave boards the probe, forward, and reflected signals of two cryomodules with eight superconducting cavities each are down converted and digitized. From the probe signals the partial vector sum is computed and sent to the master boards. On those also the probe, forward, and reflected signals of two further cryomodules with eight superconducting cavities each are down converted and digitized. Also the partial vector sum of the probe signals is computed and combined with the one from the slave boards. To the total vector sum a MIMO controller is applied. Its output is sent to the klystron, which drives all cavities in all four cryomodules.*

## 3.5 Example of an Analog LLRF System

In the past, when FPGAs or DSPs were not yet developed or not yet sufficient in performance, analog LLRF control systems were used in order to control accelerator cavities. But still at quite recently build facilities, as e.g. at ALBA[1] [27] close to Barcelona in Spain, analog LLRF control systems are in use. In this case the analog LLRF system controls a 5–cell PETRA–type cavity. The RF parameters of the ALBA booster are listed in Table [28].

[1]ALBA is not an acronym, it is the Spanish word for sunrise.

Table 3.1: RF parameters of the ALBA booster [28].

| Parameter | Value | Unit |
|---|---|---|
| RF Frequency | 499.654 | MHz |
| Repetition frequency | 3 | Hz |
| Number of cavities | 1 | |
| Cavity shunt impedance | 14 | MΩ |
| RF power (at 3 GeV) | 40 | kW |
| RF voltage (at 3 GeV) | 1 | MV |
| Beam current | 2 | mA |
| Beam power (at 3 GeV) | 1.3 | kW |
| Amplitude stability | $\leq \pm 1\%$ | |
| Phase stability | $\leq \pm 1$ | $^\circ$ |
| DAC resolution | 16 | bits |
| DAC throughput | 100 | kHz |
| LLRF bandwidth | $> 200$ | kHz |
| Loop delay | $< 1000$ | ns |
| Dynamic range | $> 23$ | dB |

Figure 3.9 shows the analog LLRF control loop [28]. It is based on a quadrature demodulation and a PID controller. The cavity pickup signal is decomposed into ±I and ±Q components. These are converted to single–end I and Q values by an IQ demodulator board. Each I and Q signal is sent to an individual analog PID controller. Beside this the single–ended I and Q signals are digitized by ADCs on a PCI DAQ card, which is connected to a PC. On the PC the I and Q signals can be monitored. Furthermore FB set values are created on the PC and sent via DACs to the two analog PID controllers. To the output of the two PID controllers a gain is applied and feedforward tables are added. The gain and the tables are also created on the PC, but are applied via analog components. In a next step the I and Q signals are fed to a base–band phase shifter, which is based on six analog adder/multipliers. By this a rotation of the IQ vector is realized for the compensation of loop delays. Also the rotation parameters are controlled by the PC. The rotated I and Q signals are converted from single–ended to differential signals and fed to a quadrature modulator board. The output of the modulator is preamplified and sent to an IOT, which drives the cavity. By this loop the cavity amplitude and phase are controlled.

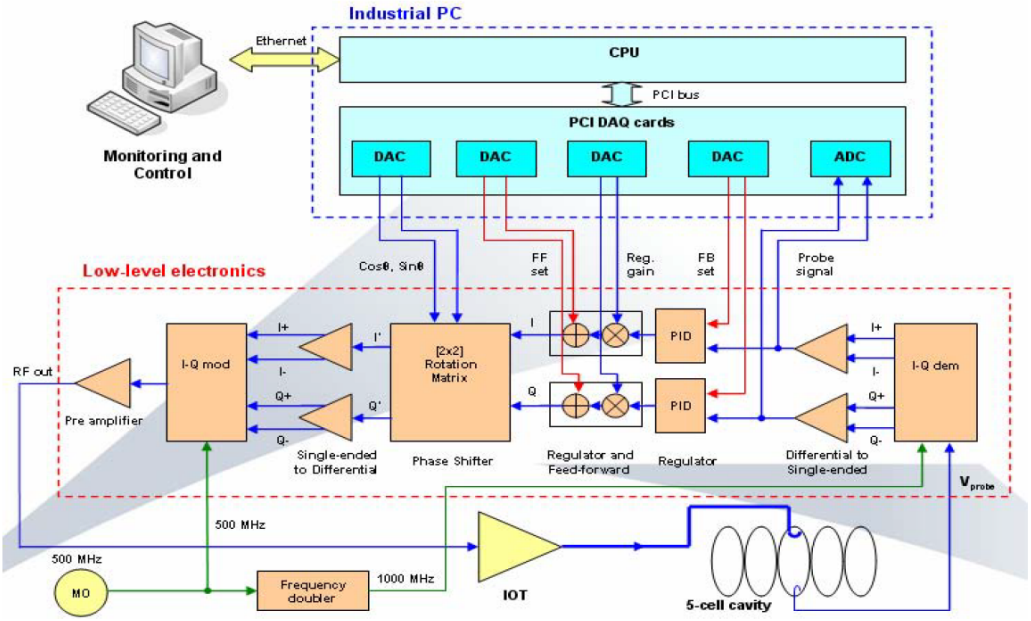


Figure 3.9: *Analog LLRF control loop at the ALBA booster [28]. IT consists of the cavity, the IQ demodulator, differential to single end converters, PID controllers, a rotation matrix realized by phase shifters, singe end to differential converters, an IQ modulator, a pre amplifier, and an IOT. The control parameters are generated using a PC.*

# Chapter 4

# Cavity Modeling

In this chapter aspects of cavity modeling essential for the understanding of the following chapters are discussed, covering the definition of the loaded quality factor, the derivation of filling and flattop powers, the description of a detuned cavity with beam loading, and $P_k Q_L$ control.

## 4.1 Definition of the Loaded Quality Factor

The definition of the loaded quality factor follows [29]. The definition of the quality factor of a resonant device such as a cavity is

$$Q = 2\pi \frac{\text{stored energy in cavity}}{\text{dissipated energy per cycle}} = \frac{2\pi f_0 W}{P_{diss}} \ , \tag{4.1}$$

where $f_0$ is the resonance frequency, $W$ stored energy, and $P_{diss}$ the dissipated power. In the case it is assumed that the loss is only due to the surface resistance of the cavity, the unloaded quality factor $Q_0$ is defined as

$$Q_0 = \frac{2\pi}{T} \cdot \frac{\frac{1}{2} C V_0^2}{\frac{1}{2}\frac{V_0^2}{R}} \ , \tag{4.2}$$

where $V_0$ is the amplitude of the oscillating voltage and T the time period of an RF cycle. Furthermore $W = \frac{1}{2} C V_0^2$ and $P_{diss} = \frac{V_0^2}{2R}$ was used. Taking into account the resonance frequency of an undamped LC circuit $\omega_0 = \frac{1}{\sqrt{LC}}$ the unloaded quality factor can be rewritten as

$$Q_0 = \omega_0 RC = \frac{R}{L\omega_0} = \frac{\omega_0 W}{P_{diss}} \ . \tag{4.3}$$

In reality energy is not only dissipated in the walls of the cavity, but also through the power coupler in an external load. The external quality factor

is defined as

$$Q_{ext} = 2\pi \frac{\text{stored energy in cavity}}{\text{dissipated energy in external devices per cycle}} = \frac{\omega_0 W}{P_{ext}} \ , \quad (4.4)$$

where $P_{ext}$ is the dissipated power in all external devices. With this the loaded quality factor is defined as

$$Q_L = 2\pi \frac{\text{stored energy in cavity}}{\text{total energy loss per cycle}} = \frac{\omega_0 W}{P_{tot}} \ . \quad (4.5)$$

From energy conversation the total power loss can be defined as

$$P_{tot} = P_{diss} + P_{ext} \ . \quad (4.6)$$

Taking into account equations (4.3), (4.4), and (4.5) yields

$$\frac{1}{Q_L} = \frac{1}{Q_0} + \frac{1}{Q_{ext}} \ . \quad (4.7)$$

In the case of superconducting cavities usually the unloaded $Q_0$ is several orders of magnitude larger than the external quality factor $Q_{ext}$, which means that the loaded quality factor $Q_L$ is in the same order of magnitude as $Q_{ext}$.

The external load $Z_{ext}$ is like a parallel resistor to the cavity resistor $R$. Due to this those can be replace by a single resistor $R_L$, which is called loaded shunt impedance.

$$\frac{1}{R_L} = \frac{1}{R} + \frac{1}{Z_{ext}} \ . \quad (4.8)$$

Using equation (4.3) yields

$$\frac{R}{Q_0} = \omega_0 = \frac{1}{\omega_0 C} = \sqrt{\frac{L}{C}} \ . \quad (4.9)$$

One can see that the ratio $\frac{R}{Q_0}$ depends on $\omega_0$, $C$, and $L$, which means it is only dependent on the cavity geometry and not the surface resistance. The definition was made in terms of the shunt impedance $R_{sh}$ and not of $R$, yielding with $R = \frac{1}{2}R_{sh} = \frac{1}{2}\frac{r}{Q}Q_0$ the definition

$$\frac{r}{Q} := \frac{R_{sh}}{Q_0} = \frac{2R}{Q_0} \ . \quad (4.10)$$

The shunt impedance of the superconducting 9–cell cavities estimated at STF is 1036 Ω.

Furthermore the coupling between the cavity and the transmission line can be defined by the coupling factor $\beta$. It is defined as the ratio of the cavity resistor $R$ and the transformed external load $Z_{ext}$

$$\beta = \frac{R}{Z_{ext}} \ . \tag{4.11}$$

Using this equation (4.8) can be rewritten as

$$R_L = \frac{R}{1+\beta} \tag{4.12}$$

and with this equation (4.13) to

$$Q_L = \frac{Q_0}{1+\beta} \ . \tag{4.13}$$

This shows that one possibility of manipulation of the loaded quality factor is the change of the coupling $\beta$.

## 4.2 Derivation of Filling and Flattop Powers

A schematic of the model for a cavity, on which the derivation of the filling and the flattop powers is based, is shown in Figure 4.1. It is a RLC circuit with the inductance $L$, the resistance $R$, and the capacitance $C$. Furthermore the generator current $I_g$ and the beam current $I_b$ add up to the current $I_{cav}$, which drives the RLC circuit.

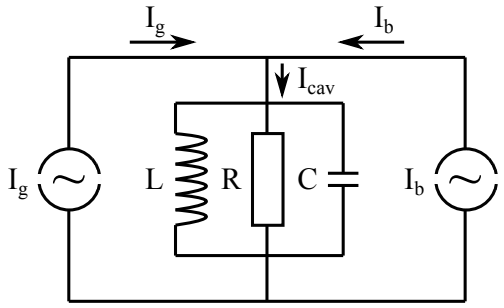


Figure 4.1: Schematic of a RLC circuit as a cavity model with generator current $I_g$ and beam current $I_b$.

The current over the inductance is $I_L$, over the resistance $I_R$, and over the capacitance $I_C$. From Kirchhoff's circuit laws the following holds

$$I_C + I_R + I_L = I_{cav} \quad . \tag{4.14}$$

Deriving for time yields

$$\dot{I}_C + \dot{I}_R + \dot{I}_L = \dot{I}_{cav} \quad . \tag{4.15}$$

Inserting $\dot{I}_C = C\ddot{V}_{cav}$, $\dot{I}_R = \frac{1}{R_L}\dot{V}_{cav}$, and $\dot{I}_L = \frac{1}{L}V_{cav}$, where $R_L$ is the loaded shunt impedance, yields

$$C\ddot{V}_{cav} + \frac{1}{R_L}\dot{V}_{cav} + \frac{1}{L}V_{cav} = \dot{I_{cav}} \quad . \tag{4.16}$$

By this the cavity voltage $V_{cav}$ and its first $\dot{V}_{cav}$ and second time derivative $\ddot{V}_{cav}$ are introduced. The division by $C$ yields

$$\ddot{V}_{cav} + \frac{1}{R_L C}\dot{V}_{cav} + \frac{1}{LC}V_{cav} = \frac{1}{C}\dot{I}_{cav} \quad . \tag{4.17}$$

Inserting $\frac{1}{LC} = \omega_0^2$ and $\frac{1}{R_L C} = \frac{\omega_0}{Q_L}$, where $\omega_0$ is the angular frequency corresponding to the resonance frequency $f_0 = \frac{\omega_0}{2\pi} = 1.3$ GHz, leads to

$$\ddot{V}_{cav} + \frac{\omega_0}{Q_L}\dot{V}_{cav} + \omega_0^2 V_{cav} = \frac{1}{C}I_{cav} \quad , \tag{4.18}$$

which is an inhomogeneous second order differential equation. The homogeneous solution is

$$V_{\mathrm{hom}} = e^{-\frac{\omega_0 t}{2Q_L}}\left(C_1 e^{i\alpha t} + C_2 e^{-i\alpha t}\right) \quad , \tag{4.19}$$

with $\alpha = \omega_0\sqrt{1 - \frac{1}{4Q_L^2}}$. $C_1$ and $C_2$ are constants and will be defined in the following. $t$ is the variable representing time. One particular solution can be found with $I_{cav} = \hat{I}e^{i\omega t}$ and $V_{cav} = \hat{V}e^{i(\omega t + \phi)}$, where $\phi$ is the angle between the generator current and the resonator voltage:

$$V_{\mathrm{par}} = \frac{R_L \hat{I} e^{i(\omega t + \phi)}}{\sqrt{1 + \tan^2\phi}} \quad , \tag{4.20}$$

with $\tan\phi = R\left(\frac{1}{\omega L} - \omega C\right) = Q\left(\frac{\omega}{\omega_0} - \frac{\omega_0}{\omega}\right)$. The particular solution is also called the stationary solution. If the generator frequency $\omega$ is very close to the cavity resonance frequency $\omega_0$, this solution and with this the voltage amplitude can be approximated with

$$\hat{V}_{\mathrm{par}}(\Delta\omega) \approx \frac{R_L \hat{I}}{\sqrt{1 + \left(2Q_L\frac{\Delta\omega}{\omega}\right)}} \quad , \tag{4.21}$$

where $\Delta\omega = \omega_0 - \omega$. The frequency dependency of the amplitude is known as Lorentz curve [29] and is shown along with the phase in Figure 4.2. The bandwidth $\omega_{1/2}$ of the cavity is defined as the frequency bandwidth where the voltage drops -3 dB (or $\frac{1}{\sqrt{2}}$) of its maximum $\hat{V}_0 = R_L \hat{I}_0$.

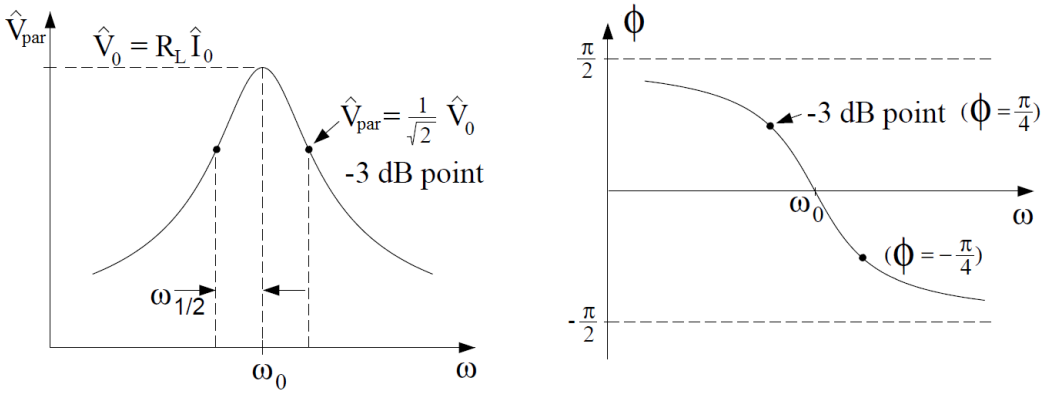


Figure 4.2: *Resonance curves for amplitude $\hat{V}_{par}$ and phase $\phi$ of a cavity. The -3 dB points are marked in both diagrams [29].*

The general solution of the differential equation (4.18) reads

$$V_{cav} = V_{\text{hom}} + V_{\text{par}} = e^{-\frac{\omega_0 t}{2Q_L}} \left( C_1 e^{i\alpha t} + C_2 e^{-i\alpha t} \right) + \frac{R_L \hat{I} e^{i(\omega t - \phi)}}{\sqrt{1 + \tan^2 \phi}} \quad . \tag{4.22}$$

Since $Q_L >> 1$, the approximation $\alpha \approx \omega_0$ can be made. For $C_1 = C_2 = -\frac{R_L \hat{I}}{2}$ the filling behavior can be found as

$$V_{\text{fill}} = V_0 \left( 1 - e^{-\frac{t}{\tau}} \right) \quad , \tag{4.23}$$

with the initial cavity voltage $V_0 = R_L \hat{I} \approx 2R_L I_g = \frac{r}{Q} Q_L I_g$ and the time constant $\tau = \frac{2Q_L}{\omega_0}$. It has to be noted that $\hat{I}$ represents an AC current at 1.3 GHz, whereas $I_g$ represents a DC current. The Fourier decomposition of the AC beam current yields $\hat{I} \approx 2I_g$. The same applies to the beam current, yielding $\hat{I}_b \approx 2I_{b0}$. Hence for the time beam is present $I_{cav} = 2I_g - 2I_{b0}$ holds. From this follows

$$V_{\text{flat}} = \frac{r}{Q} Q_L \left( I_g \left( 1 - e^{-\frac{t}{\tau}} \right) - I_{b0} \cos(\phi_b) \left( 1 - e^{-\frac{t - T_{\text{inj}}}{\tau}} \right) \right) \quad , \tag{4.24}$$

where $T_{\text{inj}}$ is the injection time of the beam and $\phi_b$ the beam phase. The cavity voltage over the flattop region, which corresponds to the beam transient time, shall be flat. This is expressed by

$$\frac{\mathrm{d}V_{\text{flat}}}{\mathrm{d}t} = 0 \ . \tag{4.25}$$

From this follows in several steps of evaluation

$$\frac{d}{dt}\frac{r}{Q}Q_L\left(I_g\left(1-e^{-\frac{t}{\tau}}\right)-I_{b0}\left(1-e^{-\frac{t-T_{inj}}{\tau}}\right)\right)=0 \tag{4.26}$$

$$\frac{d}{dt}\frac{r}{Q}Q_L\left(I_g-I_ge^{-\frac{t}{\tau}}-I_{b0}+I_{b0}e^{-\frac{t-T_{inj}}{\tau}}\right)=0 \tag{4.27}$$

$$\frac{r}{Q}Q_L\left(I_g\frac{1}{\tau}e^{-\frac{t}{\tau}}-I_{b0}\frac{1}{\tau}e^{-\frac{t-T_{inj}}{\tau}}\right)=0 \tag{4.28}$$

$$I_ge^{-\frac{t}{\tau}}=I_{b0}e^{-\frac{t-T_{inj}}{\tau}} \tag{4.29}$$

$$I_g=I_{b0}e^{\frac{T_{inj}}{\tau}} \ . \tag{4.30}$$

Inserting this in equation (4.24), evaluation yields

$$V_{\text{flat}}=\frac{r}{Q}Q_LI_{b0}\left(e^{\frac{T_{\text{inj}}\omega_0}{2Q_L}}-1\right) \ . \tag{4.31}$$

With equations (4.23) and (4.31) a set of functions has been found that describes the cavities amplitude during filling time and the flattop region for a flat flattop where $T_{\text{inj}} = T_{\text{end fill}}$ and $T_{\text{end fill}}$ is the time of the end of the filling. Figure 4.3 shows an example plot for a filling time of 923 $\mu$s and a beam current of 5.8 mA during the flattop. An optimized $Q_L$ value of $5.44 \cdot 10^6$ is assumed.

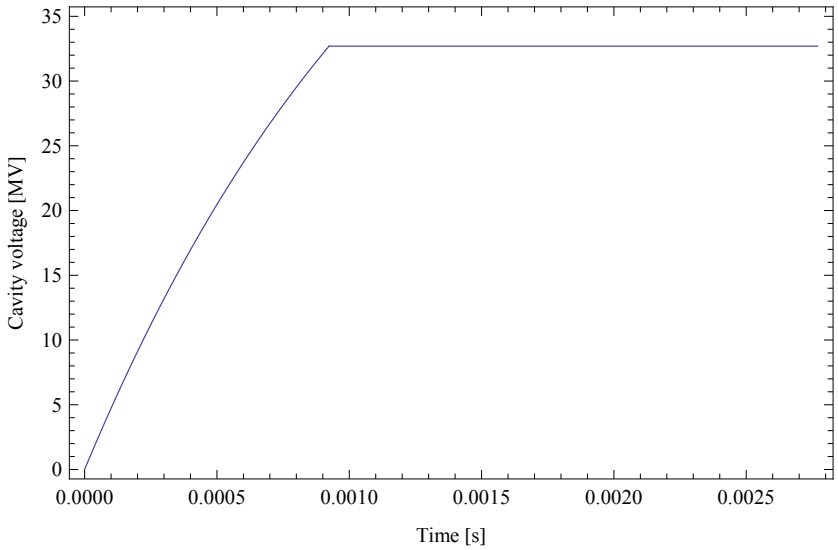


Figure 4.3: *Cavity voltage [MV] over time [s] for a filling time of 923 $\mu$s and the flattop region with a beam current of 5.8 mA.*

In order to find out the respective power $P$ needed to be provided for the filling ($P_{\text{fill}}$)

$$P = \frac{1}{4}\frac{r}{Q}Q_L I_g^2 \tag{4.32}$$

can be insert in equation (4.23), yielding

$$P_{\text{fill}} = \frac{V_{cav}^2}{4\frac{r}{Q}Q_L\left(1 - e^{-\frac{T_{\text{inj}}\omega_0}{2Q_L}}\right)^2} \tag{4.33}$$

in the case of no detune of the cavity ($\Delta\omega = 0$). In the case of a cavity voltage of $V_{cav} = 31.5$ MV/m $\cdot$ 1.038 m = 32.7 MV, a loaded quality factor of $Q_L = 5.44 \cdot 10^6$, and an injection time of $T_{inj} = 923$ $\mu$s the required filling power $P_{fill}$ is 190 kW.

Furthermore in the case the beam current $I_b$ points to the exact opposite direction as the cavity voltage $V_{cav}$ in the complex plane, which corresponds to $\phi_b$, the power at the flattop during beam ($P_{flat}$) reads

$$P_{flat} = \frac{V_{cav}^2}{4\frac{r}{Q}Q_L}\left(1 + \frac{\frac{r}{Q}Q_L I_{b0}}{V_{cav}}\right)^2 \quad . \tag{4.34}$$

In the case of a DC beam current of $I_{b0} = 5.8$ mA and the above mentioned operation parameters the required power during the flattop $P_{flat}$ is 190 kW. With equations (4.33) and (4.34) a set of equations has been found that describes the power during filling time ($P_{\text{fill}}$) and during the flattop and beam ($P_{\text{flat}}$) in dependency of the injection time $T_{\text{inj}}$, the beam current $I_{b0}$, and the $Q_L$ value in the case the beam phase $\phi_b = 180°$.

In the case the beam phase is arbitrary, the power during the flattop reads [29]

$$P_{flat} = \frac{V_{cav}^2}{\frac{r}{Q}Q_L}\frac{\beta+1}{4\beta}\left(\left(1+\frac{\frac{r}{Q}Q_L I_{b0}}{V_{cav}}\cos(\phi_b)\right)^2+\left(\tan(\phi)+\frac{\frac{r}{Q}Q_L I_{b0}}{V_{cav}}\sin(\phi_b)\right)^2\right) \ , \tag{4.35}$$

where $\beta$ is the coupling coefficient. This equation is a general one. In the the case of superconducting cavities, where $\beta \gg 1$, it can be simplified to

$$P_{flat} = \frac{V_{cav}^2}{4\frac{r}{Q}Q_L}\left(\left(1+\frac{\frac{r}{Q}Q_L I_{b0}}{V_{cav}}\cos(\phi_b)\right)^2+\left(\frac{\Delta f}{f_{1/2}}+\frac{\frac{r}{Q}Q_L I_{b0}}{V_{cav}}\sin(\phi_b)\right)^2\right) \ , \tag{4.36}$$

where $\Delta f$ is the detuning and $f_{1/2}$ the bandwidth of the cavity. Is the tuning angle $\phi$ is chosen so that the second bracket vanishes, the required power is minimized. This is the case, with $R_L = \frac{1}{2}\frac{r}{Q}Q_L$, for

$$\tan(\phi) = -\frac{\frac{r}{Q}Q_L I_{b0}}{V_{cav}}\sin(\phi_b) = -\frac{1}{\beta+1}\frac{\frac{r}{Q}Q_0 I_{b0}}{V_{cav}}\sin(\phi_b) \ , \tag{4.37}$$

where $R$ is the resistance of the cavity equivalent circuit. In this case the required power is

$$P_{flat} = \frac{V_{cav}^2}{\frac{r}{Q}Q_L}\frac{\beta+1}{4\beta}\left(1+\frac{\frac{r}{Q}Q_L I_{b0}}{V_{cav}}\cos(\phi_b)\right)^2 \ . \tag{4.38}$$

The optimum coupling $\beta_{opt}$ is found by differentiating this equation for $\beta$

$$\beta_{opt} = 1+\frac{\frac{r}{Q}Q_0 I_{b0}}{V_{cav}}\cos(\phi_b) \ . \tag{4.39}$$

The minimum power for maintaining the cavity voltage $V_{cav}$ is

$$P_{min} = \beta_{opt}\frac{V_{cav}^2}{\frac{r}{Q}Q_0} \ . \tag{4.40}$$

The optimum tuning angle of a superconducting cavity $\phi_{opt}$ reads

$$\tan(\phi_{opt}) = -\frac{\frac{r}{Q}Q_{L,opt}I_{b0}}{V_{cav}}\sin(\phi_b) \quad . \tag{4.41}$$

In case of superconducting cavities the following simplifications can be done

$$Q_{L,opt} = \frac{V_{cav}}{\frac{r}{Q}I_{b0}\cos(\phi_b)} \ , \tag{4.42}$$

$$\phi_{opt} = -\phi_b \ , \tag{4.43}$$

and

$$P_{flat,min} = \frac{V_{cav}^2}{\frac{r}{Q}Q_{L,opt}} = V_{cav}I_{b0}\cos(\phi_b) \ . \tag{4.44}$$

The minimum power is exactly the power transferred to the beam. In the case of superconducting cavities the dissipated power can be neglected.
For the above mentioned example parameters ($V_{cav} = 31.5$ MV/m $\cdot$ 1.038 m $= 32.7$ MV, $I_{b0} = 5.8$ mA) and the assumption of $\cos(\phi_b) = 1$ the optimal loaded quality factor is $Q_{L,opt} = 5.44 \cdot 10^6$. Furthermore the minimal required power during the flattop is $P_{flat,min} = 190$ kW.

## 4.3 Detuned Cavity with Beam Loading

In reality the cavity can be detuned by the tuning angle $\phi$, which is the angle between the driving current $I_{for}$ and the generator voltage $V_g$. The main sources of detuning are Lorentz force detuning and microphonics. Figure 4.4 shows the vector diagram of the cavity voltage $V_{cav}$ resulting from the generator voltage $V_g$ and the beam voltage $V_b$ ($V_{cav} = V_g + V_b$) as well as from the forward voltage $V_{for}$ and the reflected voltage $V_{ref}$ ($V_{cav} = V_{for} + V_{ref}$) [29]. The angle $\phi$ corresponds to the tuning angle, $\phi_b$ to the beam phase, and $\Theta$ to the angle of the forward voltage. $\Theta$ can be varied by the control system.

In this case the cavity voltage reads

$$V_{cav} = \frac{1}{2}\frac{1}{1+\tan^2(\phi)}(1 + i\tan(\phi))\frac{r}{Q}Q_L(2I_g + 2I_{b0}) \tag{4.45}$$

and the generator and the beam induced voltages read

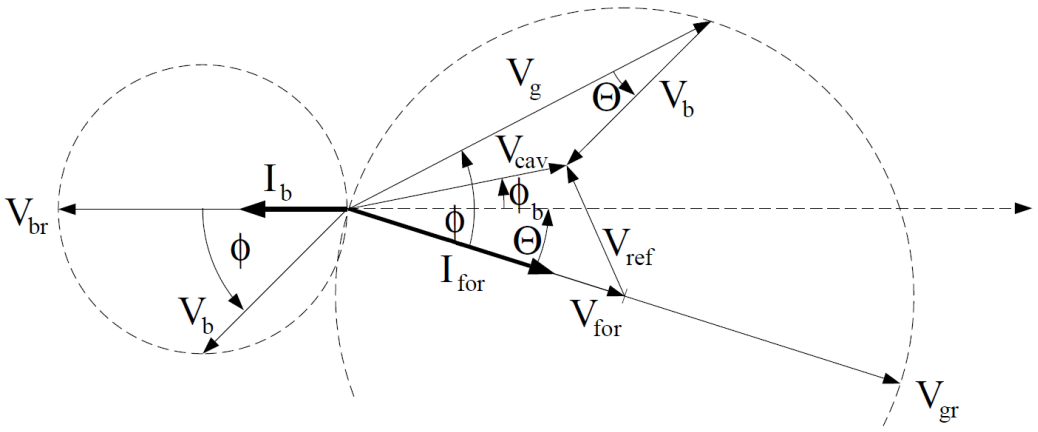


Figure 4.4: Vector diagram of generator– and beam–induced voltages in a detuned cavity, covering the beam phase $\phi_b$ and the tuning angle $\phi$ [29].

$$V_g = \frac{1}{\sqrt{1+\tan^2(\phi)}}(1+i\tan(\phi))\frac{r}{Q}Q_L I_g = \cos(\phi)e^{i\phi}\frac{r}{Q}Q_L I_g \tag{4.46}$$

and

$$V_b = \frac{1}{2}\frac{1}{1+\tan^2(\phi)}(1+i\tan(\phi))\frac{r}{Q}Q_L I_{b0} = \frac{1}{2}\cos(\phi)e^{i\phi}\frac{r}{Q}Q_L I_{b0} \ . \tag{4.47}$$

## 4.4 $P_k Q_L$ Operation Requirements

At the ILC main linacs it is required to operate multiple cavities driven by a single klystron with flat flattops 5% below their respective quench limits. Due to production variations these individual quench limits differ from cavity to cavity. A cavity gradient spread of (31.5±20%) MV/m will be allowed. The beam current will be 5.8 mA. The cavity driving power during the filling and the flattop has to be the same.

The filling behavior of the cavity following equation (4.23) is

$$V_{\text{fill}} = 2\frac{r}{Q}Q_L I_g \left(1 - e^{-\frac{t}{\tau}}\right) \quad . \tag{4.48}$$

With $\tau = \frac{2Q_L}{\omega_0}$ and $t = T_{inj}$, where $T_{inj}$ is the injection time of the beam, this can be rewritten as

$$V_{\text{fill}}\big|_{t=T_{inj}} = 2\frac{r}{Q}Q_L I_g \left(1 - e^{-\frac{T_{inj}\omega_0}{2Q_L}}\right) \quad . \tag{4.49}$$

The cavity differential equation for the flattop including the beam transient reads

$$\frac{dV_{flat}}{dt} = -\omega_{1/2}V_{flat} + R_L\omega_{1/2}\left(2I_g - 2I_{b0}\right) \quad , \tag{4.50}$$

where $\omega_{1/2}$ is the cavity half bandwidth. Furthermore a constant beam phase at $\phi_\text{b} = 180°$ (on–crest acceleration) is assumed. The condition for a flat gradient flattop is

$$\frac{dV_{flat}}{dt} = 0 \ . \tag{4.51}$$

From this follows

$$V_{flat} = R_L\left(2I_g - 2I_{b0}\right) \quad , \tag{4.52}$$

which can be rewritten with $R_L = \frac{r}{Q}Q_L$ as

$$V_{flat} = \frac{r}{Q}Q_L\left(2I_g - 2I_{b0}\right) \ . \tag{4.53}$$

With equations (4.49) and (4.53) a set of equations has been found describing the cavity voltage at the beam injection time $T_{inj}$. This also means that $V_{\text{fill}}\big|_{t=T_{inj}} = V_{flat}$. Due to this equations (4.49) and (4.53) are a system of two equations, where the parameters are the injection time $T_{inj}$, the cavity voltage $V_{\text{fill}}\big|_{t=T_{inj}} = V_{flat}$, and the beam current $I_b$. The variables are the generator current $I_g$ and the loaded quality factor $Q_L$. For a fixed set of parameters an unambiguously solution for the variables can be found. Since the generator current can be translated to the cavity driving power ($P_k$), one can see from this that the ILC main linac cavity operation requirements can only be satisfied, if both parameters $P_k$ and $Q_L$ are adjusted for each cavity. The requirement of such a $P_kQ_L$ operation is mentioned in section 2.1.

In the same section in Figure 2.3 c), in which a situation of individually adjusted $Q_L$ values is described, equation (4.51) is fulfilled. This corresponds to

$$\begin{aligned} 0 &= -V_{flat,Cav1} + R_L\left(2I_{g,Cav1} - 2I_{b0}\right) \\ 0 &= -V_{flat,Cav2} + R_L\left(2I_{g,Cav2} - 2I_{b0}\right) \quad , \end{aligned}$$

where $V_{flat,Cav1}$ and $V_{flat,Cav2}$ are representing the individual cavity voltages and $I_{g,Cav1}$ and $I_{g,Cav2}$ are representing the individual generator currents per cavity. Following this, in the situation described in Figure 2.3 b), in which the $Q_L$ values are not adjusted individually, equations

$$\begin{aligned} 0 &\neq -V_{flat,Cav1} + R_L \left(2I_{g,Cav1} - 2I_{b0}\right) \\ 0 &\neq -V_{flat,Cav2} + R_L \left(2I_{g,Cav2} - 2I_{b0}\right) \quad . \end{aligned}$$

hold.

A further way of the determination of the $P_k Q_L$ working point, which was developed in the scope of this dissertation, is based on the usage of the result of section 4.2, namely the equations

$$P_{\text{fill}} = \frac{V_0^2}{4\frac{r}{Q}Q_L \left(1 - e^{-\frac{T_{\text{inj}}\omega_0}{2Q_L}}\right)^2}$$

and

$$P_{flat} = \frac{V_{cav}^2}{4\frac{r}{Q}Q_L} \left(1 + \frac{\frac{r}{Q}Q_L I_{b0}}{V_{cav}}\right)^2 \quad .$$

These describe the power during filling time ($P_{\text{fill}}$) and during the flattop and beam ($P_{\text{flat}}$) in dependency of the injection time $T_{\text{inj}}$, the beam current $I_b$, and the $Q_L$ value. Figure 4.5 shows an example plot of $P_k$ [kW] for the filling time in blue and for the flattop in purple versus $Q_L$ for the injection time of $T_{\text{inj}} = 923\mu$s, the beam current of 5.8 mA, and a cavity gradient of 31.5 MV/m. One can see that at $Q_L = 5.44 \cdot 10^6$ both graphs intersect. At this $Q_L$ the same power is needed for the filling as for the flattop. This corresponds to an rectangular forward power pulse shape. By operating the cavity under such a condition, the output power of the klystron can be used most effectively, especially when operating near saturation. This operation mode is planned to be used at ILC. The method of finding the crossing point is used in section 6.6.

$P_k Q_L$ operation has several advantages and disadvantages. A first disadvantage of $P_k Q_L$ operation is that it requires more power compared to operation of cavities with optimal coupling (matched condition). In case of $P_k Q_L$ operation the coupling of every cavity is adjusted individually in order to set the required $Q_L$ values. Is the coupling different from the optimal value, which is the case for the majority of the cavities, power is reflected.

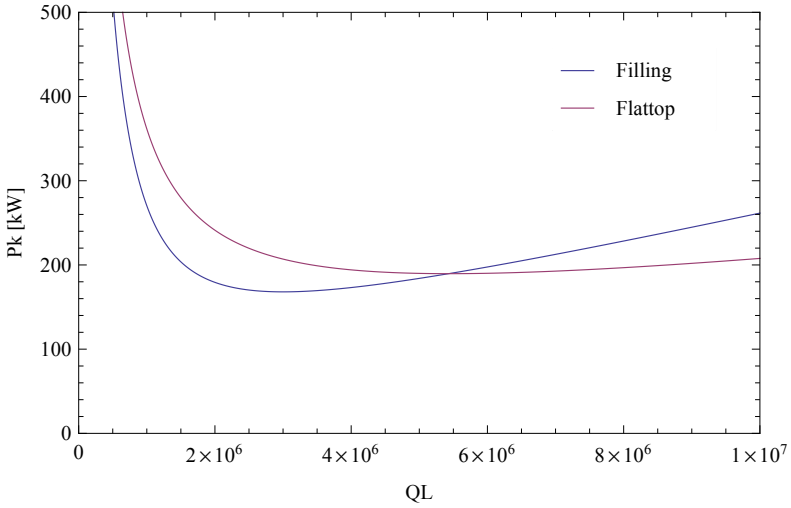


Figure 4.5: *Driving powers $P_k$ [kW] (blue for filling and purple for flattop) versus cavity $Q_L$ values for a filling time of 923 µs, a cavity gradient of 31.5 MV/m, and a beam current of 5.8 mA.*

For $P_kQ_L$ operation about 8% more power has to be supplied in order to compensate the total reflected power. This number is based on the comparison of the minimum driving power for 39 cavities at 31.5 MV/m and a beam current of 5.8 mA yielding 7.40 MW and the required driving power for 39 cavities calculated in the simulation as shown in section 6.6 yielding 8.05 MW.

A second disadvantage is that $P_kQ_L$ operation delivers flat cavity gradients only for a specific working point. Consequences are that it is sensitive to operation parameter deviations (in section 6.6 a more detailed study is presented) and that for a different working point (e.g. for a different beam current) a new set of operation parameters ($P_k$, $Q_L$, etc.) has to be computed and applied.

An advantage of $P_kQ_L$ operation is that it is the only way of realizing flat gradient flattops at different gradients within multiple cavities driven by a single klystron. Thus it is a main requirement for the operation of the superconducting cavities in the main linacs of ILC.

# Chapter 5

# Past Efforts Towards ILC

Worldwide already huge efforts were made in order to push ILC towards its realization. In this chapter the results of two major efforts regarding the demonstration of the feasibility of required technology and procedures are introduced, namely the S1–Global at KEK STF and the 9mA Tests at FLASH at DESY. Beside this also the klystron linearization implemented at FLASH at DESY is introduced. These past studies are an essential background for the studies presented in this dissertation.

## 5.1 S1–Global at STF

In 2010 the S1–Global test was conducted at KEK STF. Its purpose was the evaluation of the compatibility and overall performance developed towards ILC [30]. In its scope a total of 8 superconducting 9-cell cavities were installed in two half-size cryomodules. Two cavities provided by FNAL and two by DESY were installed to a cryomodule constructed at INFN/Milano. For the tuning of the FNAL cavities a blade tuner developed at FNAL was used. For the tuning of the DESY cavities a Saclay tuner was used. In the case of all four cavities TTF–III couplers were used. Furthermore four cavities from KEK were mounted in a cyro–module constructed at by KEK. In order to tune those a slide–jack tuner developed at KEK was used. For the four KEK cavities STF–II couplers made by KEK were used.

Regarding the RF system, the studies performed at S1–Global can be separated into three phases [31]. In the first phase the cavity performances regarding e.g. Lorentz force detuning and the individual quench limits were investigated. To this end two 5 MW klystrons were used to drive the cavities in two groups of four cavities each. Figure 5.1 shows a schematic of the setup

of the high level RF (HLRF) system. The outputs of the klystrons were controlled using a commercial DSP board (Barcelona) including an FPGA board. The features beside others of the FPGA board were 10 16–bit ADCs, 2 14–bit DACs, and an FPGA installed to a cPCI card.

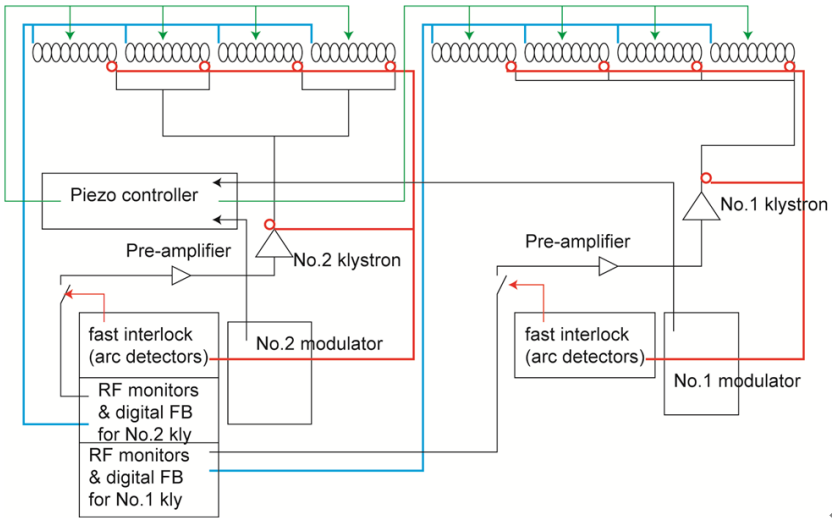


Figure 5.1: *Schematic of the HLRF system at S1–Global in phase 1 [31]. Eight cavities were driven in two groups of four by two klystrons. In both groups RF monitors and digital feedback control loops were realized. Furthermore fast interlocks with arc detection were included in the two control loops. Beside this a piezo tuner control for all cavities was implemented.*

In the second phase the scheme for driving the cavities was changed. In this case only one klystron was used in order to drive all 8 cavities. Figure 5.2 shows the corresponding schematic.

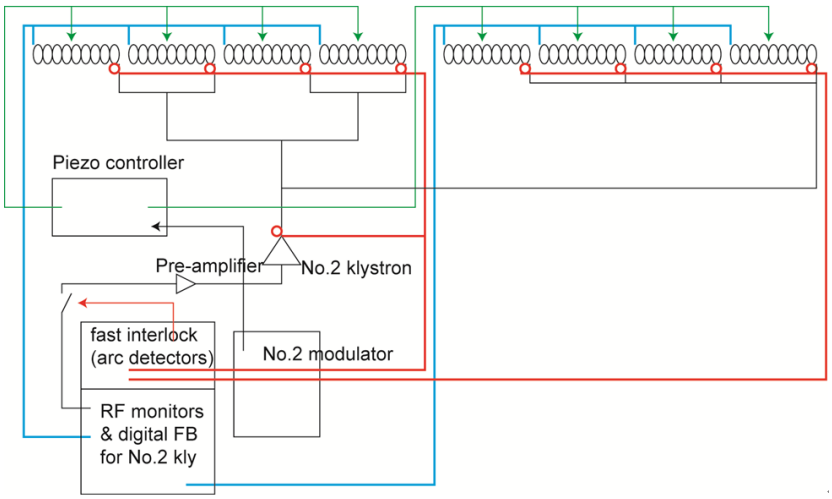


Figure 5.2: *Schematic of the HLRF system at S1–Global in phase 2 [31]. All eight cavities were driven by a single klystron within a single control loop. A fast interlock with arc detectors was included. A piezo controller for all cavities was implemented.*

The goal of the second phase was to evaluate the vector sum performance. In order to maximize the gradients of every cavity, variable hybrids and variable tap–offs were used. The vector sum stabilities during the flattop (from 690 to 1590 $\mu$s) for seven cavities operated at an average gradient of 26 MV/m were 0.0067%rms in amplitude and 0.0165° in phase. The corresponding plots of the individual cavity amplitudes and phases as well as the vector sum amplitude and phases are shown in Figure 5.3.

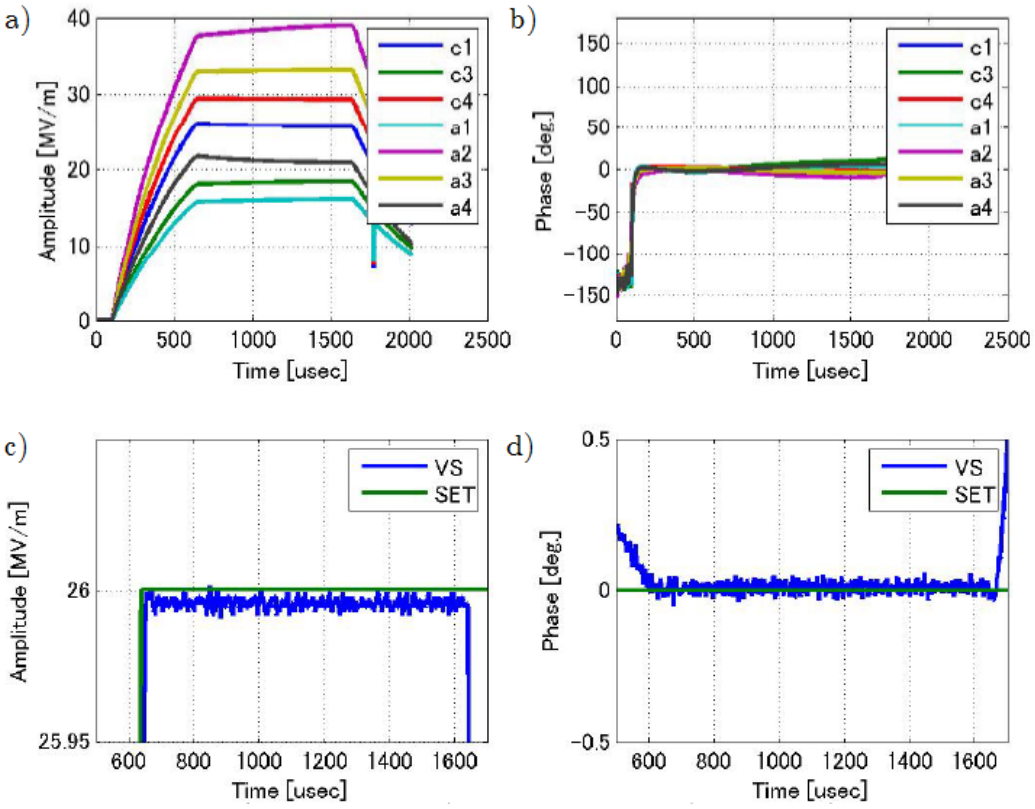


Figure 5.3: *Vector sum operation during S1–Global: a) Individual cavity amplitudes [MV/m] versus time, b) individual cavity phases [°] versus time, c) vector sum amplitude [MV/m] versus time, and d) vector sum phase [°] versus time [31].*

Since the number of klystrons was reduced to one, for the LLRF control only one cPCI board was required. A detailed schematic of it is shown in Figure 5.4.

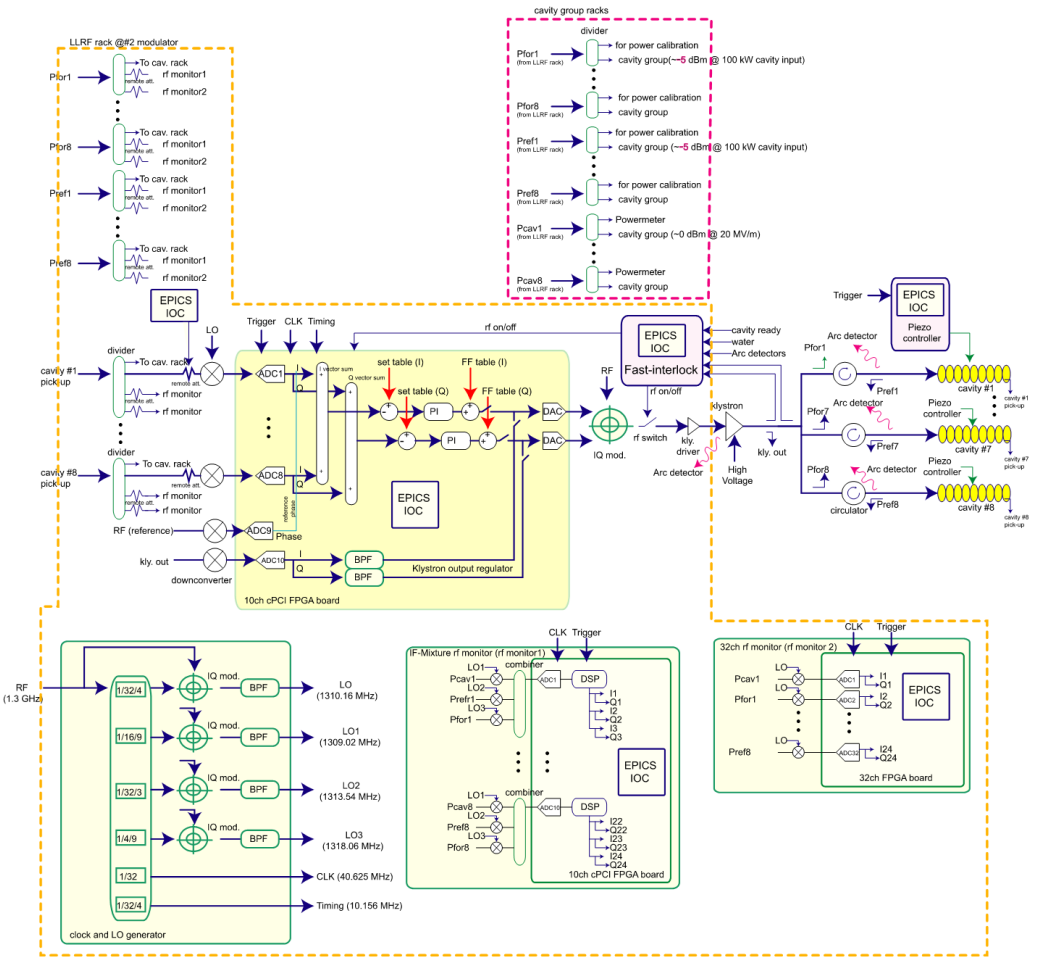


Figure 5.4: *Schematic of the LLRF system at S1–Global in phase 2 [31]. The forward and reflected signals of the eight cavities are monitored. The eight cavity pickup signals are down converted, digitized, and their vector sum is computed. To this a PI controller is applied. After the application of feedforward tables and the klystron output regulator, the output is converted to analog and sent to the klystron, which drives all eight cavities.*

The eight cavity pickup, forward, and reflected signals were split into four ports. These were fed 1) via a down converters to the cPCI card, 2) to the IF mix RF monitor, 3) to RF power meters (Gigatronics), and 4) to hardware used by the cavity group. Beside this the klystron forward and reflected signals were fed to a VSWR meter used as an interlock for machine protection of the klystron. The local oscillator (LO, 1310.16 MHz) was generated by clock dividers and an IQ modulator. The clock signals (40.625 MHz) were

generated using clock dividers. Furthermore for the definition of the I and Q components a timing clock with a frequency of 10.16 MHz was used. Three different IF signals were used, namely 9.02 MHz, 13.54 MHz, and 18.06 MHz [32]. By this up to 30 RF signals could be detected with 10 ADCs. On the FPGA on the cPCI board, the vector sum of the cavity pickup signals was computed and compared to a set point. Furthermore a proportional integral (PI) controller was applied and feedforward tables were added. The feedback control was performed with the clock frequency of 40.625 MHz.

In the third phase a Distributed RF Scheme (DRFS) was tested. To this end four cavities were driven in groups of two by two modulating anode (MA) 800 kW klystrons (TOSHIBA E37501) [33]. The klystrons were located inside the tunnel and were connected to a single MA modulator located on ground floor. Figure 5.5 shows a schematic of the setup. Figure 5.6 shows a schematic of the DRFS layout.

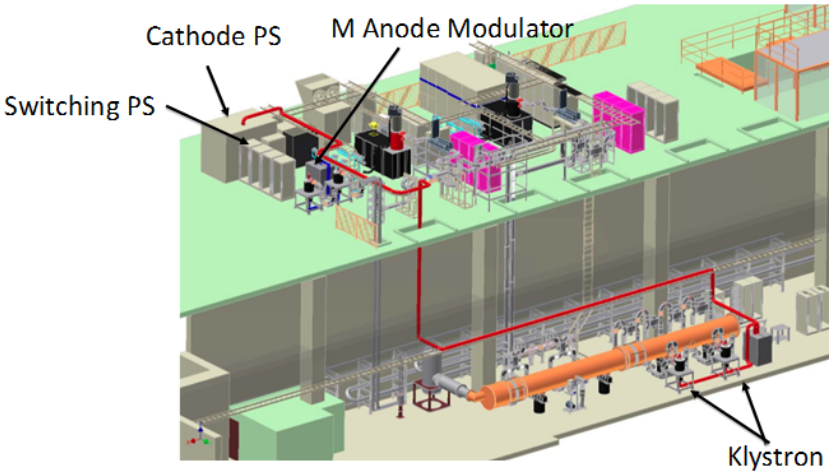


Figure 5.5: *Schematic RF generation path at S1–Global [33]. On ground level the anode modulator, cathode PS, and switching PS are located. Their output is sent to the klystron located in the accelerator tunnel.*

The RF output of the klystrons were distributed to the cavities using two DRFS systems. Figure 5.6 shows the schematic of the DRFS configuration. For cost reduction the layout is kept as simple as possible. Thus e.g. no circulators were included.

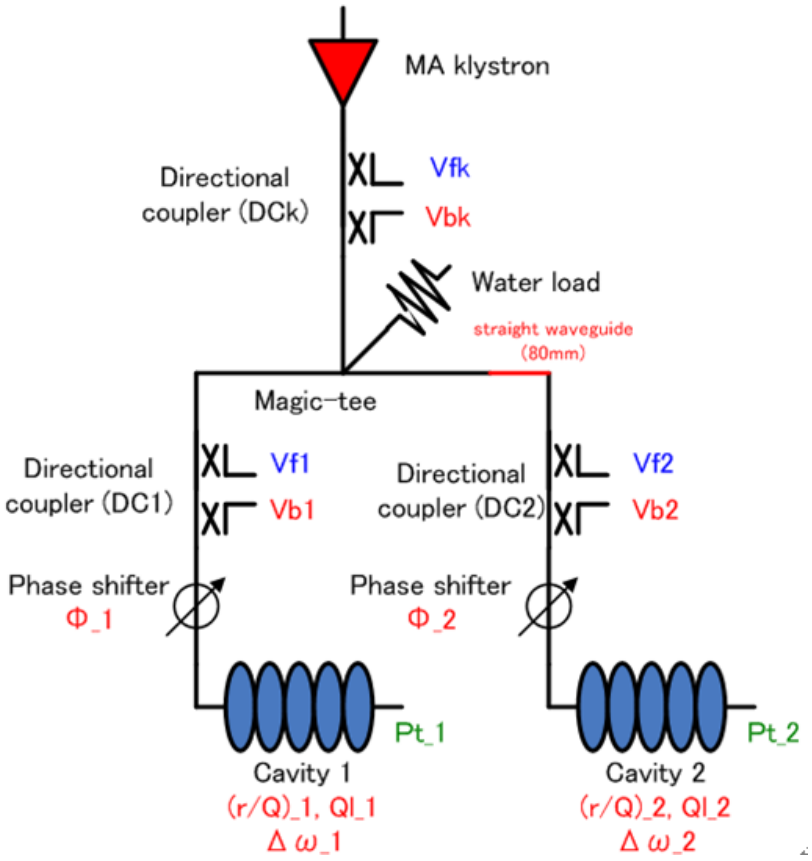


Figure 5.6: *Schematic RF generation path at S1–Global [2, 33]. The forward and reflected signals at the output of the klystron are coupled out using a directional coupler. The RF power is divided by a magic-tee. In both paths the forward and reflected signals are coupled out using directional couplers. Furthermore by phase shifter the phases of the RF signals fed to cavity 1 and 2 are controlled.*

Figure 5.7 shows a schematic of the LLRF system in phase 3 of S1–Global. The LLRF system was located inside the tunnel. Two feedback loops were controlling the output powers of both klystrons. In this case a $\mu$TCA–based FPGA system was installed. The $\mu$TCA board features 4 16–bit ADCs and 4 16–bit DACs. Two cavity pickups, the klystron output, and the reflection were observed.

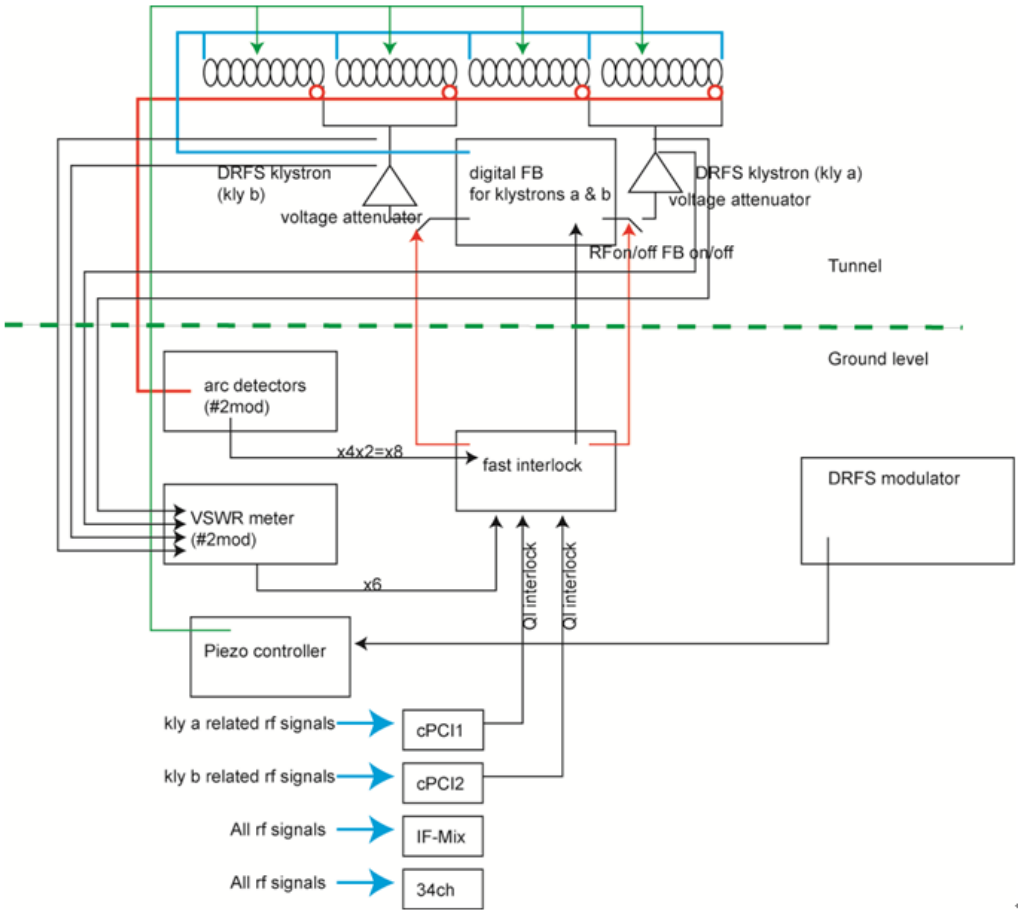


Figure 5.7: *Schematic of the LLRF system at S1–Global in phase 3 [31]. Four cavities are driven in two groups of two by two klystrons in two DRFS configurations. In the two feedback loops fast interlocks with arc detectors are included. Piezo control for all cavities was implemented.*

As stated before, in the DRFS no circulators were included. In the case two cavities are operated the RF reflections can be canceled in the case the operation parameters of the cavities, such as dynamic detuning and loaded quality factors, are exactly the same. If this is not the case, reflection towards the klystron occurs, which may lead to damage of the klystron. Beside this cross–talk between the cavities occurs. Due to these reasons correct online cavity diagnostics had to be developed. In order to realize this, the cavity equation can be rewritten. The cavity differential equation reads

$$\frac{d}{dt}V_{cav} = -(\omega_{1/2} - j\Delta\omega(t))V_{cav} + 2\omega_{1/2}V_{for} \ , \tag{5.1}$$

where $\omega_{1/2} = \frac{\omega_0}{2Q_L} = \frac{\pi f_0}{Q_L}$ is the cavity half bandwidth and $\Delta\omega(t)$ the dynamic detuning. By inserting $V_{cav} = V_{for} + V_{ref}$, where $V_{for}$ is the forward voltage and $V_{ref}$ the reflected voltage, it can be rewritten as

$$\frac{d}{dt}V_{cav} - j\Delta\omega(t)V_{cav} = -\omega_{1/2}(V_{for} + V_{ref}) + 2\omega_{1/2}V_{for} \ , \tag{5.2}$$

which evaluates to

$$\frac{d}{dt}V_{cav} - j\Delta\omega(t)V_{cav} = \omega_{1/2}(V_{for} - V_{ref}) \ . \tag{5.3}$$

At this point let $V_{dif} = V_{for} - V_{ref}$. From this follows

$$\frac{d}{dt}V_{cav} - j\Delta\omega(t)V_{cav} = \omega_{1/2}V_{dif} \ . \tag{5.4}$$

This equation can be represented by two equations; one for the real part and one for the imaginary part.

$$\begin{array}{rcl} \dot{V}_{cav,R} + \Delta\omega V_{cav,I} & = & \omega_{1/2}V_{dif,R} \\ \dot{V}_{cav,I} - \Delta\omega V_{cav,R} & = & \omega_{1/2}V_{dif,I} \end{array} \tag{5.5}$$

Multiplying $V_{cav,R}$ to the first and $V_{cav,I}$ to the second equation yields

$$\begin{array}{rcl} \dot{V}_{cav,R}V_{cav,R} + \Delta\omega V_{cav,I}V_{cav,R} & = & \omega_{1/2}V_{dif,R}V_{cav,R} \\ \dot{V}_{cav,I}V_{cav,I} - \Delta\omega V_{cav,R}V_{cav,I} & = & \omega_{1/2}V_{dif,I}V_{cav,I} \ . \end{array} \tag{5.6}$$

By adding up both equations, the mixed terms with the detuning component vanish, yielding

$$\dot{V}_{cav,R}V_{cav,R} + \dot{V}_{cav,I}V_{cav,I} = \omega_{1/2}(V_{dif,R}V_{cav,R} + V_{dif,I}V_{cav,I}) \ . \tag{5.7}$$

With $V_{dif,R} = V_{for,R} - V_{ref,R}$ and $V_{dif,I} = V_{for,I} - V_{ref,I}$ as well as $V_{cav,R} = V_{for,R} + V_{ref,R}$ and $V_{cav,I} = V_{for,I} + V_{ref,I}$ the equation can be rewritten to

$$\dot{V}_{cav,R}V_{cav,R} + \dot{V}_{cav,I}V_{cav,I} = \omega_{1/2}(V_{for,R}^2 + V_{for,I}^2 - V_{ref,R}^2 - V_{ref,I}^2) \ . \tag{5.8}$$

This can be rewritten as

$$\frac{1}{2}\frac{d}{dt}|V_{cav}|^2 = \omega_{1/2}(|V_{for}|^2 - |V_{ref}|^2) \tag{5.9}$$

and rearranged to

$$Q_L = \frac{|V_{for}|^2 - |V_{ref}|^2}{\frac{d}{dt}|V_{cav}|^2} \ . \tag{5.10}$$

With this equation the loaded quality factors of the cavities were calculated even in the case of unbalanced DRFS operation. This is not possible with the evaluation of the cavity gradient decays, since even after the end of the RF pulse cavity input signals exist. With the calculation of the dynamic detuning the piezo control was optimized.

In the case the RF is off ($V_{for} = 0$), equation (5.10) changes to

$$Q_L = \frac{|V_{cav}|^2}{\frac{d}{dt}|V_{cav}|^2} \ , \tag{5.11}$$

since $V_{cav} = V_{for} + V_{ref}$ holds at all times. $|V_{cav}|^2$ can be interpreted as the energy stored in the cavity and $\frac{d}{dt}|V_{cav}|^2$ as the change in the stored energy or the dissipated energy, respectively. This is consistent with the description of the cavity voltage of $V_{cav} \sim \mathrm{e}^{-\frac{\omega_0 t}{2Q_L}}$.

In the case RF is fed to the cavity ($V_{for} \neq 0$), equation (5.10) applies. In this case $|V_{for}|^2 - |V_{ref}|^2$ can be interpreted as the difference of the energy fed into and dissipated from the cavity. Furthermore is can be seen, that the evaluation of the $Q_L$ value is not possible, when the energy stored in the cavity stays constant ($\frac{d}{dt}|V_{cav}|^2 = 0$), which also corresponds to the case the energy fed to the and dissipated from the cavity is the same ($|V_{for}|^2 = |V_{ref}|^2$).

A further development at S1–Global was the implementation of a fast quench detection system. It is based on the computation of the loaded quality factor during the cavity gradient decay as described in Appendix B. If the loaded quality factor of a cavity drops below a predefined limit, a quench is detected and the RF is stopped at the following pulse. Due to this the cryogenic heat load during the event of a quench was reduced.

## 5.2 9mA Test at FLASH

Beginning in 2009 a series of studies was conducted at DESY FLASH aiming for the investigation of technical challenges in the scope of ILC, such as cavity operation near their respective quench limits with high beam loading or near klystron saturation operation [34]. The last study has been the 9mA test in February 2012, in which automated algorithms for quench detection, for the adjustment of the loaded quality factor, and for the compensation of Lorentz force detuning were implemented and tested. Using those tools, the goal of the 9mA test in 2012 was the gradient flattening of multiple cavities by the individual adjustment of their loaded quality factors. The test was carried

out on two cryomodules of FLASH, namely ACC6 and ACC7. These were chosen because those contained the cavities with the highest gradient performance. Furthermore those were equipped with motorized couplers, with which the loaded quality factors could be adjusted.

In order to control the loaded quality factors of the cavities a discrete–time feedback control scheme was applied [35]. The measured loaded quality factor was compared to the set value and the controller output was directly drove the coupler motor. Measures for exception handling were taken for cases such as out–of–range setting or invalid loaded quality factor measurements.

For rough cavity tuning motorized cavity tuners were used at FLASH. For fine tuning and the compensation of Lorentz force detuning piezo tuners were used. This process was automated. To this end the detuning is computed during the pulse and the piezo stimulus parameters were adjusted in order to maintain a minimal detuning over the flattop.

In scope of machine protection, cavity gradient limiters were implemented on the controller board. These were comparing the actual cavity gradients to preset limits. Were those limits hit, the RF drive pulse length was truncated. For normal operation the limits were set between 1 and 2 MV/m below the quench limits, yielding a good compromise between safety and performance. Furthermore cavity gradient pre–limiters were implemented. The limits of those were set typically 0.5 to 1 MV/m below the limits of the cavity gradient limits. Were the limits of the pre–limiter hit, the vector sum set point was lowered within the pulse by 1 $\mu$s increments until the cavity gradient was decreased to a safe level or a maximal number of steps was reached. The gradient pre–limiters were only functional in feedback operation.
Beside this a cavity quench protection was implemented. To this end the loaded quality factors of the cavities were monitored. In the case value drops higher than $5 \cdot 10^5$ occurred, the RF was stopped on the next pulse.

Figure 5.8 shows the result of the loaded quality factor tuning in the scope of the 9mA test at FLASH in 2012. Figure 5.8 a) shows the cavity gradients during the operation of the cavities with nominal loaded quality factors of $3 \cdot 10^6$ and a beam with a pulse length of 400 $\mu$s and a current of 4.2 mA. Clearly the tilts in the cavity gradients during the beam transient time can be observed. Due to the different gradients, the beam loading effects were different.
Figure 5.8 b) shows the cavity gradients during the operation of the cavities

with tuned loaded quality factors and the same beam properties as in a). During the beam transient time the cavity gradients were nearly flat.
Figure 5.8 c) shows the cavity gradients during the operation of the cavities with tuned loaded quality factors and a beam with the pulse length of 800 $\mu$s. Since the beam transient time covered the whole flattop, all cavity gradients were nearly flat.

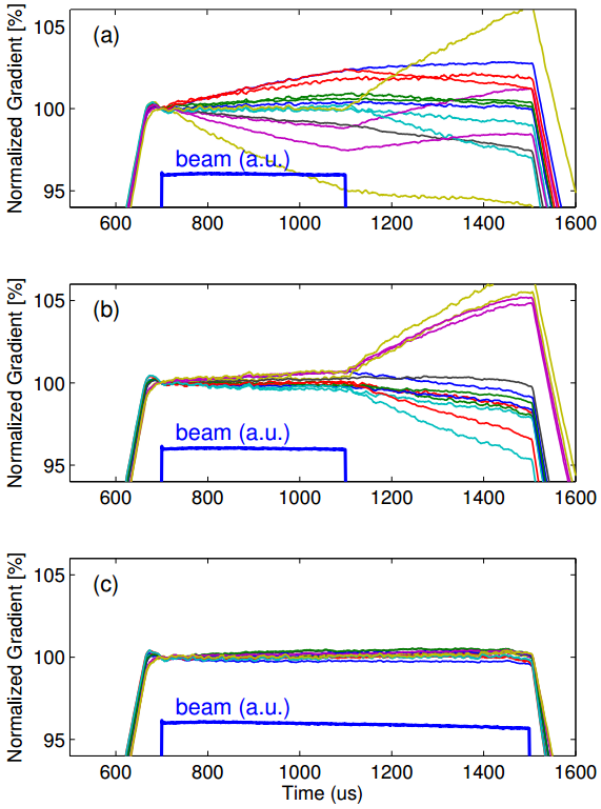


Figure 5.8: *Result of 9mA Test at FLASH in 2012: a) cavity gradients with default loaded quality factors, b) after loaded quality factor optimization, and c) with optimized loaded quality factors and full beam pulse length [34].*

With this a proof of principle for the operation of multiple cavities with different gradients with flat flattops was demonstrated. It should be noted that the test was performed at beam currents of 4.2 mA, which is well below the 6 mA design value of ILC. Furthermore the used procedure is not applicable for engaging in beam operation at ILC. At ILC the requirement is on operation of the cavity at gradients 5% below their respective quench limits.

As shown in Figure 5.8 b) the cavity gradients of four cavities are exceeding this level and would hit the quench limit. Beside this the conducted operation was, as stated, tuning of the loaded quality factor only, which means no actual $P_k Q_L$ control was performed.

It should be noted that already before this a similar study of $Q_L$ tuning was performed at FLASH in the scope of the 9mA test in 2011. At that time beams of currents of up to 4.5 mA and beam pulse length of 400 $\mu$s have been used. For more detailed information see elsewhere [36].
It should be noted as well that theoretical concepts of $P_k Q_L$ control have been studied about half a decade before the 9mA tests at DESY. For more detailed information see elsewhere [37].

## 5.3 Klystron Linearization at FLASH

At DESY in the scope of FLASH and the European X–FEL a klystron linearization was implemented and tested [38]. The target was to linearize the klystron output amplitude and phase. To this end a predistortion–type linearization algorithm based on direct lookup tables (LUTs) was implemented on the Xilinx Virtex II Pro FPGA on the Simcon–based controller card. A schematic of the algorithm is shown in Figure 5.9. From the I and Q values of the controller the squared amplitude is computed. The highest 11 bits of the squared amplitude are used as addresses for the LUTs, which contain I and Q correction values. These values are generated based on a klystron characterization using a Matlab script. The looked up I and Q correction values are applied to the I and Q values of the controller corresponding to a complex multiplication. The corrected I and Q values are the output of the algorithm.

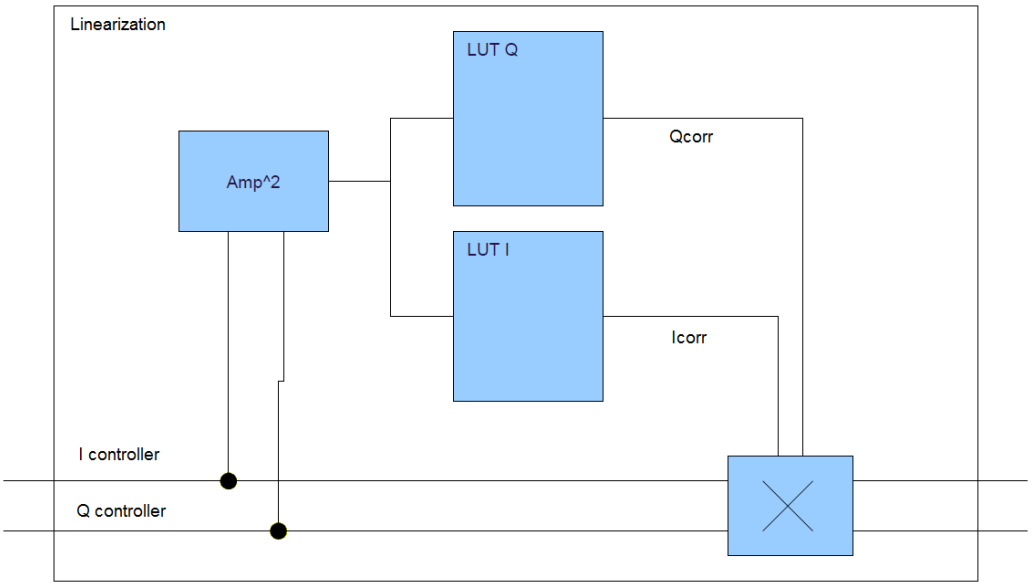


Figure 5.9: *Schematic of the LUT–based klystron linearization algorithm implemented at FLASH at DESY [39]. From the input I and Q values the squared amplitude is computed. Based on this correction values from I and Q lookup tables are read and applied to the I and Q input values in a complex multiplication. The resulting I and Q values are outputted.*

A test of this algorithm was performed at FLASH in the high power chain of cryomodule ACC67. Figure 5.10 shows the klystron characteristic without linearization in blue for the amplitude (left) and the phase (right). In both cases a strong nonlinear behavior can be observed. In the same figure the klystron output with the applied linearization is shown in red in terms of amplitude (left) and phase (right). In the case of the amplitude a clear linear behavior above a controller output value of 0.25 [a.u.] until the point of saturation can be observed. In case of the phase the linearization seems to be effective above a controller output value of 0.25 [a.u.]. Above a controller output value of 0.7 [a.u] a slight nonlinear phase rotation can be observed. With this result the test of the klystron linearization was successful. It should be noted that as soon the working point, e.g. the high voltage of the klystron, is changed, a new characterization has to be performed and based on this new correction LUTs have to be generated and programmed.

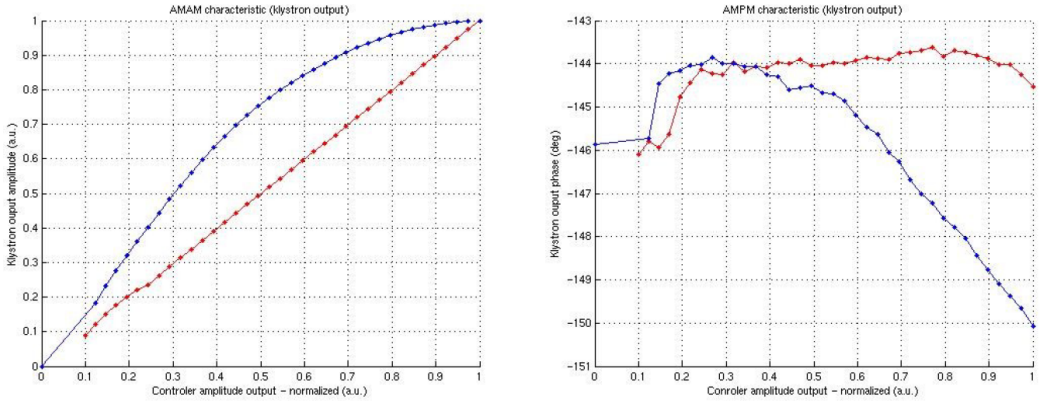


Figure 5.10: *Result of klystron linearization implemented at FLASH [39]. On the left side the klystron output amplitude characteristics without (blue) and with (red) the linearization algorithm are shown. On the right side the klystron output phase characteristics without (blue) and with (red) the linearization algorithm are shown.*

# Chapter 6

# $P_k Q_L$ Control

In this chapter the development and the world's first time successful test of an automated actual $P_k Q_L$ controlled operation is described [40]. This covers also the development and usage of preparatory procedures such as the identification of RF phases for on–crest beam acceleration, beam–based gradient calibration, and automated beam compensation. This work was performed in the scope of this dissertation.

## 6.1 Identification of RF Phase for On–crest Beam Acceleration

### 6.1.1 Principle of Algorithm

In the initial situation before operation, the RF phases of the superconducting cavities were random and needed to be calibrated for on–crest beam acceleration. For this calibration the cavity voltage changes induced by beam–loading effects were used. From the cavity differential equation

$$\frac{dV_{cav}}{dt} = -\omega_{1/2} V_{cav} + R_L \omega_{1/2} \left(2I_g - 2I_{b0}\right) \ , \tag{6.1}$$

the condition of a constant beam phase at $\phi_\mathrm{b} = 180°$, and substituting $R_L$ and $\omega_{1/2}$, the beam–induced change in the cavity voltage is

$$\Delta V_{ind} = 2\pi \frac{r}{Q} f_0 I_{b0} \cos(\phi_\mathrm{RF}) \Delta t \ , \tag{6.2}$$

where $\phi_\mathrm{RF}$ is the RF phase and $\Delta t$ is the beam transient time. From this is can be seen that the change in the cavity voltage has a minimum at the RF phase for on–crest beam acceleration. At this point the phase difference

between the beam and the RF phase is $\phi_{\mathrm{RF}} - \phi_{\mathrm{b}} = 180°$. By performing an RF phase scan during beam operation, the RF phase for the maximal cavity voltage drop can be found, and thus the RF phase for on–crest beam acceleration.

Theoretically an evaluation of the zero crossing, which corresponds to the point of no change in cavity voltage, would be more sensitive, compared to the evaluation of the minimum. In practice this evaluation was not chosen due to machine protection reasons. The beam energy directly after the RF gun was about 3 MeV. In the case of deceleration of the beam within the superconducting cavities the possibility was given that the beam would be accelerated backwards towards the RF gun. By evaluation of the beam induced cavity voltage change corresponding to the on–crest beam acceleration (finding the minimum) this situation was avoided. In the case the accelerator consists of a higher number of cavities (as in the case of e.g. ILC), the beam energy is sufficiently high after the acceleration within the first cavities, so that in all following cavities the zero crossing of the beam induced change in cavity voltage can be evaluated in order to estimate the phase for on crest beam acceleration.

### 6.1.2 Implementation and Application of Algorithm

The method described in the previous section 6.1.1 was applied in an automated way individually to both cavities at STF. To this end a Matlab script was written, which controlled via EPICS the waveguide phase shifters of both cavities. The scan of the cavity phases was performed in steps of 2.5°. At every step 10 waveforms of the respective cavity gradient was recorded, from which the beam induced change in gradient was obtained. Beside this also the corresponding charge per bunch values of the beam were recorded. After the correction of the beam induced change in cavity gradient by the charge per bunch value, the average of all 10 samples was calculated.

The result of the applied procedure is shown in Figure 6.1 in terms of the beam–induced change in the cavity gradient, corrected by the beam charge [ADC value/pC] versus the RF phase shift [°] for both cavities (cavity 1: Figure 6.1 a), cavity 2: Figure 6.1 b)). The minima were determined by a sine–function fit and are indicated by the red arrows. After the scans were finished the cavity phases corresponding to the found minima were set.

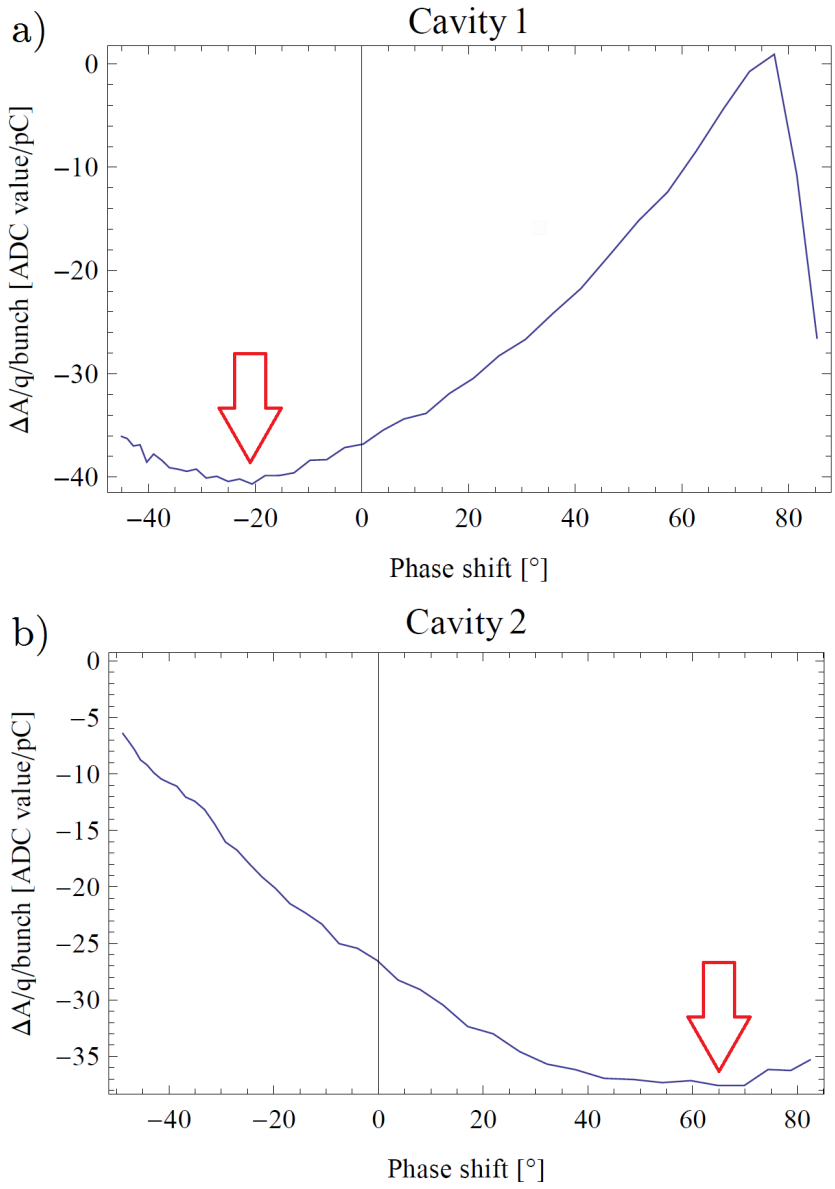


Figure 6.1: Beam–induced change in the cavity gradient corrected by the beam charge [ADC value/pC] versus RF phase shift [°] for a) cavity 1 and b) cavity 2. The red arrows indicate the locations of the minima.

### 6.1.3 Low Power Measurement of Relative Cavity Phases

The distance between both cavities correspond to a phase difference of 90°. In order to check the phase difference for the estimated phases for on–crest

beam acceleration a low power measurement after the calibration was conducted. To this end the DRFS system was disconnected from the klystron and the cavities. A network analyzer was connected to the waveguide in two configurations as shown in Figure 6.2. First from point A to point B and then from point A to point C. For the first measurement a phase shift of $\phi_1 = -167°$ was found out, for the second measurement of $\phi_2 = -74°$. The difference between both computes to $\phi_2 - \phi_1 = 93°$. With this it was shown that the deviation of the relative cavity RF phases set using the automated identification algorithm for the RF phase for on–crest beam acceleration was 3°.

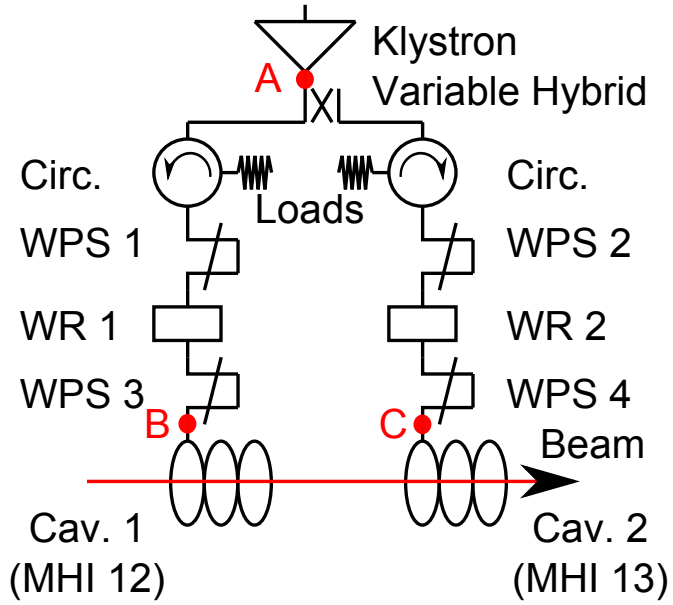


Figure 6.2: *Schematic of DRFS waveguide system in scope of the QB project including the klystron, the variable hybrid, two circulators (Circ.) with loads, four waveguide phase shifters (WPS1, WPS2, WPS3, WPS4), two waveguide reflectors (WR1, WR2), and two cavities (Cav. 1, Cav. 2). The points of measurement are marked in red (A, B, and C).*

## 6.2 Beam–based Gradient Calibration

### 6.2.1 Principle of Algorithm

In order to transform the picked–up, down–converted, and digitized cavity signals to a gradient, the ADC numbers had to be calibrated for each cavity.

For this calibration beam–loading effects on the cavity voltage as described in the previous section were used. In the case of an on–crest beam acceleration, equation (6.2) can be simplified to

$$\Delta V_{ind} = 2\pi \frac{r}{Q} f_0 I_{b0} \Delta t \ . \tag{6.3}$$

By this the beam induced change in cavity voltage can be calculated in MV. A linear correction function is determined by taking into account the calculated cavity voltage drop, the corresponding measured change in ADC counts, and the point of origin, which can be written as

$$V = \frac{\Delta V_{ind}}{\Delta C_{ind}} C \ , \tag{6.4}$$

where $V$ is the voltage value to be computed corresponding to the measured ADC count value $C$, $\Delta V_{ind}$ the calculated drop in cavity voltage during the calibration, and $\Delta C_{ind}$ the measured ADC count of the voltage drop during the calibration.

### 6.2.2 Application of Algorithm

The procedure described in section 6.2.1 was performed for the digitized pickup signals of both cavities. Figure 6.3 shows an example of a cavity voltage versus time with a beam transient of 31.3 $\mu$s. The average beam current was 4.95 mA, which, according to equation (6.3), corresponds to a cavity voltage drop of 1.31 MV. In order to calculate the beam induced drop in gradient, the cavity length of 1.038 m has to be considered: 1.31 MV / 1.038 m = 1.26 MV/m. This result agrees very well with the cavity gradient drop of 1.26 MV/m measured using a power meter.

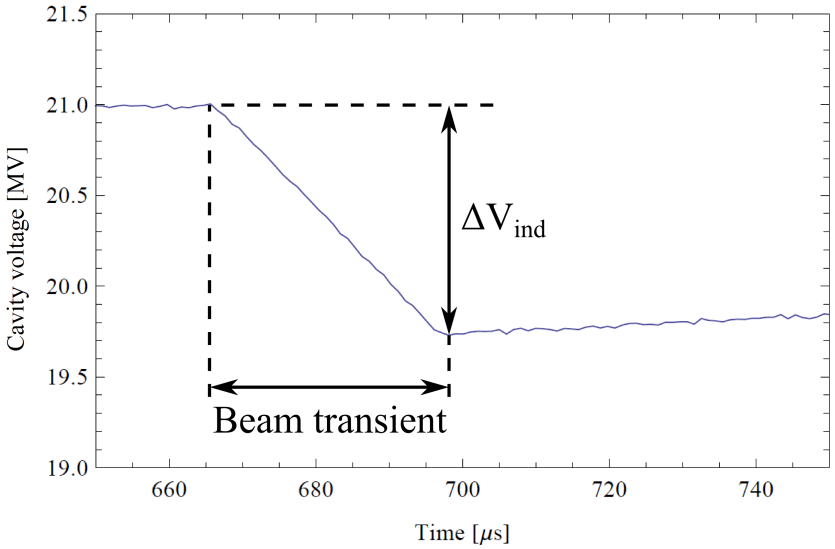


Figure 6.3: Cavity 1 voltage [MV] versus time [$\mu$s] during the flattop covering the beam transient, where the beam-loading induced the voltage drop $\Delta V_{ind} = 1.31$ MV.

## 6.3 Automated Beam Compensation

### 6.3.1 Principle of Algorithm

In order to realize a flat flattop during beam acceleration, which is a requirement for stable beam acceleration, the beam induced drop in cavity gradient has to be compensated. To this end additional driving power has to be supplied during the beam transient. This can be achieved by the addition of a beam FF table to the base FF table as shown in Figure 6.4.

The beam FF table shown in Figure 6.4 is of a rectangular shape. In reality this is not applicable, since the beam current profile has a non–constant structure over the whole pulse. Figure 6.5 shows an example measurement of the beam current profile.

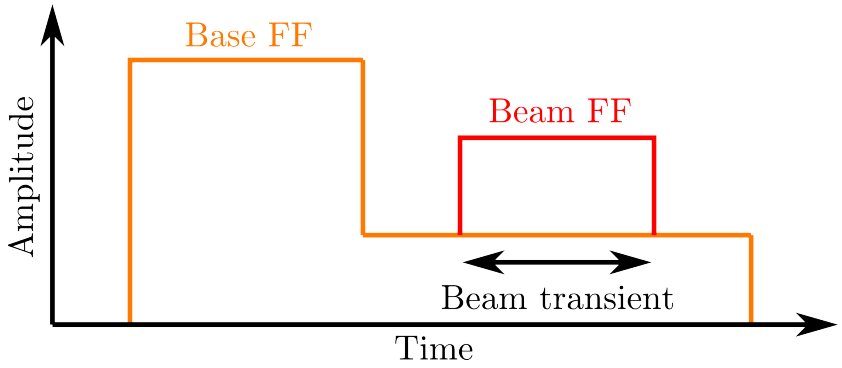


Figure 6.4: Schematic of amplitude versus time for a base FF table (orange) and a beam FF table (red).

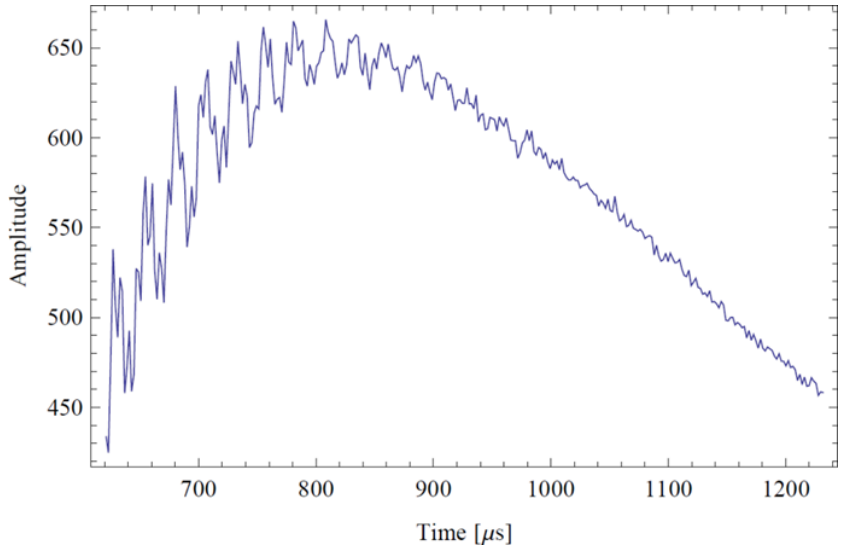


Figure 6.5: Example beam current profile measured by BPM: amplitude [a.u.] versus time [$\mu$s]. Beside a global maximum for the current distribution also the effect of the individual bunches can be seen.

Furthermore this current profile varies over time. During the accelerator operation at STF in the scope of the QB project, this profile changed day by day. In order to cope with this situation and to guarantee an optimal beam compensation, a fully automated beam FF amplitude shape generation was established.

It was realized by a Matlab script and was applied during beam operation, before the beam time for the user began. The algorithm of the script divides

the beam FF amplitude table during the beam transient time in equidistant time intervals. In order to have a good compromise in resolution and in time required for the algorithm, the time intervals between the nodes were chosen to be 25 $\mu$s. Between the nodes the beam FF amplitude was linear interpolated. In the first step the first two nodes of the segmented beam FF amplitude table were risen simultaneously until in this time interval the vector sum cavity gradient was flat within a predefined range. In case an overcompensation occurred, the algorithm adjusted the beam FF segment until the cavity gradient was flat within the predefined range. In a next step the amplitude of the third node was adjusted until in the second time interval the vector sum gradient was compensated. This was repeated for all remaining nodes.

### 6.3.2 Application of Algorithm

Figure 6.6 shows an example of an automatically generated beam FF table for a 5.5 mA beam with a pulse width of 308 $\mu$s. Due to beam current fluctuations during the generation procedure, the beam FF amplitude table is not smooth. Since the cavity itself acts like a low–pass filter, the high–frequency components of this structure are not an issue.

Figure 6.7 shows the vector–sum gradient after the automated generation and the appliance of a beam FF table during nominal operation. The stabilities are presented in Table 6.1.

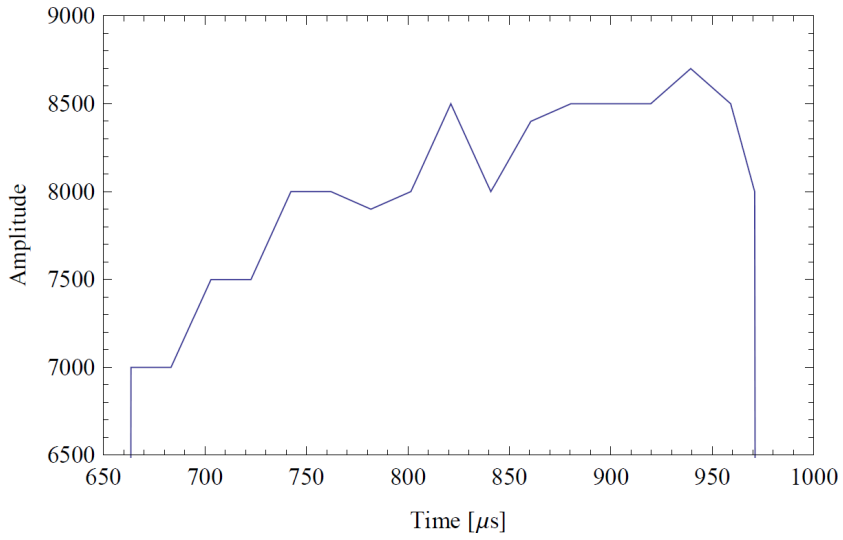


Figure 6.6: Amplitude [counts] versus time [$\mu$s] of an automatically generated beam FF table.

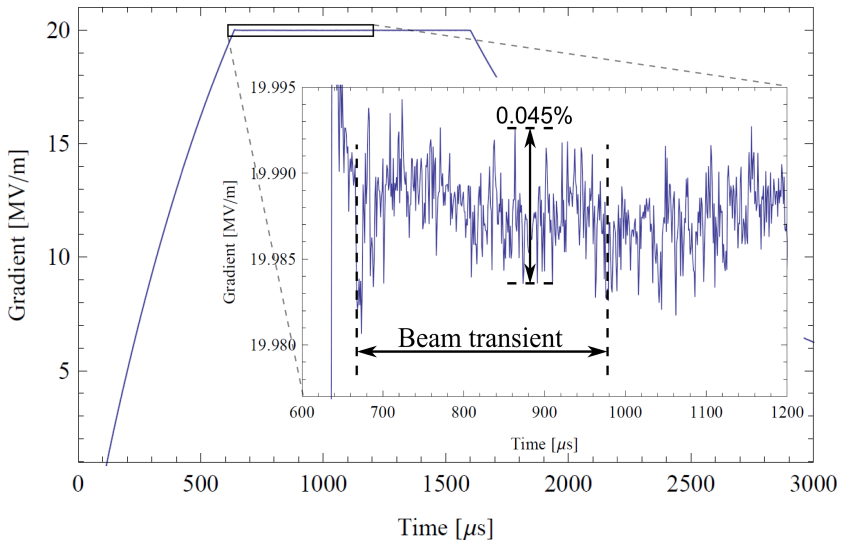


Figure 6.7: Vector–sum gradient [MV/m] versus time [$\mu$s] after the automated generation and application of the beam feedforward table during nominal operation.

Table 6.1: Best snapshot vector–sum amplitude and phase stabilities under long–time nominal operation (root–mean–square (rms) values)

| Beam | 6.6 mA | Off |
|---|---|---|
| $\Delta$A/A Vector sum | 0.009% | 0.008% |
| $\Delta\phi$ Vector sum | 0.009° | 0.008° |

## 6.4 Long–time Nominal Operation

In the scope of the QB project, the nominal operation parameters were cavity gradients of $E_{Cav1} = 16$ MV/m and $E_{Cav2} = 24$ MV/m. The loaded Q values were $Q_{L,Cav1} = Q_{L,Cav2} = 3 \cdot 10^6$. Therefore the filling time was set to 540 $\mu$s. In preparation for the long–time nominal operation all procedures as described in sections 6.1 to 6.3 were applied. The vector–sum stabilities during the beam transient achieved in a 60 minutes long–time run with and without a 6.6 mA beam with a pulse length of 615 $\mu$s are listed in Table 6.1. A snapshot of the vector–sum gradient is shown in Figure 6.7. With this it was demonstrated that the requirements for the nominal operation were fulfilled and that this situation was maintained over a long time.

## 6.5 Automated $P_kQ_L$ Operation

### 6.5.1 Motivation for Automated $P_kQ_L$ Operation

Since in the case of ILC a high number of cavities (15814) will be operated with $P_kQ_L$ control, this has to be done in an fully automated way. In order to demonstrate the feasibility of $P_kQ_L$ operation and its automation, a corresponding algorithm was developed, implemented, and applied at KEK STF.

### 6.5.2 Principle of Algorithm

In order to engage in the automated $P_kQ_L$ operation two steps are necessary. As a first step the working point in terms of the cavity driving powers $P_k$ and of cavity loaded Q values $Q_L$ have to be determined. As the second step the automated $P_kQ_L$ setting procedure has to be performed.

#### Determination of $P_kQ_L$ Working Point

The working points for the $P_kQ_L$ control of all cavities can be determined using the results of section 4.2. To this end the functions (4.33) and (4.34) are generated for all cavities, corresponding to the cavity gradients, which depend on the individual cavity quench limits. Since, in the case of KEK STF, both cavities (in case of ILC 39 cavities) are driven by a single klystron, the power ratio of filling to flattop has to be the same. By setting a low limit for the $Q_L$ for the cavity with highest gradient, this ratio is defined. By finding the same ratio for all remaining cavities, the $P_kQ_L$ working points for all cavities are determined as shown in Figure 6.8 indicated by the blue diamonds ($Q_{L,Cav1} = 9.0 \cdot 10^6$ and $Q_{L,Cav2} = 3.0 \cdot 10^6$) for the case of KEK STF.

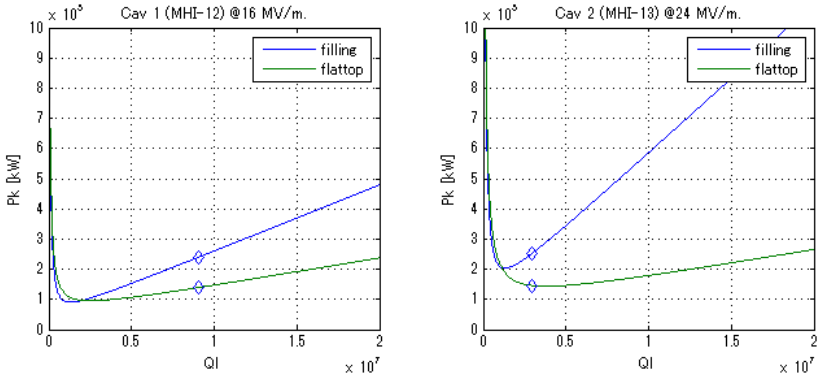


Figure 6.8: Driving power [kW] versus $Q_L$ values for a) cavity 1 (16 MV/m) and b) cavity 2 (24 MV/m). The working points are marked by blue diamonds.

### Automated $P_kQ_L$ Setting Procedure

A schematic of the automated $P_kQ_L$ setting procedure to engage in $P_kQ_L$ operation is shown Figure 6.9 and covers the following steps:

- Setting the $Q_L$ value of cavity 1 using the corresponding waveguide reflector (automated)
- Detuning compensation using piezo tuners (automated)
- Lowering the base FF table amplitude during the flattop (FFY2) time (automated)
- Adjusting the ratio of the variable hybrid in order to achieve the same gradient for both cavities after the filling time (automated)
- Rise the base FF table amplitude until both cavities reach a gradient of 15 MV/m (automated)
- Change the ratio of the variable hybrid in order to set the final gradient ratio of 12 MV/m for cavity 1 and 18 MV/m for cavity 2 (automated)
- Shorten the flattop duration (automated)
- Rise the base FF table amplitude during filling (FFY1) until the final gradients of 16 MV/m for cavity 1 and 24 MV/m for cavity 2 are reached (automated)

- Rise the base FF table amplitude during flattop (FFY2) so that the gradient tilts of both cavities are symmetric (automated)
- Phase compensation using waveguide phase shifters (automated)
- Turning on feedback (manually)
- Turning on beam (manually)
- Turning on beam compensation (manually)
- Simultaneous extension of the beam pulse and cavity gradient flattop lengths until final value (automated)

The manual steps were not automated because of machine protection concerns.

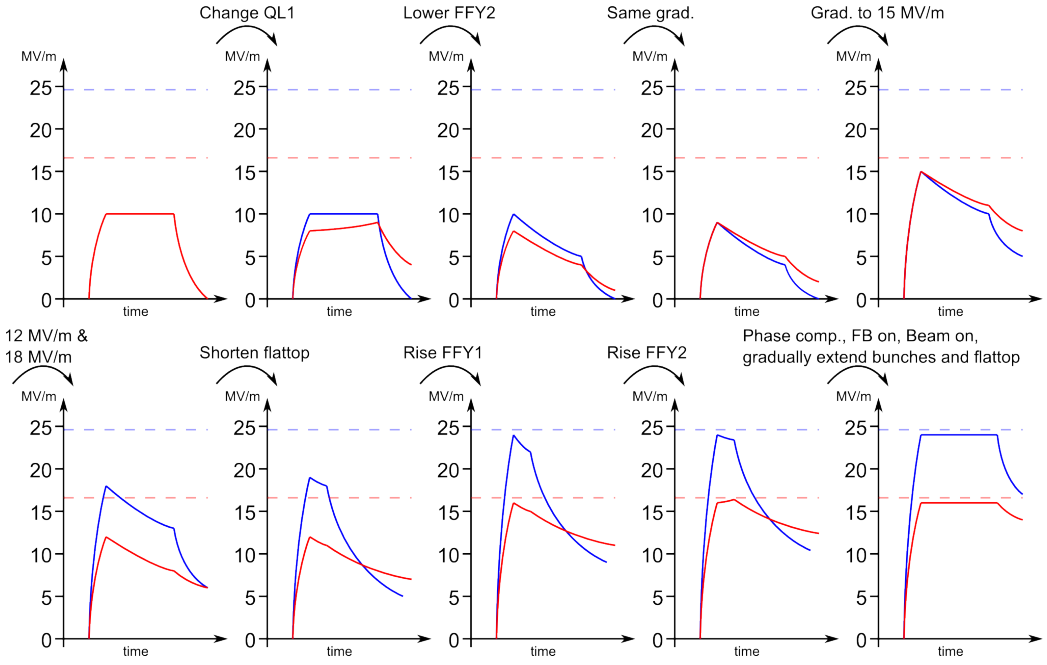


Figure 6.9: *Automated $P_k Q_L$ setting sequence for ILC-like operation at KEK STF. Both cavities start at 10 MV/m and the same $Q_L$ values. The adjustments as indicated over the arrows at each step are performed. The result is an operation with individually controlled $P_k$ and $Q_L$ values and flat flattop close the the individual virtual quench limits for both cavities.*

### 6.5.3 Automated Long–time $P_kQ_L$ Operation at KEK STF

The operation parameters for a $P_kQ_L$ operation and maintaining a long–time $P_kQ_L$ operation were gradients of $E_{Cav1}$=16 MV/m and $E_{Cav2}$=24 MV/m, loaded Q values of $Q_{L,Cav1} = 9 \cdot 10^6$, $Q_{L,Cav2} = 3 \cdot 10^6$, a filling time of 410 $\mu$s, an average beam current of 6.4 mA, and a beam pulse length of 615 $\mu$s. The virtual quench limits were defined to be 16.8 MV/m and 25.2 MV/m, respectively. In order to engage in $P_kQ_L$ operation the procedure described in section 6.5.2 was applied. Figures 6.10 to 6.20 are showing single shot recordings of cavity and vector sum gradients and phases during the automated sequence. In Figure 6.20 a snapshot of the final $P_kQ_L$ operation is shown. Although the vector sum phase is flat, it shows rather large phase deviations for the individual cavities. This originated from the large beam energy fluctuation.

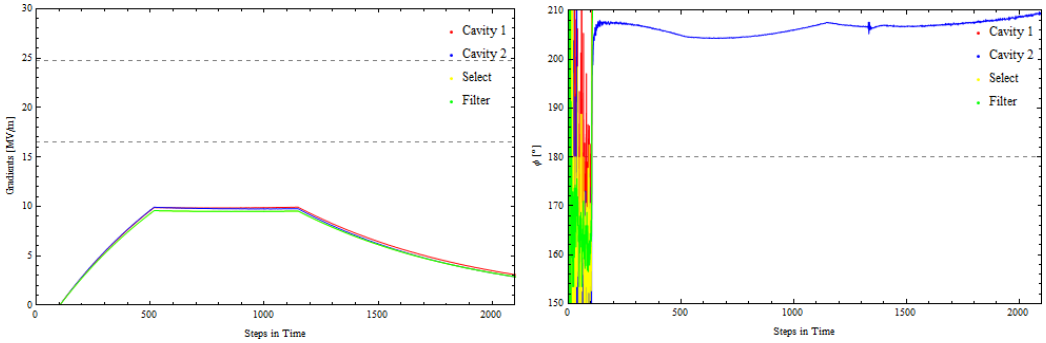


Figure 6.10: *Snapshot of gradients [MV/m] on the left and the phase [$\phi$] on the right versus time [$\mu$] (cavity 1 in red, cavity 2 in blue, vector sum in green) during $P_kQ_L$ control sequence for ILC-like operation at STF: Step 0, initial situation, both cavity gradient are 10 MV/m, both $Q_L$ values are $3 \cdot 10^6$, no beam.*

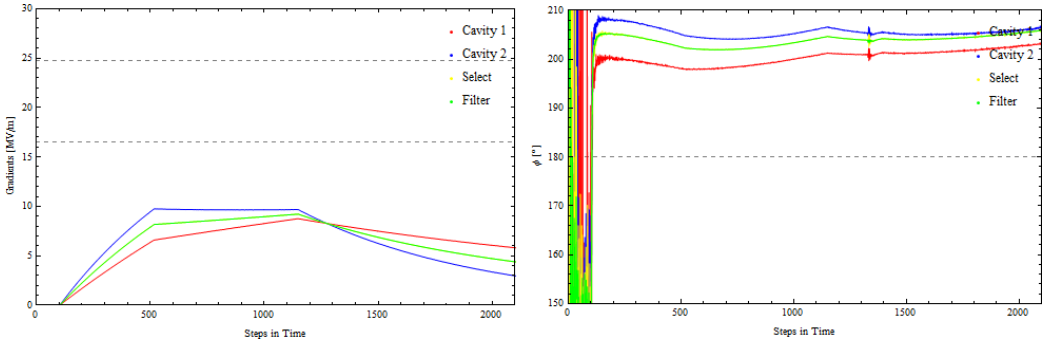


Figure 6.11: *Snapshot of gradients [MV/m] on the left and the phase [$\phi$] on the right versus time [$\mu$] (cavity 1 in red, cavity 2 in blue, vector sum in green) during $P_k Q_L$ control sequence for ILC-like operation at STF: Step 1, the $Q_L$ value of cavity 1 was set to $9 \cdot 10^6$.*

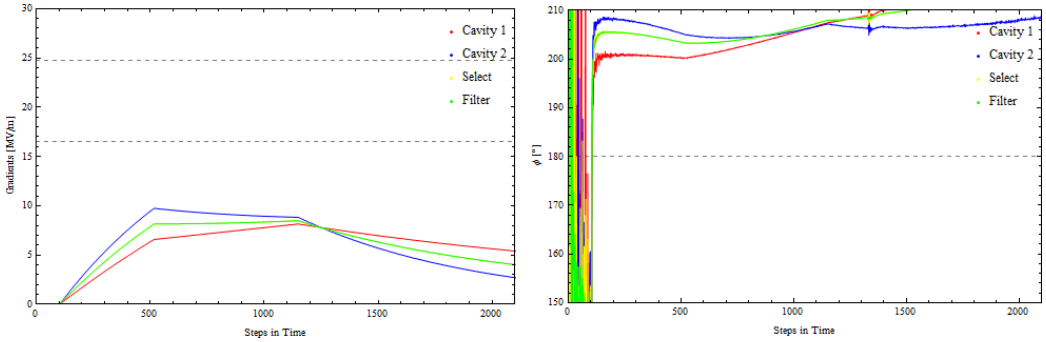


Figure 6.12: *Snapshot of gradients [MV/m] on the left and the phase [$\phi$] on the right versus time [$\mu$] (cavity 1 in red, cavity 2 in blue, vector sum in green) during $P_k Q_L$ control sequence for ILC-like operation at STF: Step 2, the flattop power was decreased.*

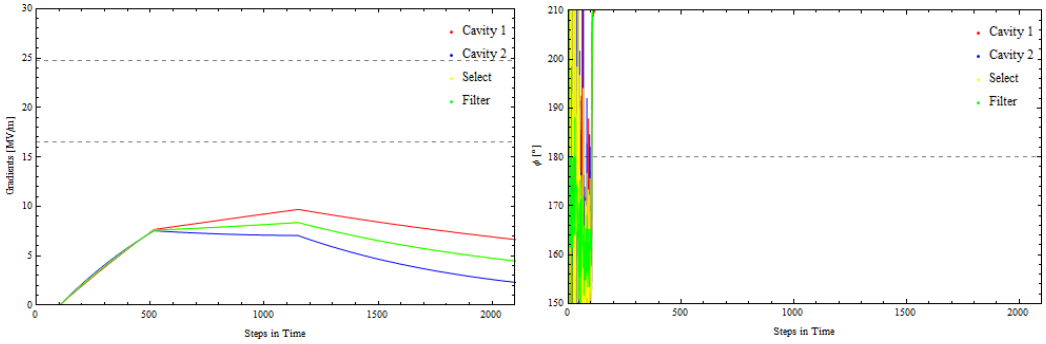


Figure 6.13: *Snapshot of gradients [MV/m] on the left and the phase [$\phi$] on the right versus time [$\mu$] (cavity 1 in red, cavity 2 in blue, vector sum in green) during $P_kQ_L$ control sequence for ILC-like operation at STF: Step 3, the ratio of the variable hybrid was changed so that the cavity gradients were the same at the end of the filling time.*

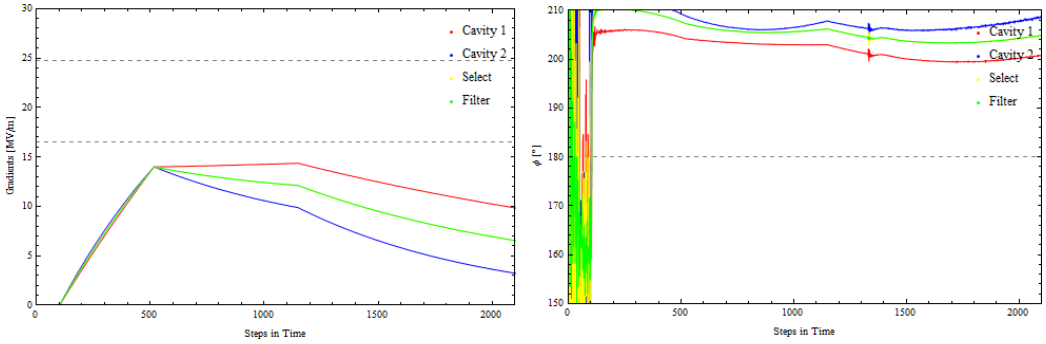


Figure 6.14: *Snapshot of gradients [MV/m] on the left and the phase [$\phi$] on the right versus time [$\mu$] (cavity 1 in red, cavity 2 in blue, vector sum in green) during $P_kQ_L$ control sequence for ILC-like operation at STF: Step 4, the driving power during the filling was increase so that both cavities reached a gradient of 14 MV/m at the end of the filling.*

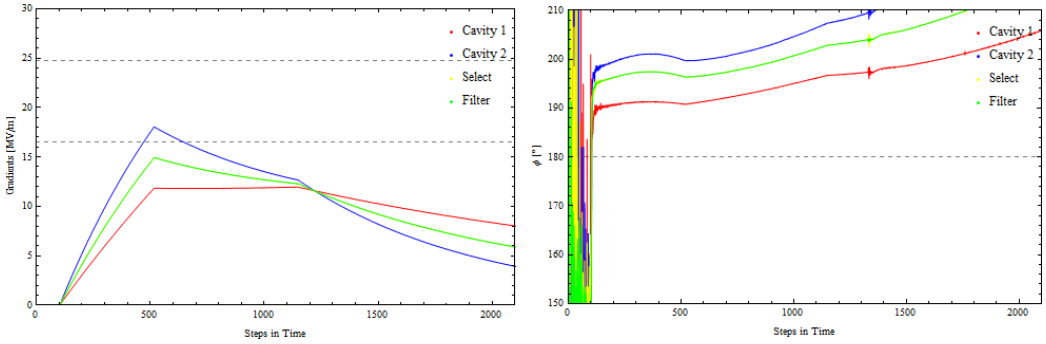


Figure 6.15: *Snapshot of gradients [MV/m] on the left and the phase [$\phi$] on the right versus time [$\mu$] (cavity 1 in red, cavity 2 in blue, vector sum in green) during $P_k Q_L$ control sequence for ILC-like operation at STF: Step 5, the final ratio of the driving powers was set.*

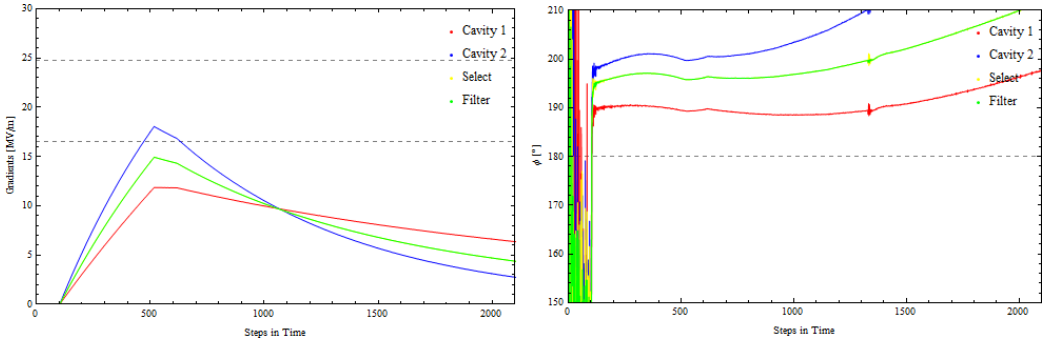


Figure 6.16: *Snapshot of gradients [MV/m] on the left and the phase [$\phi$] on the right versus time [$\mu$] (cavity 1 in red, cavity 2 in blue, vector sum in green) during $P_k Q_L$ control sequence for ILC-like operation at STF: Step 6, the flattop was shortened to 100 $\mu$s.*

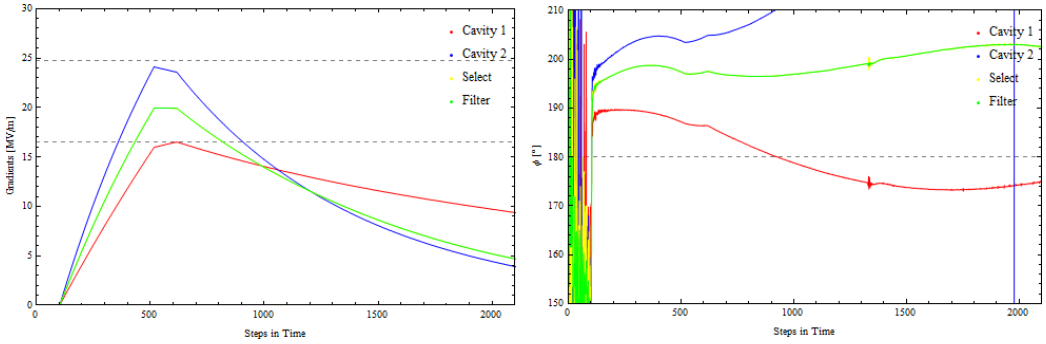


Figure 6.17: *Snapshot of gradients [MV/m] on the left and the phase [$\phi$] on the right versus time [$\mu$] (cavity 1 in red, cavity 2 in blue, vector sum in green) during $P_k Q_L$ control sequence for ILC-like operation at STF: Step 7, the filling power was increased in order to reach the final cavity gradients of 16 MV/m and 24 MV/m at the end of the filling.*

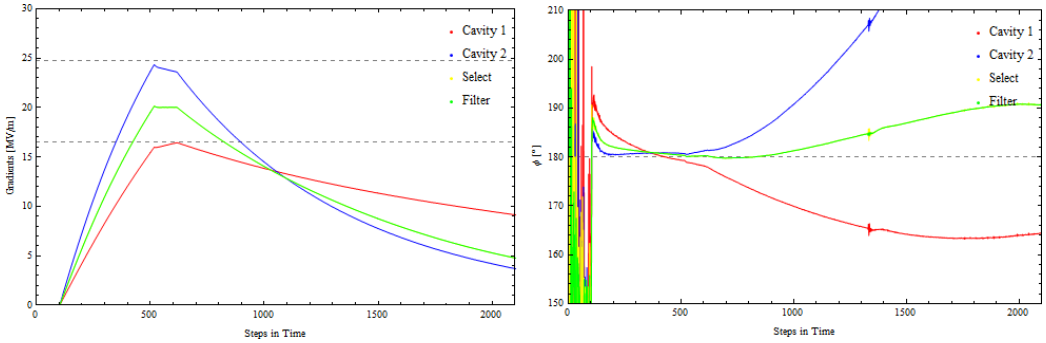


Figure 6.18: *Snapshot of gradients [MV/m] on the left and the phase [$\phi$] on the right versus time [$\mu$] (cavity 1 in red, cavity 2 in blue, vector sum in green) during $P_k Q_L$ control sequence for ILC-like operation at STF: Step 8, the cavity phases were compensated using the waveguide phase shifters.*

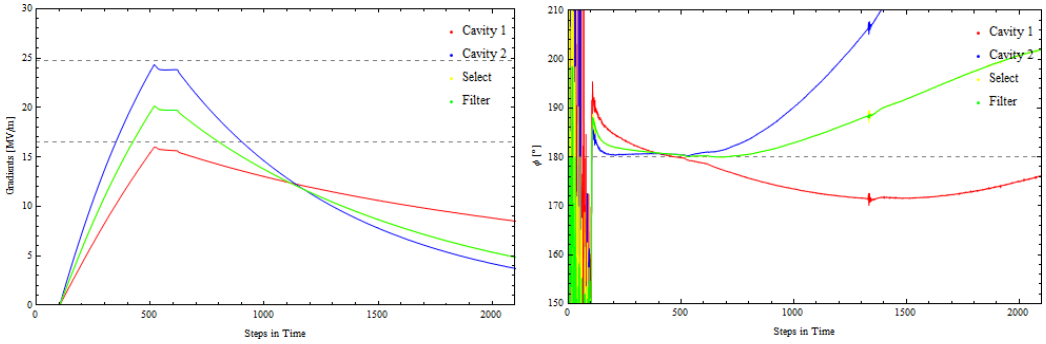


Figure 6.19: *Snapshot of gradients [MV/m] on the left and the phase [$\phi$] on the right versus time [$\mu$] (cavity 1 in red, cavity 2 in blue, vector sum in green) during $P_kQ_L$ control sequence for ILC-like operation at STF: Step 9, the feedback, the beam compensation, and the beam (6.4 mA) were turned on.*

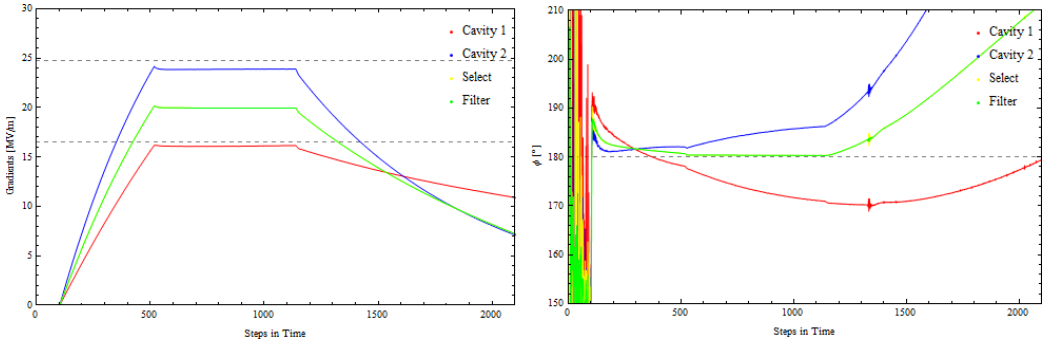


Figure 6.20: *Snapshot of gradients [MV/m] on the left and the phase [$\phi$] on the right versus time [$\mu$] (cavity 1 in red, cavity 2 in blue, vector sum in green) during $P_kQ_L$ control sequence for ILC-like operation at STF: Step 10, final situation of $P_kQ_L$ operation, the beam pulse length was extended to 615 $\mu$s as well as RF flattop.*

During the setting procedure the virtual quench limits were never exceeded. Figure 6.21 shows a snapshot of the cavity 1, cavity 2, and vector–sum gradients during the established $P_kQ_L$ operation. It can be seen that both cavity gradients during the beam transient time are flat with deviation of 0.34% for cavity 1 and 0.28% for cavity 2. Both cavity gradients were 5% below their respective virtual quench limits. Also the vector sum gradient was flat during the beam transient time with a deviation of 0.11%.

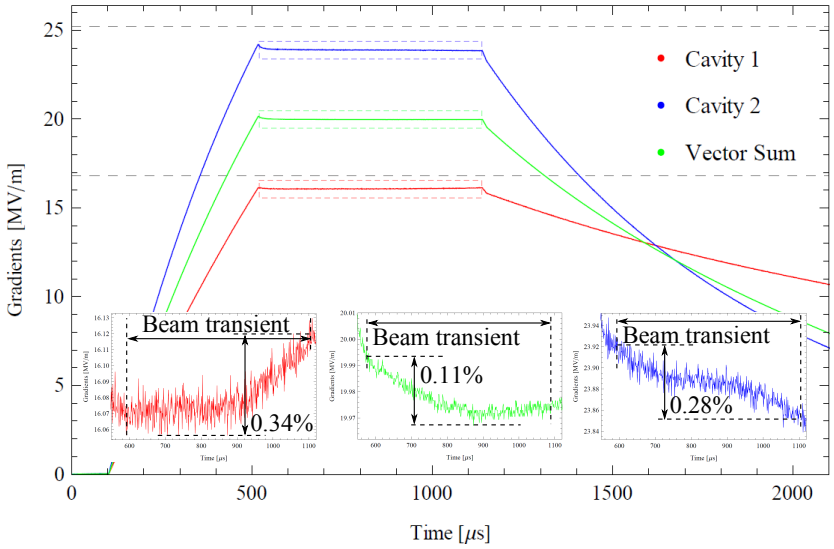


Figure 6.21: Cavity 1, cavity 2, and the vector–sum gradients [MV/m] versus time [s] during $P_kQ_L$ operation. The dashed lines indicate the virtual quench limits of 16.8 MV/m and 25.2 MV/m, respectively.

Figure 6.22 shows the gradient stabilities for cavities 1 and 2 versus time for a 800 second sample time span of the performed 60 minutes long–time operation with beam. The mean cavity stabilities were $\Delta A/A_{Cav1,mean}$= 0.211%rms for cavity 1 and $\Delta A/A_{Cav2,mean}$ = 0.132%rms for cavity 2. The best snap shot cavity stabilities were $\Delta A/A_{Cav1,best}$ = 0.041%rms for cavity 1 and $\Delta A/A_{Cav2,best}$ = 0.031%rms for cavity 2.

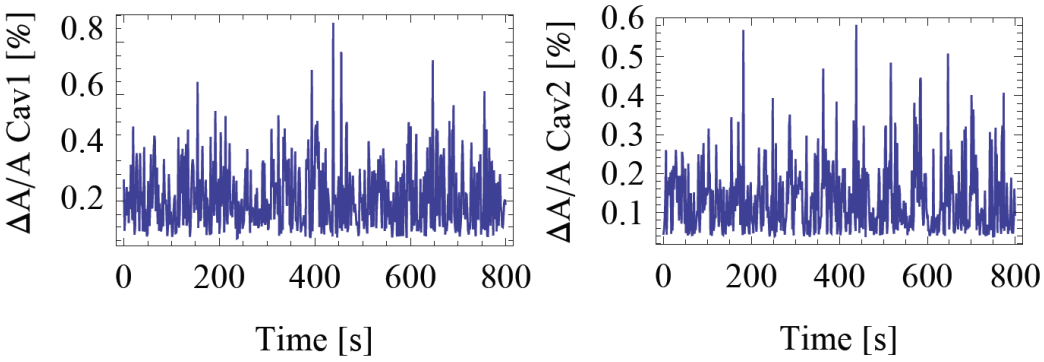


Figure 6.22: Cavity 1 (left) and 2 (right) gradient stabilities during beam transient versus time [s] while $P_kQ_L$ operation.

At ILC it is required that the beam energy gain deviation is $\leq 1\%$ [6]. Figure 6.23 a) shows the beam energy gain deviations for cavity 1 and Figure 6.23 b) for cavity 2 during a 1500 second sample time span during the $P_k Q_L$ operation at STF. In both cases 0 corresponds to a flat gradient and a flat phase during the beam transient time. The large fluctuations are dominated by the beam current fluctuation of about $\pm 20\%$ at that time. Furthermore, due to the vector sum feedback operation of the two cavities, the two beam energy gain deviation plots correlate. The mean beam energy gain deviation over the sample time span for cavity 1 is 1.04% and for cavity 2 $-0.41\%$. The corresponding standard deviation for cavity 1 is 1.04% and for cavity 2 0.51%. In the case the beam current fluctuation can be reduced sufficiently, the beam energy gain deviation can be kept at $\leq 1\%$ at all times.

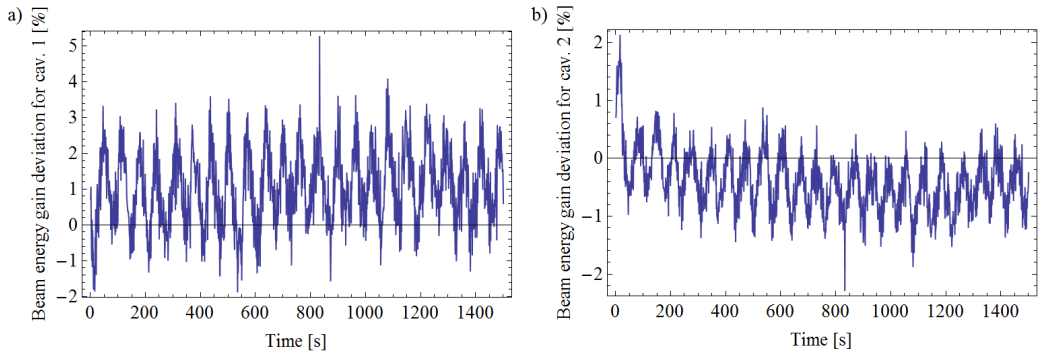


Figure 6.23: Beam energy gain deviation versus time for a) cavity 1 and b) cavity 2.

Figure 6.24 shows the vector–sum gradient and phase stabilities during the beam transient versus time for the same 800 second sample time span. The vector–sum amplitude and phase stabilities are listed in Table 6.2. These are comparable to the stabilities during nominal operation and hence allow a very stable actual $P_k Q_L$ operation. With this the first time an actual $P_k Q_L$ operation was successfully demonstrated.

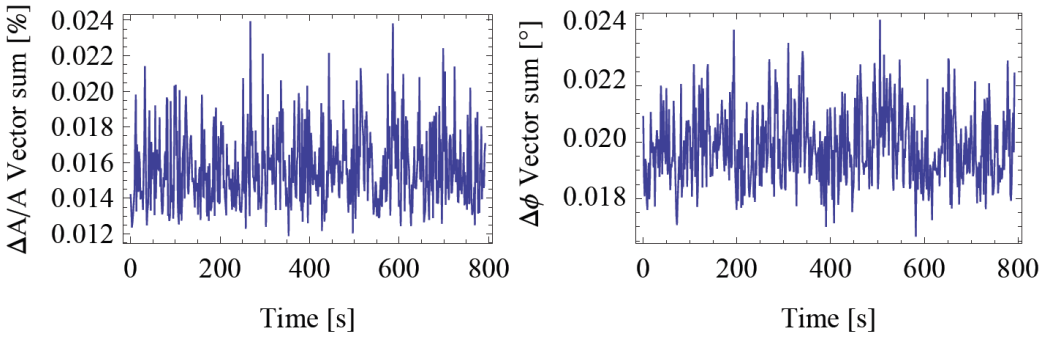


Figure 6.24: Vector–sum gradient (left) and phase (right) stabilities during beam transient versus time [s] while $P_kQ_L$ operation.

Table 6.2: Vector–sum amplitude and phase stabilities under $P_kQ_L$ operation (rms values)

| Beam | 6.1 mA |
|---|---|
| Best vector sum ΔA/A | 0.009% |
| Mean vector sum ΔA/A | 0.016% |
| Best vector sum $\Delta\phi$ | 0.009° |
| Mean vector sum $\Delta\phi$ | 0.019° |

The dominant source for the cavity as well as vector–sum stability fluctuations was a beam current fluctuation of about 20%. Even under this condition, the average vector–sum stabilities, indicated as "mean" in Table 6.2, were maintained fulfilling the ILC requirements. If the beam current could be controlled precisely and the matched condition maintained, the vector–sum stabilities would be as good as the ones indicated "best" in Table 6.2 over the whole time.

### 6.5.4 Lessons Learned During the Development of the $P_kQ_L$ Control Procedures

#### Manual $P_kQ_L$ Setting

At the beginning of the $P_kQ_L$ control studies the working points could already be calculated, but no automated setting procedure was developed yet. For its development first manual attempts of setting the system parameters were performed. Since the tuning of the combination of the driving powers $P_k$ and

the $Q_L$ values is not intuitive several times the operation points could not be reached.

Furthermore at the beginning of the study the filling time of only 400 $\mu$s was used. This delivered reasonable $Q_L$ values ($3 \cdot 10^6 < Q_L < 10 \cdot 10^6$) only for rather low beam currents ($< 3.5$ mA). It was realized that the filling time is one of the key parameters for an reasonable and realistic $P_k Q_L$ working point. After varying the filling time reasonable $P_k Q_L$ working points for a beam current of 6 mA were found.

During the performance of the manual $P_k Q_L$ control the experience was gained that it is better to tune the $Q_L$ values as well as the ratio of the variable hybrid and by this the cavity driving powers $P_k$ in small steps at the same time. By this the operation parameters for stable $P_k Q_L$ operation were found faster and more reliably. In the case only one parameter was set first and then a second one, the first had to be adjusted again. Nevertheless during the development and implementation of the automated $P_k Q_L$ setting procedure is was found out that two iterations of setting each parameter yielded sufficient precisions.

### Automated Setting Algorithm

In the $P_k Q_L$ setting procedure values such as the driving powers $P_k$, the $Q_L$ values, and the cavity phases have to be set in an automated way. In order to realize this an setting algorithm was implemented. The structogram of the algorithm used for this is shown in Figure 6.25 for the case of setting an $Q_L$ value. In a first step the $Q_L$ value is changed (usually risen) with steps of a width as predefined as the first element of the step list until it exceeds the target value. Then the $Q_L$ value decreased with a step width as defined by the second element in the step list. This alternating process is continued until the system parameter is within a predefined range around the target value or until the step list reaches its end.

In the case of changing the loaded Q values "get data" means to get a full set of data via EPICS from the $\mu$TCA controller board combined with the calculation of the $Q_L$ value by the evaluation of the amplitude decays of both cavities corresponding to equation (B.8) Appendix B. In the event "save data" all acquired and calculated data is written to a text file. The accuracy "acc" for the setting of $Q_L$ is usually 4% of the desired value "desired_val". This is good enough since the fluctuation of $Q_L$ usually observed is about 3%. Would the accuracy be smaller than the fluctuation, the occurrence of a situation of not finding a finial position within the length of the step list is probable and was observed several times during the test runs. The variable "set value" is the step motor position of waveguide phase shifter 1 or 2,

respectively. After a new system parameter is set to the system, which is represented by "set setvalue", a time delay of 1.5 seconds follows. This time period is required since the step motors of the variable hybrid, the waveguide reflectors, and the waveguide phase shifters need some time to move to the new position. Furthermore this gives enough time for obtaining a respective EPICS record. Its refresh rate is 1 Hz.

The disadvantage of the used method is that there is always an error in setting the parameter to the system, which can be as large as the order of the variation of the measured value of the respective parameter. Furthermore since it is an iterative procedure it takes a certain time, which depends e.g. on the step widths and the difference between the start and target value. During the experiments performed at STF the required time for setting a system parameter was in the order of one minute. It occurred several times, that the fluctuations of the measured value of the system parameter were too large. In this case the setting procedure failed to reach its target before the step list ended.

The advantage of the used method is that especially in long time operation the error in setting the system parameter stays constant since hysteresis effects of the step motors are compensated automatically. The usage of a lookup table for example becomes more and more inaccurate over long operation time including a large number of step motor position changes.

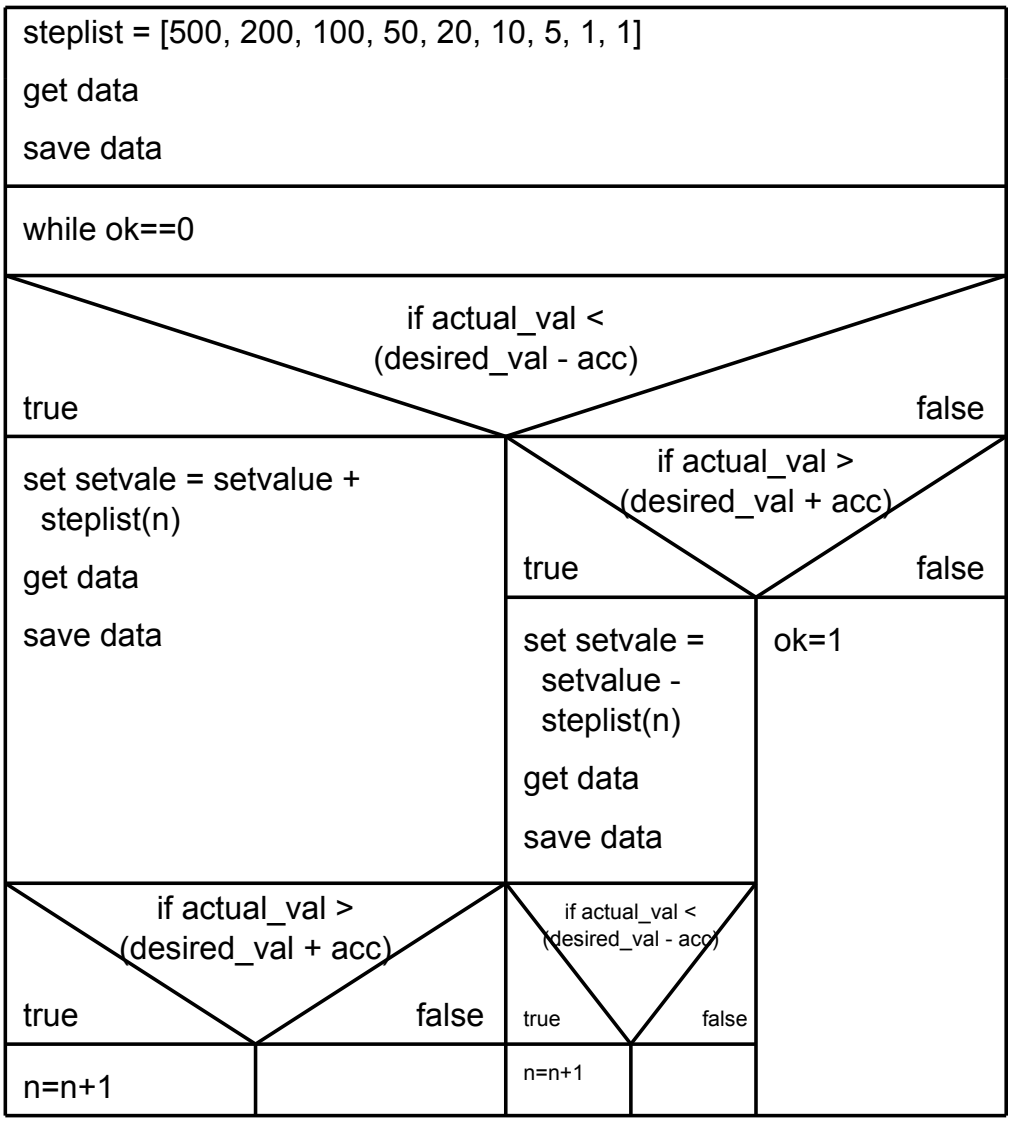


Figure 6.25: *Structogram of algorithm for setting system parameters (in this case for a $Q_L$ value) without the usage of a lookup table. The system parameter is changed e.g. raised with steps as predefined as the first element of the step list until it exceeds the target value. Then the system parameter is lowered with a step width as defined by the second element in the step list. This alternating process is performed until the system parameter is within a predefined range around the target value or until the step list reaches its end.*

## 6.6 Simulation of $P_kQ_L$ Operation for ILC

As described in section 2.1, it is planned to drive the superconducting cavities of the ILC main linacs in groups of 39 by a single klystron for each group. Figure 2.5 shows a schematic of such a group. Each group is divided into three sections covering 13 cavities in a 4–4–5 configuration. In order to demonstrate the feasibility of operating the 39 cavities in the presented configuration under $P_kQ_L$ control, a MATLAB script for the determination of the $P_kQ_L$ working point with ILC parameters has been created. The input parameters are the number of cavities, the individual cavity accelerating gradients, the minimum $Q_L$ value, the filling time, and the beam current. The cavity gradients were distributed in equidistant steps from 25.2 MV/m to 37.8 MV/m with an average of 31.5 MV/m. This corresponds to (31.5 ± 20%) MV/m, which covers the whole range of the ILC requirement. The filling time was chosen to be 832 $\mu$s. This filling time was chosen in order to keep the lowest $Q_L$ value equal to $3 \cdot 10^6$ and the highest $Q_L$ value smaller than $10 \cdot 10^6$. The calculated ratio of filling power over flattop power is 1.0001. In theory this should be 1. The small deviation originates from the used data resolution. Nevertheless the chosen precision is sufficient in case of a real system. Figure 6.26 shows plots of filling and flattop powers versus loaded Q values (lines) as well the indication of the working points (diamonds) for all 39 cavities. Beside this the script also outputs the working points in terms of cavity number, accelerating gradient, loaded Q value, filling power, and flattop power, which is shown in Table 6.3. The summation of all filling powers yields 8.05 MW. In this special case a 10 MW klystron is sufficient for driving all cavities. Furthermore this simulation shows, that the intended range of loaded Q values for the cavities in ILC from $3 \cdot 10^6$ to $10 \cdot 10^6$ is sufficient.

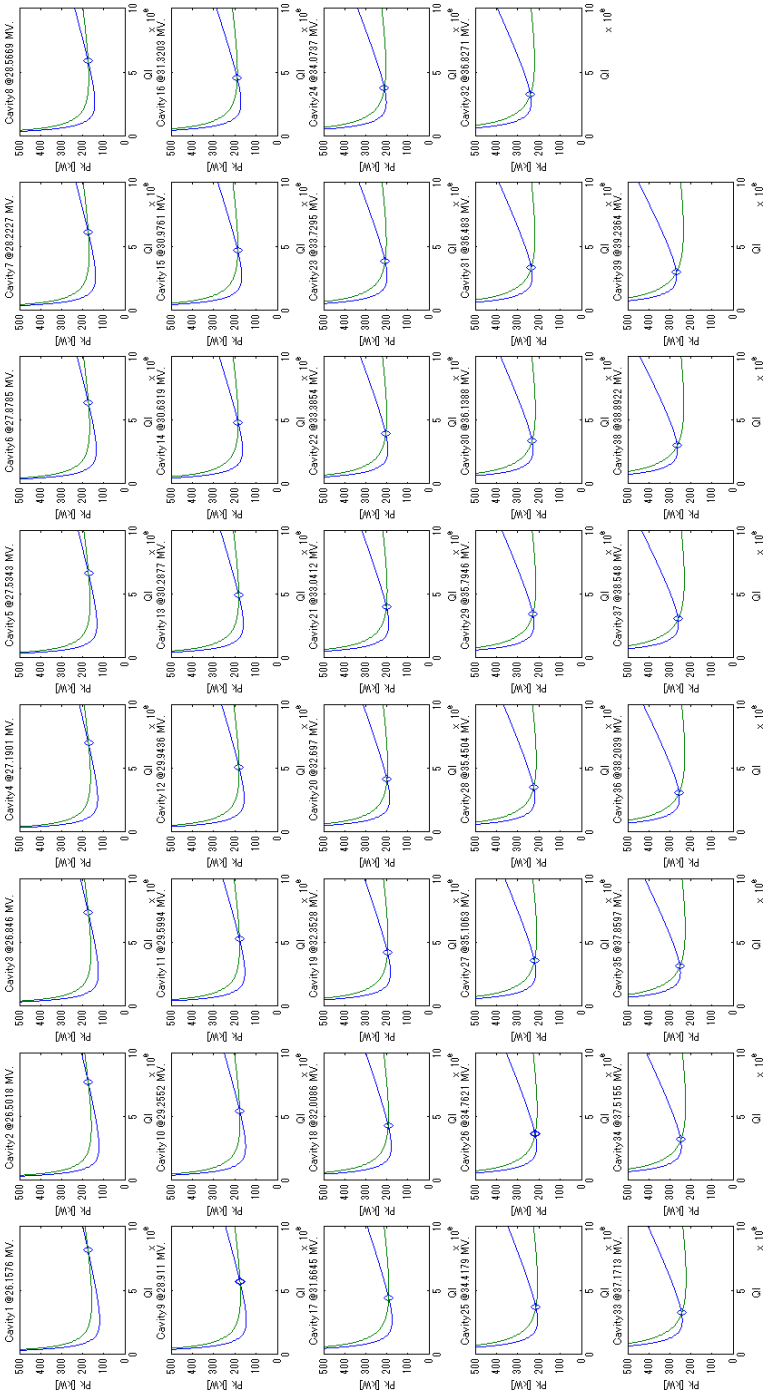

Figure 6.26: *Plots of driving power (Pk) [kW] during filling (blue) and flattop (green) versus loaded Q values of 39 cavities at voltages ranging from 26.2 MV to 39.2 MV. The working points, at which the ratio of filling power to flattop power is the same, are indicated by diamonds.*

Table 6.3: Estimated $P_k Q_L$ working point for ILC operation: Cavity numbers, accelerating gradients $E_{acc}$, $Q_L$ values, filling powers $P_{k,fill}$, and flattop powers $P_{k,flat}$.

| Cavity # | $E_{acc}$ [MV/m] | $Q_L$ | $P_{k,fill}$ [kW] | $P_{k,flat}$ [kW] |
|---|---|---|---|---|
| 1 | 25.2000 | 8220000 | 175.21 | 175.20 |
| 2 | 25.5315 | 7762000 | 173.72 | 173.71 |
| 3 | 25.8631 | 7358000 | 172.79 | 172.78 |
| 4 | 26.1947 | 7000000 | 172.33 | 172.32 |
| 5 | 26.5263 | 6680000 | 172.28 | 172.27 |
| 6 | 26.8578 | 6393000 | 172.59 | 172.58 |
| 7 | 27.1894 | 6133000 | 173.20 | 173.19 |
| 8 | 27.5210 | 5897000 | 174.08 | 174.07 |
| 9 | 27.8526 | 5682000 | 175.22 | 175.21 |
| 10 | 28.1842 | 5485000 | 176.57 | 176.56 |
| 11 | 28.5157 | 5303000 | 178.11 | 178.11 |
| 12 | 28.8473 | 5136000 | 179.85 | 179.84 |
| 13 | 29.1789 | 4981000 | 181.75 | 181.74 |
| 14 | 29.5105 | 4837000 | 183.81 | 183.80 |
| 15 | 29.8421 | 4704000 | 186.02 | 186.01 |
| 16 | 30.1736 | 4579000 | 188.36 | 188.35 |
| 17 | 30.5052 | 4462000 | 190.83 | 190.82 |
| 18 | 30.8368 | 4352000 | 193.42 | 193.41 |
| 19 | 31.1684 | 4249000 | 196.12 | 196.12 |
| 20 | 31.5000 | 4152000 | 198.94 | 198.93 |
| 21 | 31.8315 | 4061000 | 201.87 | 201.86 |
| 22 | 32.1631 | 3974000 | 204.89 | 204.89 |
| 23 | 32.4947 | 3893000 | 208.02 | 208.00 |
| 24 | 32.8263 | 3815000 | 211.23 | 211.23 |
| 25 | 33.1578 | 3742000 | 214.55 | 214.53 |
| 26 | 33.4894 | 3672000 | 217.95 | 217.93 |
| 27 | 33.8210 | 3605000 | 221.43 | 221.42 |
| 28 | 34.1526 | 3542000 | 225.01 | 224.99 |
| 29 | 34.4842 | 3481000 | 228.66 | 228.66 |
| 30 | 34.8157 | 3423000 | 232.40 | 232.40 |
| 31 | 35.1473 | 3368000 | 236.22 | 236.21 |
| 32 | 35.4789 | 3315000 | 240.12 | 240.11 |
| 33 | 35.8105 | 3265000 | 244.10 | 244.07 |
| 34 | 36.1421 | 3216000 | 248.15 | 248.13 |
| 35 | 36.4736 | 3169000 | 252.27 | 252.27 |
| 36 | 36.8052 | 3125000 | 256.48 | 256.45 |
| 37 | 37.1368 | 3081000 | 260.75 | 260.75 |
| 38 | 37.4684 | 3040000 | 265.10 | 265.09 |
| 39 | 37.8000 | 3000000 | 269.52 | 269.51 |

Similar to the procedure shown in Figure 6.9 a automated $P_kQ_L$ setting procedure was simulated for 39 cavities. To this end the following definition was used. The in Figure 2.5 shown variable hybrids have corresponding to Figure 6.27 an input port and two output ports.


Figure 6.27: *Symbol representing a variable hybrid and its ports: top left port connected to a load, top right port as output port out1, bottom left port as input port, and bottom right port as output port out2.*

In the scope of the simulation it is assumed that the sum of the powers at both output ports is equal to the power at the input port. Thus one can define the power ratio $r$ as

$$r = \frac{P_{out1}}{P_{in}} \quad \text{or} \quad 1 - r = \frac{P_{out2}}{P_{in}} \ , \tag{6.5}$$

where $P_{in}$ is the power at the input port, $P_{out1}$ the output power at port out1, and $P_{out2}$ the output power at port out2. The starting point of the $P_kQ_L$ setting procedure is shown in Figure 6.28 a) and covers the following RF parameter: a filling time of 832 $\mu$s, cavity gradients of 10 MV/m for all 39 cavities, the variable hybrid ratios were set accordingly, the filling and flattop powers were set accordingly, and the $Q_L$ values of all cavities were $3 \cdot 10^6$. It should be noted this simulated operation is not a matched condition.

As a first step in the $P_kQ_L$ setting procedure simulation the $Q_L$ values of all cavities were set to the ones estimated before as shown in Table 6.3. The outcome is shown in Figure 6.28 b). A clear impact on the gradient pulse shapes of cavities 1 to 38 can be observed. The gradient pulse shape of cavity 39 stays unchained, since its $Q_L$ value was not altered.

In the second step the ratios of the variable hybrid are adjusted in order to realize the power distribution as previously estimated and shown in Table 6.3. The outcome is shown in Figure 6.29 a). The cavity driving power distribution is not constant anymore, but has a minimum for cavity 6. This shows that most of the cavities are not operated in a matched condition. Cavity 6 is the one closest to it.

In the third step the flattop is shortened to 10 $\mu$s. The result is shown in Figure 6.29 b).

In the fourth step the filling power is increased until every cavity gradient reached the design value as listed in Table 6.3. The outcome is shown in Figure 6.30 a). It should be noted that due to the short flattop (of only 10 $\mu$s) no cavity exceeds their respective quench limit.

In the fifth step of the simulated $P_kQ_L$ setting procedure a beam of 6.0 mA is introduced during the whole flattop. Furthermore the cavity driving power during the flattop is risen until the level as shown in Table 6.3. The result is shown in Figure 6.30 b). In this situation the cavity driving powers during filling and flattop is the same, which corresponds to a rectangular pulse shape for the power. This fulfills the corresponding ILC requirement. Furthermore in this situation the gradients during the flattop of all cavities are flat 5% below their respective quench limits.

In the last step the RF flattop length as well as the beam pulse length are extended simultaneously to a length of 1 ms. The outcome is shown in Figure 6.31. In this situation all cavity gradients during the flattops are flat 5% below their respective quench limits. With this simulation the feasibility of the $P_kQ_L$ operation fulfilling all corresponding ILC requirements ($Q_L$ range, gradient distribution, beam current, 5% below quench limits, rectangular power pulse shape, etc.) is demonstrated.

Since at the current point in time no ILC test accelerator with 39 cavities and the corresponding waveguide exists, this kind of simulation is at the moment the best way for the validation of the requirements and for the proof of feasibility. Although STF–2 will have a smaller number of cavities, it is recommended to demonstrate a similar $P_kQ_L$ control operation there.

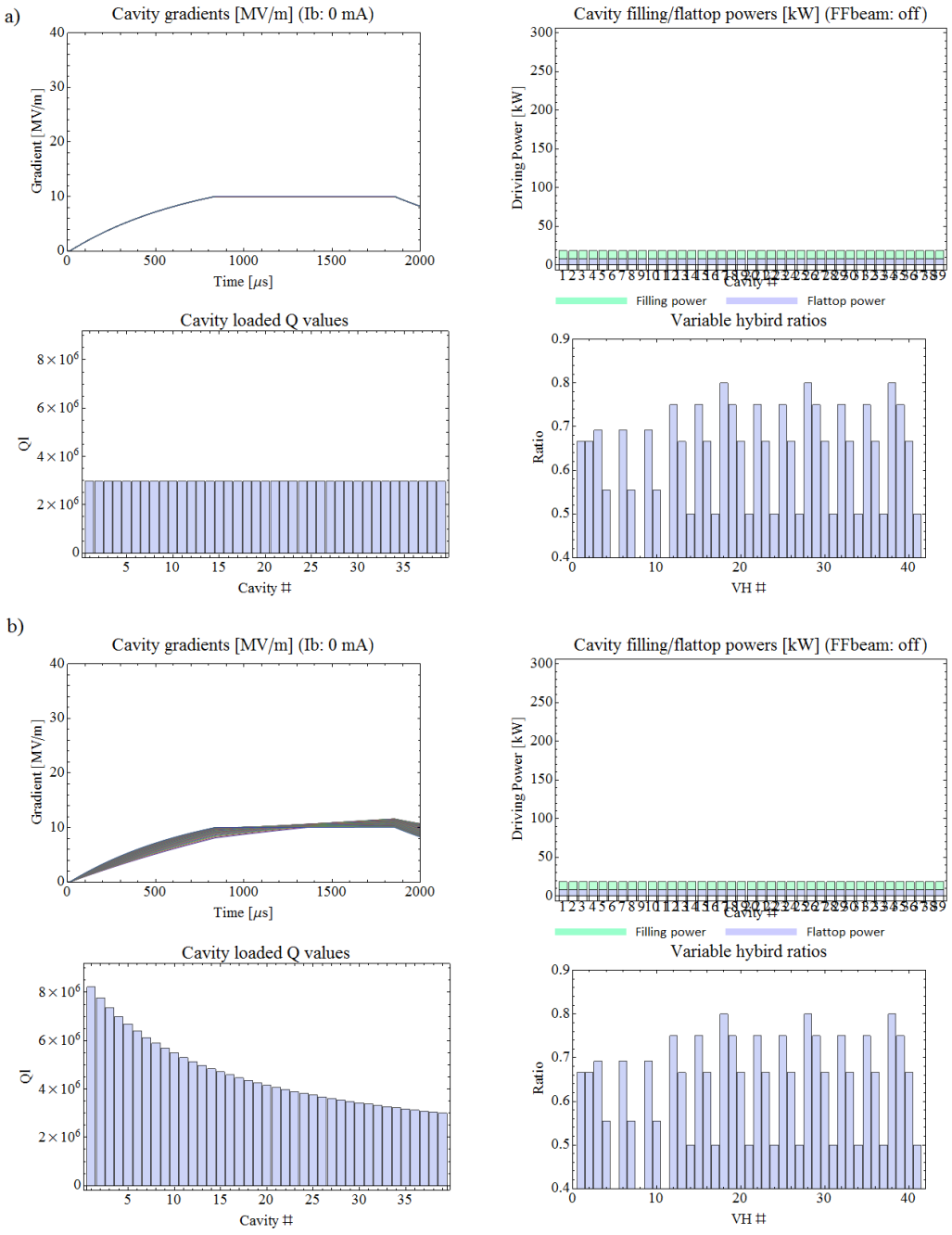


Figure 6.28: *$P_kQ_L$ setting procedure simulation for ILC: Gradient [MV/m] versus time for all 39 cavities (top left), cavity driving powers during filling in light green and flattop in light purple (top right), loaded quality factors of all cavities (bottom left), and the ratio r of all 41 variable hybrids (bottom right). a) Starting point, b) Step 1.*

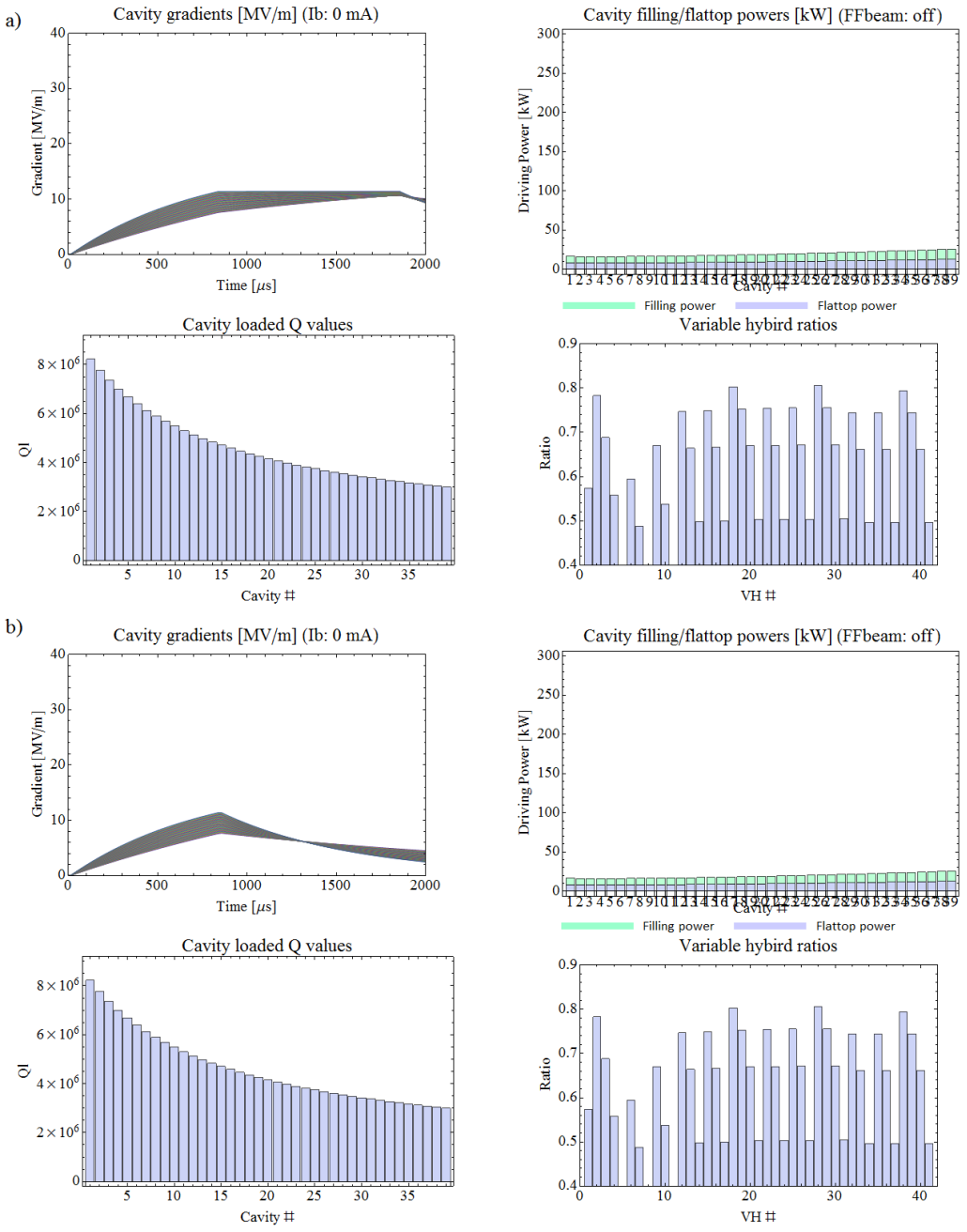


Figure 6.29: *$P_k Q_L$ setting procedure simulation for ILC: Gradient [MV/m] versus time for all 39 cavities (top left), cavity driving powers during filling in light green and flattop in light purple (top right), loaded quality factors of all cavities (bottom left), and the ratio r of all 41 variable hybrids (bottom right). a) Step 2, b) Step 3.*

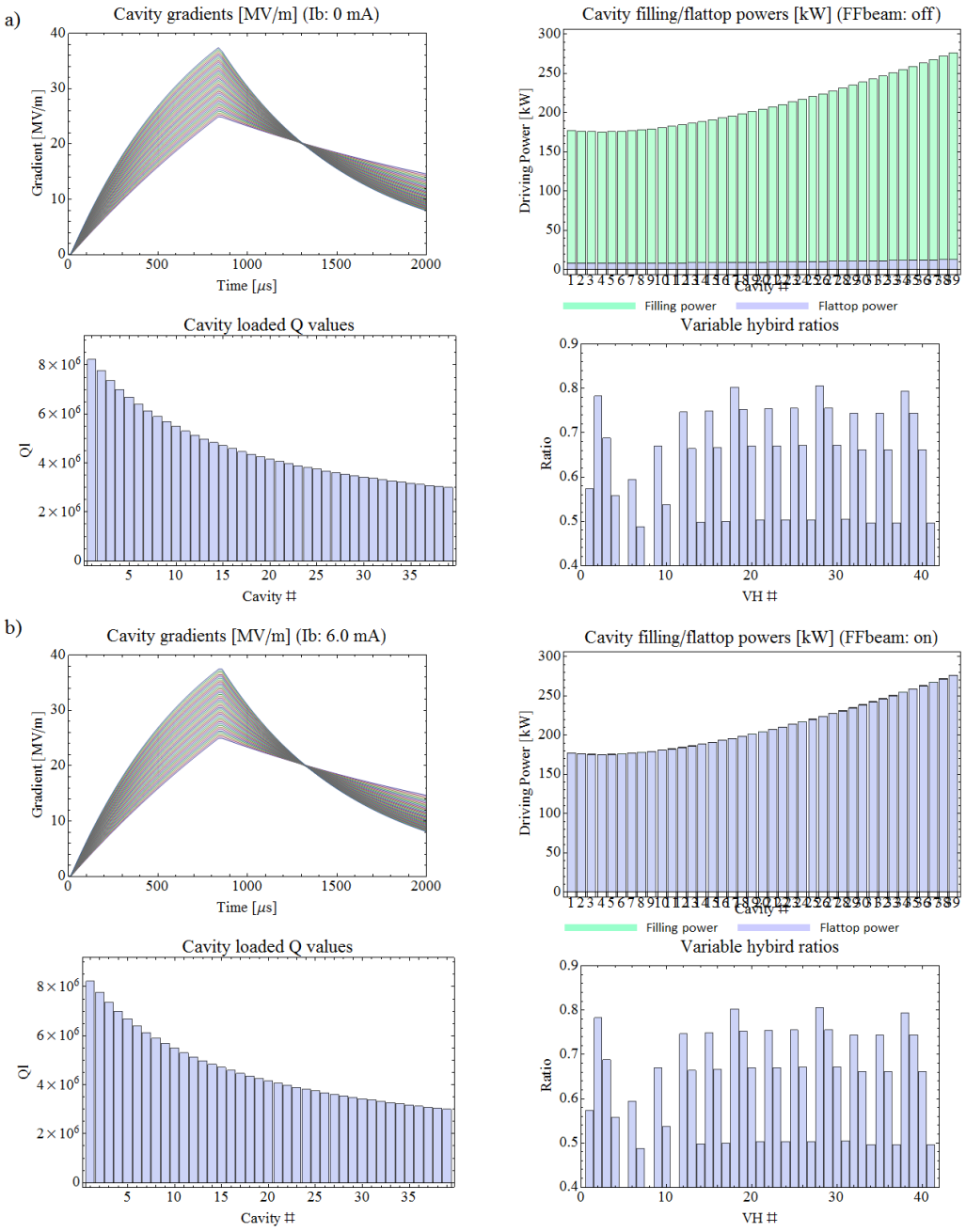


Figure 6.30: *$P_kQ_L$ setting procedure simulation for ILC: Gradient [MV/m] versus time for all 39 cavities (top left), cavity driving powers during filling in light green and flattop in light purple (top right), loaded quality factors of all cavities (bottom left), and the ratio r of all 41 variable hybrids (bottom right). a) Step 4, b) Step 5.*

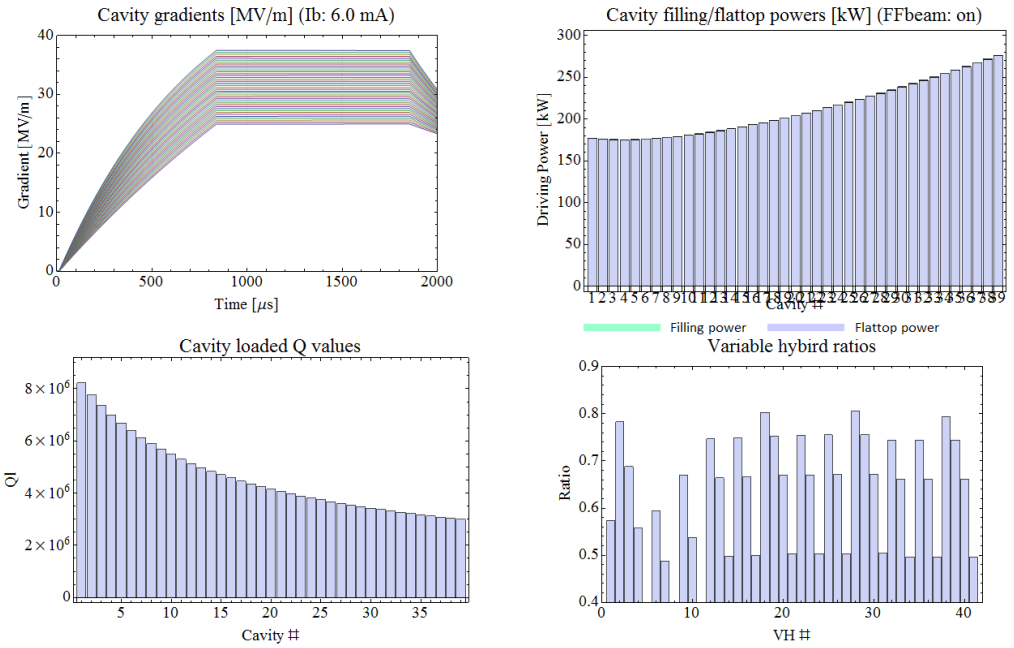


Figure 6.31: *$P_kQ_L$ operation simulation for ILC: Gradient [MV/m] versus time for all 39 cavities (top left), cavity driving powers during filling in light green and flattop in light purple (top right), loaded quality factors of all cavities (bottom left), and the ratio r of all 41 variable hybrids (bottom right). $P_kQ_L$ operation.*

A further important issue, which can be checked in such a simulation is the margin of acceptable deviations in RF parameters such as the cavity driving powers $P_k$ and the $Q_L$ values and acceptable deviations in the beam current.

Figure 6.32 shows the gradient [MV/m] versus the cavity driving power $P_k$ deviation [kW] from the design values in a range of $\pm 35$ kW for cavities with design gradients of 37.8 MV/m (red), 31.5 MV/m (blue), and 25.2 MV/m (purple). Solid lines indicate the corresponding quench limits, dotted lines indicate the corresponding cavity gradient at the beginning of the flattop and beam transient time, and dashed lines indicate the corresponding cavity gradient at the end of the flattop and beam transient time. Deviations in the driving power can occur when the power measurement is not calibrated correctly. It can be seen that for the cavity with the lowest design gradient (25.5 MV/m) an additional driving power of about 9.8 kW would lead to a quench event at the end of the flattop and an additional driving power of about 6.1 kW would lead to slope of 3% over the flattop. This means in a

$P_kQ_L$ operation as assumed in the previously shown simulation the output power deviation of the klystron has to be lower than 5.3% in order to prevent quenching and lower than 3.2% in order to fulfill the stability requirements.

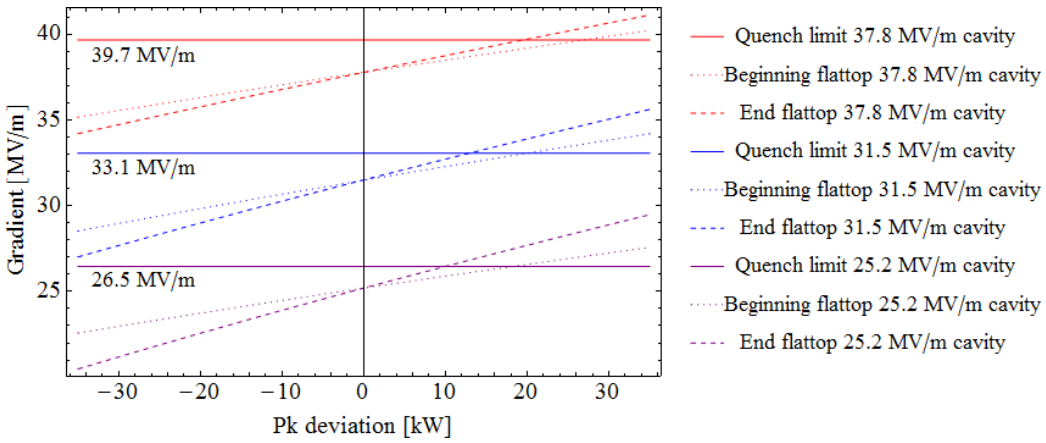


Figure 6.32: *Cavity gradient [MV/m] versus $P_k$ deviation [kW] from the design values for cavities with design gradients of 37.8 MV/m (red), 31.5 MV/m (blue), and 25.2 MV/m (purple). Solid lines indicate the corresponding quench limits, dotted lines indicate the corresponding cavity gradient at the beginning of the flattop and beam transient time, and dashed lines indicate the corresponding cavity gradient at the end of the flattop and beam transient time.*

Figure 6.33 shows the cavity gradient [MV/m] versus $Q_L$ deviation from the design values in a range of $\pm 2.5 \cdot 10^6$ for cavities with the same design gradients as in the figure before. A deviation in $Q_L$ values can result from errors in the estimation algorithm and thus in errors in the setting of the waveguide reflector, by which the $Q_L$ value is controlled. The experience during the operation of the accelerator at STF during the QB project was, that the estimated $Q_L$ values were fluctuating less than 3%. From Figure 6.33 it can be seen that a deviation from the design $Q_L$ value ($8.6 \cdot 10^6$) of $-1 \cdot 10^6$ would lead the cavity with the lowest gradient (25.5 MV/m) to quench. This corresponds to a deviation of about -11.6%. For a deviation of $-0.6 \cdot 10^6$ a slope of 3% would be introduced. This corresponds to a deviation of about -7.0%. This means that in the case of a gradient operation 5% below the quench limit it is imperative to calibrate the $Q_L$ properly.

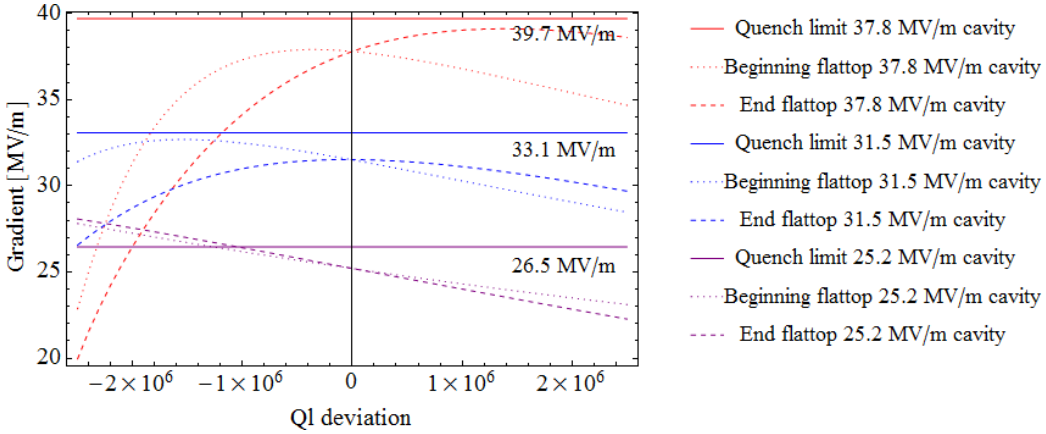


Figure 6.33: *Cavity gradient [MV/m] versus $Q_L$ deviation from the design values for cavities with design gradients of 37.8 MV/m (red), 31.5 MV/m (blue), and 25.2 MV/m (purple). Solid lines indicate the corresponding quench limits, dotted lines indicate the corresponding cavity gradient at the beginning of the flattop and beam transient time, and dashed lines indicate the corresponding cavity gradient at the end of the flattop and beam transient time.*

Figure 6.34 shows the cavity gradient [MV/m] versus the RF phase deviation [°] from the design values in a range of ±1.5 mA for cavities with the same design gradients as in the figure before. Since no beam is present during the filling time, the gradient values at the beginning of the flattop are not influenced by the beam phase deviation. At a deviation of about ±13.6° the cavity with the lowest gradient (25.2 MV/m) would quench at the end of the flattop. At a deviation of about ±11.8° a slope of 3% over the flattop would be reached. This is a wide margin for the deviation, since usually the phase can be set with an error in the order of a degree.

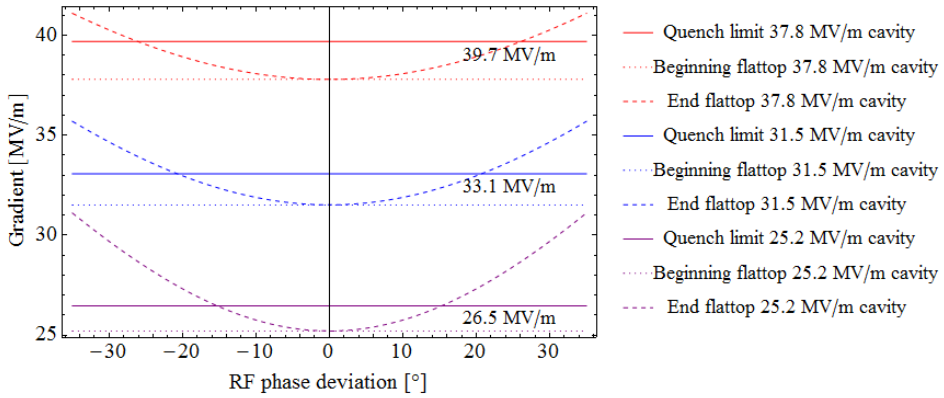


Figure 6.34: *Cavity gradient [MV/m] versus RF phase deviation [°] from the design values for cavities with design gradients of 37.8 MV/m (red), 31.5 MV/m (blue), and 25.2 MV/m (purple). Solid lines indicate the corresponding quench limits, dotted lines indicate the corresponding cavity gradient at the beginning of the flattop and beam transient time, and dashed lines indicate the corresponding cavity gradient at the end of the flattop and beam transient time.*

Figure 6.35 shows the cavity gradient [MV/m] versus the beam current deviation [mA] from the design values in a range of ±1.5 mA for cavities with the same design gradients as in the figure before. Since no beam is present during the filling time, the gradient values at the beginning of the flattop are not influenced by the beam current deviation. It can be seen that a beam current deviation of -0.38 mA or more would lead the cavity with the lowest design value for the gradient (25.5 MV/m) to quench. This corresponds to deviation in the beam current of about -6.3%. In the case of a deviation of -0.21 mA, corresponding to a change of -3.5%, the slope of 3% over the flattop would be reached. It is imperative that the beam current stability at ILC is (much) better that this value. For a comparison, during the studies at the accelerator at STF in the scope of the QB project, the beam current deviation has been up to about ±20%. Since the LLRF control system has no influence on the beam current, the task is to generate a beam with a stable beam current at the RF gun.

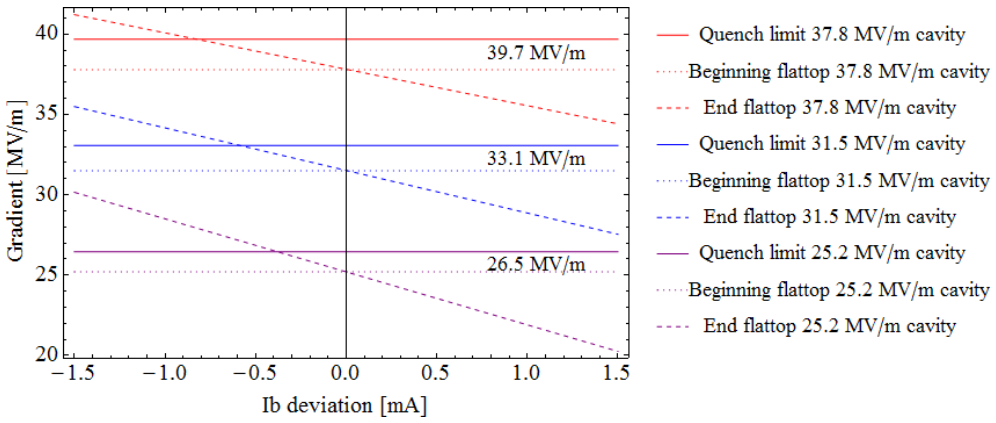


Figure 6.35: *Cavity gradient [MV/m] versus beam current deviation [mA] from the design values for cavities with design gradients of 37.8 MV/m (red), 31.5 MV/m (blue), and 25.2 MV/m (purple). Solid lines indicate the corresponding quench limits, dotted lines indicate the corresponding cavity gradient at the beginning of the flattop and beam transient time, and dashed lines indicate the corresponding cavity gradient at the end of the flattop and beam transient time.*

In a conclusion of the simulation regarding the margin of acceptable deviations in RF parameters it can be said, that generally the cavity with the lowest gradient and thus with the highest $Q_L$ (and most narrow bandwidth) is most sensitive and with this the limiting cavity. Furthermore is should be kept in mind, that the presented simulation show variations only of one parameter at the time. In reality all parameters fluctuate at the same time, which means the actual operational margins for the parameters will be actually smaller than the margins shown. Nevertheless the precisions in control of the $Q_L$ values, the driving powers, and the RF phases are already sufficient. With the practical experience gained as a background, especially a very stable beam current is important in the scope of the operation of ILC.

# Chapter 7

# High $Q_L$ Operation

In this chapter the successful test of a stable long–time operation of cavities with high loaded quality factors is described. Also the characterization of the possible range of the loaded quality factors at KEK STF in the scope of the QB project and the impact on the cavity phases is covered. These studies were performed in the scope of this dissertation.

## 7.1 Motivation for High $Q_L$ Operation

The operational cavity gradients at ILC will be (31.5 ± 20%) MV/m. The variation of 20% in the gradient stems from the quench limits, which differ between cavities. This requires a $Q_L$ range from $3 \cdot 10^6$ to $10 \cdot 10^6$ (also refer to section 6.6). Since $f_{1/2} = \frac{f_0}{2Q_L}$ the cavity bandwidth becomes narrow at high $Q_L$ values, e.g. $f_{1/2} = 32.5$ Hz at $Q_L = 2 \cdot 10^7$ and $f_0 = 1.3$ GHz. Because of this, cavity detuning, induced by e.g. microphonics, is expected to become severe. At KEK STF, the range of $Q_L$ values of both superconducting cavities is $2.5 \cdot 10^6$ to $5 \cdot 10^7$, which is a predestined environment for a long–time high $Q_L$ operation test run.

## 7.2 Low Power $Q_L$ and Phase Measurement

In order to perform a $Q_L$ measurement of both cavity 1 (MHI-12) and cavity 2 (MHI-13), a network analyzer was used. Port 1 was connected via a transducer to the respective waveguide between the klystron and the cavity. By this the waveguide phase shifter and waveguide reflector for changing the $Q_L$ value were included in the measurement. Port 2 was connected to the respective cavity pickup. An overview of the waveguide including the points of connections is shown in Figure 7.1. Furthermore Figure 7.2 shows a picture

of the connection of port 1 of the network analyzer to the waveguide to point A1. The $Q_L$ value was determined by the measurement of the respective cavity bandwidth by observing S21. A scan of the step motor positions of both the waveguide phase shifter as well as of the waveguide reflector while observing the $Q_L$ value and the phase was performed. Figures 7.3 and 7.4 are showing the results of the scans regarding the $Q_L$ values. It should be noted that due to time limitations for the measurements only 17 measurement points are included in Figure 7.3 and 81 in Figure 7.4. But even the scans are only rough, it can be seen that the shape of the graphs for both cavities is similar. In both cases the behavior for the waveguide reflectors is symmetric around the step motor zero position. Furthermore the data shows that the range in $Q_L$ of cavity 2 is larger compared to cavity 1. Table 7.1 gives an overview of the ranges.

Table 7.1: Overview of $Q_L$ ranges of cavity 1 and cavity 2.

| Cavity 1 | $Q_L$ | WR SMP | WPS SMP |
|---|---|---|---|
| Max | $8.13 \cdot 10^6$ | -2000 | 4500 |
| Min | $1.36 \cdot 10^6$ | 2000 | 500 |
| $Q_L$ range | $6.77 \cdot 10^6$ | | |
| Cavity 2 | $Q_L$ | WR SMP | WPS SMP |
| Max | $10.68 \cdot 10^6$ | -1500 | 4000 |
| Min | $1.03 \cdot 10^6$ | 2000 | 500 |
| $Q_L$ range | $9.65 \cdot 10^6$ | | |

The plots for the phase $\phi$ versus step motor positions of waveguide reflector and waveguide phase shifter are shown in figures 7.5 and 7.6. As mentioned above the scan of cavity 1 was rough. Still for both cavities on can see that the phase shift is mainly caused by the waveguide phase shifters.

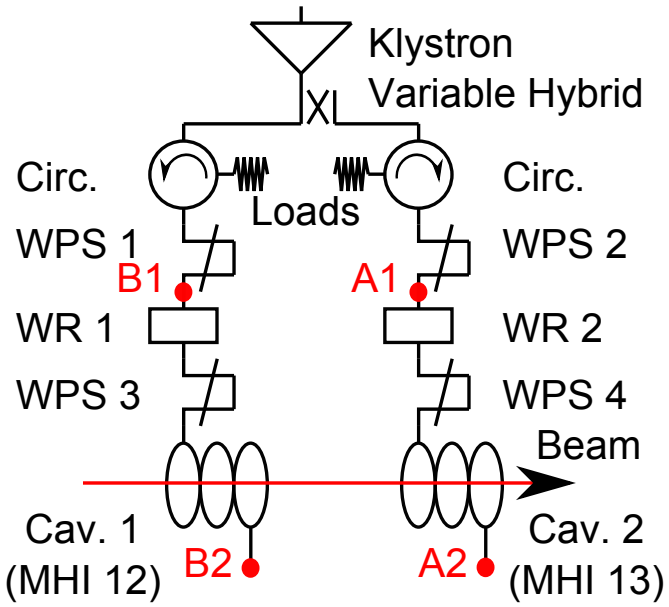


Figure 7.1: *Overview of the waveguide system in the scope of the QB project including the connection points for scans of waveguide reflectors and phase shifters (A1 to A2 and B1 to B2). The waveguide system consists of a klystron, a variable hybrid, two circulators with loads, and waveguide phase shifters (WPS 1, WPS 2, WPS 3, and WPS 4), waveguide reflectors (WR 1 and WR 2). It is connected to cavity 1 and 2, in which an electron beam is accelerated.*

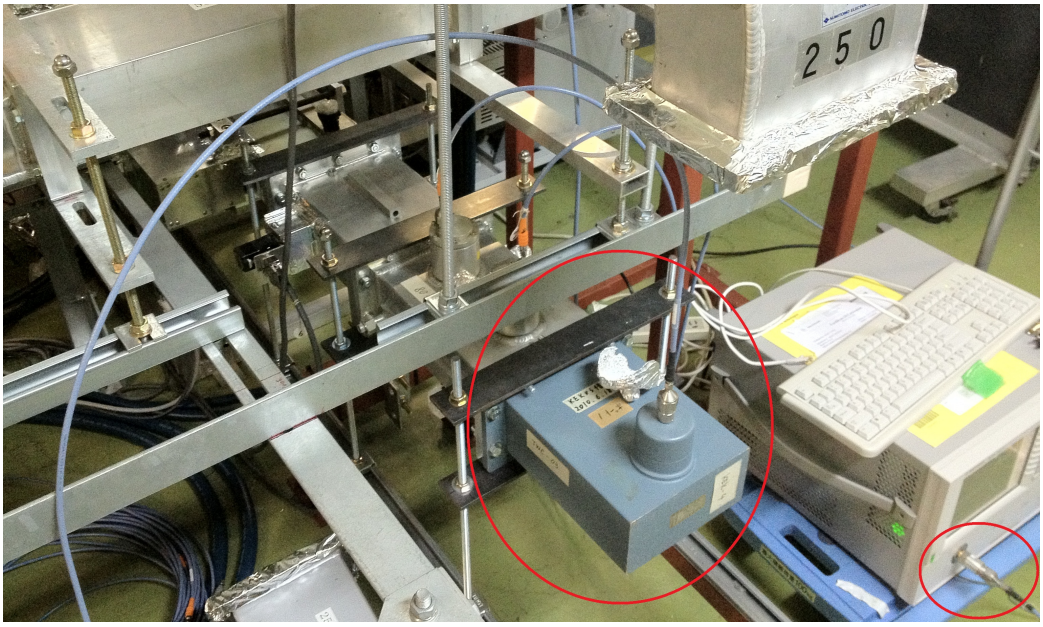


Figure 7.2: *Picture of port 1 to waveguide connection. Both, port 1 and the cable to waveguide connector are indicated by red circles.*

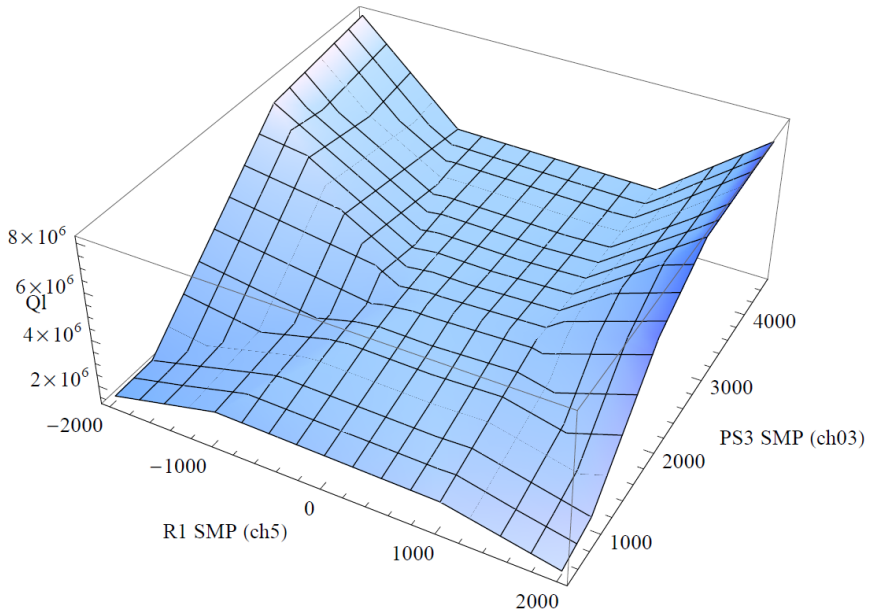


Figure 7.3: $Q_{L,cav1}$ *versus step motor positions of waveguide reflector 1 and waveguide phase shifter 3 (17 points of measurement).*

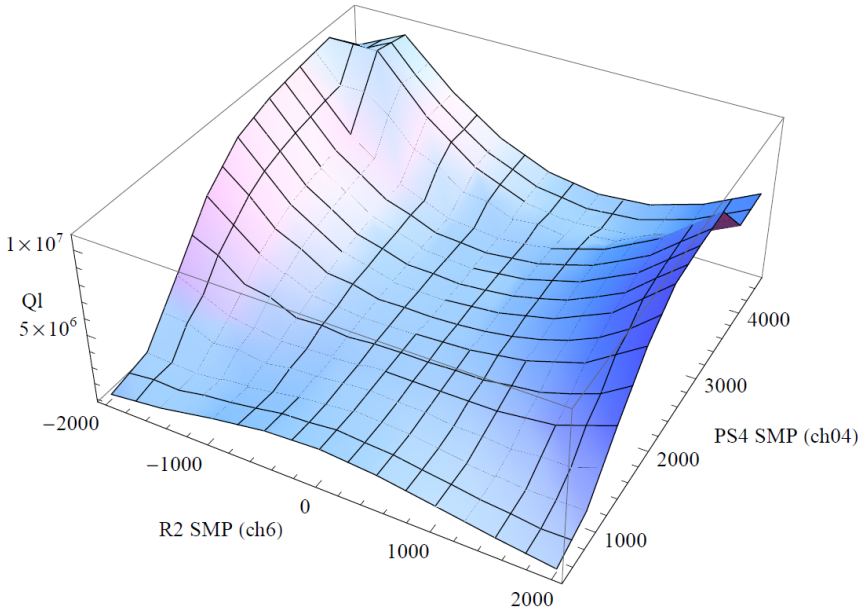


Figure 7.4: *$Q_{L,cav2}$ versus step motor positions of waveguide reflector 2 and waveguide phase shifter 4 (81 points of measurement).*

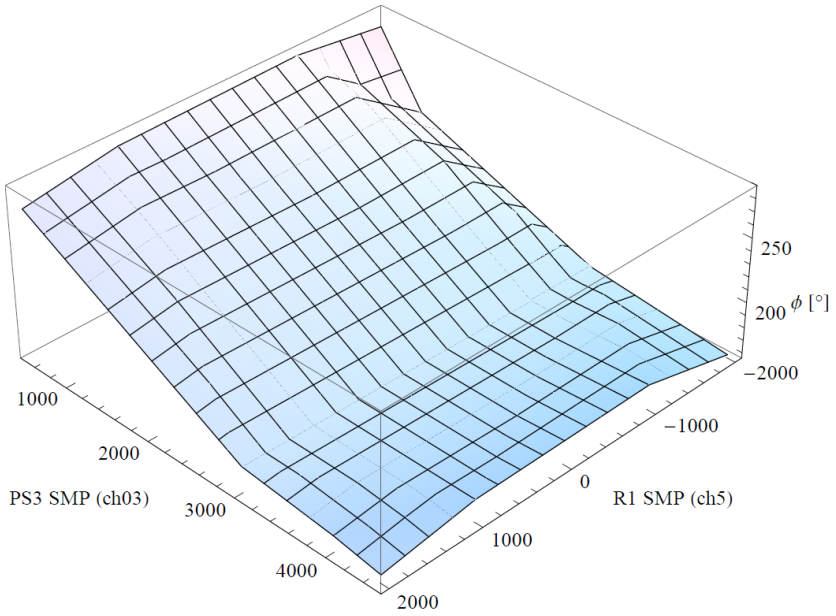


Figure 7.5: *Phase $\phi$ [°] versus step motor positions of waveguide reflector 1 and waveguide phase shifter 3 (17 points of measurement).*

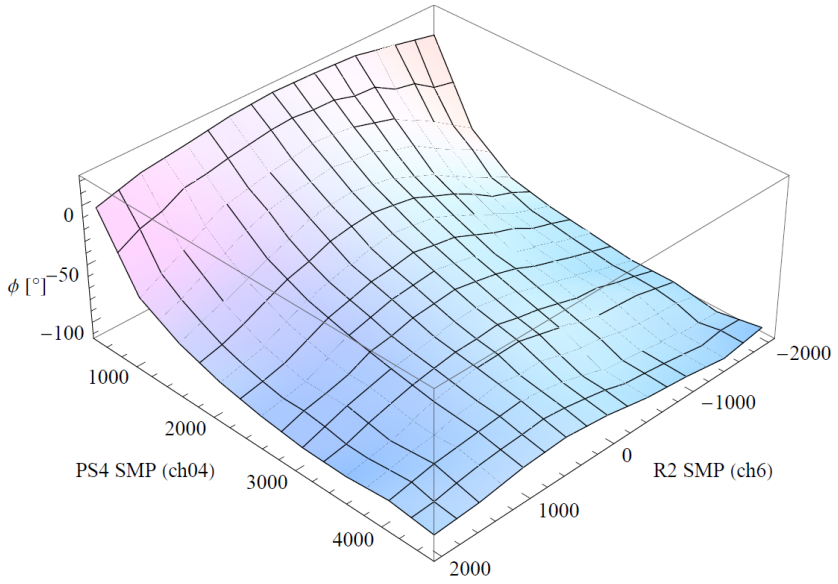


Figure 7.6: *Phase $\phi$ [°] versus step motor positions of waveguide reflector 2 and waveguide phase shifter 4 (81 points of measurement).*

## 7.3 Possible $Q_L$ Range at STF

As shown in the previous section 7.2 the $Q_L$ value of the superconducting cavities can be adjusted by using the respective waveguide phase shifter and/or waveguide reflector. More detailed information about the functionality of the waveguide reflector can be found elsewhere [41]. In the presented measurement the step motor position range of the waveguide reflectors has been limited between -2001 and 2001. For a new measurement presented in the following, this limit was extended to values in a range between -5001 and 5001, which covers the maximal range possible. This time the waveguide phase shifter was not altered and was kept at the default position. Figure 7.7 shows the $Q_L$ value versus the waveguide reflector 1 step motor position. With this measurement it could be shown that $Q_L$ values larger than $5 \cdot 10^7$ can be achieved.

Figure 7.8 shows the phase $\phi$ versus the waveguide reflector 1 step motor position. The phase changes about 90° over the scan.

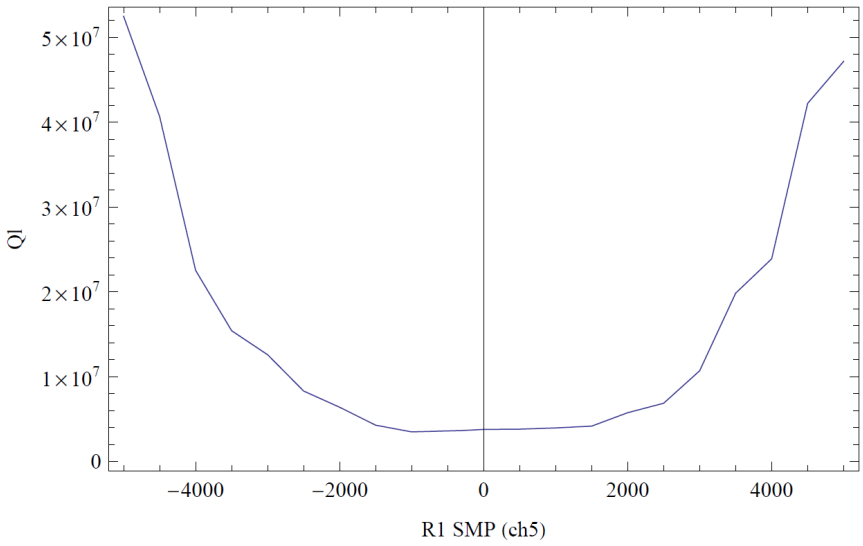


Figure 7.7: *$Q_{L,cav1}$ versus step motor positions of waveguide reflector 1.*

With this the possible range of the loaded quality factor range was characterized. Furthermore it was found out that the waveguide reflector had an influence on the cavity phase. In the configuration of the DRFS system in the scope of the QB project, this influence can be compensated using waveguide phase shifters.

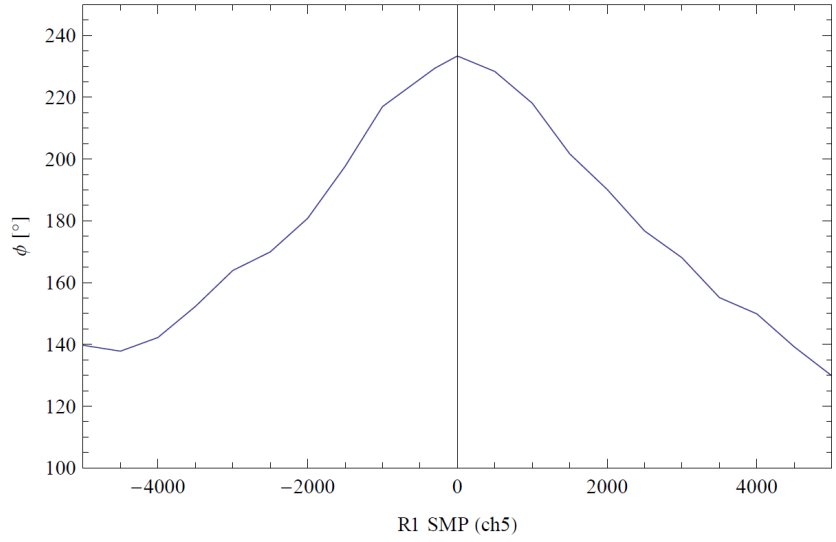


Figure 7.8: *Phase $\phi$ [°] versus step motor positions of waveguide reflector 1.*

## 7.4 Long–time High $Q_L$ Operation

For the demonstration of high $Q_L$ operation, the $Q_L$ values of both cavities were set to $2 \cdot 10^7$ using the waveguide reflectors. Because of the increased $Q_L$ values, the filling time was extended to 800 $\mu$s. Both cavity gradients were set to 20 MV/m. In an 60 minutes long–time run with a beam of an average current of 6.1 mA with a pulse length of 615 $\mu$s and beam compensation and feedback (FB) turned on, amplitude and phase stabilities were achieved as listed in Table 7.2. Figure 7.9 shows a snapshot of the vector–sum gradient. A run of 20 minutes at the same condition without beam was also performed. The corresponding stabilities are also listed in Table 7.2.

Table 7.2: Best snapshot vector–sum amplitude and phase stabilities under high $Q_L$ operation (rms values)

| Beam | 6.1 mA | Off |
|---|---|---|
| $\Delta$A/A Cavity 1 | 0.12% | 0.03% |
| $\Delta$A/A Cavity 2 | 0.16% | 0.03% |
| $\Delta$A/A Vector sum | 0.011% | 0.008% |
| $\Delta\phi$ Cavity 1 | 0.03° | 0.03° |
| $\Delta\phi$ Cavity 2 | 0.03° | 0.03° |
| $\Delta\phi$ Vector sum | 0.015° | 0.014° |

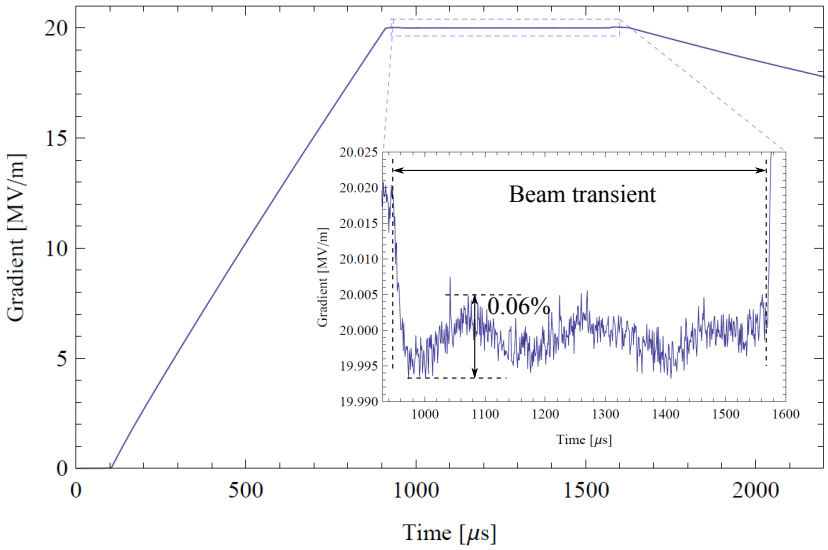


Figure 7.9: Vector–sum gradient [MV/m] versus time [s] during high $Q_L$ operation.

The measured $Q_L$ values of both cavities during beam operation, which were determined by the evaluation of the cavity gradient decays (refer Appendix B), were on average $Q_{L,Cav1} = 21 \cdot 10^6$ and $Q_{L,Cav2} = 22 \cdot 10^6$. Figure 7.10 a) shows the detuning for both cavities during the 60 minutes time span. The corresponding histograms are shown in Figure 7.10 b). The standard deviations are $\sigma_{\Delta f,\mathrm{Cav1}} = 10.1$ Hz and $\sigma_{\Delta f,\mathrm{Cav2}} = 4.7$ Hz. These values are comparable with values at other facilities, e.g. of up to 7 Hz measured at DESY FLASH [29]. The average detuning smaller than the cavity bandwidths allowed the successful demonstration of very stable high $Q_L$ operation of both cavities at STF, with stabilities comparable to nominal operation. With this the ILC requirements regarding high loaded Q operation were fulfilled.

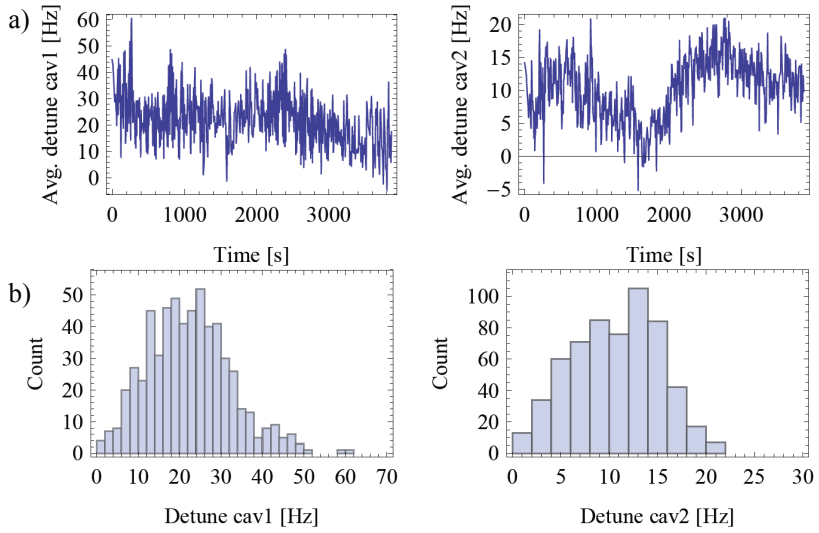


Figure 7.10: a) Detuning [Hz] of cavity 1 (left) and cavity 2 (right) versus time [s] as well as b) detuning histogram for cavity 1 (left) and cavity 2 (right) during high $Q_L$ operation.

# Chapter 8

# Klystron Linearization

In this chapter the development and test of three different predistortion–type FPGA–based klystron linearization algorithms at FNAL NML are described [42]. Furthermore the reimplementation of a klystron linearization at DESY in the scope of the uTCA.4 standard is covered. Beside this the development of an FPGA–based klystron and cavity simulator at KEK is described. This work was performed in the scope of this dissertation.

## 8.1 Klystron Linearization in General

### 8.1.1 Motivation for Klystron Linearization

Klystrons are commonly used for the HLRF generation for driving cavities in particle accelerators. It is planned to adopt the same technology also at ILC. At ILC the klystrons will be one part in the chain of the LLRF control loop. Typically the input to output characteristics of a klystron in both amplitude and phase are not linear, as illustrated in Figure 8.1. Since the feedback gain is proportional to the slope of the amplitude, it becomes very small this region, typically $< \frac{1}{10}$ of the feedback gain in the linear region. In order to keep the feedback effective, it is required to keep the amplitude slope constant and the phase rotation at $0^\circ$ until the point of saturation. This can be accomplished only by a klystron linearization.

Until now analog klystron linearizations were not adopted at accelerators using klystrons. This is due to the fact that it is difficult to apply both amplitude and phase linearizations in an analog realization. Typically such a realization is feedback–based, similar to an operational amplifier regulation. In case of accelerators this is not suitable due to the long feedback delay time, especially in case of pulsed operation and sudden changes such

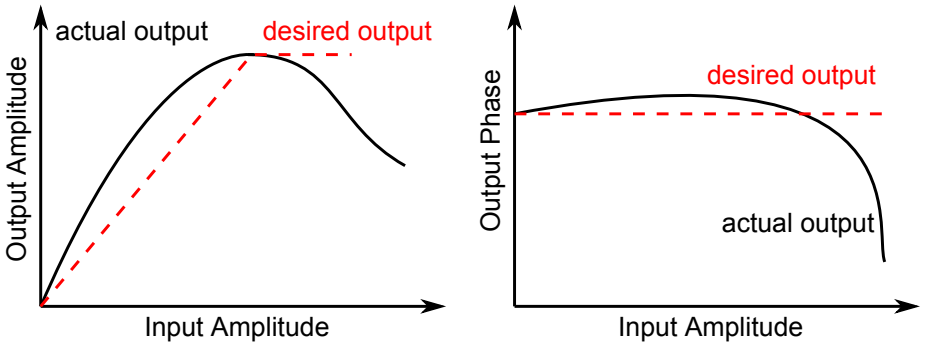


Figure 8.1: Schematic of the klystron amplitude and phase output characteristics. Typical (black) and desired (red) klystron amplitude output on the left side and typical (black) and desired (red) klystron phase output on the right side

as e.g. beam loading, which requires compensation. Nowadays the implementation of klystron linearizations became possible due to large sized Field Programmable Gate Arrays (FPGAs), on which real time processing can be performed. Digital signal processors (DSPs) or former small sized FPGAs were not sufficient. In the FPGA-based solution not a feedback but feedforward–type correction is used. At the so far typical operation point of klystrons about 60% of their maximal power is outputted. The advantage of the linearization is that klystrons can be operated at about 90% of the maximal output power. In order to operate the klystrons at ILC most cost effectively it is intended to operate them within an power overhead of 7% until the point of saturation. This is an improvement of 1.55 times in power, which means that this technique is beneficial for power saving. Furthermore in case of the implementation of FPGA–based klystron linearizations no changes to the already existing hardware have to be made. Such klystron linearization techniques are not only suitable for ILC but also can be applied at all accelerators using klystrons. With this the development of klystron linearization algorithms is a contribution to the whole worldwide accelerator society.

### 8.1.2 Types of Klystron Linearization

The most common types of linearizations are feedforward, feedback, and predistortion.

Linearizations based on feedforward usually are quite complex. They have to be integrated into the system and cannot be added as a simple element of

e.g. the feedback loop.

The type of linearization described in the following is a predistortion linearization placed in the firmware of the FPGA, on which beside others the controller is realized. The predistortion is the inverse of the non-linear characteristics of the klystron. Such concepts were already implemented in the past by using e.g. analog circuits. The capabilities of FPGAs, which were improved over the recent years, now allow not only the implementation of digital LLRF feedback controllers but also the implementation of klystron linearization algorithms with high effectiveness and flexibility.

## 8.2 Lookup Table–based Klystron Linearization at DESY

At DESY a klystron linearization based on a direct lookup table algorithm was implemented on the VME hardware at FLASH (refer to [38]). In the present the VME hardware is obsolete since it was replaced by the MTCA.4–based hardware. The target of the studies in scope of this dissertation was to implement a similar lookup table based klystron linearization algorithm conform to the requirements of the new MTCA.4 hardware standard. A further goal was the improvement of the lookup table creation script .

### 8.2.1 Principle of Lookup Table–based Klystron Linearization

A schematic of the developed direct lookup table–based klystron linearization package is shown in Figure 8.2. The 18 bit I and Q signals outputted by the controller are the input of the klystron linearization algorithm. From those using two multipliers and their squared values are calculated. By adding both products the squared amplitude of the IQ input signal is computed. The highest 12 bit of the squared amplitude are used as an address vector, which is sent to two lookup tables with a 12 bit address range and 18 bit words each. The correction values, which originate from the lookup tables, are multiplied to the input I and Q values corresponding to a multiplication of complex numbers. In order to realize this four multipliers, one adder, and one subtractor is used.

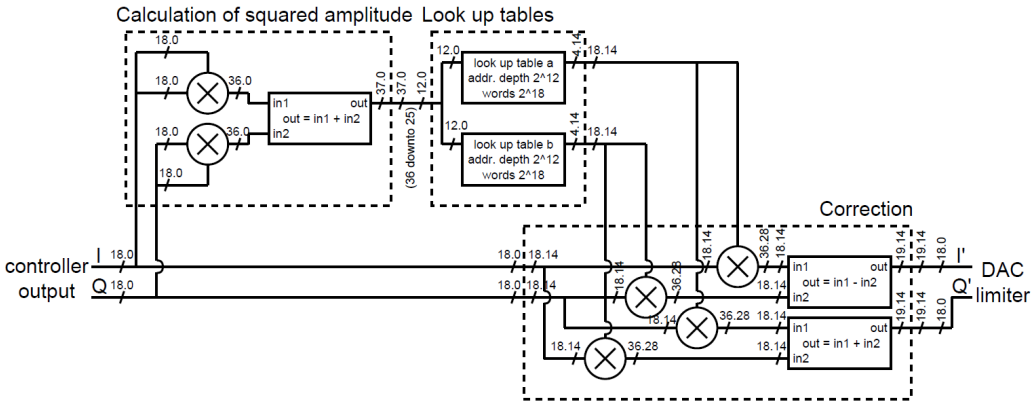


Figure 8.2: *Klystron linearization algorithm developed for the usage on MTCA.4 board at DESY. From the input I and Q values the squared amplitude is computed. It is truncated and used as the address for two lookup tables for the generation of I and Q correction factors, which are applied by a complex multiplication to the input I and Q values.*

The firmware creation tool set covered the following software:

- Notepad ++ 5.9.4
- ISE Design Suite 14.4
- ISim

In Notepad ++ the VHDL files of the klystron linearization package were coded manually. Furthermore a VHDL test bench was created in order to test the programmed algorithm. In ISE a klystron linearization project including the linearization package and the test bench was created and compiled. By this bugs in the code were straightened out. After the code was finalized and complied, a simulation in ISim was performed.

### 8.2.2 LUT Calculation Script

In order to create the content of the lookup tables, a Matlab script was written. The lookup table creation consists of three steps. The first two steps follows the same principle the first two steps discussed in section 8.3.2. In the third step from the calculated correction values for I and Q lists of 12 bit length are generated. Thereby the I and Q correction values are distributed not linear but following a squared function, reflecting that as the lookup address the squared amplitude is used.

### 8.2.3 ISim Simulation

In order to demonstrate the functionality of the algorithm implemented an iSim simulation was performed. Figure 8.3 shows a screen shot of the observed signals.

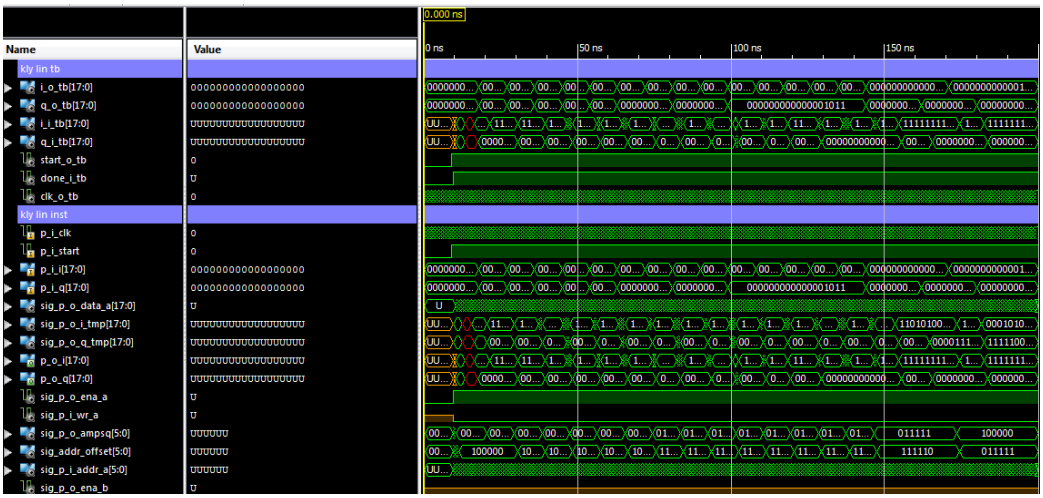


Figure 8.3: *iSim simulation of the LUT–based klystron linearization algorithm.*

The input to the linearization algorithm defined on the test bench reflected a klystron characteristic previously recorded. The outcome of the simulation with and without the klystron linearization algorithm active in terms of amplitude and phase is shown in Figure 8.4. In case of the amplitude the linearization works well. On case of the phase, slight fluctuations can be observed a high input amplitudes. It is assumed that this originates from rounding errors during the computation of the lookup table addresses. By this simulation the functionality of the created klystron linearization package was demonstrated.

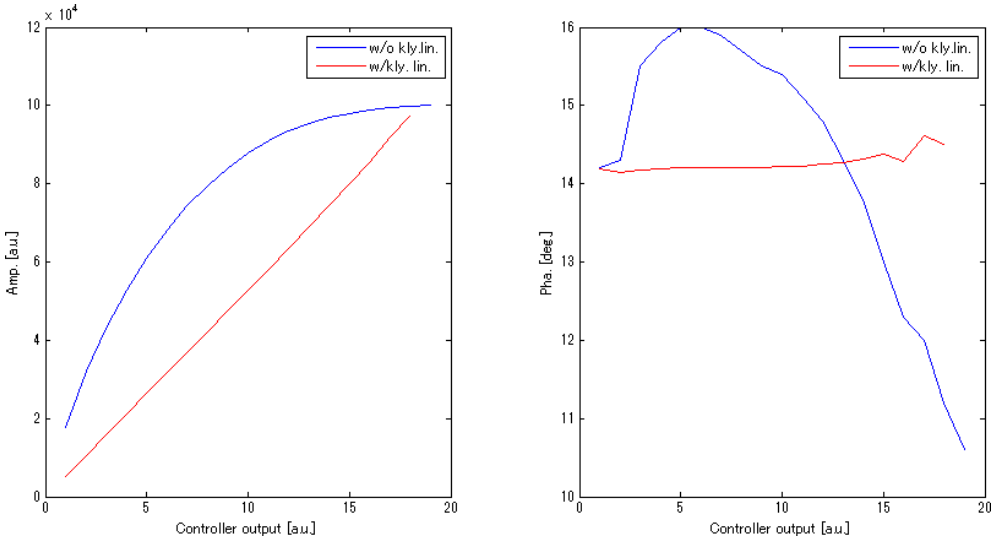


Figure 8.4: *Plots of result of iSim simulation without the klystron linearization (blue) and with linearization (red). Left: Klystron linearization output amplitude [a.u.] versus simulated controller output amplitude [a.u.]. Right: Klystron linearization output phase [°] versus simulated controller output amplitude [a.u.].*

### 8.2.4 Test on uADC Board

Due to the limitation in time the integration and test of the algorithm on the uTCA controller board (uTC) was not possible. Instead of this the algorithm was programmed on a uTCA analog to digital converter board (uADC). Due to a lack of a signal source the input I and Q values of the linearization were hard coded. Signals of the algorithm on the board were observed in real time by using ChipScope. The output signals were consistent with the iSim simulation. By this is it was demonstrated that the linearization algorithm implementation on the uTCA.4 hardware was successful. The next step would be to test the implemented algorithm on the uTC board and then in combination with an actual klystron.

## 8.3 Klystron Linearization Algorithm Developments at FNAL

### 8.3.1 Third Order Polynomial–based Klystron Linearization

#### Principle of Third Order Polynomial–based Klystron Linearization

In the scope of this dissertation a new kind of klystron linearization algorithm was developed, implemented, and tested at FNAL ASTA. The requirement for this algorithm was the linearization of only the amplitude. Depending on the operation range around the working point as well as the used klystron this may be sufficient. In Figure 8.5 a schematic of the algorithm is shown. It is based on a real–time computation of a correction factor on the FPGA. To this end the amplitude $A$ of the input signals $I_{in}$ and $Q_{in}$ is computed. In dependency on the amplitude $A$ the correction factor $f_{corr}$ is computed by a third order polynomial function. In a next step the correction factor $f_{corr}$ is multiplied with the amplitude $A$ and compared to the preset *limit*. If it exceeds the limit, the correction factor $f_{corr}$ is replaced by the ratio $limit/A$. The $I_{in}$ and $Q_{in}$ values are scaled by the correction factor $f_{corr}$. By two switches the corrected or the original I and Q values can be choses as output signals $I_{out}$ and $Q_{out}$.

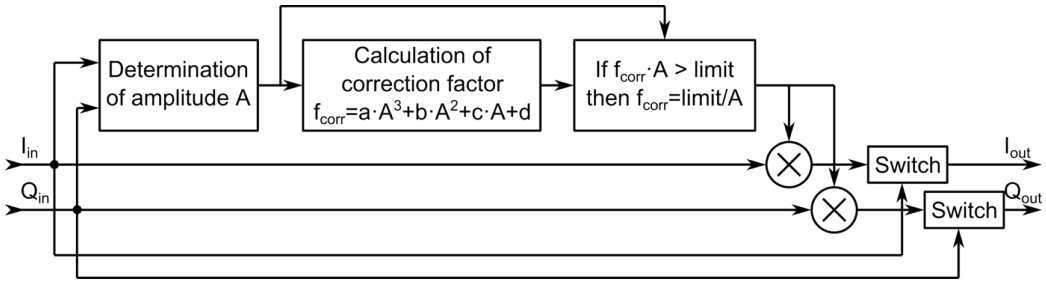


Figure 8.5: *Schematic of third order polynomial–based klystron linearization algorithm. From the input I and Q values the amplitude is calculated. Based on it using a 3rd order polynomial function $f_{corr}$ a correction factor is computed, which is, after an amplitude limit algorithm, applied to the input I and Q values.*

This method has the advantage to require less memory resources on the FPGA compared to a lookup table solution, since no lookup tables are used. This results also in a very resource–saving way of configuration. Instead of

large arrays only four parameters for the polynomial function plus the limit have to be stored in the memory. A further advantage is that at the same time an amplitude limiter is included, which provides additional safety in respect to machine protection.

Figure 8.6 shows the estimated klystron output in a linearized case for a 2nd, a 3rd, and a 4th order polynomial function. Table 8.1 lists the standard deviation of the difference between the three functions and the linear function. This shows that a higher order function provides a better agreement with the desired linear function. Nevertheless using the 3rd order polynomial function is a good compromise between precision and required hardware resources (FPGA hardware multipliers).

Table 8.1: Estimated of error using lower order fits.

| | |
|---|---|
| $\Delta$ (lin - 4th order) | 0.257 |
| $\Delta$ (lin - 3th order) | 0.667 |
| $\Delta$ (lin - 2th order) | 0.860 |

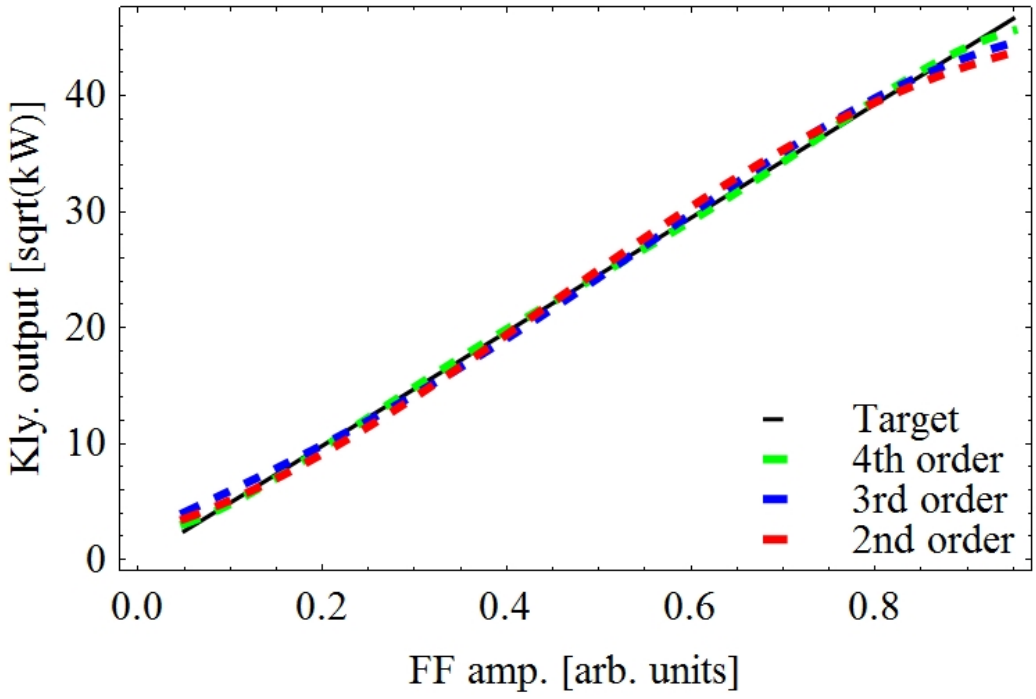


Figure 8.6: *Linear function (black) and estimated klystron output using 4th (green), 3rd (blue), and 2nd order (red) linearization functions.*

The tools used for the manipulation and creation of the FPGA firmware were:

- Matlab 2012b
- Simulink 2012b
- DSP Builder 13.0
- ModelSim
- Quartus II 13.0

### Parameter Calculation Script

In the following the functionality of the parameter calculation script for the 3rd order polynomial function–based klystron linearization is explained. In Figure 8.7 the schematic of the klystron linearization and the klystron is shown. The output amplitude of the klystron linearization $A_{out}$ is a function of the input amplitude $A_{in}$ and can be written as:

$$\begin{aligned} A_{out}(A_{in}) &= A_{in}(aA_{in}^3 + bA_{in}^2 + cA_{in} + d) \\ &= aA_{in}^4 + bA_{in}^3 + cA_{in}^2 + dA_{in} \quad . \end{aligned} \tag{8.1}$$

The square root of the klystron output $P_{sqrt}$ is a function of the klystron linearization output amplitude $A_{out}(A_{in})$ and can be written as:

$$\begin{aligned} P_{sqrt}(A_{out}) &= P_{sqrt}(A_{out}(A_{in})) \\ &= P_{sqrt}(aA_{in}^4 + bA_{in}^3 + cA_{in}^2 + dA_{in}) \quad . \end{aligned} \tag{8.2}$$

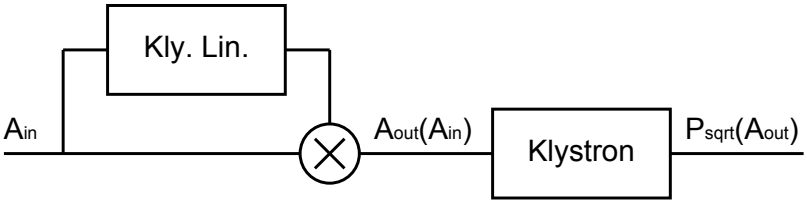


Figure 8.7: *Schematic of the combination of a klystron linearization and a klystron. The input amplitude of the linearization algorithm is $A_{in}$. Its output amplitude, which is the input amplitude of the klystron, is $A_{out}(A_{in})$. The output amplitude of the klystron is $P_{sqrt}(A_{out})$.*

The function $P_{sqrt}$ is determined by a FF amplitude scan without the klystron linearization. In this case

$$P_{sqrt}(A_{out}) = P_{sqrt}(A_{in}) \quad . \tag{8.3}$$

An example of such a FF amplitude scan is shown in Figure 8.8 as red dots. In order to estimate $P_{sqrt}(A_{in})$ a 3rd order polynomial fit is performed on the recorded data. This yields for the shown example:

$$P_{sqrt}(A_{in}) = 67.4 \cdot A_{in}^3 - 168.7 \cdot A_{in}^2 + 147.9 \cdot A_{in} + 0.97 \quad . \tag{8.4}$$

This function is shown in Figure 8.8 as a blue line. From the recorded data also the desired linear klystron output can be found out. It is a linear function through the origin and the point of saturation. In the case of the example it is:

$$f_{lin} = 49.1 \cdot A_{in} \quad . \tag{8.5}$$

This function is represented in Figure 8.8 as blue dots. In order to find out the linearization parameters a, b, c, and d the following equation can be used:

$$P_{sqrt}(aA_{in}^4 + bA_{in}^3 + cA_{in}^2 + dA_{in}) = 49.1A_{in} \quad , \tag{8.6}$$

with $P_{sqrt}$ as estimated in equation (8.4). Using a fit algorithm on this function, e.g. the 'FindFit' function in Mathematica, delivers the following linearization parameters:

Table 8.2: Estimated linearization parameters.

| Parameter | Value |
|---|---|
| a | 1.91 |
| b | -2.38 |
| c | 1.19 |
| d | 0.16 |

The result of inserting those parameters in equation (8.2) with $P_{sqrt}$ as estimated in equation (8.4) is shown in Figure 8.8 in green. The deviation from the desired function is very small over the whole range of the FF amplitude.

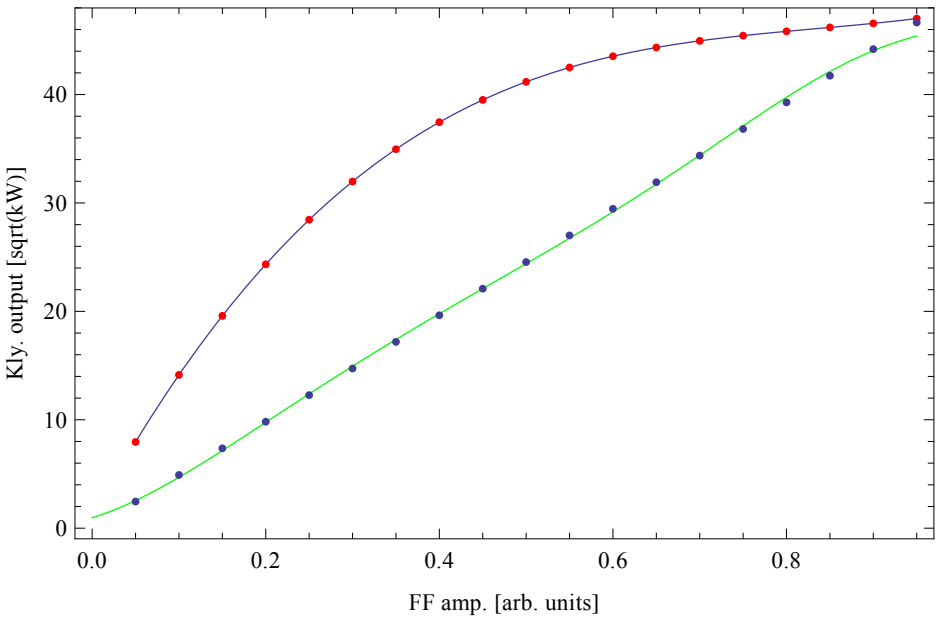


Figure 8.8: *Klystron output [sqrt(kW)] versus FF amplitude for recorded klystron output (red dots), fit to klystron output (blue line), target klystron output (blue dots), and klystron output with estimated linearization parameters (green line).*

### Simulink Implementation

In Simulink with the the DSP Builder plug–in the klystron linearization algorithm was implemented. Figure 8.9 shown a respective screen shot of the working area of Simulink. The input ports of the algorithm are in_I and in_Q, which are the output signals of the controller block, as well as Klys_Lin_Par_A, Klys_Lin_Par_B, Klys_Lin_Par_C, Klys_Lin_Par_D, and Klys_Lin_Par_L, which are configuration parameters for the algorithm. The input I and Q signals are squared using two multipliers. The results are summed up by an adder. From the sum the square root is calculated by an corresponding block. This way the amplitude of the IQ signal is computed. In a next step the signal format is changed from 18 bit unsigned to signed fractional signal [4 : 14]. This is also done for all configuration parameters. From the amplitude signal the squared value and the cubed values are calculated using a cascade of multipliers. The cubed amplitude signal is multiplied by the configuration parameter A, the squared amplitude signal is multiplied by the configuration parameters B, and the amplitude signal is multiplied by

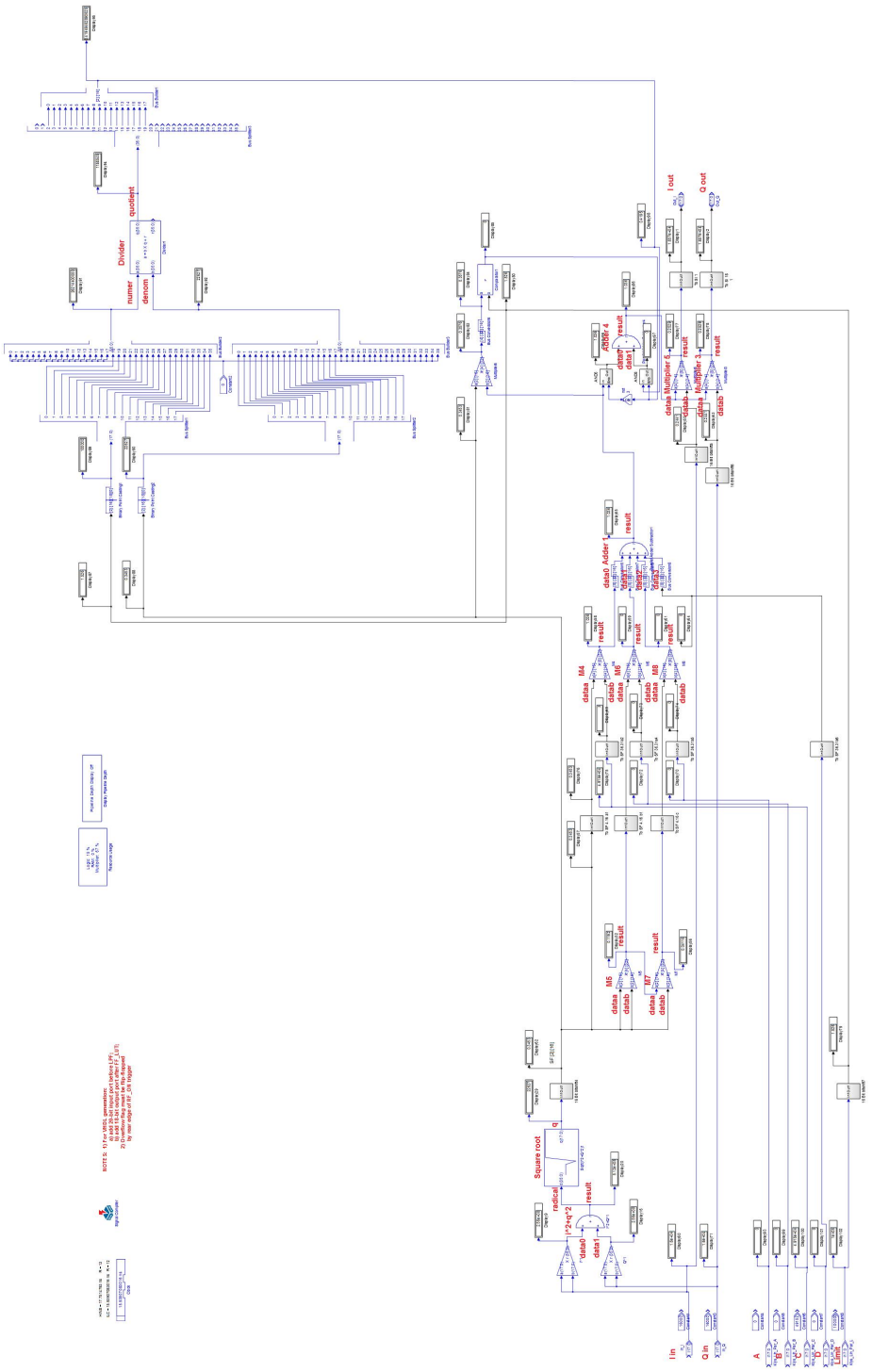


Figure 8.9: *Simulink model of the klystron linearization algorithm showing the channels observed in ModelSim in red.*

the configuration parameter C. The sum of all these products plus the configuration parameter D is computed using a four channel adder. The by this created correction factor is multiplied with the original amplitude of the IQ input. The product is compared to a limit value, which is defined by the configuration parameter L. Is the product smaller than the limit, it is multiplied with the I and Q input values, which are also converted to a signed fractional [4 : 14] using two multipliers. Is the product larger or equal the limit, the I and Q input values are multiplied by the limit value divided by their amplitude divided. By this the output amplitude of the I and Q values is limited. Before the I and Q signals are sent to the corresponding output ports, they are converted from singed fractional [4 : 14] to signed 18 bit signals.

Beside the implementation also the simulation capabilities of Simulink were used in order to test and confirm the functionality of the linearization algorithm. This validation was performed only for varies points of interest as for example at full scale input in order to make sure no signal saturation occurs.

After sufficient testing the function Signal Compiler, which is part of the DSP Builder plug–in, was used in order to create VHDL code based on the Simulink model.

Although the usage of DSP Builder within Simulink is a convenient and straight forward way for the VHDL code creation, which includes the possibility of easily testing the functionality of the algorithm created, it limits the control over the implementation. For example within DSP Builder it is not possible to select the kind of implementation of a multiplier. In the MegaWizzard Plug–In Manager within Quartus II between the implementations using hardware multipliers or logic elements can be chosen. A further disadvantage is that the VHDL code created is nearly impossible to read, since several hundred VHDL files are created. This makes a manually manipulation of the code impossible. A possibility for gaining more control is the fragmentation of the algorithm into parts created by DSP Builder, by the MegaWizzard Plug–In Manager, and by hand. The connection between those parts then is established in Quartus II.

### ModelSim Simulation

In Simulink only the functionality of the mathematical model of the algorithm can be validated. In order to test the functionality of the algorithm as an implementation on an FPGA as well as the functionality and quality of the VHDL code created by the Signal Compiler, a ModelSim simulation was performed. In this simulation it was found out, that the computation of the amplitude is done in 15 clocks, which covers 3 clocks for the multipliers and

the adder as well as 12 clocks for the square root (pipelined). The calculation and application of the correction factor requires 16 clocks. With this the algorithm takes 31 clocks to compute and apply the amplitude correction. This corresponds to a time of about 0.48 $\mu$s, since the FPGA clock is 65 MHz. Although the algorithm is quite slow it is sufficient in the case of superconducting cavities.

### Test in Development Environment

In order to test the functionality of the klystron linearization implementation several measurements have been performed within the development environment. Figure 8.10 shows the schematic of the LLRF setup of the development rack. The output of the cavity simulator on the MFC FPGA is up converted, amplified, attenuated, split in eight channels, and down converted. These signals are digitized on the MFC. The vector sum is computed and the controller, feedforward tables, and the klystron linearization are applied. The output is sent to the cavity simulator.

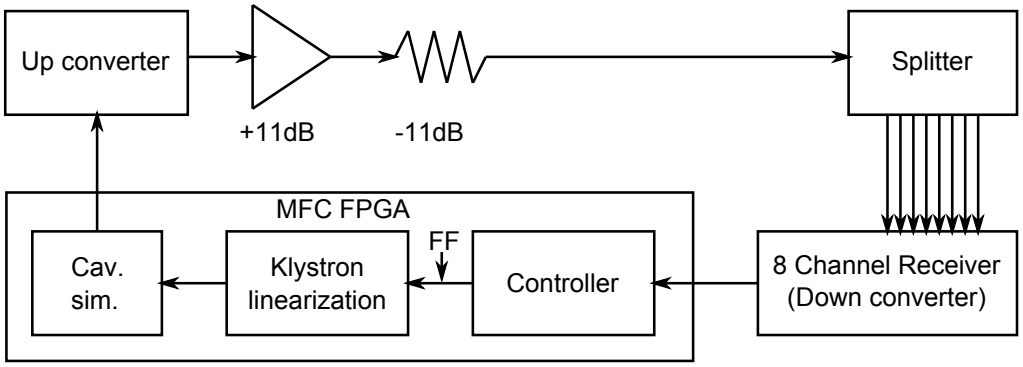


Figure 8.10: *Schematic of test rack at FNAL. The output of the cavity simulator on the MFC FPGA is up converted, amplified, attenuated, split in eight channels, and down converted. These signals are digitized on the MFC. The vector sum is computed and the controller, feedforward tables, and the klystron linearization are applied. The output is sent to the cavity simulator.*

Figure 8.11 shows a comparison of FF amplitude scans in the Simulink simulation and the measurement in the development rack. Both agree very well with each other, which indicates that the klystron linearization algorithm was implemented correctly on the FPGA.

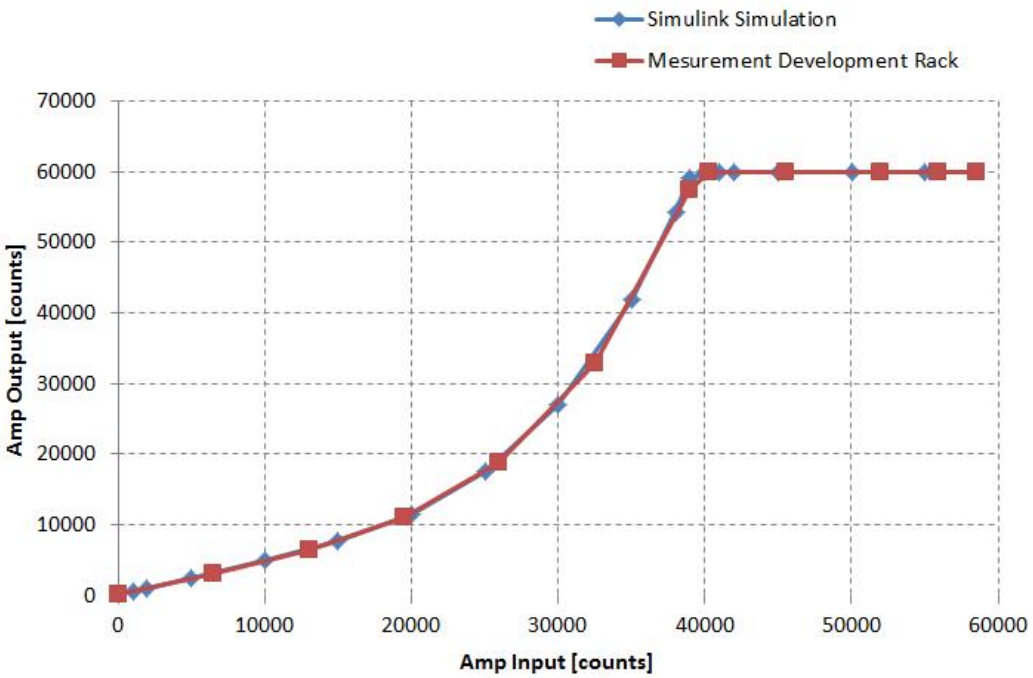


Figure 8.11: *Comparison of FF amplitude scan of Simulink simulation (blue) and measurement in the development rack (red).*

In the following the characterization of the circular limiter is described. To this end a 360° phase scan with increments of 20° was performed. Figure 8.12 shows the corresponding vector sum amplitude, phase, amplitude stability, and phase stability versus FF phase. It can be seen that the flattop amplitude has two major slopes, which means the limitation is of an slightly elliptical shape. Since the count variation is only 7 counts (or 0.06%) it is negligible. Also the phase shows some structure at every 90°. The amplitude and phase stabilities underlie a slight fluctuation but can be treated at constant.

These test results justified to proceed with a test of the algorithm at ASTA linearizing the actual klystron.

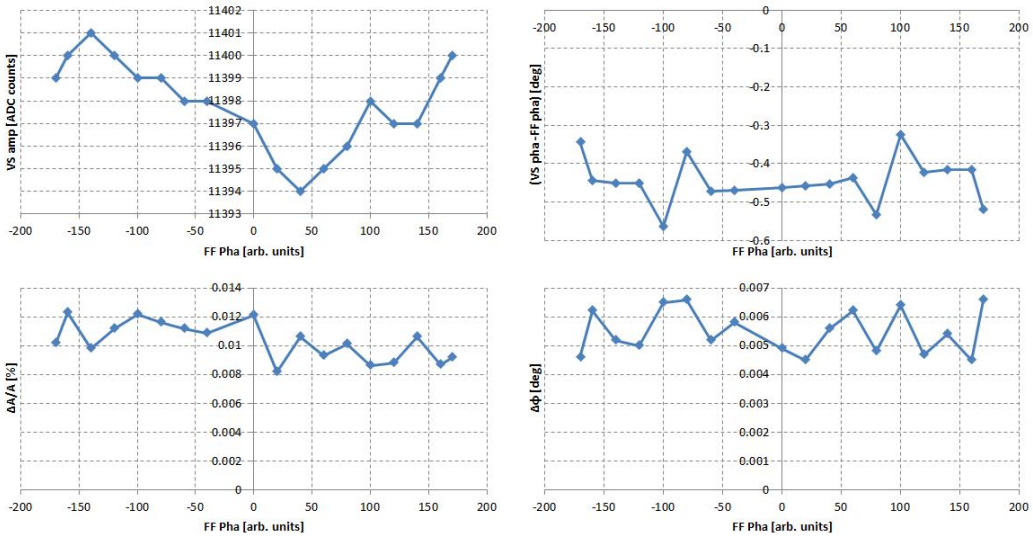


Figure 8.12: *Test results for the limiter functionality. Top left: Vector sum amplitude versus FF Phase [°], top right: vector sum phase versus FF Phase [°], bottom left: amplitude stability versus FF Phase [°], and bottom right: phase stability versus FF Phase [°].*

### Test at ASTA

In preparation of the test the firmware version including the klystron linearization algorithm was uploaded to the MFC FPGA at ASTA. Figure 8.13 shows the schematic and Figure 8.14 a picture of the setup for the evaluation of the klystron linearization algorithm. The 5 MW klystron for the cryomodule (8 cavities) was operated using the MFC card in FF only mode. The klystron output power was monitored on a power meter via a directional coupler. The klystron output was sent by a switch to a water load (not to the cavities). For further preparation 8 dB of attenuation was added to the RF drive in order to be able to use the whole FF amplitude range.

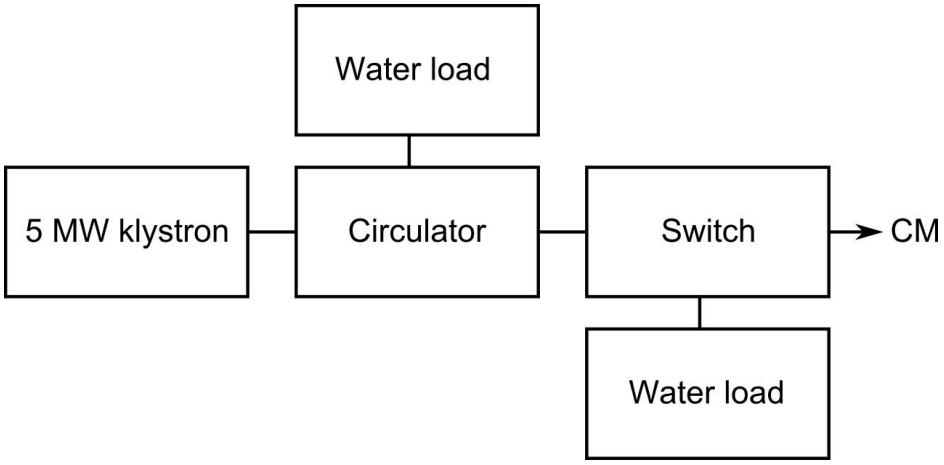


Figure 8.13: *Schematic of setup of klystron linearization measurement. The RF is generated by a 5 MW klystron, which is sent through a circulator and a switch to the water load.*

Figure 8.14: *Photo of setup of klystron linearization measurement. On the left side the klystron is located, in the middle the circulator, and on the right side the water load.*

As a first step the klystron input-output behavior was characterized. To this end a FF amplitude scan was performed while monitoring the klystron output power. Figure 8.15 shows the corresponding plot (in pink). Clearly a maximum can be seen, which marks the point of full saturation.

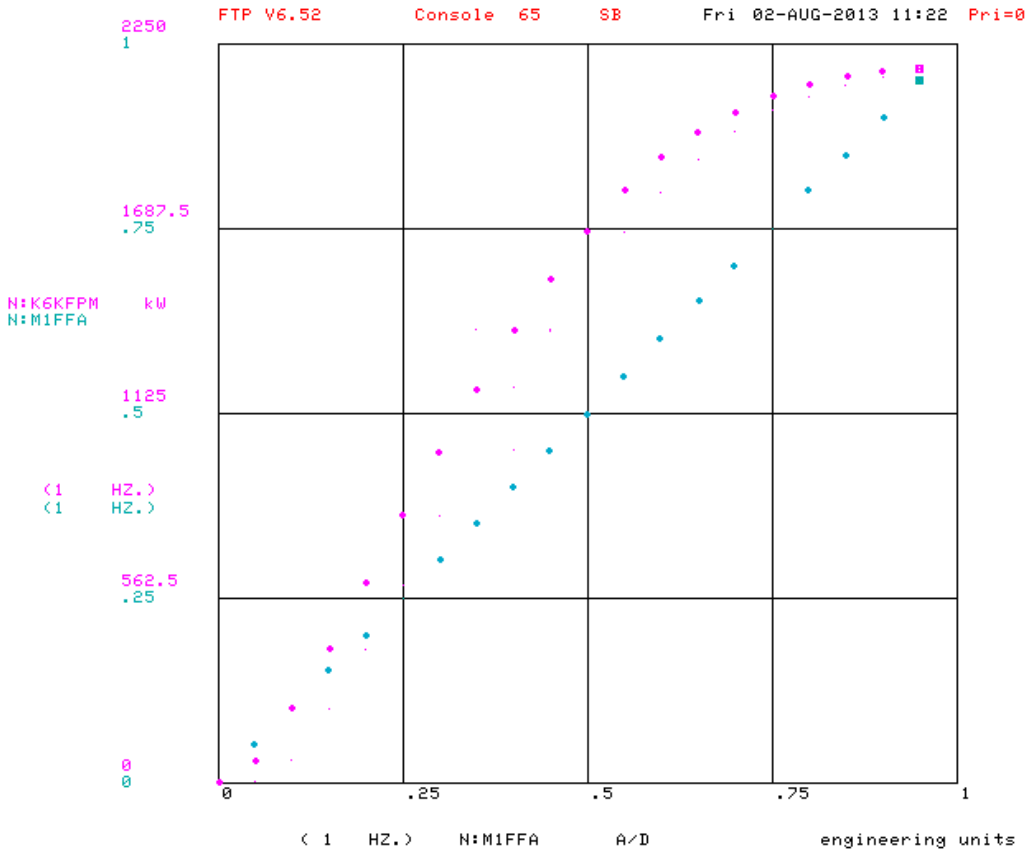


Figure 8.15: *Klystron output power [kW] (pink) and FF amplitude (blue) versus FF amplitude (8 dB attenuation on RF drive during klystron characterization).*

Based on this the linearization parameters have been estimated and set to the algorithm. In order to test the algorithm a new FF amplitude scan was performed. The result is shown in Figure 8.16 as blue dots. At a range below 0.4 of the FF amplitude slight bumps can be seen. Those agree with the expected output as shown in the same figure as a green line. Above an FF amplitude of 0.4 the klystron output is linear up to an FF amplitude of 0.95. Above a FF amplitude of 1 the limiter keeps the klystron amplitude constant. With this the successful realization and implementation of a

klystron algorithm on the MFC board at ASTA was demonstrated.

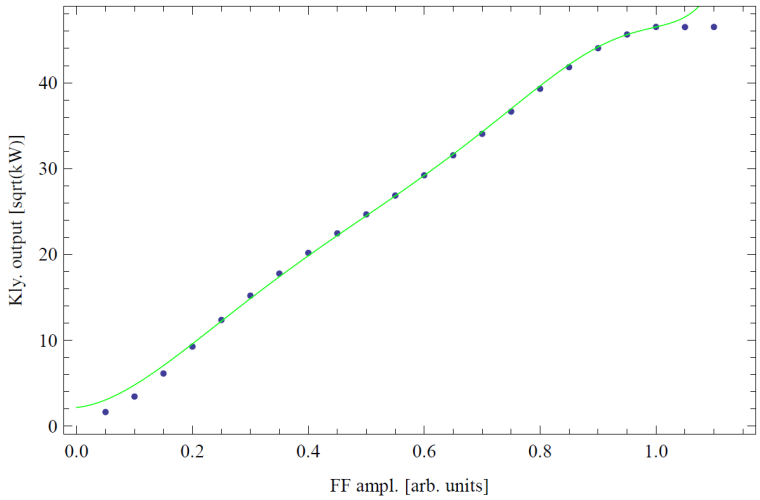


Figure 8.16: *Klystron output [sqrt(kW)] versus FF amplitude during final test of klystron linearization (blue) as well as simulated klystron output (green).*

### 8.3.2 Second Order Polynomial–based Klystron Linearization

#### Principle of Second Order Polynomial–based Klystron Linearization

Since the 3rd order polynomial function–based klystron linearization was designed for amplitude linearization only, the goal was to further develop this algorithm in the scope of this dissertation in order to add the support for phase linearization. The result was a klystron linearization algorithm based on the real time computation of a complex correction factor using two 2nd order polynomial functions. Figure 8.17 shows its schematic. From the input $I_{in}$ and $Q_{in}$ values the amplitude $A$ is calculated. It is then fed into the two 2nd order polynomial functions, which are realized by cascades of multipliers. For each polynomial function three parameters ($b$, $c$, $d$ and $f$, $g$, $h$) can be configured. These parameters are factors for the squared term, the linear term, and the offset. By the two polynomial functions matrix elements for a input amplitude dependent amplitude and phase correction matrix are calculated, as shown in equation (8.7).

$$\begin{pmatrix} I'(A,\phi) \\ Q'(A,\phi) \end{pmatrix} = \begin{pmatrix} f_{corr,i}(A^2) & -f_{corr,q}(A^2) \\ f_{corr,q}(A^2) & f_{corr,i}(A^2) \end{pmatrix} \begin{pmatrix} I(A,\phi) \\ Q(A,\phi) \end{pmatrix} \tag{8.7}$$

This matrix multiplication is realized by four multipliers and two adders. From the corrected I and Q values the amplitude $B$ is calculated and compared to a configurable limit. If the amplitude exceeds the limit the correction factor $f_{limit} = limit/B$ calculated. Otherwise the correction factor is set to 1. The I and Q values are scaled by $f_{limit}$, which is realized by two multipliers. By this the output amplitude of the algorithm can be limited, which is required for machine protection reasons. Instead of the I and Q output of the algorithm also the input I and Q values can be chosen as the output $I_{out}$ and $Q_{out}$, which sent to the upconverter package and then to the DAC. To this end switches for both I and Q values are implemented at the output of the algorithm. The switches are set by a single bit signal.

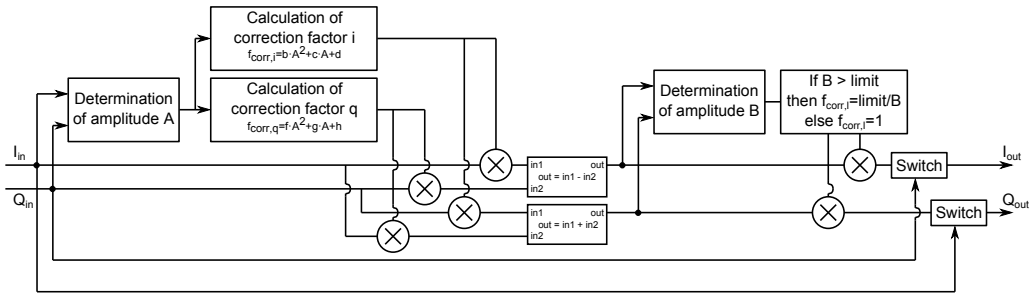


Figure 8.17: *Schematic of second order polynomial–based klystron linearization algorithm. Based on the amplitude of the input I and Q values I and Q correction factors a computed using two 2nd order polynomial functions. After the application of those to the input I and Q values, the output amplitude is limited.*

### Parameter Calculation Script

The calculation of the parameters for the 2nd order polynomial function–based klystron linearization algorithm is performed in three steps as described in the following. As a first step from the klystron characterization the function of the klystron output phase in dependency of the klystron output amplitude is estimated. At this point an interpolation between the nearest neighbors is sufficient. A plot of the data is shown in Figure 8.18.

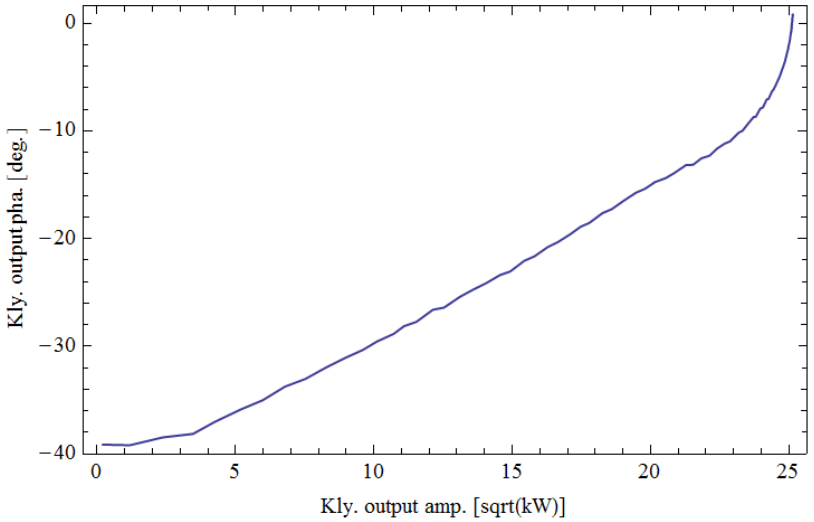


Figure 8.18: *Klystron output phase [°] versus klystron output amplitude [sqrt(kW)] during klystron characterization.*

In a second step the data of the linear target amplitude and phase are generated. Furthermore based on the linear target amplitude, the data of the expected klystron output phase is estimated. From this the expected klystron output is estimated in terms of I and Q values resulting in the complex list $z$. From the linear target function a complex list $z'$ list is generated. The complex correction list $\alpha$ is calculated by

$$\alpha = \frac{z'}{z} \ , \tag{8.8}$$

since $z' = \alpha \cdot z$, as shown in equation (8.7).

In the last step the I and Q values of $\alpha$ are fitted by second order polynomial functions. Figure 8.19 shows the I (blue) and Q (purple) values of the correction $\alpha$ and the corresponding fits by 2nd order polynomial functions (green) versus FF amplitude. The resulting parameters are listed in Table 8.3 as well as their conversion to the appropriate hexadecimal values, which were written to the memory of the FPGA in order to configure the algorithm.

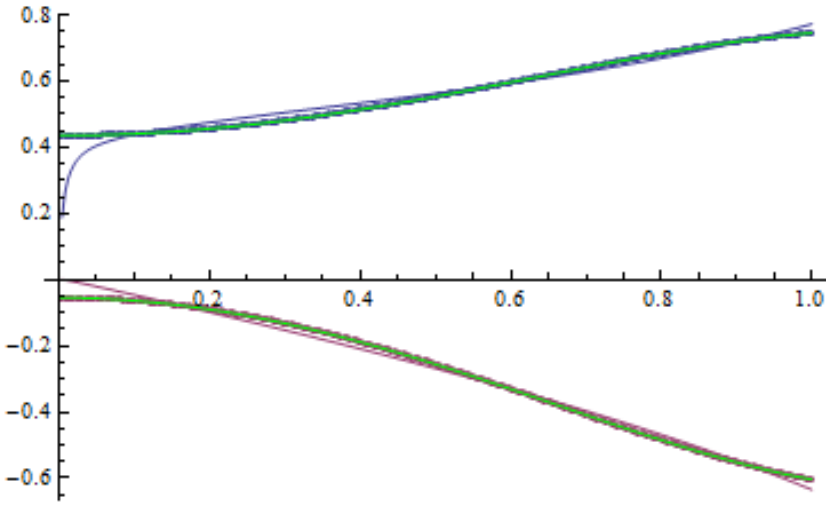


Figure 8.19: *I (blue) and Q (purple) values [a.u.] of the correction $\alpha$ and the corresponding fits by 2nd order polynomial functions (green) versus FF amplitude [a.u.].*

Table 8.3: Estimated parameters for the 2nd order polynomial function–based klystron linearization algorithm

| Parameter | value [dec] | value·$2^{14}$ [hex] |
|---|---|---|
| b | 0.1342 | 00898 |
| c | 0.2918 | 012AE |
| d | 0.3093 | 013CB |
| f | -0.2283 | FF163 |
| g | -0.4365 | FE410 |
| h | 0.0008 | 0000D |

### Test in Development Environment

In a first test in the development rack only a rudimentary check of functionality could be performed, since no nonlinear element was included in the control loop. Linearization parameters based on a previously characterized klystron were used in order to demonstrate that an amplitude and phase correction was possible by using the implemented algorithm. Figure 8.20 shows the amplitude (left) and phase (right) of the 8 cavity simulator versus the FF amplitude in an open loop operation. As expected in both amplitude and phase nonlinearities could be introduced.

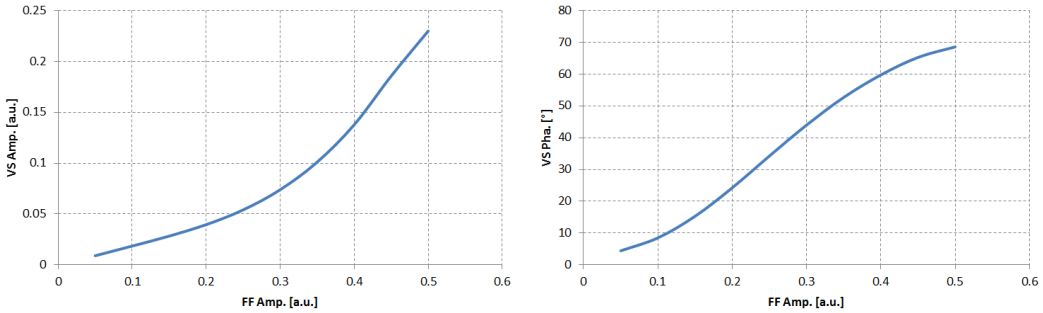


Figure 8.20: *VS amplitude [a.u.] (left) and VS phase [°] (right) of the 8 cavity simulator versus FF amplitude [a.u.] during a preliminary test of the 2nd order polynomial function–based klystron linearization algorithm.*

In order to establish a more realistic test environment, an active amplifier was added to the loop of the development rack. A schematic of the new test setup within the development rack with the modified part covering the added amplifier and attenuator is shown in Figure 8.21. The amplifiers were chosen so that the total gain was kept at 1.

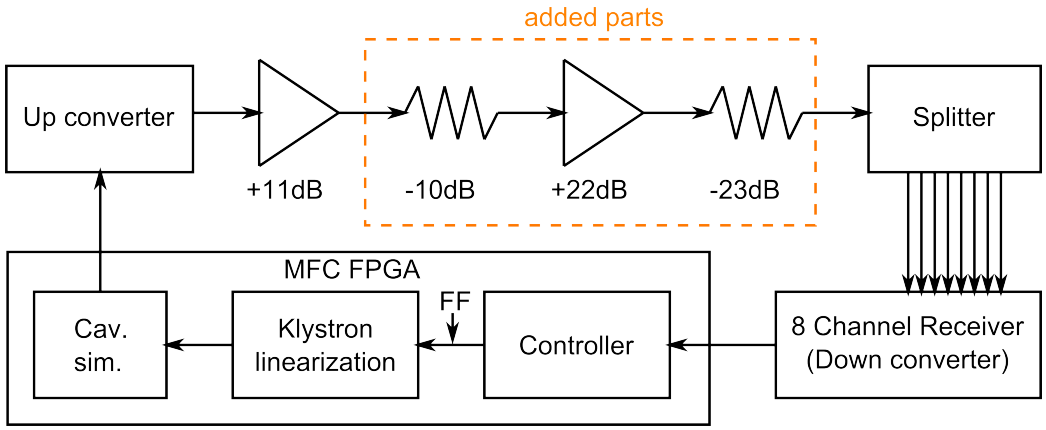


Figure 8.21: *Schematic of modified part of setup of the development rack covering the added amplifier. The output of the cavity simulator on the MFC FPGA is up converted and amplified. Another amplifier was included for the simulation of a klystron. Furthermore two more attenuators were included in order to keep the gain constant. The signal is split in eight channels, down converted, and digitized on the MFC. The vector sum is computed, the controller, feedforward table, and klystron linearization is applied.*

In the presented configuration it also was possible to drive the amplifier into saturation. Figure 8.22 shows its characteristics in terms of amplitude and phase recorded during a FF amplitude scan. The amplitude characteristic was very similar to the characteristic of a klystron. The phase characteristic on the other hand was quite different. The phase rotation over the evaluated region was with less than 1° quite small. Nevertheless it could be object to linearization.

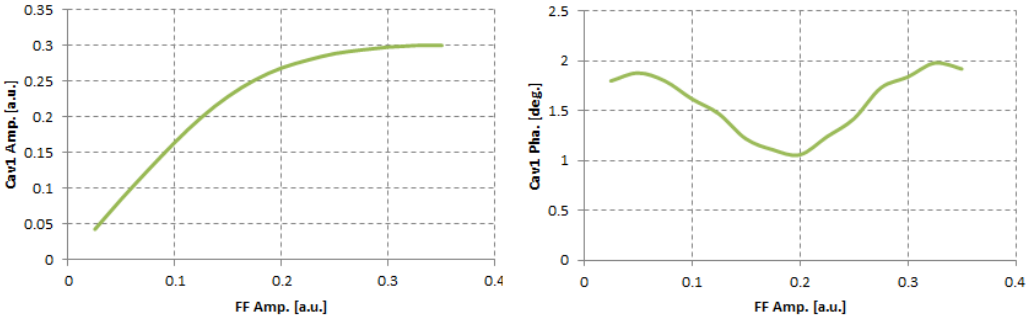


Figure 8.22: *Cavity 1 amplitude [a.u.] (left) and phase [°] (right) of the 8 cavity simulator versus FF amplitude [a.u.] during characterization of active amplifier.*

Due to time shortage the final version of the 2nd order polynomial function–based klystron linearization algorithm was only tested at ASTA as shown in section 8.3.2. A test of a preliminary 2nd order polynomial function–based klystron linearization algorithm is shown in Figure 8.23. It can be seen that the amplitude linearization worked for low FF amplitudes, but a compression behavior occurred already 32% below the point of saturation. Also in the case of the phase linearization seemed to be effective only for low FF amplitudes. About 50% below saturation a phase rotation occurred. Later it was found out, that there has been a bug in the parameter computation script.

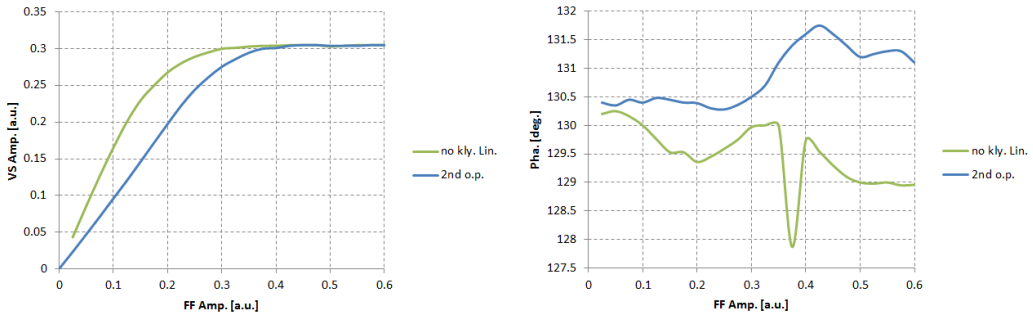


Figure 8.23: *Cavity 1 amplitude [a.u.] (left) and phase [°] (right) of the 8 cavity simulator versus FF amplitude [a.u.] during characterization of preliminary 2nd order polynomial function–based klystron linearization algorithm.*

### Test at ASTA

At the time of the test run the 5 MW klystron was connected to cavity 5 of the ILC RF unit, which contains eight superconducting TELSA-type 9-cell cavities in total. Figure 8.24 shows the schematic of the test setup. Since the test run was conducted during cavity conditioning, the administrative limit for the klystron output power was 800 kW. In order to drive the klystron into saturation at such a low output power, the attenuation on the RD drive was reduced to 2 dB. Furthermore the klystron gun voltage was reduced to -89.6 kV.

In preparation for the test of the klystron linearization algorithm a klystron characterization was conducted. To this end under open loop operation a FF amplitude scan over the whole range possible (from 0 to 1 [a.u.]) was performed. The klystron output characteristics in terms of amplitude, square root of the output power, and phase were recoded. These are shown in Figures 8.25 and 8.26. In amplitude a distinct saturation behavior can be observed. In phase also a nonlinear behavior was observed. It differs from a typical phase behavior of a klystron (refer to Figure 8.1), due to the reduced klystron gun voltage.

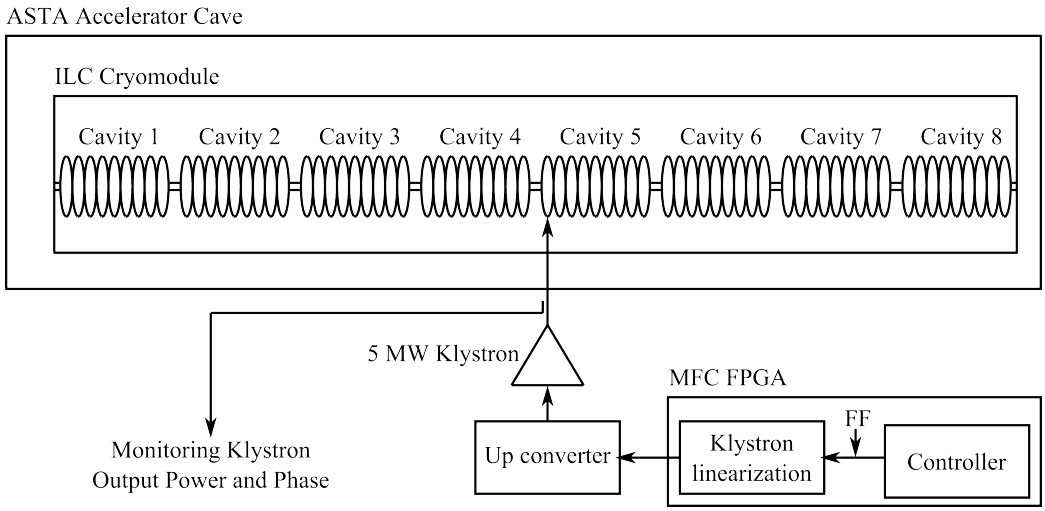


Figure 8.24: *Schematic of the test setup at ASTA. On the MFC a driving signal is generated using the feedforward table. It is processed by the klystron linearization algorithm. The output is up converted and sent to the 5 MW klystron, which drives cavity 5. The klystron output amplitude and phase are monitored.*

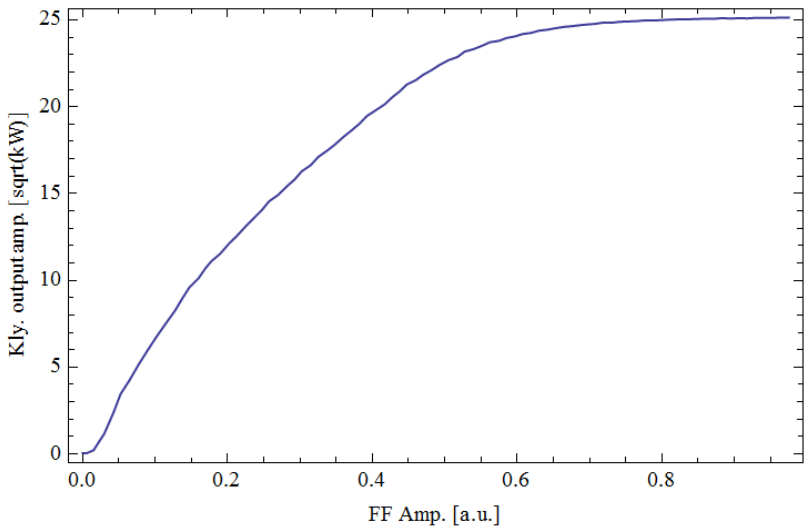


Figure 8.25: *Klystron output amplitude [sqrt(kW)] versus FF amplitude [a.u.] during klystron characterization.*

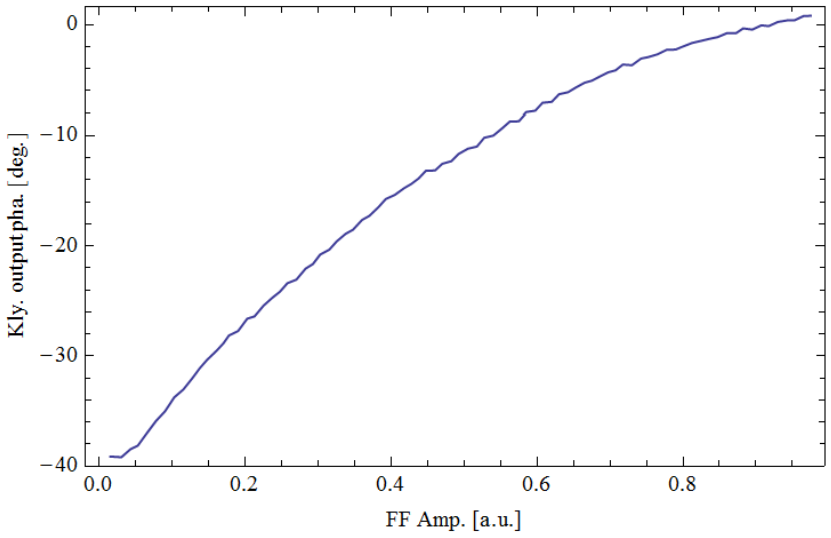


Figure 8.26: *Klystron output phase [°] versus FF amplitude [a.u.] during klystron characterization.*

From the recorded klystron characteristics the parameters for the klystron linearization algorithm were generated as described in section 8.3.2 and set. In order to test the functionality of the algorithm, it was activated and FF amplitude scan for the full range under open loop operation was performed. The result in terms of amplitude and phase is shown and compared to the klystron characteristics without linearization in Figures 8.27 and 8.28.

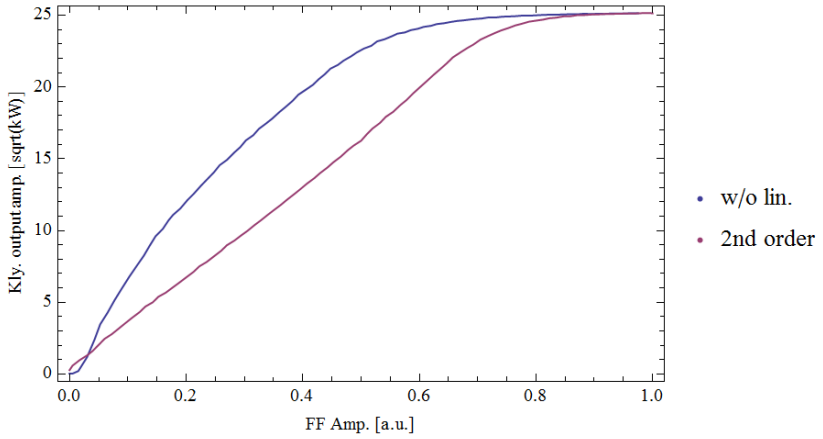


Figure 8.27: *Klystron output amplitude [sqrt(kW)] versus FF amplitude [a.u.]: without linearization (blue) and with 2nd order polynomial function–based linearization (purple).*

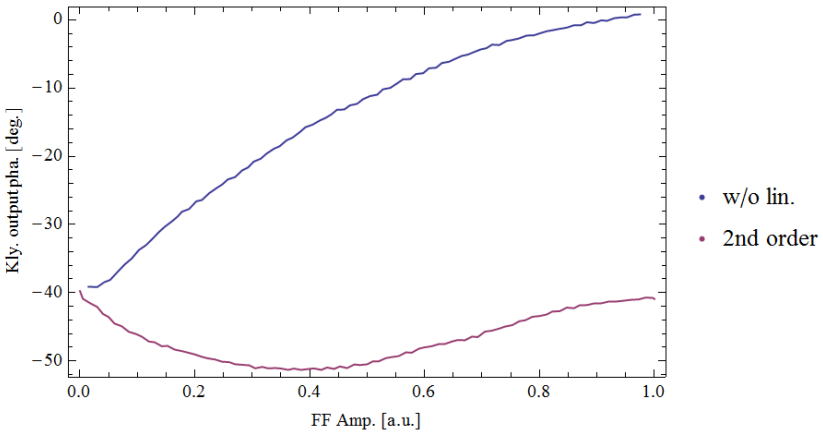


Figure 8.28: *Klystron output phase [°] versus FF amplitude [a.u.]: without linearization (blue) and with 2nd order polynomial function–based linearization (purple).*

In order to analyze the linearization performance the slope of the klystron output amplitude was computed. Figure 8.29 shows the corresponding plot. In case of the klystron output amplitude it can be seen that the slope is linear (including some fluctuations) below a FF amplitude of 0.66 a.u.. Above this value compression occurs. In case of the phase the total phase rotation over

the whole FF range was reduced from 40.17° to 11.56°. This proves that the linearization algorithm is effective.

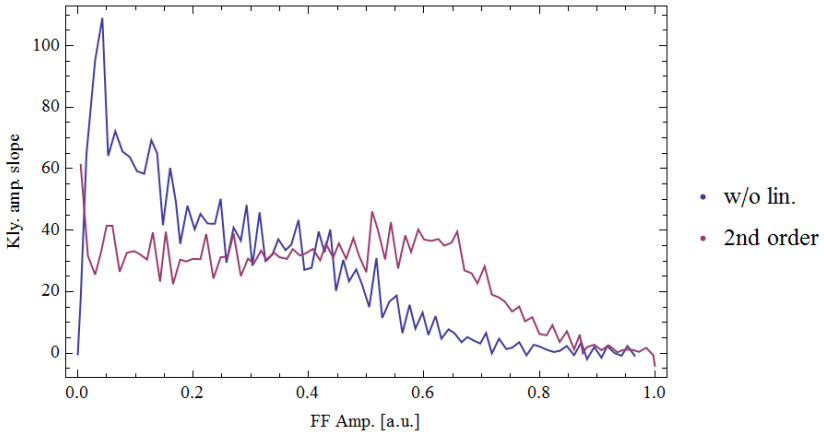


Figure 8.29: *Slopes of klystron output amplitude [sqrt(kW)] versus FF amplitude [a.u.]: without linearization (blue) and with 2nd order polynomial function–based linearization (purple).*

### 8.3.3 LUT with Interpolation–based Klystron Linearization

#### Motivation for and Principle of LUT with Interpolation–based Klystron Linearization

In the case of a direct lookup table, an example is shown in section 8.2.1, usually the address width (e.g. 12 bit) is smaller than the bit width of the signal that is looked up and/or corrected (e.g. 18 bit). This is done in order to save FPGA logic cells or memory space, depending on how the direct lookup table is implemented. As long as the address width is smaller than the word bit width, quantization of the lookup table output occurs. This quantization leads to an error, which depends on the lookup table address width, corresponding to the number of nodes, and the slope of the function to be modeled. In order to reduce the error caused by the quantization in case of a direct lookup table, interpolation between the nodes can be added. In the following a algorithm using linear interpolation based on the slopes between the nodes is introduced.

Figure 8.30 shows a schematic of a random function. Indicated are pairs of nodes equidistant in x as well as the slopes m. The slopes are calculated by the differential quotient for every pair of next neighbor nodes. The target

is to calculate the y values corresponding to the x value indicated in green. A linear interpolation can be achieved by

$$y = y_n + (x - x_n) \cdot m_n \ . \tag{8.9}$$

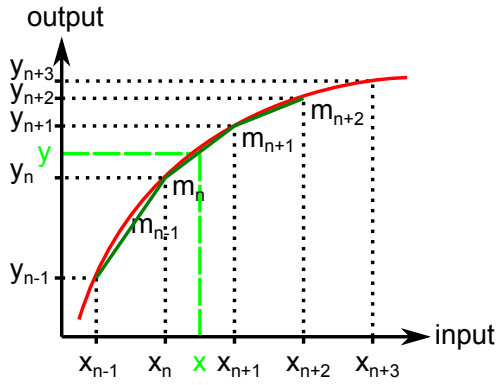


Figure 8.30: *Schematic of a random function (red), its model (green), and nodes for x and y.*

In the case of an FPGA implementation of the algorithm, $y_n$ corresponds to nodes in a first lookup tables. The slopes $m_n$ are stored in a second lookup table. In order to realize the subtraction of $(x - x_n)$ the input signal is split up. The most significant bits are used as the address for the two lookup tables, whereas the least significant bits are multiplied to the slope. Figure 8.31 shows a schematic of an example of such an implementation on an FPGA.

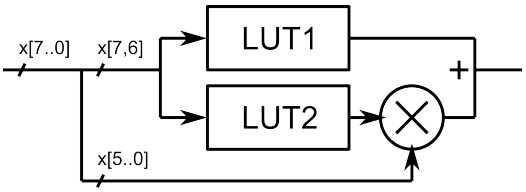


Figure 8.31: *Schematic of an example of an implementation of a lookup table with linear interpolation algorithm on an FPGA.*

Based on this method the klystron linearization algorithm was implemented as shown in Figure 8.32.

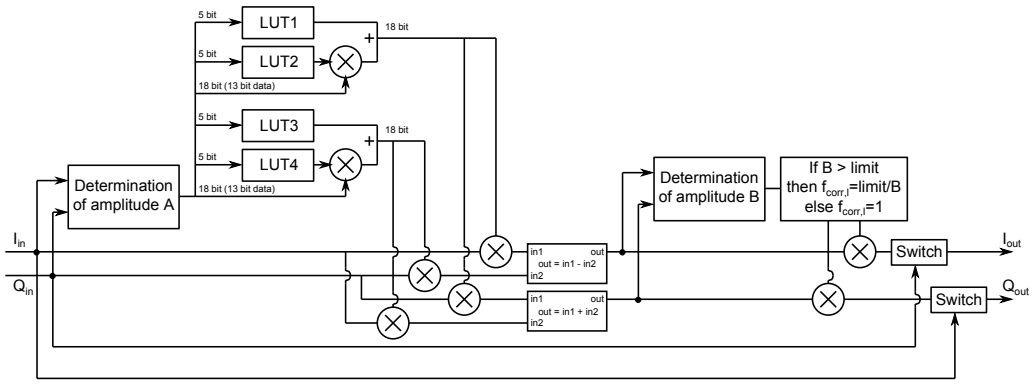


Figure 8.32: *Schematic of the lookup table with interpolation–based klystron linearization package. Based on the amplitude of the input I and Q values I and Q correction factors are generated using two lookup table with linear interpolation algorithms. The correction factors are applied to the input I and Q values. Before they are outputted and amplitude limitation algorithm is applied.*

### LUT Calculation Script

The creation of the lookup tables is performed in four steps. The first two steps are the same as the first two steps described in section 8.3.2.

In the third step the number of I and Q correction value list entries are adjusted to fit the lookup table address width. In the presented case this width was 32 (or 5 bits). This number was chosen in order to keep the time for writing the lookup tables reasonably, since at the time of the test of the implementation the data had to be written manually to the memory. The list of I correction values corresponds to the content of LUT1 and the list of Q correction values to LUT3.

In the last step the slopes between the nearest neighbor pairs of points of the I and Q correction value lists are computed. The list of slopes of the I correction values corresponds to LUT2 and the list of slopes of the Q correction values to LUT4.

### Test in Development Environment

The LUT with interpolation–based klystron linearization algorithm was developed and tested at the same time as the 2nd order polynomial function–based klystron linearization algorithm. Due to this fact the same modified test setup within the development rack as described in chapter 8.3.2 was used

for the development of the LUT with interpolation–based klystron linearization algorithm. The final test of the algorithm was performed at ASTA.

### Test at ASTA

The test of the LUT with interpolation–based linearization algorithm at ASTA ASTA was performed at the same time as the test of the 2nd order polynomial function–based linearization algorithm. Due to this, the same klystron characteristics as described in section 8.3.2 were used for the creation of the lookup tables following the procedure as described in section 8.3.3.

In order to test the functionality of the algorithm, it was activated and a FF amplitude scan for the full range under open loop operation was performed. The result in terms of amplitude and phase is shown and compared to the klystron characteristics without linearization in Figures 8.33 and 8.34.

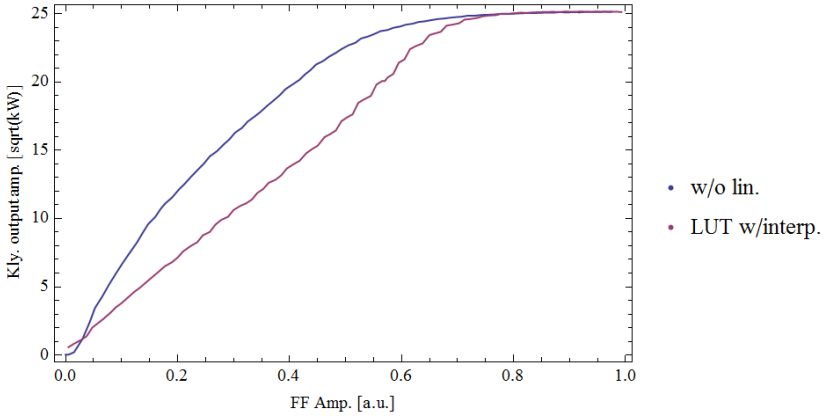


Figure 8.33: *Klystron output amplitude [sqrt(kW)] versus FF amplitude [a.u.]: without linearization (blue) and with LUT with interpolation–based linearization (purple).*

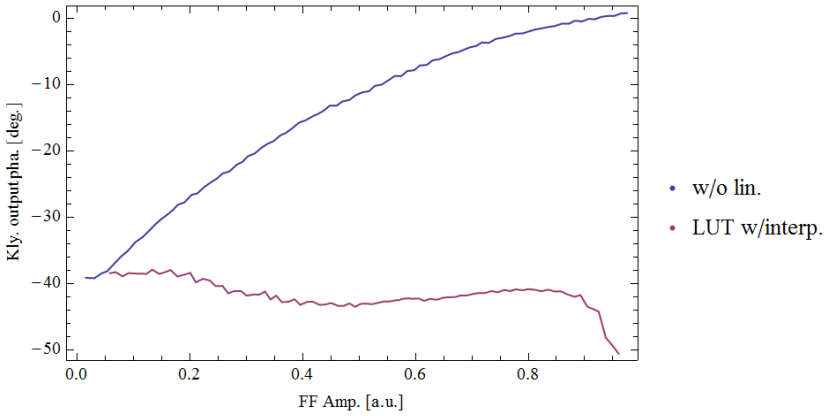


Figure 8.34: *Klystron output phase [°] versus FF amplitude [a.u.]: without linearization (blue) and with LUT with interpolation–based linearization (purple).*

In order to analyze the linearization performance the slope of the klystron output amplitude was computed. Figure 8.35 shows the corresponding plot. In case of the klystron output amplitude, it can be seen that the slope in principle is linear below a FF amplitude of 0.62 a.u., but with quite high fluctuations. This fluctuation is caused by a step–like structure in the klystron output amplitude characteristic. This structure originates from an error in the slope lookup tables. Above a FF value of 0.62 a.u. compression occurs. Also in case of the phase such a step–like structure due to the same reason can be observed. The total phase rotation over the whole FF range was reduced from 40.17° to 12.64°. The phase rotation until the point of saturation at a FF amplitude of 0.9 a.u. with the klystron linearization was 5.60°. Even with the error in the slope lookup tables, the presented test run proved that the linearization algorithm is effective.

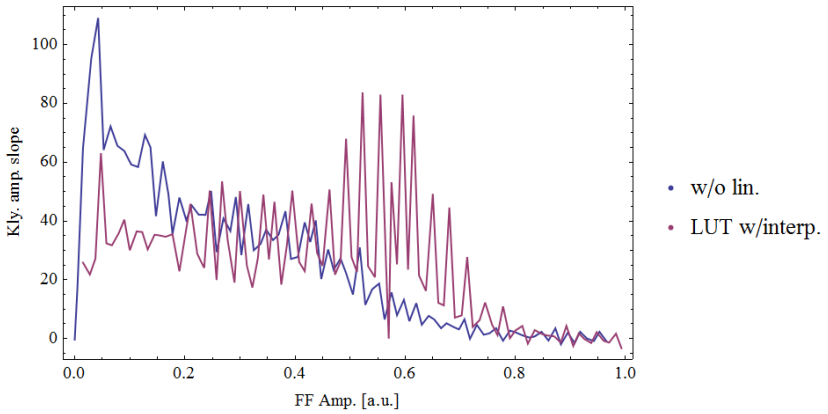


Figure 8.35: *Slopes of klystron output amplitude [sqrt(kW)] versus FF amplitude [a.u.]: without linearization (blue) and with LUT with interpolation–based linearization (purple).*

### 8.3.4 Comparison of Linearization Methods

In the following the three klystron linearization algorithms tested at ASTA are compared. These cover the 3rd order polynomial–based klystron linearization, the 2nd order polynomial–based klystron linearization, and the lookup table with interpolation–based klystron linearization. Figure 8.36 shows klystron output amplitude versus the FF amplitude in case of all three linearization algorithms as well as in the case of no linearization active. The slopes of all of these curves are shown in Figure 8.37. From this it can be seen that the 2nd order polynomial–based klystron linearization has the best linearization performance concerning the amplitude.

Figure 8.38 shows the klystron output phase for all three klystron linearization algorithms as well as in the case of no linearization. From this plot it can be seen that the lookup table with interpolation–based klystron linearization algorithm has the best linearization performance concerning the phase.

In theory the LUT with interpolation–based klystron linearization should deliver the best linearization performance since the errors in modeling the correction factor functions are the lowest. For more details refer to section 8.5. The tasks for the future are to find out the reason for the fluctuations of the lookup table with interpolation–based klystron linearization algorithm (maybe a bug in the script for the calculation of the slope lookup tables) and to find the reason of the remaining phase rotation, which is strongly related to the amplitude linearization performance, since the linearizations

are performed in terms of I and Q values.

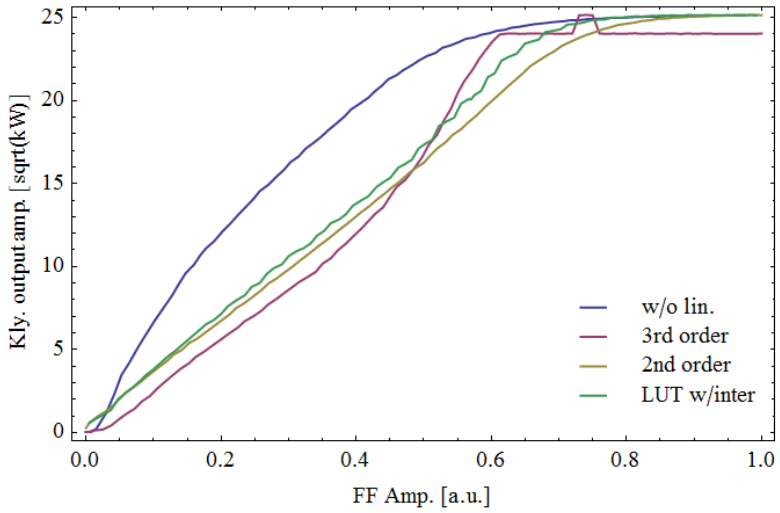


Figure 8.36: *Klystron output amplitude [sqrt(kW)] versus FF amplitude [a.u.]: without linearization (blue), with 3rd order polynomial function–based linearization (purple), 2rd order polynomial function–based linearization (brown), and with LUT with interpolation–based linearization (green).*

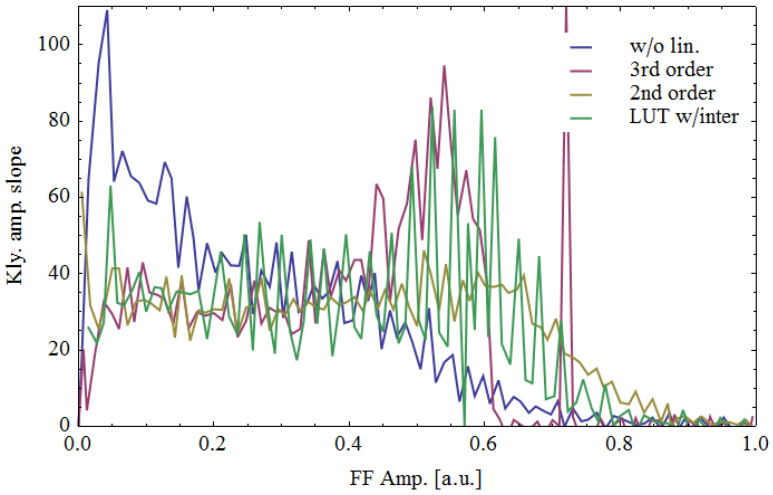


Figure 8.37: *Slopes of klystron output amplitude [sqrt(kW)] versus FF amplitude [a.u.]: without linearization (blue), with 3rd order polynomial function–based linearization (purple), 2rd order polynomial function–based linearization (brown), and with LUT with interpolation–based linearization (green).*

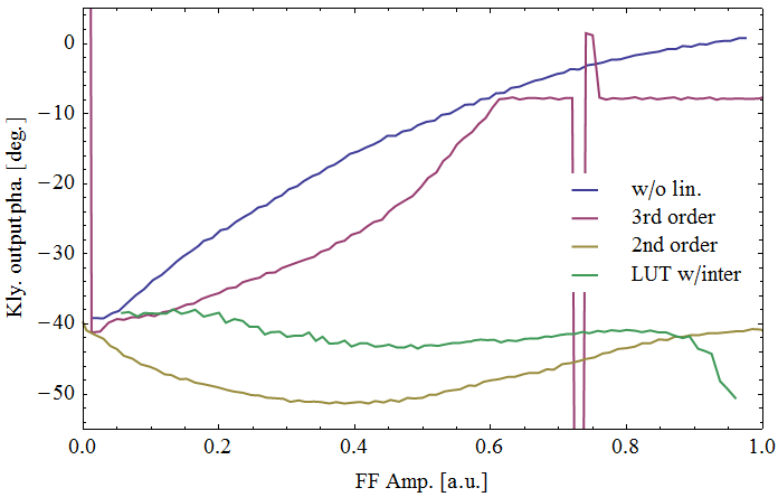


Figure 8.38: *Klystron output phase [°] versus FF amplitude [a.u.]: without linearization (blue), with 3rd order polynomial function–based linearization (purple), 2rd order polynomial function–based linearization (brown), and with LUT with interpolation–based linearization (green).*

## 8.4 Klystron Linearization based on LUTs with Interpolation and Adaptive Grid Spacing

The direct lookup table with linear interpolation–based algorithm has already a high precision in modeling a function. Due to the fact that the grid spacing is equidistant and fixed, this precision depends on the change in slope of the function to be modeled. Thus the goal of study in the scope of this dissertation was to develop an algorithm with and adaptive grid spacing in order to increase the precision.

The lookup table with interpolation–based klystron linearization method so far used is based on equation (8.9), which on the FPGA is realized as shown in Figure 8.31. This algorithm can be used only with a constant grid spacing distribution, since the calculation of $(x - x_n)$ is realized by a truncation of the signal, which cannot be changed. In order to implement a lookup table with interpolation and an adaptive or arbitrary grid spacing, equation (8.9) can be rewritten as

$$y = y_n + x \cdot m_n - x_n \cdot m_n \ , \tag{8.10}$$

which can be rewritten as

$$y = (y_n - x_n \cdot m_n) + x \cdot m_n \ . \tag{8.11}$$

In this case no computation of a difference or signal truncation is required. Lets identify $(y_n - x_n \cdot m_n)$ with $\nu_n$. Both $\nu_n$ and $m_n$ can be calculated e.g. in Matlab. For the implementation as shown below $\nu_n$ and $m_n$ would be stored in two separate lookup tables. If the grid spacing is adaptive or arbitrary actually the counter $n$ depends on the input amplitude $x$, thus it is $n(x)$. Furthermore the maximum of $n$ corresponds to the address width of both lookup tables of $\nu_n$ and $m_n$. For the example shown in the figure below the width is 11 bit. The generation of the 11 bit addresses respective the adaptive or arbitrary grid spacing can be simply realized by a lookup table with 16 bit of 11 bit words. In this case for every value of the input amplitude $x$ an arbitrarily address can be generated. The final implementation on the FPGA combining equation (8.11) and all three lookup tables for the creation of $n(x)$, $\nu_n$, and $m_n$ is shown in Figure 8.39.

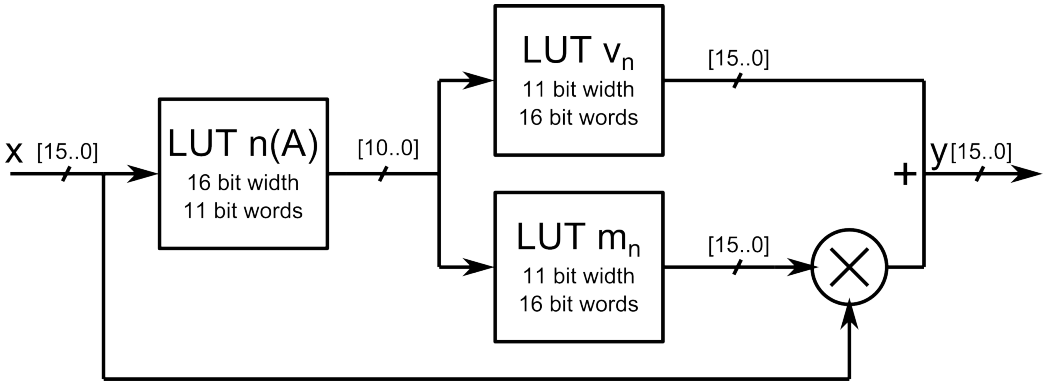


Figure 8.39: *Algorithm based on lookup tables with linear interpolation and arbitrary grid spacing.*

In order to generate an adaptive grid spacing, it is suggested to base the grid spacing distribution of the slope of the function to be modeled. In the case the slope of the function to be modeled is very high or even diverges at some point the problem occurs that most of the grid nodes will be located close to this point. In order to overcome this situation it is suggested to fit a function to the slope, such as e.g. a 5th order polynomial function. This method was used the comparison as shown in the following section.

## 8.5 Simulation–based Comparison of All Developed Algorithms

The expected linearization performances of all in this dissertation introduced algorithms are compared in the following. To this end an arbitrary correction function was generated. This function is shown in Figure 8.40 in green. Furthermore this function was modeled using all algorithms mentioned before in this chapter. The results are also shown in Figure 8.40. For a better visibility a depth of only 32 words was simulated for all lookup table–based algorithms.

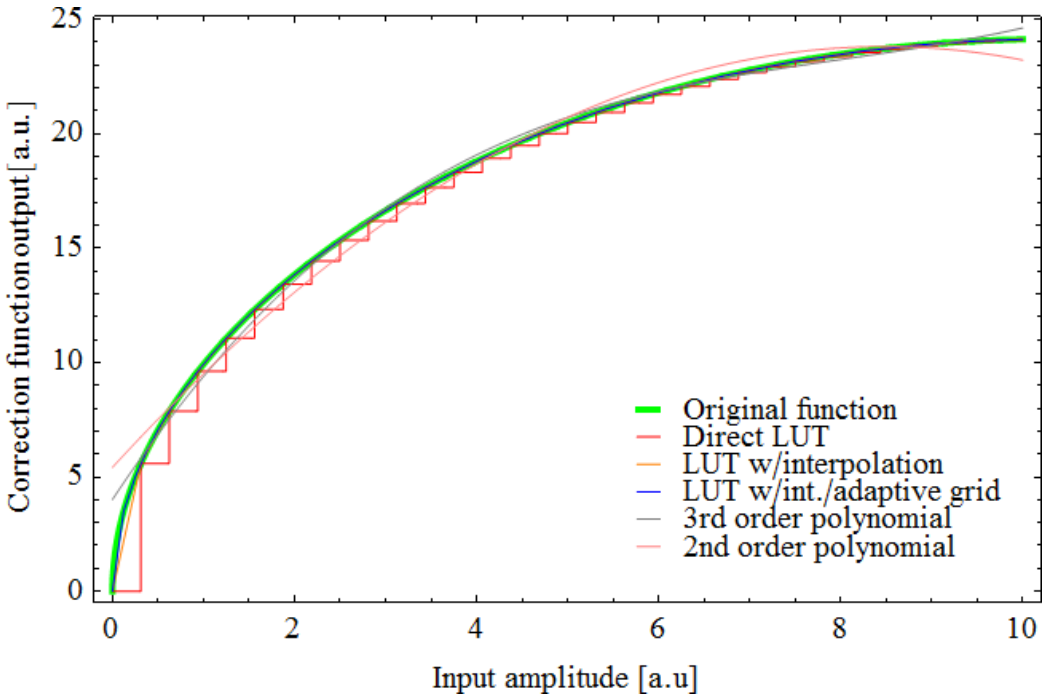


Figure 8.40: *Simulated arbitrary correction function output [a.u.] versus input amplitude [a.u.] for the original function (green), a direct LUT (red), LUT with interpolation (orange), LUT with interpolation and an adaptive grid (blue), a 3rd order polynomial function–based algorithm (grey), and a 2nd order polynomial function–based (pink).*

In order to compare the simulated modeling performances of the algorithms the differences between the original function and the modeled output was computed. The result is shown in Figure 8.41.

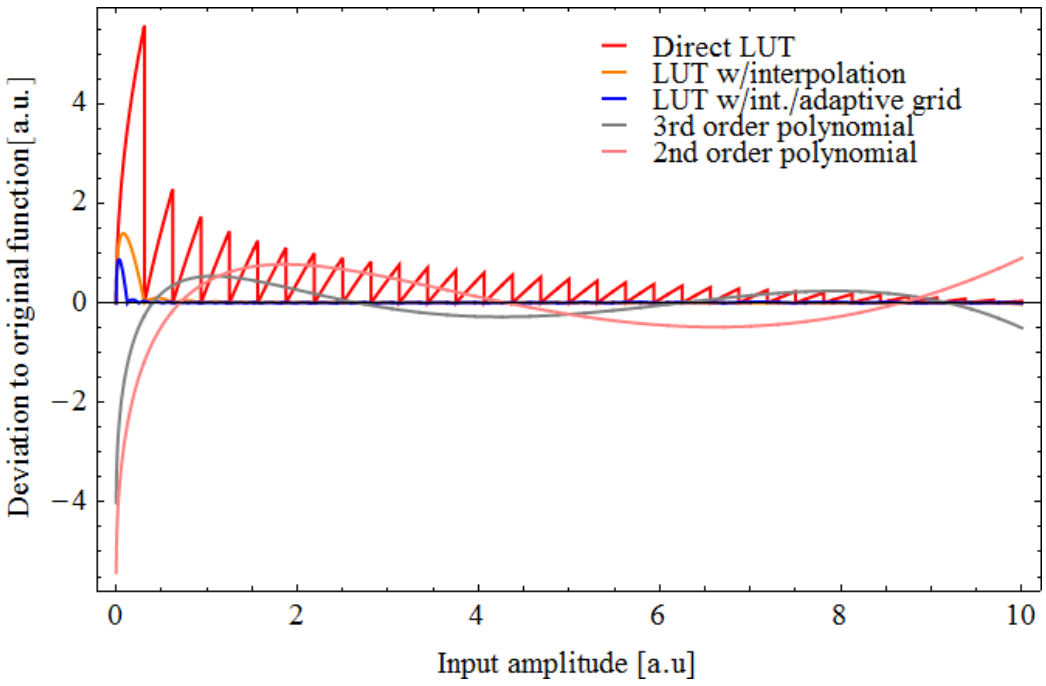


Figure 8.41: *Simulated deviation to original arbitrary correction function [a.u.] versus input amplitude [a.u.] for a direct LUT (red), LUT with interpolation (orange), LUT with interpolation and an adaptive grid (blue), a 3rd order polynomial function–based algorithm (grey), and a 2nd order polynomial function–based (pink).*

From the deviation plots the sums of absolute values of the deviations over all plotted points were computed for all simulated algorithms. This yields a similar information as the integral over the error functions. The computed sums are listed in Table 8.4.

Table 8.4: Sums of absolute values of deviations over all plotted points for all simulated algorithms.

| Algorithm | Sum of errors |
|---|---|
| Direct LUT | 6752.3 |
| LUT w/int. | 588.1 |
| LUT w/int./ad. grid | 250.8 |
| 3rd order | 3964.5 |
| 2nd order | 7584.0 |

This shows from the viewpoint of simulated linearization performance in

theory the best choice within the group of implemented algorithms is the lookup table with interpolation–based klystron linearization. Due to the interpolation the quantization errors are eliminated. Even it is notable that also the 3rd order polynomial function based algorithm yields a better performance than the direct lookup table solution, it should be kept in mind that the performance of the lookup table solution strongly depends on the grid spacing. The best performance of all algorithms presented in the simulation yielded the lookup table with interpolation and adaptive grid spacing–based algorithm. It is recommended to implement and test it in future studies.

## 8.6 Concepts in the Scope of Klystron Linearization

### 8.6.1 Exception Handling

One of the most important requirements for the operation of accelerators and its components is safety and machine protection. Due to this the goal was to develop measures of exception handling in the scope of klystron linearization. Table 8.5 shows a list of cases of exceptions and how to handle them. The handling details are specific for DESY, but the exceptions apply in general to all FPGA–based klystron linearization implementations.

Table 8.5: Table of cases of exceptions in the scope of FPGA–based klystron linearization and how to handle them.

| Case # | What could go wrong | How to detect | Where to detect | How to react | How to recover |
|---|---|---|---|---|---|
| 1 | Inactive firmware with max DAC output | I'm alive signal from firmware, DAC output monitor, VM output monitor | Server | Stop RF output of klystron | Reboot board and initilize with default parameter / update firmware |
| 2 | VM malfunction | Comparison DAC output monitor and VM output monitor | Server | Stop RF output of klystron, set DAC output to 0 | Restart / replace VM |
| 3 | Kly. lin. wrong correction function | After correction factor check, if always $< 1$; if klystron output is linear | Matlab, firmware, server | Set correction function values bigger 1 automatically to 1 in matlab and output an error; if klystron output is not linear, generate GUI error message | Calculate and set new correction function fulfilling the requirements |
| 4 | DAC limit (user set) $<$ Kly. lin. limit | Compare DAC and kly. lin. limits | Server | Generate GUI error message | Adjust DAC limit, update correction function / kly. lin. limit, adjust ORC |
| 5 | ORC (amplitude set to high) in combination with kly. lin. exceeds DAC limit | Compare DAC and max. ORC output in combination with kly. lin. limits | Server | Generate GUI error message | Adjust DAC limit, adjust ORC |
| 6 | Kly. working point changed without updating the correction function | Kly. parmeter (e.g. HV) monitor | Server | Turn off kly. lin., generate GUI error message | Go back to initial klystron working point, update correction function |
| 7 | Kly. lin. out I and Q values switched | Comparison with expected kly. lin. output | Server | Set DAC output to 0, generate GUI error message | Update firmware |
| 8 | Kly. lin. out I and/or Q signs inverted | Comparison with expected kly. lin. output | Server | Set DAC output to 0, generate GUI error message | Update firmware |
| 9 | Klystron fails | Observe klystron output | MPS RF inhibit | Turn off kly. lin., generate GUI error message | Check and rest interlocks and HV / restart klystron |
| 10 | Modulator fails | Observe modulator output | MPS RF inhibit | Turn off kly. lin., generate GUI error message | Check and rest interlocks / restart modulator |
| 11 | LLRF and RF gate not synchronized | Compare gate settings / monitor output (full range available?) | Server | Generate GUI error message | Adjust LLRF gate or RF gate |
| 12 | Lookup table can't be read anymore (e.g. radiation damage) | Check memory data output concistency; check, if klystron output is linear | Server | Turn off kly. lin., generate GUI error message | Rewrite memory / replace hardware |

### 8.6.2 Klystron Characterization During Accelerator Operation with Beam

For all predistortion–based klystron linearization algorithms the klystron characteristics have to be obtained. Based on this the characteristics of the predistortion are created. From the experiences of the test runs performed, it can be assumed that a klystron characterization takes about 5 to 10 minutes. When ever the working point of the klystron changes (e.g. the high voltage of the klystron), also its characteristics changes, which means that a new characterization has to be performed. In the procedure applied until now no beam operation is possible. When operating a particle accelerator such e.g. ILC it is imperative to have as less down time as possible. Due to this the goal was to develop concepts of klystron characterization procedures, which can be applied without causing down time.

A possible solution would be to map the klystron characteristics before beam operation for several different working points corresponding to all parameters that are likely to be changed (e.g. klystron high voltage). In the case such a parameter is changed during operation, from this map the new klystron characteristics could be interpolated. Based on this a new predistortion characteristics could be computed and set. The disadvantage of such a solution is that maybe not all operation point changes that will occur during operation are mapped from the beginning and due to this no adequate klystron characteristic can be found. In order to overcome this situation a klystron characterization during accelerator operation with beam is necessary.

In a pulsed accelerator operation the cavity gradient versus time looks as shown in the schematic in Figure 8.42 a) top. Also in Figure 8.42 a) at the bottom the corresponding schematic of the FF amplitude is shown. The time of the pulse is divided in three sections; the filling time, the flattop time, and the time of decay. The beam is present only during the flattop time, which means that during this time no changes in the cavity gradient must occur. On the other hand during the filling time most important is to deliver a defined amount of power to the cavity in order to reach the defined cavity gradient at the end of the filling time. This corresponds to a certain area of the FF amplitude pulse shape during the filling, which is marked in orange in Figure 8.42 a).
Based on this a procedure could be to change the filling time and correspondingly the FF amplitude, in order to keep the area occupied from the FF amplitude table during the filling time constant, pulse by pulse as shown in Figure 8.42 b). By this a pulse by pulse klystron characterization could be performed while beam is accelerated during the flattop time. For the re-

alization of this procedure timing signals respective to the accelerator have to be changed.

Another procedure could be to use a step–like function for the FF table during filling as shown in Figure 8.42 c). By this a klystron characterization could be performed within a single pulse. This could be applied when ever the working point is changed. Another possibility would be to use the filling pattern all the time. In this case the predistortion characteristics could be updated continuously. Also for this procedure the timing signals respective to the accelerator have to be changed.

Since the bandwidth of a klystron is typically several MHz, this step–like filling pattern could be performed during a short time of the filling pattern as shown in Figure 8.42 d). In this case as well a klystron characterization can be performed within a single pulse. Furthermore in this case no adjustments to the timing signals have to be made, since the characterization pattern can be very short.

For all suggested procedures for a klystron characterization during operation it is assumed that the klystron characteristic over the whole pulse it the same as during the time of the characterization.

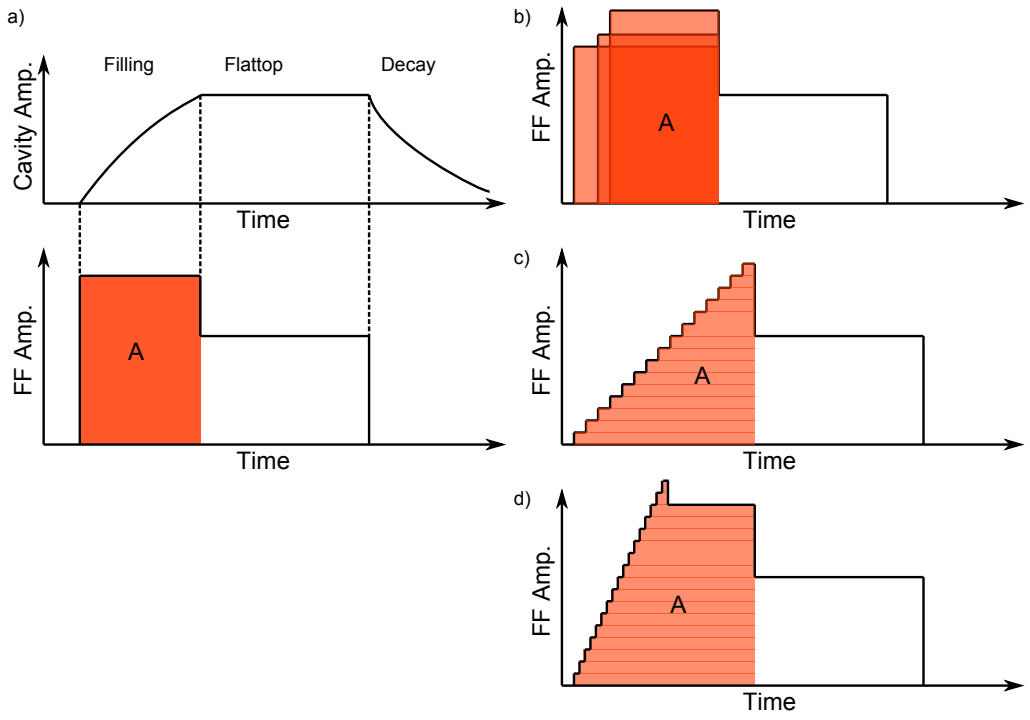


Figure 8.42: Possible filling scheme for klystron characterization during accelerator operation with beam: a) normal filling scheme, b) filling scheme with variable filling time and amplitude, c) step–like function of amplitude during the whole filling time, and d) step–like function of amplitude during only a short time at the beginning of the filling time.

## 8.7 Klystron–Cavity Simulator

In this chapter the first time development, implementation, and test of a combined FPGA–based klystron–cavity simulator is described.

### 8.7.1 Motivation for the Klystron–Cavity Simulator

Nowadays FPGA–based cavity simulators are a common tool for the development and test of digital LLRF control system in times no actual cavity is available. Nevertheless simulating only a cavity does not reflect the entire actual system including high power amplifiers such as e.g. klystrons. As described in section 8.3.2 the situation can be improved by including an active analog amplifier within the feedback loop simulating nonlinear effect

similar to a klystron. This allowed the development and test of two klystron linearization algorithms as part of the MFC FPGA firmware. The disadvantage of using such an analog amplifier is that it has a different characteristic (especially regarding the phase) compared to a klystron. This situation can be overcome by extending the FPGA–based cavity simulator by a klystron simulator package. By this a realistic test environment for offline developments and tests can be realized, since nonlinearities of the klystron and also other components can be simulated. Since such an FPGA–based klystron simulator is highly configurable and flexible, it is possible to simulate any possible nonlinear characteristics both in amplitude and phase.

### 8.7.2 Principle of Klystron–Cavity Simulator

A klystron–cavity simulator was developed and implemented on a uTCA board at KEK cERL. Figure 8.43 shows a schematic of the implementation. The IF signal is digitized by the ADC1 on the $\mu$TCA board. The digitized signal is sent to the FPGA, on which an IQ conversion is performed. These I and Q signals are available for monitoring via EPICS as data channel ADC1.

These I and Q signals are furthermore the input of the klystron simulator package. This package is realized using the direct lookup table–based algorithm as described in section 8.2.1. The only difference is that the bit width of the I and Q signals is 16 bit and accordingly the bit width of the word in the lookup tables. In future it is planned to make the lookup tables configurable via EPICS. Until now these are hard coded. The output of the klystron simulator package can be monitored via EPICS using data channel ADC3.
The following package is the IQ offset and noise cut package. In this package an offset to the I and Q values can be added. This part is used only for development purposes in order to quick fix a problem with the cavity simulator package. It is planned to exclude this functionality in future, since it adds unwanted nonlinearities. The second part of the the package is the noise cut part. In this signals lower than a certain limit certain limit are set to zero. By this noise is cut in times no actual input signal is inputted. In future it is planned to make these limits configurable via EPICS. The output of the IQ offset and noise cut package can be monitored via EPICS using data channel ADC2.
The last package the algorithm is the cavity simulator package. It is based on the time discrete cavity differential equation.

$$\begin{bmatrix} V_{i,n} \\ V_{q,n} \end{bmatrix} = \begin{bmatrix} 1 - T\omega_{1/2} & -T\Delta\omega \\ T\Delta\omega & 1 - T\omega_{1/2} \end{bmatrix} \begin{bmatrix} V_{i,n-1} \\ V_{q,n-1} \end{bmatrix} + T\omega_{1/2} R_L \begin{bmatrix} I_{i,n-1} \\ I_{q,n-1} \end{bmatrix} . \quad (8.12)$$

It was simplified for the case no detuning is present. In future it is planned to make the cavity properties configurable via EPICS. Until now these are hard coded. The output of the cavity simulator package can be monitored via EPICS using data channel ADC4.
The output I and Q values of the cavity simulator are converted to differential signals $I^+$, $I^-$ and $Q^+$, $Q^-$, which are outputted by DAC1P, DAC1N, DAC2P and DAC2N.

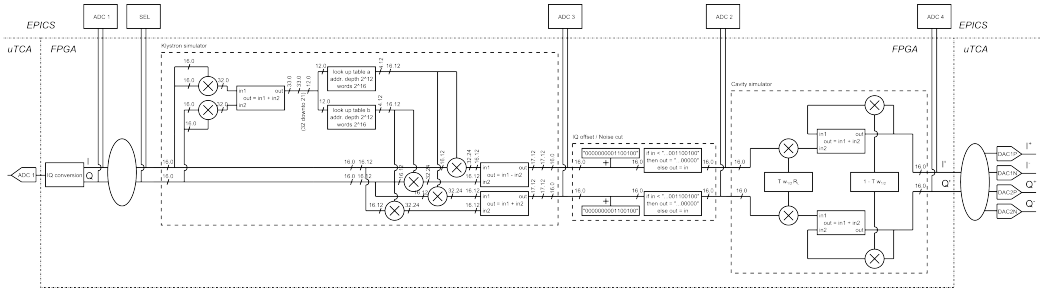


Figure 8.43: Schematic of the klystron–cavity simulator: digitalization of the input signals, klystron simulator package, IQ offset and noise cut package, cavity simulator package, and conversion from digital to analog of the output signals.

For the development and implementation the following software tools were used:

- Notepad ++ 5.9.4
- ISE Design Suite 14.4
- ISim

The VHDL code for the klystron–cavity simulator was written in Notepad ++, compiled in ISE, and tested in the ISim simulator. After sufficient testing in the simulator, ISE was used in order to create the firmware file (.bit file). This bit file was uploaded to the FPGA on the uTCA board.

### 8.7.3 Test Setup

The test of implementation of the klystron–cavity simulator was performed using two uTCA boards in the development rack at cERL. Figure 8.44 shows a schematic of the test setup. On one uTCA board the original controller

firmware was kept. It covers ADC rotation, the CAV SIM IIR filter, a proportional and integral gain, the addition of FF tables, the DAC filter, and DAC rotation. The output of the DACs of the controller board are converted from differential to single end using two analog converters. The restored I and Q values are sent to an IQ vector modulator. A second input of it is a 10 MHz signal. By the vector modulator the I and Q values, which are baseband, are converted to an IF signal. This signal is split into two paths. One is connected to the ADC2 channel of the controller board. The second one is connected to the ADC1 channel of the uTCA board, on which the klystron–cavity simulator firmware was programmed. The details of the firmware are described in section 8.7.2. The differential baseband I and Q output of the klystron–cavity simulator board is converted to single end signals by two analog converters. The single end I and Q signals are fed to a IQ vector modulator. Beside this also a 10 MHz signal is fed to the IQ vector modulator. By this an IF signal is generated, which is filtered by a band pass filter and fed to ADC1 on the controller board. With this configuration an open loop as well as a closed loop operation driving the klystron–cavity simulator can be established. A second possibility is to operate the loop via ADC2 on the controller board. In this case a filter on the controller board is used in order to simulate a cavity.

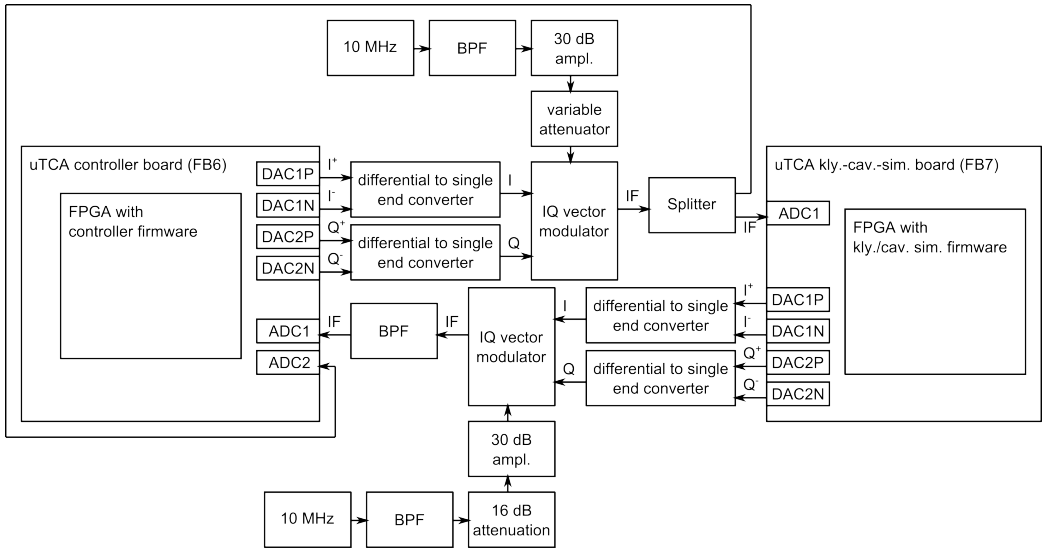


Figure 8.44: Schematic of the setup for testing the klystron–cavity simulator. The uTCA controller board (left) and the uTCA klystron–cavity simulator (right) are connected using differential to single end converters and IQ vector modulators. Furthermore the output of the uTCA controller board is fed back to its ADC2 channel.

### 8.7.4 Test Measurements at Development Crate

#### Test of Simulator Response in FF Only Operation

In a first test the response of the klystron–cavity simulator response in open loop (FF only) operation was observed. To this end a previously recorded klystron characteristic was programmed to the lookup tables. The half bandwidth for the cavity simulator was set to $f_{1/2} = 216.7$ Hz corresponding a loaded Q value of $3 \cdot 10^6$. For the test a full range FF amplitude scan with a rectangular FF table was performed. Figure 8.45 shows the output of the klystron simulation package on the klystron–cavity simulator board in terms of amplitude and phase versus the FF amplitude on FB6. A clear nonlinear behavior can be observed.
Figure 8.46 shows for the same measurement the output of the IQ offset and noise cut package. An influence on both the amplitude and phase can be observed. Due to the additional nonlinearity introduced the maximum of the amplitude is shifted and the phase stays constant.
Figure 8.47 shows the output of the cavity simulator. The values are taken during the flattop time, in which the cavity simulator reached the steady

state condition. It can be observed, that the cavity simulator output follows its input.

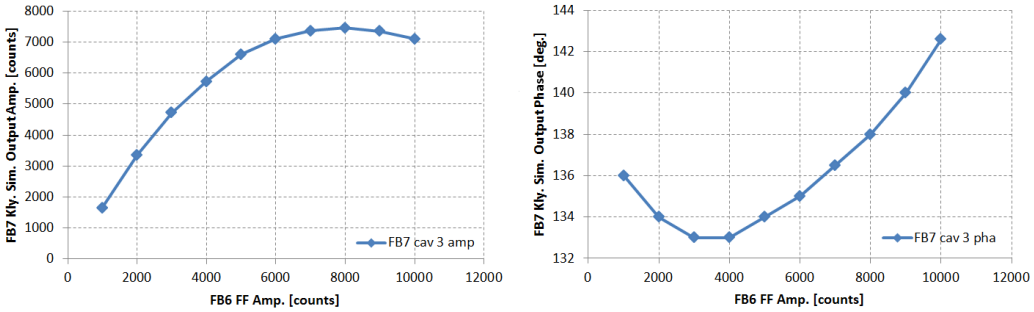


Figure 8.45: Amplitude [counts] and phase [°] of the klystron simulator package (nonlinear LUT) output on the klystron–cavity simulator card versus the FF amplitude [counts] on the controller card.

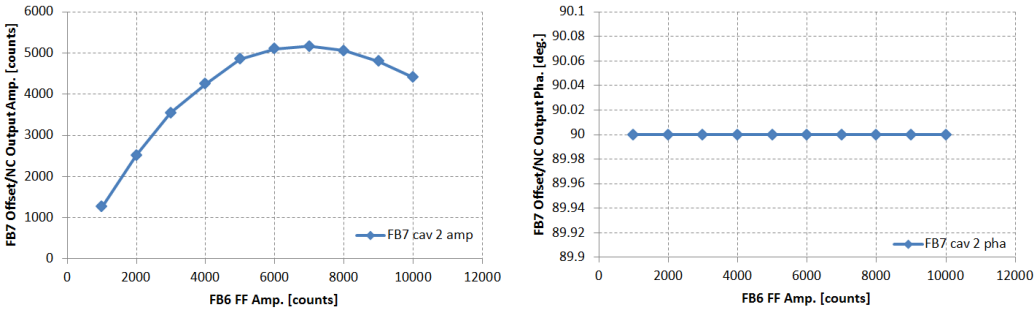


Figure 8.46: Amplitude [counts] and phase [°] of the I/Q offset and noise cut package output on the klystron–cavity simulator card versus the FF amplitude [counts] on the controller card.

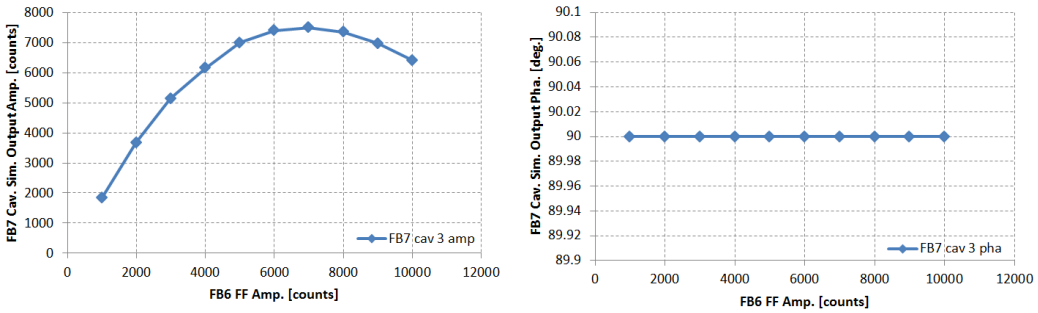


Figure 8.47: Amplitude [counts] and phase [°] of the cavity simulator package output on the klystron–cavity simulator card versus the FF amplitude [counts] on the controller card.

The same measurement was repeated with a linear lookup table programmed for the klystron–cavity simulator. Figure 8.48 shows the output of the klystron simulator package. The amplitude is linear as expected. The phase on the other hand shows a rotation of 7.7° over the whole FF amplitude range. It has to found out, where this phase rotation caused.
Figure 8.49 shows the output of the cavity simulator package. Also in this case the amplitude characteristic is linear. Due to the IQ offset and noise cut package the phase rotation was suppressed.

With these two measurements a proof of concept of the algorithm implementation was shown. It is strongly recommended to exclude the IQ offset and noise cut package in the final version.

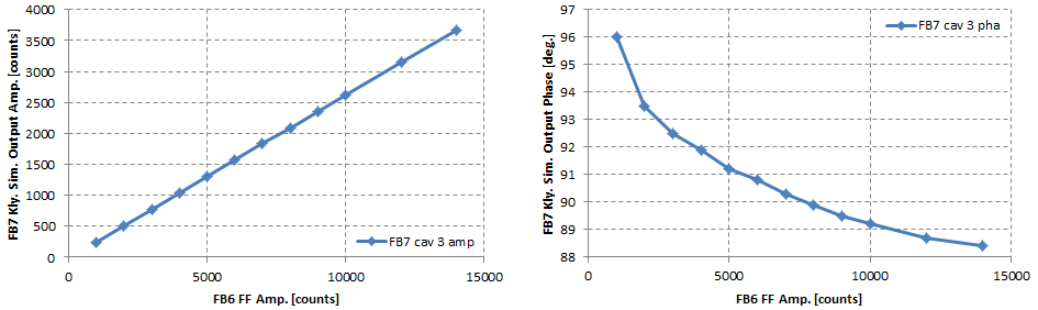


Figure 8.48: Amplitude [counts] and phase [°] of the klystron simulator package (linear LUT) output on the klystron–cavity simulator card versus the FF amplitude [counts] on the controller card.

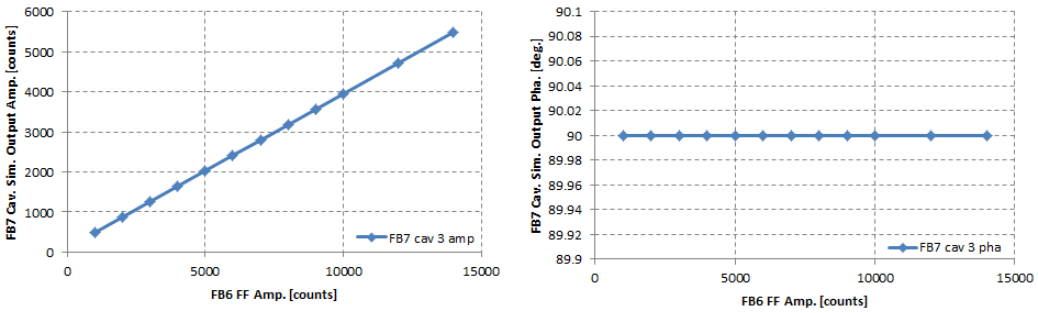


Figure 8.49: Amplitude [counts] and phase [°] of the cavity simulator package output on the klystron–cavity simulator card versus the FF amplitude [counts] on the controller card.

### Proportional Gain Scans

In a next step the klystron–cavity simulator was tested under feedback operation. To this end the previously recorded klystron characteristic was programmed to the lookup tables of the klystron simulation package. The addition of the FF table turned off. A set point table was calculated and set. The integral gain was set to 0 and a proportional gain scan was performed. Figure 8.50 shows the received amplitude pulse shapes at ADC1 on the controller board (FB6) for set values of the proportional gain ranging from 20 to 1200 as well as the set point amplitude. It can be observed that as higher the gain is set, the better agrees the ADC1 pulse shape with the set point.

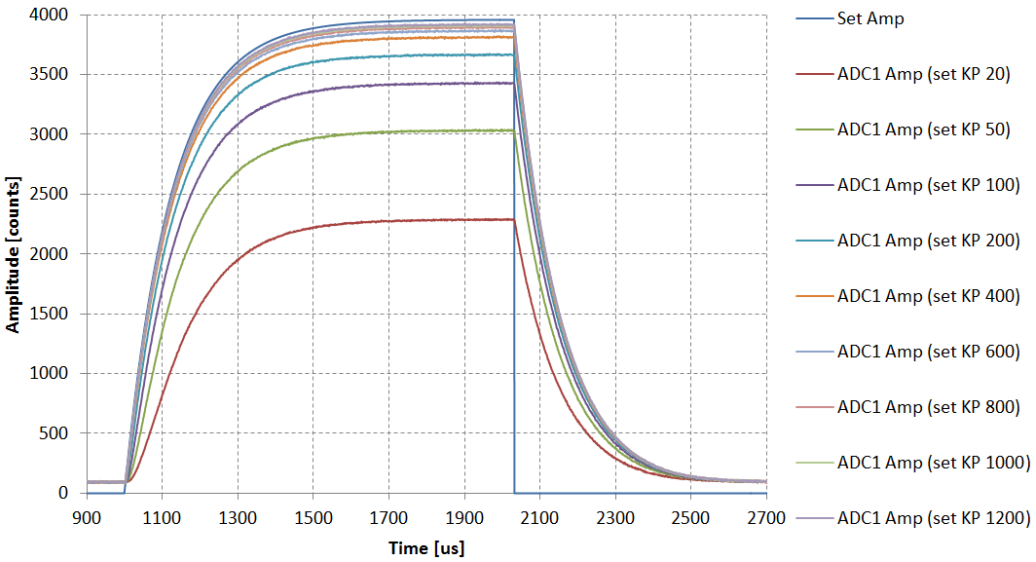


Figure 8.50: Set point (blue) and ADC1 (all other colors) amplitudes [counts] versus time [$\mu$s] of the controller board during a proportional gain scan with nonlinear LUT for the klystron simulator package.

Based on

$$K_P = \frac{A_{actual}}{A_{set} - A_{actual}} \tag{8.13}$$

the actual proportional gain for each case was calculated. Figure 8.51 shows the plot of the actual proportional gain versus the set value of the proportional gain. It can be observed that the relation is not linear. Since the klystron–simulator introduced a nonlinearity such a behavior is reasonable.

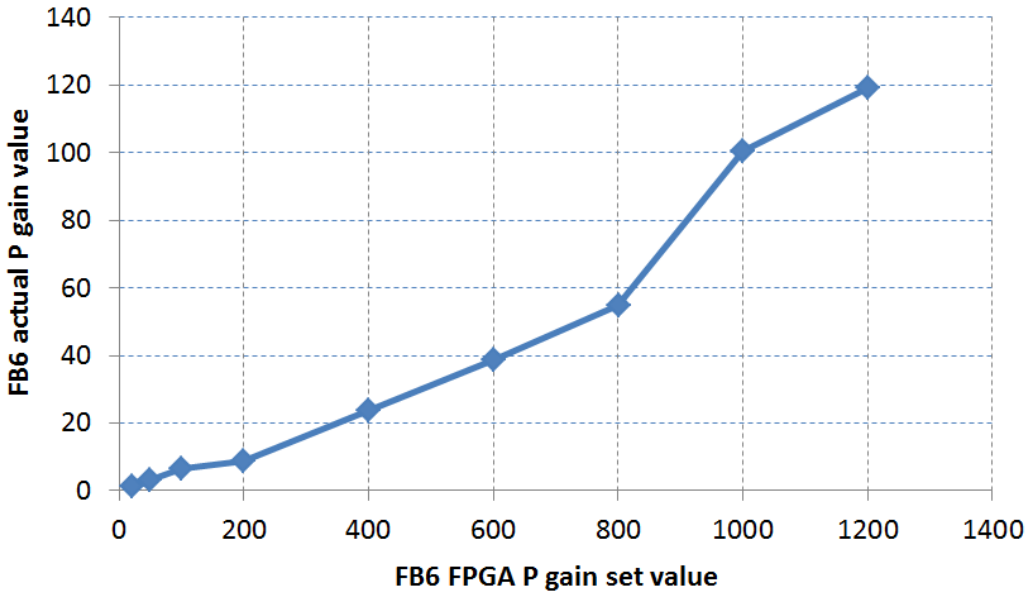


Figure 8.51: Actual proportional gain versus FPGA P gain set value for the proportional gain scan for nonlinear LUT for the klystron simulator package.

In order to demonstrate that in the case no nonlinear element is included the actual gain to set value of the proportional gain is linear, the test setup was changed. In this case the output of the controller board was fed back to ADC2 of the controller board and the DAC IIR filter was used as a cavity simulator. Figure 8.52 shows the amplitude pulse shapes observed at ADC2 for proportional gain set values ranging from 20 to 1200 as well as the set point amplitude. From this data the actual proportional gain was calculated. Figure 8.53 shows the plot of the actual proportional gain versus the set value of the proportional gain. In this case it is, as expected, a linear relation.

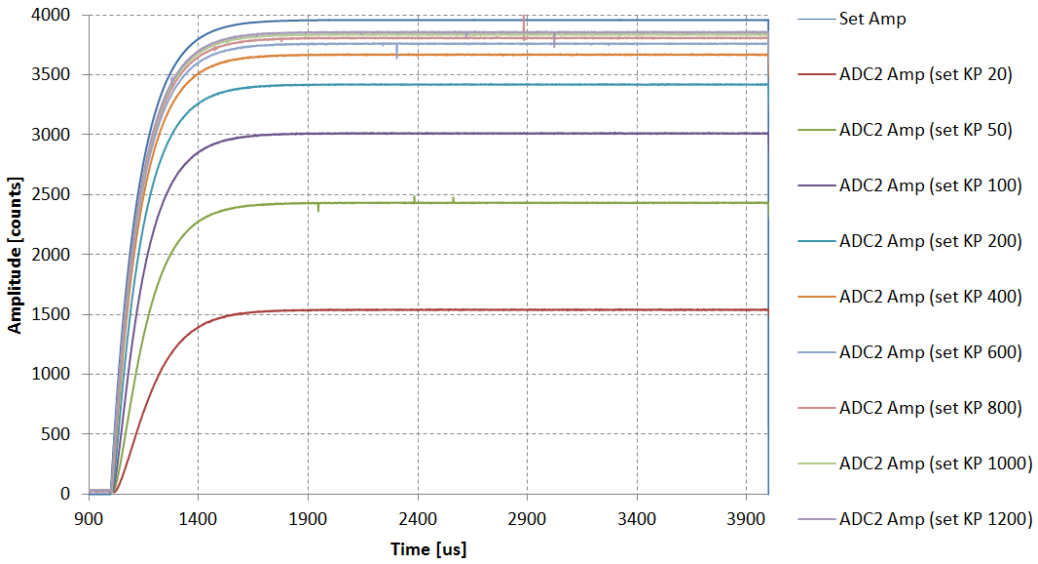


Figure 8.52: Set point (blue) and ADC2 (all other colors) amplitudes [counts] versus time [$\mu$s] of the controller board during a proportional gain scan with DAC IIR filter as cavity simulator.

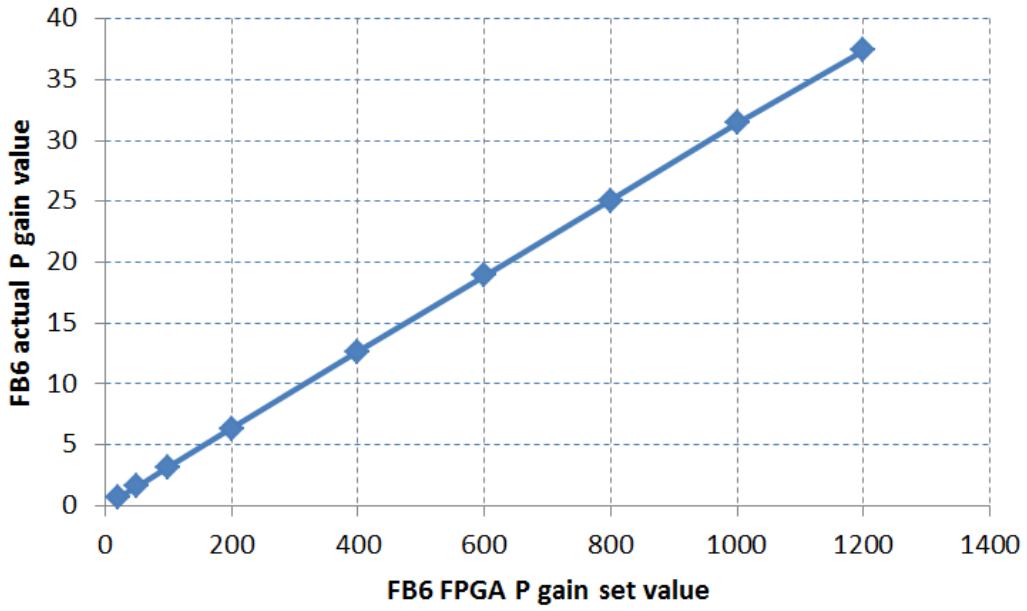


Figure 8.53: Actual proportional gain versus FPGA P gain set value for the proportional gain scan with DAC IIR filter as cavity simulator.

In Figure 8.54 the two gain scans are compared in terms of actual proportional gain versus the set value of the proportional gain. With this a proof of concept of the klystron–cavity simulator under feedback operation was shown. It is recommended to to include a klystron linearization algorithm on the controller board and repeat the open and closed loop operation tests again.

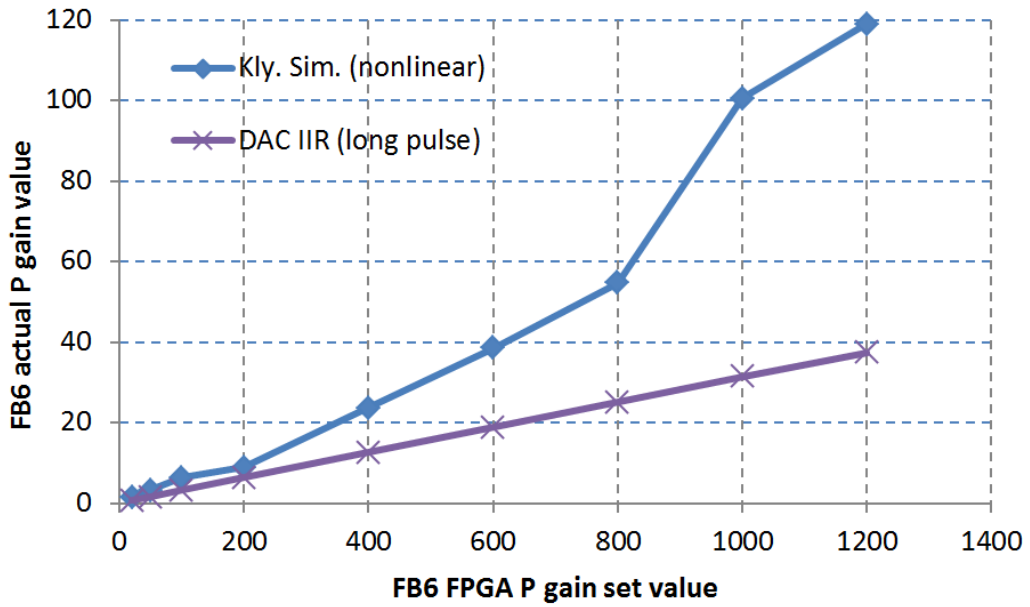


Figure 8.54: Comparison of actual proportional gain versus FPGA P gain set value for proportional gain scans with and without nonlinearities included.

# Chapter 9

# Conclusion and Future Prospects

ILC is a proposed future electron–positron collider. In its two main linacs 15814 superconducting L–band TESLA–like cavities will be operated. The problems discussed in this dissertation are related to the digital LLRF control system of those cavities. LLRF control is necessary in order to maintain suitable and stable acceleration fields inside the cavities. This is a requirement for good quality beams.

The motivation of this work is to develop and provide digital LLRF control techniques and procedures required for the realization of ILC. With a successful demonstration of those at an ILC–like accelerator, the feasibility of the realization of ILC was demonstrated.

In the scope of this dissertation ILC and ILC–like facilities around the world were described. Furthermore introductions to the theory of digital LLRF control and cavities were given.

The main objects of the study were stable operation of multiple cavities driven by a single klystron at high gradients close to their respective quench limits over the whole flattop ($P_kQ_L$ control), stable long–time operation of cavities with a high loaded quality factors $Q_L$, and the improvement of existing as well as the development of new predistortion–type klystron linearization algorithms. Solutions of the corresponding problems have been proposed and evaluated during the dissertation studies. The work can be summarized as follows:

- A script for the determination of the $P_kQ_L$ working point for an arbi-

trary number of cavities driven by a single klystron was written. Its functionality was evaluated using a cavity simulator.

- A $P_kQ_L$ setting procedure in order to reach reach the determined $P_kQ_L$ working point was developed and a corresponding script for the application at STF was written.

- The world's first actual $P_kQ_L$ operation with beam and ILC–like operation parameters was demonstrated at STF using two superconducting cavities driven by a single klystron. In a stable long–time operation the ILC stability requirements were fulfilled.

- The same $P_kQ_L$ setting procedure was validated in a simulation for the ILC configuration, covering 39 cavities driven by a single klystron and the respective waveguide system.

- The waveguide reflectors and waveguide phase shifters of the waveguide distribution system for the two superconducting cavities at STF in the scope of the QB project were characterized in respect their change of cavity phases and cavity loaded Q values.

- A successful long–time high $Q_L$ operation at $Q_L = 2 \cdot 10^7$ with beam was demonstrated fulfilling the ILC stability requirements.

- At DESY an FPGA–based predistortion–type klystron linearization algorithm was reimplemented for the MTCA.4 hardware. Furthermore the lookup table creation script was improved.

- At FNAL three different kinds of FPGA–based predistortion–type klystron linearization algorithms were developed. A proof of concept of all algorithms was demonstrated during test runs at ASTA.

- At KEK a further FPGA–based predistortion–type klystron linearization algorithm was proposed, which has regarding the simulation the best linearization performance of all introduced algorithms.

- At KEK an FPGA–based klystron–cavity simulator was developed, implemented, and tested.

The result of the successfully implemented $P_kQ_L$ control procedure and successful demonstration of the $P_kQ_L$ operation at STF is a very important milestone for the development of technologies towards the realization of ILC. In combination with the simulation of the $P_kQ_L$ control of 39 cavities the feasibility of ILC from the viewpoint of digital LLRF control was proven.

Nevertheless, it is important to repeat a similar study with actual test runs at higher cavity gradients corresponding to the ILC design values. Furthermore, the procedure should to be tested in a setup with a larger amount of cavities driven by a single klystron, preferably with 39 cavities and an ILC–like waveguide distribution system. In the near future the accelerator closest to these demands will be STF–2.

The successful long–time high $Q_L$ operation was a further important milestone on the way to the realization of ILC. The operation of the cavities with high $Q_L$ values becomes necessary in the scope of the previously discussed $P_k Q_L$ operation. It was proven that even in the case of very narrow cavity bandwidths the detuning mainly induced by microphonics can be kept sufficiently low due to the compensation via piezo tuners.

In the comparison of the actual implemented and tested FPGA–based predistortion–type klystron linearization algorithms, the algorithm based on lookup tables with linear interpolation is the best choice, since it has the best linearization performance. The development and test of the polynomial function–based algorithms showed that klystron linearizations can also be realized in a more memory efficient way. Since high power amplifiers are widely used, this algorithm can be implemented in appropriate cases. Corresponding to the simulation, the proposed algorithm, which is based on lookup tables with interpolation and adaptive grid spacing, has the best linearization performance. In future this algorithm should be tested in an actual setup and be used at ILC. For future developments and testing also the klystron–cavity simulator could be used. A further recommended field of study is the klystron characterization during operation in order to keep the accelerator downtime as low as possible.

# Appendix A

# Estimation of I and Q Values in IQ Sampling

The following calculation follows [49]. In general the value measured by an ADC can be described as

$$x = I\cos(\phi) + Q\sin(\phi) \ , \tag{A.1}$$

which means that for $n$ samples the ADC measures

$$\begin{aligned} x_1 &= I\cos(\phi_1) + Q\sin(\phi_1) \\ x_2 &= I\cos(\phi_2) + Q\sin(\phi_2) \\ &... \\ x_n &= I\cos(\phi_n) + Q\sin(\phi_n) \ . \end{aligned} \tag{A.2}$$

In order to calculate $I$ and $Q$ $\cos(\phi_1)...\cos(\phi_n)$ and $\sin(\phi_1)...\sin(\phi_n)$ are substituted by $a_1...a_n$ and $b_1...b_n$. Subtracting also $x_1...x_n$ yields

$$\begin{aligned} a_1 I + b_1 Q - x_1 &= 0 \\ a_2 I + b_2 Q - x_2 &= 0 \\ &... \\ a_n I + b_n Q - x_n &= 0 \ . \end{aligned} \tag{A.3}$$

Adding all these equations and multiplying those with $a_1$ and $b_2$ results in the following linear system

$$
\begin{aligned}
I\sum_{i=1}^{n} a_i^2 + Q\sum_{i=1}^{n} a_i b_i - \sum_{i=1}^{n} a_i x_1 = 0 \\
I\sum_{i=1}^{n} a_i b_i + Q\sum_{i=1}^{n} b_i^2 - \sum_{i=1}^{n} b_i x_1 = 0 \ .
\end{aligned}
\tag{A.4}
$$

Adding all summands without $I$ and $Q$ and substituting the following

$$
\begin{aligned}
s_1 &= \sum_{i=0}^{n-1} x_i \sin(i\phi) \\
s_2 &= \sum_{i=0}^{n-1} x_i \cos(i\phi) \\
a_{11} &= \sum_{i=0}^{n-1} \cos^2(i\phi) \\
a_{12} = a_{21} &= \sum_{i=0}^{n-1} \sin(i\phi)\cos(i\phi) \\
a_{22} &= \sum_{i=0}^{n-1} \sin^2(i\phi)
\end{aligned}
\tag{A.5}
$$

yields

$$
\begin{aligned}
a_{11}I + a_{12}Q = s_1 \\
a_{12}I + a_{22}Q = s_2 \ .
\end{aligned}
\tag{A.6}
$$

$n\phi = k \cdot 2\pi$ holds, where $k$ is an integer. In the case of IQ sampling $n = 4$ and $k = 1$. This yields

$$
\begin{aligned}
\sum_{i=0}^{n-1} \sin(i\phi)\cos(i\phi) = a_{12} = a_{21} = 0 \\
\sum_{i=0}^{n-1} \sin^2(i\phi) = \sum_{i=0}^{n-1} \cos^2(i\phi) = a_{11} = a_{22} = \frac{n}{2} = 2 \ .
\end{aligned}
\tag{A.7}
$$

Inserting this into (A.6) yields

$$\begin{aligned} \frac{n}{2} + 0 \cdot Q &= s_1 \\ 0 \cdot I + \frac{n}{2} Q &= s_2 \ , \end{aligned} \tag{A.8}$$

which can be rewritten as

$$\begin{aligned} I &= \frac{2s_1}{n} \\ Q &= \frac{2s_2}{n} \ . \end{aligned} \tag{A.9}$$

Resubstituting (A.5) yields

$$\begin{aligned} I &= \frac{2}{n} \sum_{i=0}^{n-1} x_i cos(i\phi) \\ Q &= \frac{2}{n} \sum_{i=0}^{n-1} x_i sin(i\phi) \ . \end{aligned} \tag{A.10}$$

# Appendix B

# Estimation of $Q_L$ Value During Cavity Voltage Decay

In general the decay of the cavity voltage after turning off the driving power in the case of a time discrete representation can be described by

$$V_{cav}(N_{\text{off}} + n) = V_{cav}(N_{\text{off}}) \cdot e^{-\frac{n}{\tau}} \quad , \tag{B.1}$$

where $N_{\text{off}}$ is the time step on which the RF power is turned off, $n$ a arbitrary number of steps in time, $V_{cav}(N_{\text{off}} + n)$ the voltage at the time $N_{\text{off}} + n$, $V_{cav}(N_{\text{off}})$ the voltage at the time of turning off the RF power, and $\tau$ the mean lifetime. In order to compute the value for $Q_L$, equation B.1 can be rewritten as

$$\ln\left(V_{cav}(N_{\text{off}} + n)\right) = -\frac{n}{\tau} + \ln\left(V_{cav}(N_{\text{off}})\right) \quad . \tag{B.2}$$

Using a general linear equation

$$y = a \cdot n + b \tag{B.3}$$

the following identifications can be made:

$$a = -\frac{1}{\tau} \tag{B.4}$$

$$b = \ln\left(V_{cav}(N_{\text{off}})\right) \tag{B.5}$$

In order to compute the steepness $a$ by evaluating a range of $N$ points in time the following expression can be used

$$a = \frac{N\sum_{i=1+l}^{N+l} x_i y_i - \sum_{i=1+l}^{N+l} x_i \sum_{i=1+l}^{N+l} y_i}{N\sum_{i=1+l}^{N+l} x_i^2 - \left(\sum_{i=1+l}^{N+l} x_i\right)^2} \quad , \tag{B.6}$$

where $l$ represents delay time steps between $N_{\text{off}}$ and the evaluation range of $N$. refer to Figure B.1 for an example.

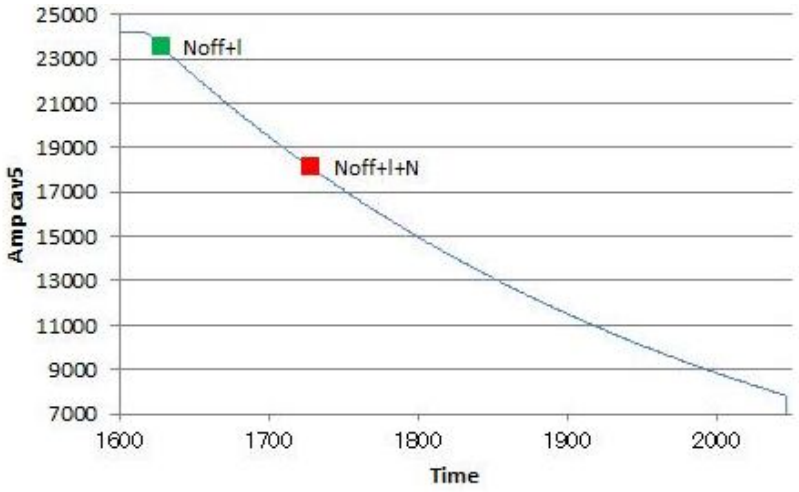


Figure B.1: *Decay of cavity voltage (blue), startig point of evaluation range (green), and end point of evaluation range (red). In this case Noff=1618, l=10, and N=100.*

By knowing the steepness $a$ one can use the equation

$$Q_L = \frac{\omega_{\text{RF}}}{2}\tau \cdot 10^{-6} \tag{B.7}$$

in order to calculate $Q_L$, where $\omega_{\text{RF}} = 2\pi \cdot f_0$. In this case $f_0 = 1.3 \cdot 10^9$ GHz. Inserting equation B.6 in equation B.4 and this in equation B.7 yields

$$Q_L = -1300\pi \frac{N\sum_{i-1+l}^{N+l} x_i^2 - \left(\sum_{i=1+l}^{N+l} x_i\right)^2}{N\sum_{i=1+l}^{N+l} x_i y_i - \sum_{i=1+l}^{N+l} x_i \sum_{i=1+l}^{N+l} y_i} \quad . \tag{B.8}$$

This is a general expression of $Q_L$ at $f_0 = 1.3$ GHz. In case of parameters shown in Figure B.1 $Q_L = 1.554 \cdot 10^6$.

By setting $N_{\text{off}}$ and $l$ to a arbitrary values and varying $N$ the dependency of $Q_L$ regarding $N$ can be described. Figure B.2 shows a plot of $Q_L$ over $N$ with $N_{\text{off}} = 1618$ and $l = 10$.

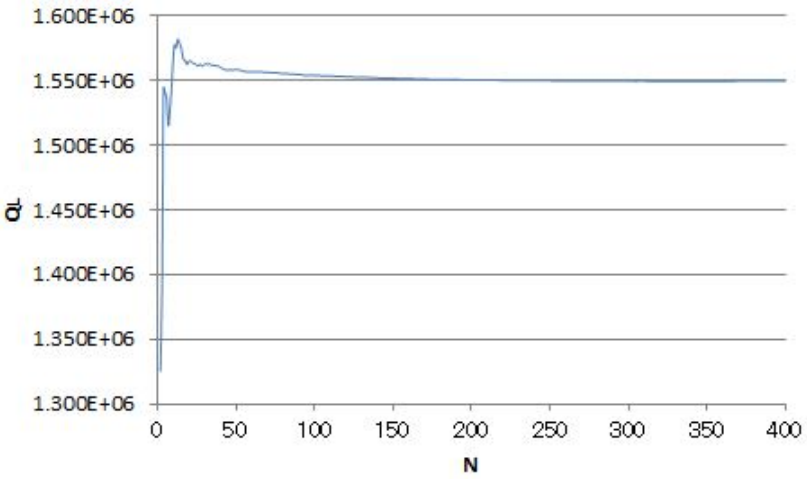


Figure B.2: *$Q_L$ over N with Noff=1618 and l=10.*

The outcome of this analysis is that $N$ should be not smaller than about 25 in order to keep the error of $Q_L$ low.

# Abbreviations

| | |
|---|---|
| ACNET | Accelerator network |
| ADC | Analog to digital converter |
| AMC | Advanced Mezzanine Cards |
| AMTF | Accelerator module test facility |
| ASTA | Advanced superconducting test accelerator |
| BBFB | Beam based feedback |
| BLC | Beam loading compensation |
| CA | Channel access |
| CAV | Cavity |
| cERL | Compact energy recovery linear accelerator |
| CERN | Conseil Européen pour la Recherche Nucléaire |
| CIC | Cascaded integrator—comb |
| CM | Cryomodule |
| CMTB | Cryomodule test bench |
| CORDIC | Coordinate rotation digital computer |
| cPCI | Compact peripheral component interconnect |
| DAC | Digital to analog converter |
| DOOCS | Distributed object oriented control system |
| DSP | Digital signal processor |
| EPICS | Experimental physics and industrial control system |
| FEL | Free electron laser |
| FF | Feedforward |
| FIR | Finite impulse response |
| FLASH | Free Electron Laser in Hamburg |
| FNAL | Fermi National Accelerator Laboratory |
| FPGA | Field programmable gate array |
| HLRF | High level radio frequency |
| IF | Intermediate frequency |
| IIR | Infinite impulse response |
| ILC | International Linear Collider |
| INFN | Istituto Nazionale di Fisica Nucleare |
| IOTA | Integrable Optics Test Accelerator |
| JDDD | Java DOOCS Data Display |
| KEK | Ko Enerugi Kasokuki Kenkyu Kiko |
| LabCA | Laboratory channel access |
| LFF | Learning feedforward |
| LHC | Large Hadron Collider |

| | |
|---|---|
| Linac | Linear accelerator |
| LLRF | Low level radio frequency |
| LO | Local oscillator |
| LUT | Lookup table |
| MA | Modulating anode |
| MFC | Multi–channel field controller |
| MIMO | Multiple input multiple output |
| PI | Proportional integral |
| PVS | Partial vector sum |
| R&D | Research and development |
| RF | Radio frequency |
| RTM | Rear transition module |
| SASE | Self–amplified stimulated emission |
| SCC | Superconducting cavity |
| SMP | Step motor position |
| SNR | Signal to noise ratio |
| STF | Superconducting RF test facility |
| TESLA | TeV–Energy Superconducting Linear Accelerator |
| TTF | TESLA test facility |
| uDWC | uTCA down converter |
| uTC | uTCA controller |
| uTCA | Micro telecommunications computing architecture |
| uVM | uTCA vector modulator |
| VH | Variable hybrid |
| VME | Versa module eurocard |
| VSWR | Voltage standing wave ratio |
| WPS | Waveguide phase shifter |
| WR | Waveguide reflector |
| XUV | Extreme ultraviolet |

# Symbols

| | |
|---|---|
| $a$ | Parameter |
| $A$ | Amplitude |
| $A_{actual}$ | Actual amplitude |
| $A_{in}$ | Input amplitude |
| $A_{LO}$ | Amplitude of local oscillator signal |
| $A_{out}$ | Output amplitude |
| $A_{RF}$ | Amplitude of radio frequency signal |
| $A_{set}$ | Set point amplitude |
| $\alpha$ | Complex correction function list |
| $b$ | Parameter |
| $B$ | Amplitude |
| $\beta$ | Coupling factor |
| $\beta_{opt}$ | Optimal coupling factor |
| $c$ | Parameter |
| $C$ | Capacitance, measured ADC count |
| $C_1$ | Constant |
| $C_2$ | Constant |
| $d$ | Parameter |
| $\delta C_{ind}$ | Measured ADC count for beam induced change in gradient |
| $\delta\omega$ | Detuning of cavity |
| $\delta\phi$ | Vector rotation between two steps in time |
| $\delta V_{ind}$ | Beam induced change in gradient |
| $E_{Cav1}$ | Gradient of cavity 1 |
| $E_{Cav2}$ | Gradient of cavity 2 |
| $f$ | Parameter |
| $f_0$ | Resonance frequency |
| $f_{corr}$ | Correction factor |
| $f_{corr,l}$ | Correction factor for amplitude limitation |
| $f_{corr,i}$ | I component of complex correction factor |
| $f_{corr,q}$ | Q component of complex correction factor |
| $f_{IF}$ | Frequency of intermediate frequency signal |
| $f_{lin}$ | Linear function |
| $f_{LO}$ | Frequency of local oscillator signal |
| $f_{RF}$ | Frequency of radio frequency signal |
| $f_s$ | Sampling frequency |
| $g$ | Parameter |

| | |
|---|---|
| $h$ | Parameter |
| $I$ | In–phase component |
| $I'$ | Corrected in–phase component |
| $\hat{I}$ | Phasor of current $I_{cav}$ |
| $I_0$ | Initial in–phase component |
| $I_b$ | Beam current |
| $\hat{I}_b$ | Phasor of beam current |
| $I_C$ | Current over $C$ |
| $\dot{I}_C$ | Time derivative of current over $C$ |
| $I_{cav}$ | Current driving the RLC circuit or cavity |
| $\dot{I}_{cav}$ | Time derivative of current driving the RLC circuit or cavity |
| $\hat{I}_{cav}$ | Amplitude of of current driving the RLC circuit or cavity |
| $I_{for}$ | Forward current |
| $I_g$ | Generator current |
| $\hat{I}_g$ | Phasor of generator current |
| $I_{in}$ | Input in–phase component |
| $I_{i,n-1}$ | In–phase component of current at time step $n-1$ |
| $I_L$ | Current over the inductance $L$ |
| $\dot{I}_L$ | Time derivative of current over the inductance $L$ |
| $I_{out}$ | Output in–phase component |
| $I_{q,n-1}$ | Quadrature component of current at time step $n-1$ |
| $I_R$ | Current over the resistance $R$ |
| $\dot{I}_R$ | Time derivative of current over the resistance $R$ |
| $k$ | Integer |
| $k_p$ | Proportional gain |
| $L$ | Inductance, Integer |
| $limit$ | Preset limit value |
| $M$ | Integer |
| $m$ | Ratio between M and |
| $m_n$ | List of slopes between nodes |
| $n$ | counter of steps or nodes |
| $N_{off}$ | Step of RF off |
| $\nu_n$ | List of $(y_n - x_n \cdot m_n)$ |
| $\omega_0$ | Angular frequency |
| $P$ | Driving power |
| $P_{diss}$ | Dissipated power |
| $P_{ext}$ | Dissipated power in external devices |
| $P_{fill}$ | Power during filling |
| $P_{flat}$ | Power during flattop |

| | |
|---|---|
| $P_{flat,min}$ | Minimal driving power during flattop and beam transient |
| $P_{in}$ | Input power at input port in |
| $P_k$ | Cavity driving power |
| $P_{min}$ | Minimal driving power |
| $P_{out1}$ | Output power at output port out1 |
| $P_{out2}$ | Output power at output port out2 |
| $P_{sqrt}$ | Square root of klystron output power |
| $P_{tot}$ | Total power loss |
| $\phi$ | Phase |
| $\phi_1$ | Phase difference between measurement points A and B |
| $\phi_2$ | Phase difference between measurement points A and C |
| $\phi_b$ | Beam phase |
| $\phi_{LO}$ | Phase of local oscillator signal |
| $\phi_{opt}$ | Optimal phase |
| $\phi_{RF}$ | Phase of radio frequency signal |
| $Q$ | Quadrature component |
| $Q'$ | Corrected quadrature component |
| $Q_0$ | Initial quadrature component, unloaded quality factor |
| $Q_{ext}$ | External quality factor |
| $Q_{in}$ | Input quadrature component |
| $Q_L$ | Loaded quality factor |
| $Q_{L,cav1}$ | Loaded quality factor of cavity 1 |
| $Q_{L,cav2}$ | Loaded quality factor of cavity 2 |
| $Q_{L,opt}$ | Optimal loaded quality factor |
| $Q_{out}$ | Output quadrature component |
| $R$ | Resistance |
| $r$ | power ratio |
| $R_L$ | Loaded shunt impedance |
| $R_{sh}$ | Shunt impedance |
| $S_{IF}(t)$ | Time dependent intermediate frequency signal |
| $S_{LO}(t)$ | Time dependent local oscillator signal |
| $S_{LO\cdot RF}(t)$ | Time dependent signal of $S_{LO}(t)$ mixed with $S_{RF}(t)$ |
| $S_{RF}(t)$ | Time dependent radio frequency signal |
| $\sigma_{\Delta f,cav1}$ | Standard deviation of detuning of cavity 1 |
| $\sigma_{\Delta f,cav2}$ | Standard deviation of detuning of cavity 2 |
| $t$ | Variable representing time |
| $T$ | Time period of an RF cycle |
| $\tau$ | Cavity time constant |
| $T_{inj}$ | Injection time of the beam |

| | |
|---|---|
| $t_n$ | Time of step n |
| $T_s$ | Sampling time |
| $\Theta$ | Angle of forward voltage |
| $V$ | Cavity gradient to be calculated |
| $\hat{V}$ | Phasor of voltage $V_{cav}$ |
| $V_0$ | Initial cavity voltage |
| $V_{cav}$ | Cavity voltage or RLC circuit voltage |
| $\dot{V}_{cav}$ | Time derivative of cavity or RLC circuit voltage |
| $\ddot{V}_{cav}$ | Second time derivative of cavity or RLC circuit voltage |
| $V_{fill}$ | Cavity voltage during filling |
| $V_{flat}$ | Cavity voltage during flattop |
| $V_{for}$ | Forward voltage |
| $V_{hom}$ | Homogeneous solution of cavity differential equation |
| $V_{i,n}$ | In–phase component of the voltage at time step $n$ |
| $V_{par}$ | Particular solution of cavity differential equation |
| $V_{q,n}$ | Quadrature component of the voltage at time step $n-1$ |
| $V_{ref}$ | Reflected voltage |
| $W$ | Stored energy |
| $w_{1/2}$ | Half bandwidth |
| $x$ | Input value |
| $x_n$ | Nodes of input values |
| $y$ | Estimated output value |
| $y_{IF,n}$ | Amplitude of IF signal at time step n |
| $y_n$ | Nodes of output values, vector component at step n |
| $z$ | Complex list of expected klystron output |
| $z'$ | Complex list of linear target function |
| $Z_{ext}$ | External load |

# List of Figures

# List of Tables

# Bibliography


[1] "The International Linear Collider – Technical Design Report – Volume 1: Executive Summary", CERN, FNAL, KEK (2013).

[2] "The International Linear Collider – Technical Design Report – Volume 3.II: Accelerator Baseline Design", CERN, FNAL, KEK (2013).

[3] T. Saito, Masaki Asano et al., "Extra dimensions and Seesaw Neutrinos at the International Linear Collider", Physical Review D, Vol. 82, Issue 9, id. 093004 (2010).

[4] H. Dreiner, M. Huck et al., "Illuminating Dark Matter at the ILC", Physical Review D, Vol. 87, id. 075015 (2013).

[5] "TESLA Technical Design Report - PART II - The Accelerator ", http://flash.desy.de

[6] K. Kubo, "Summary of ILC Main Linac Specs", Presentation at the International Workshop on Linear Colliders 2010 (ECFA-CLIC-ILC Joint Meeting), Geneva (2010), http://agenda.linearcollider.org/conferenceOtherViews.py?view=standard&confId=4507

[7] E. Kako, H. Hayano et al., "Cryomodule Tests of Four TESLA–like Cavities in the STF Phase–1.0 for ILC", TU3RAI04, Proceedings of PAC09, Vancouver (2009).

[8] A. Kuramoto and H. Hayano, "Alignment Detection Study using Beam Induced HOM at STF", MOPME019, Proceedings of IPAC2013, Shanghai (2013).

[9] J. Urakawa, "Compact X–Ray Source at STF (Super Conducting Accelerator Test Facility", Journal of Physics: Conference Series 357 012035, doi: 10.1088/1742-6596/357/1/012035, (2012).

[10] M. Kuriki, H. Iijima et al., "RF Processing of L-Band RF Gun for KEK–STF", MOPC014, Proceedings of IPAC2011, San Sebastian (2011).

[11] H. Shimizu, Y. Higashi et al., "Stable Planar Type Four–Mirror Cavity Develoment for X–Ray Production as Basic Development of Quantum Beam Technology Program", TUPO012, Proceedings of IPAC2011, San Sebastian (2011).

[12] http://www.aps.anl.gov/epics/

[13] N. Arnold, "Getting Started with EPICS Lecture Series at APS", Argonne National Laboratory, Argonne (2004).

[14] http://asta.fnal.gov/

[15] E. Harms, "ASTA Update" (Presentation), FNAL, Batavia (2014).

[16] R. Kammering and C. Schmidt, "Feedbacks and Automation at the Free Electron Laser in Hamburg (FLASH)", THPPC121, Proceedings of ICALEPCS2013, San Francisco (2013).

[17] A. Kondratenko and E. L. Saldin, "Generation of Coherent Radiation by a Relativistic Electron Beam in a Ondulator", Particle Accelerators Vol. 10 (1980).

[18] M. Vogt, B. Faatz et al., "The Free–Electron Laser FLASH at DESY", TUPEA004, Proceedings of IPAC2013, Shanghai (2013).

[19] "The European X-Ray Free Electron Laser Technical Design Report", http://xfel.desy.de

[20] J. Branlard, G. Ayvazyan et al., "The European XFEL LLRF System", MOOAC01, Proceedings of IPAC2012, New Orleans (2012).

[21] T. Schilcher, "Applications in Digital Signal Processing", CAS - CERN Accelerator School: Course on Digital Signal Processing, Sigtuna (2007).

[22] T. Miura, D. Arakawa et al., "Performance of the $\mu$TCA Digital Feedback Board for DRFS Test at KEK–STF", MOPC155, Proceedings of IPAC2011, San Sebastian (2011).

[23] E. Vogel, "High Gain Proportional RF Control Stability at TESLA Cavities", Physical Review Special Topic - Accelerator and Beams, 10, 052001 (2007).

[24] S. Kazakov, S. Fukuda et al., "L–Band Waveguide Elements for SRF Application", Proceedings of Particle Accelerator Society Meeting 2009, Tokai (2009).

[25] Y. Yamamoto, C. Pagani et al., "Test Results of the International S1-Global Cryomodule", THIOA01, Proceedings of SRF2011, Chicago (2011).

[26] P. Varghese, "Multi–cavity Field Control (MFC) Module Description", FNAL, Batavia (2009).

[27] http://www.cells.es/en

[28] H. Hassanzadegan and F. Perez, "Analogue LLRF for the ALBA Booster", TUPC147, Proceedings of EPAC08, Genoa (2008).

[29] T. Schilcher, "Vector Sum Control of Pulsed Accelerating Fields in Lorentz Force Detuned Superconducting Cavities" (PhD Thesis), Universität Hamburg, Hamburg (1998).

[30] S. Michizono, D. Arakawa et al. "Digital LLRF System for STF S1 Global", TUPEA047, Proceedings of IPAC2010, Kyoto (2010).

[31] S. Michizono, "LLRF", http://ilc.kek.jp/S1G/S1G_LLRFv4.docx , KEK, Tsukuba (2014).

[32] T. Matsumoto, S. Fukuda et al., "Development of Digital Low–Level RF Control System Using Multi–Intermediate Frequencies", WEPMN028, Proceedings of PAC2007, New Mexico (2007).

[33] T. Matsumoto, "Demonstration of DRFS", http://ilc.kek.jp/S1G/DRFS_20120316.doc , KEK, Tsukuba (2014).

[34] J. Branlard, V. Ayvazyan et al., "LLRF Automation for the 9mA ILC Tests at FLASH", THPB085, Proceedings of LINAC2012, Tel–Aviv (2012).

[35] W. Cichalewski, J. Branlard et al., "Superconducting Cavities Automatic Loaded Quality Factor Control at FLASH", Proceedings of RT2012, Berkeley (2012).

[36] J. Carwardine, S. Schreiber et al., "Report on the Second Workshop on Linac Operations with Long Bunch–trains", ILC report, 2011-032 (2011).

[37] K.L.F. Bane, C. Adolphsen et al., "RF Distribution Optimization in the Main Linacs of the ILC", WEPMS037, Proceedings of PAC07, New Mexico (2007).

[38] W. Cichalewski, "Linearization of Microwave High Power Amplifiers Chain in the RF Systems of Linear Accelerators for FLASH and X-FEL" (PhD Thesis), Technical University of Lodz, Lodz (2008).

[39] W. Cichalewski, "High Power Amplifier Chain Transfer Characteristics Linearization at FLASH - 9mA Studies & Future Plans" (Presentation), DESY, Hamburg (2012).

[40] M. Omet, H. Hayano et al., "High–gradient near–quench–limit Operation of Superconducting Tesla–type Cavities in Scope of the International Linear Collider", Physical Review Special Topics - Accelerator and Beam, 17, 072003 (2014).

[41] M. Yoshida, S. Fukuda et al., "The Quality Factor Adjustment of the Superconducting Cavity Using Waveguide Components in STF", Proceeding of Particle Accelerator Society Meeting 2009, Tokai (2009).

[42] M. Omet, S. Michizono et al., "FPGA–based Klystron Linearization Implementations in Scope of ILC", Nuclear Instruments and Methods in Physics Research Section A: Accelerators, Spectrometers, Detectors and Associated Equipment, DOI: 10.1016/j.nima.2014.09.007 (2014).

[43] J. Patrick, "The Fermilab Accelerator Control System", WEA2IS03, Proceedings of ICAP2006, Chamonix (2006).

[44] J. Branlard, V. Ayvazyan et al., "Equipping FLASH with a MTCA.4–based LLRF System" Proceeding of SRF2013, Paris (2013).

[45] J. Branlard, G. Ayvazyan et al., "MTCA.4 LLRF System for the European XFEL" Proceeding of MIXDES 2013, Gdynia (2013).

[46] J. Branlard, "Update on XFEL LLRF system development and production" (Presentation), LLRF2013, Tahoe (2013).

[47] http://tesla.desy.de/doocs/doocs.html

[48] http://jddd.desy.de/

[49] M. Grecki, "Measurements of RF Field Vector", Technical University of Lodz, Lodz.

# Acknowledgments

I thank everyone who supported me writing this thesis starting with my supervisor Shinichiro Michizono. His advices were always helpful and his support amazing. Furthermore I thank Toshihiro Matsumoto especially for the time during the accelerator operation at STF and the fruitful discussions. Beside this I thank Takako Miura and Feng Qiu.

Outside the LLRF group at KEK I thank Akira Yamamoto for believing in me and supporting me by making my participation in the PhD course in Japan possible. I thank Kei Sugita for the introduction to KEK and his support in Germany. Furthermore I would like to thank Hitoshi Hayano for his support before and during my PhD studies. I also thank Ayaka Kuramoto, Taro Konomi, and Tokio Ohska.

From the Fermilab LLRF department I thank Brian Chase, Philip Varghese, Ed Cullerton, and Dave Vander Meulen for their great support and the good time during two stays.

From the DESY MSK department I thank Holger Schlarb, Julien Branlard, Wojciech Cichalewski, Christian Schmidt, Sven Pfeifer, and Uros Mavric for their great support and the good time during the stay.

I thank my entire family for their great support even over the long distance at any time. I also thank my fiancé and her parents for the great support in Japan. Furthermore I thank all friends who also supported me.

Mathieu Omet

# Declaration

I declare that I wrote this preliminary Ph.D.–thesis independently and without any other references and resources than stated in the bibliography.

Tsukuba, September 2014